PNNL-30047

Evaluation of Containment and Geomechanical Risks at Integrated Mid-Content Stacked Carbon Storage Hub Sites

National Risk Assessment Partnership Tool Application

August 2020

D Appriou
NJ Huerta
ZF Zhang
JA Burghardt
DH Bacon

Prepared for the U.S. Department of Energy
under Contract DE-AC05-76RL01830

PACIFIC NORTHWEST NATIONAL LABORATORY
operated by
BATTELLE
for the
UNITED STATES DEPARTMENT OF ENERGY
under Contract DE-AC05-76RL01830

Printed in the United States of America

Available to DOE and DOE contractors from the
Office of Scientific and Technical Information,
P.O. Box 62, Oak Ridge, TN 37831-0062;
ph: (865) 576-8401
fax: (865) 576-5728
email: reports@adonis.osti.gov

Available to the public from the National Technical Information Service
5301 Shawnee Rd., Alexandria, VA 22312
ph: (800) 553-NTIS (6847)
email: orders@ntis.gov <https://www.ntis.gov/about>
Online ordering: http://www.ntis.gov

PNNL-30047

Evaluation of Containment and Geomechanical Risks at Integrated Mid-Content Stacked Carbon Storage Hub Sites

National Risk Assessment Partnership Tool Application

August 2020

D Appriou
NJ Huerta
ZF Zhang
JA Burghardt
DH Bacon

Prepared for
the U.S. Department of Energy
under Contract DE-AC05-76RL01830

Pacific Northwest National Laboratory
Richland, Washington 99354

Executive Summary

Carbon capture and storage (CCS) is one technology in the advanced stages of development that can mitigate the anthropogenic release of CO_2 to the atmosphere from fossil fuel power production and other industrial facilities. While this technology can leverage knowledge from analogous subsurface activities, such as oil and gas production and wastewater disposal, there is inherent risk in injecting vast quantities of CO_2 into the subsurface over several decades.

The U.S. Department of Energy is leading the development of CCS through collaborative projects and programs to not only develop and demonstrate the technology but to also quantify the risks and provide tools that site operators can use to develop a site-specific understanding of their risk to enable successful project operations.

This report summarizes results and findings from the application of risk-assessment tools to an industrial-scale Geologic Carbon Storage (GCS) project. Specifically, we applied the National Risk Assessment Partnership's (NRAP) Open Integrated Assessment Model (NRAP-Open-IAM) and State of Stress Assessment Tool (SOSAT) to two candidate sites being considered for storage by the Integrated Midcontinent Stacked Carbon Storage Hub (IMSCS-HUB) project team. These sites, the Sleepy Hollow Field in Nebraska and Patterson-Heinitz-Hartland (PHH) Field in Kansas, have historical oil and gas production. Each are attractive candidates to meet the CarbonSAFE objective to store the 50 million metric tons (Mt) . Because these sites have historical operations, they have a significant number of existing wells that pose a risk for well leakage. Additionally, the storage formations will undergo significant pore pressure perturbation (i.e., increase due to CO_2 injection). Hence, we have selected the two NRAP tools best suited to study the risks associated with well leakage and geomechanical risks. The objective of the study was not only to assess the risk at the site, but to also improve the NRAP tools through application using real site data on an ongoing project.

Our Key Findings for this work are:

1. When using the NRAP-Open-IAM and allowing for leakage to occur in all wells the amount of CO_2 leaked is significantly below the 1% CO_2 leakage metric commonly stated as an acceptable threshold. Further, the detectability of such leaks is generally limited to a few 10s of meters around the well, making impact detection a challenge.

2. While a high-level risk estimation is possible with little data, uncertainty in the parameters used to estimate well leakage risk need to be reduced to enable more impactful results. For example, a better understanding of overlying aquifer properties would improve impact estimation and a better estimate for the probability and magnitude of well leak permeability would guide monitoring and corrective action decisions. Characterization of groundwater aquifers is a requirement under Class VI UIC.

3. The PHH and Sleepy Hollow sites are in a transition zone between an extensional tectonic province and a strike-slip tectonic province and more site-specific data are needed to reduce the uncertainty in geomechanical risks. The risk of shear failure on a hypothetical critically-oriented fault is relatively high for both sites and is primarily due to the absence of stress measurement. Stress measurements obtained in the

targeted formations would constrain the state of stress and significantly reduce the uncertainties.

4. Similarly, the risk of unintentional hydraulic fracturing exists given substantial uncertainty at the Sleepy Hollow site based on the current information available. With more information, the uncertainty will go down and the risk may go down. The risk is limited at the PHH site with the maximum injection pressures considered. Uncertainties related to the elastic properties will be reduced by performing analysis on the core collected as part of the current phase of the project.

5. When applying the NRAP tools, it is important that the study objective and expected outcome are defined early in the project's lifecycle. Doing so would improve data collection efforts and lead to more robust and less uncertain risk assessments.

6. While the NRAP tools have a robust design basis, they should be improved to more clearly identify what project risks they are addressing and how they can be used by site operators to enable project activities, like obtaining a Class VI permit.

Acknowledgments

This work was completed as part of the U.S. Department of Energy's (DOE's) CarbonSAFE project, which was supported by the DOE Office of Fossil Energy. The work was performed by Pacific Northwest National Laboratory (PNNL) under DOE contract number DE-AC05-76RL01830.

The authors want to thank the Battelle Columbus team, especially Mackenzie Scharenberg, Valerie Smith, and Jared Hawkins as well as Jenny Meng and Eugene Holubnyak from the Kansas Geological Survey for their support. The authors would also like to thank Chris Brown at PNNL for his review of this report.

Acronyms and Abbreviations

AZMI	Above Zone Monitoring Interval
bgs	Below ground surface
CarbonSAFE	Carbon Storage Assurance Facility Enterprise
CCS	Carbon capture and storage
CO_2	Carbon Dioxide
DITF	Drilling induced tensile fracture
EOR	Enhanced oil recovery
GCS	Geologic Carbon Storage
GUI	Graphical User Interface
IMSCS-HUB	Integrated Midcontinent Stacked Carbon Storage Hub
Mt	Million metric tons
NRAP	National Risk Assessment Partnership
NRAP-Open-IAM	NRAP’s Open Source Integrated Assessment Model
RCSP	Regional Carbon Sequestration Partnership
SOSAT	NRAP’s State of Stress Assessment Tool
TDS	Total Dissolved Solids
U.S. DOE	U.S. Department of Energy
USDW	Underground Source of Drinking Water

Contents

Figures

Tables

1.0 Introduction

Geologic carbon storage (GCS) is part of the portfolio of solutions aimed to reduce anthropogenic atmospheric emissions of carbon dioxide from industrial point sources. Over the last two decades, several initiatives led by the U.S. Department of Energy's Office of Fossil Energy (DOE) aimed to accelerate the development of this technology. The National Risk Assessment Partnership (NRAP) was initiated in 2011 with the goal of developing science-based methodologies and platforms for quantifying risks amidst system uncertainty, and to better inform decision making for carbon storage sites[1]. In parallel, DOE created a network of seven Regional Carbon Sequestration Partnership (RCSPs) to support the development of regional infrastructure for carbon capture and storage (CCS). The RCSPs contributed to the development and verification of carbon storage related technologies including characterization, modeling and simulation, mitigation, and risk assessment and to the identification of the most promising storage opportunities in each region.

The lessons learned from the RCSPs led to the creation of the Carbon Storage Assurance Facility Enterprise (CarbonSAFE) initiative (U.S. DOE). This initiative is perceived as one of the last steps to address technical barriers to commercial-scale carbon storage and focuses on the development of GCS sites that can be used to store more than 50 million metric tons of CO_2 from industrial sources.

The study presented in this report intends to leverage efforts and lessons learned from the different U.S. DOE initiatives mentioned above. Two tools developed as part of the NRAP initiative were applied to two sites of the IMSCS-HUB CarbonSAFE project with the goal of 1) estimating the risk of CO_2 leakage at a site (NRAP-Open-IAM tool), and 2) evaluating the geomechanical risks associated with CO_2 injection (SOSAT).

1.1 CarbonSAFE and the IMSCS-HUB

The CarbonSAFE Initiative is aimed at developing multiple integrated carbon storage complexes across the United States with targeted deployment between 2025 and 2030. Each subsurface storage complex should be suited to receive and safely store 50 Mt of industrially sourced CO_2. As a follow-on to the RCSPs, the CarbonSAFE initiative aims to provide greater assurance that commercial-scale CCS projects can be technically and economically integrated and deployed.

The CarbonSAFE initiative is a four-phase effort[2]: (1) Pre-Feasibility, (2) Storage Complex Feasibility, (3) Site Characterization, and (4) Permitting and Construction. As of Spring 2020, six projects, including the IMSCS-HUB, are concluding work performed as part of Phase II. One main objective of this phase of the IMSCS-HUB project, led by Battelle Memorial Institute, is to evaluate and demonstrate the feasibility of stacked storage complexes at two potential sites, one located in southwest Nebraska and one in western Kansas.

This CO_2 storage hub will gather CO_2 from multiple sources from eastern and central Nebraska, transport it southwest toward Red Willow County, Nebraska along a CO_2-source collection corridor (Bacon et al. 2018). The captured CO_2 will be injected in local stacked-storage reservoirs located at the end of the source corridor, and piped further southeast into central

[1] https://netl.doe.gov/sites/default/files/rdfactsheet/R-D179_0.pdf

[2] https://www.netl.doe.gov/coal/carbon-storage/storage-infrastructure/carbonsafe

Kansas accessing additional storage sites and used in existing oilfields for carbon storage and enhanced oil recovery (EOR) (Bacon et al. 2018).

The candidate sites considered to safely, permanently and economically store anthropogenic CO_2 through stacked-storage are the Sleepy Hollow field, Nebraska and PHH field, Kansas (Figure 1.1).

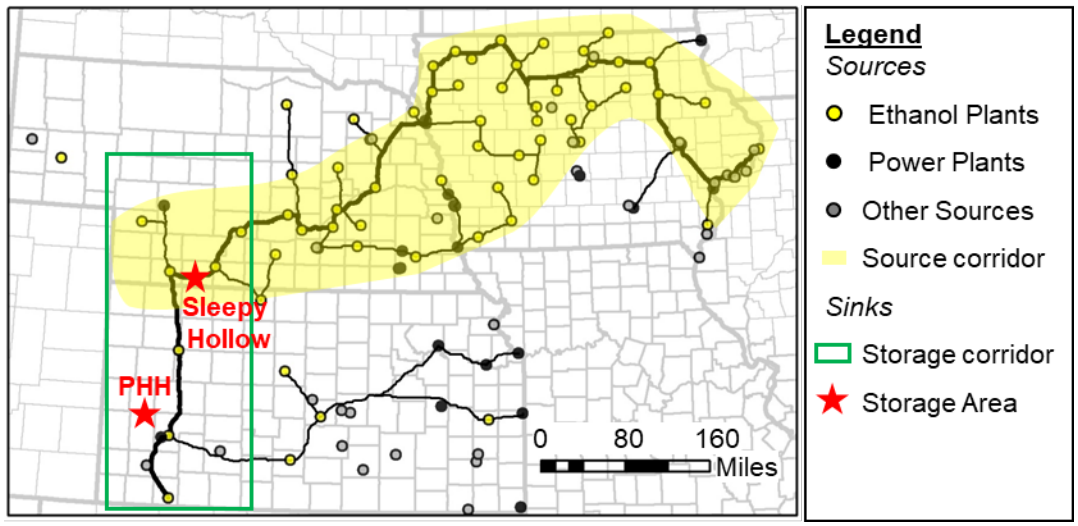

Figure 1.1. Location of the two candidate sites in southeast Nebraska (Sleepy Hollow) and Kansas (PHH), (Bacon et al. 2018).

1.2 Scope and objective

This study focuses on the application of two NRAP tools to assess risks associated with CO_2 injection of at these two candidate sites. Risks evaluated include the risk of endangering Underground Sources of Drinking Water (USDWs) by through two mechanisms: (1) migration of CO_2 and/or brine from the storage reservoir and (2) re-activating existing faults or creating new hydraulic fractures by altering the state of stress by injection of CO_2.

The overall objective of this study is to present a methodology for each tool, accessible to operators, that could be applied to a proposed GCS site to evaluate potential risks associated with CO_2 injection. This risk evaluation is essentially based on the integration of uncertainties inherent to the subsurface in which engineering operations should be performed safely to maintain the integrity of the storage complex and protect overlying groundwater aquifers.

1.2.1 NRAP's Integrated Assessment Model

The NRAP open-source integrated assessment model (NRAP-Open-IAM) is a python-based, publicly available[1] systems-level model that can be used to stochastically simulate risk at a GCS. The NRAP-Open-IAM takes in the reservoir simulation results, along with data on the stratigraphy, well leak properties, fluid properties, and utilizes component modules to conduct an analysis to estimate risk over time. Risk in this exercise focuses on brine and/or CO_2 leakage into aquifers from the two wells that will be used in the GCS operation, the injection well, and a

[1] https://gitlab.com/NRAP/OpenIAM

single monitoring well. In addition to leak rates for brine and CO_2, the NRAP-Open-IAM analysis looks at the impact of this leakage on three metrics (pressure, total dissolved solids [TDS], and pH) that are indicators of changes to aquifer quality and are also used as monitoring metrics to detect leaks.

For both the Sleepy Hollow and PHH field the NRAP-Open-IAM was used to understand leakage risk and uncertainty. Because site characterization data was still being collected and interpreted, this assessment south to quantify different aspects of risk and uncertainty for the two sites and to study their impacts. Given that these sites were also fields with a history of oil and gas production, the risk of well leakage and the subsequent impact into an overlying aquifer was the principal focus of the study.

The version of the NRAP-Open-IAM we used was Release alpha 2.0.0-20.02.02; component modules used are: Reservoir Lookup Table, Multisegmented Well Model, and the Aquifer Impact Model.

Reservoir look up table

A Lookup Table Reservoir component model is a reduced order model based on interpolation of data from a set of lookup tables. The lookup tables are based on the results of multiphase flow simulations of CO_2 into a storage reservoir. Each row of the lookup table is related to a particular set of model input parameters and contains pressures and saturations at selected time steps for a particular horizontal layer of the multiphase flow model.

This linkage is not fully coupled, and thus the reservoir simulations and associated look up table do not respond to losing mass due to well leakage. This assumption results in a conservative estimate (i.e., over-estimate) of the brine and CO_2 leakage rates, although this factor is not as significant for smaller leak rates.

Multisegmented well model

The multisegmented wellbore component uses a semi-analytic solution (Nordbotten, Celia, and Bachu 2004; Nordbotten et al. 2005; Nordbotten et al. 2009) to simulate the leakage of CO_2 and brine along a wellbore. The Multisegmented Wellbore component model assumes that leakage is occurring in the annulus between the outside of the casing and borehole. This area is assigned an effective permeability for the flow path. This model allows for the leakage of fluid phases into multiple aquifers and allows each well segment to have a different permeability.

The component model takes in pressures and saturations as a function of time and well parameters to calculate brine and CO_2 leakage rates into overlying aquifers and back to the atmosphere. The total mass of CO_2 and brine leaked are also calculated. The outputs from the multisegmented wellbore component are used as inputs to calculate the leakage impact to overlying aquifers.

Aquifer impact model

The FutureGen2 aquifer impact model was developed to quantify impacts to an aquifer due to CO_2 and brine leakage (Bacon et al. 2019) along wells. The FutureGen2 Aquifer component model is a regression model, fitted to these simulations of CO_2 and brine leakage into an aquifer. The aquifer simulations were performed with a wide range of input parameters (Table

1.1) and CO_2 and brine leakage rates, ranging from $1x10^{-9}$ kg/s to 31.6 kg/s, so that the resulting aquifer Component model could be applicable to other sites.

Table 1.1 Ranges of input parameters for aquifer component.

Aquifer Parameters	min	max
Thickness (m)	30	90
Depth (m bgs)	-700	-100
Porosity	0.02	0.2
Horizontal Permeability ($\log_{10}$ m^2)	-14	-11
Anisotropy ($\log_{10}$ Kh/Kv)	0	3
Calcite (solid volume fraction)	0	1
Leakage Parameters	min	max
CO_2 Rate ($\log_{10}$ kg/s)	-9	1.5
Brine Rate ($\log_{10}$ kg/s)	-9	1.5

The impact metrics used in this study where dissolved CO_2 concentration, pH change, TDS, and pressure change. The impact thresholds were selected due to their potential use as a monitoring signal for leakage.

The thresholds values used are:

- Dissolved CO_2: change above 100 mg/L
- pH: value below 6.75
- TDS: change above 100 mg/L
- Pressure: change of 500 Pa above or below initial

These metric thresholds are used to calculate the bulk volume of an aquifer that is above the threshold and to calculate a diameter of aquifer impacted (centered around the leaky well). These results not only give a sense of the dimensions of an aquifer impact but can also be used to inform monitoring well placement.

1.2.2 State of Stress Assessment Tool

The state of stress influences several potential risks associated with fluid injection as part of the exploitation of natural resources such as hydrocarbon, geothermal energy, or CO_2 storage. Recently, the strong increase in injection-induced seismicity associated with deep wastewater injection has received widespread attention (Langenbruch and Zoback 2016; Walsh and Zoback 2015). Because of the similarities between CO_2 injection and other subsurface activities involving fluid injection, the seismic risk associated with carbon storage operations is real and risk assessment is critical to informing any decision-making, ranging from site screening and characterization to the determination of operational parameters.

Pore pressure increase associated with subsurface operations perturbs in-situ stress conditions and can cause suitably oriented faults or fractures to slip because of reduced normal effective stress and increased shear stress. Fault activation can generate problematic seismicity and can potentially be a leak path. Faults that are oriented to maximize the possibility of slip are referred to as “critically oriented” fractures. Similarly, faults that would require only a minor increase in fluid pressure to slip are referred to as “critically stressed” faults. For any activities involving fluid injection, such as CO_2 injection, evaluation of critically stressed faults and prediction of the geomechanical behavior is therefore fundamental for understanding the placement and orientation of injection wells, determining the main operational parameters such as the injection rate and maximum allowable injection pressure, or for deploying a risk-based monitoring strategy.

Several deterministic methods have been developed over the last three decades to estimate in situ stresses. However, none of these approaches quantify uncertainties. While unquantified uncertainties are acceptable for some applications because the risks associated with incorrect estimation are limited (Burghardt 2018), geomechanical concerns are among the principal project risk factors for other applications, including CCS. For large-scale CO_2 injection projects, incorrect estimations of stress tensor components leading to fault reactivation and threatening seal integrity can potentially cause property damage, public nuisance and concern, or contamination of drinking water with brine or CO_2 (Nicol et al. 2011; White et al. 2016; Mark D. Zoback and Gorelick 2012). These extreme consequences could eventually jeopardize the viability of a project and the entire industry (Burghardt 2018).

Burghardt (2018) developed a comprehensive Bayesian approach and demonstrated its use on an active enhanced oil recovery/geologic carbon sequestration field in estimating in situ stress and geomechanical risk associated with fluid disposal. This approach modifies two commonly used stress estimation methods—the stress polygon approach developed by (M. D. Zoback et al. 2003) and the one-dimensional (1D) tectonic-elastic approach of Thiercelin and Plumb (1994)—using a Bayesian method to account for uncertainty in some of the input parameters. The details related to the Bayesian method are extensively detailed in Burghardt (2018).

This approach was incorporated into a user-friendly environment developed as part of NRAP, known as the SOSAT, which is available on the National Energy Technology Laboratory’s Energy Data eXchange platform[1]. SOSAT provides an easy to use physics-based tool to calculate a probability distribution for in situ stress at a particular vertical location using a variety of common data types. The parameters used to estimate the state of stress can be expressed either as a probability distribution reflecting the degree of certainty with which the parameters are known or as deterministic parameters. These parameters, some required and some optional, include information about the storage formation (e.g., injection depth, pore pressure), about the regional stress regime, and about the elastic properties of the formations considered for analysis.

Using this stress state probability distribution, SOSAT calculates the probability of activating a critically oriented fault at a specified range of pore pressures. The result can then be used for estimating the risk of induced seismicity and unintentional hydraulic fracturing. The approach used in SOSAT is conservative because it assumes that a critically oriented fault exists (i.e., a fault is aligned with a plane of maximum shear stress) in the storage site. Furthermore, because faults can be activated aseismically, which may pose little to no risk, making decisions based on the risk of activation is also inherently conservative. For this effort, we assessed the geomechanical risks associated with CO_2 injection at the Sleepy Hollow and PHH sites based on the current data available for each site.

[1] https://edx.netl.doe.gov/nrap_wpsandbox/state-of-stress-analysis-tool-sosat/

1.3 Document structure

The report is organized as follows. Section 2.0 introduces the Sleepy Hollow site context, with information about the field history, general stratigraphy, key formations targeted for CO_2 operations, geomechanical information and main operational parameters relevant to perform the assessment of leakage risks and evaluate the state of stress at the site. The evaluation of leakage risks and the assessment of the state of stress respectively performed with NRAP-Open-IAM and SOSAT are then presented in Sections 3.0 and 4.0. Similarly, the PHH Site general context is introduced in Section 5.0, with leakage risk assessment and evaluation of the state of stress described in Sections 6.0 and 7.0, respectively.

Key findings from the application of the NRAP tools and subsequent recommendations to users and operators are discussed in section 8.0

2.0 Overview of Sleepy Hollow Site, NE

2.1 Setting and field history

The Sleepy Hollow site is in Red Willow County, southwestern Nebraska (Figure 2.1). The oil field, discovered in 1960, is the most productive field in Nebraska and is delineated by a high-density cluster of wells (about one well per 40 acres) over a surface of 28 mi^2. The field consists of a northeast-southwest trending anticlinal structure located on the southwestern flank of a deeply buried structure feature, the Cambridge Arch (Christopher, Clark, and Gibson 1988). This arch formed in granitic basement rock about 470 million years ago and has uplifted several times over geologic time. Fluvial channels incised the Precambrian surface while it was exposed in Early Pennsylvania time. Erosion and runoff on the arch produced a sandstone unit from the base of the Pennsylvanian, also referred to as the Basal sandstone.

Historically, oil production at the Sleepy Hollow field started with the development of the Basal Desmoinesian sandstone (Figure 2.2) (Rogers 1977), that produced more than 38 million barrels. Zones in the Lansing and Kansas City groups, consisting mostly of alternating limestone and shale layers deposited after the sandstone, were later developed and supplied an equivalent of about 20% of the total production at the field (Carlson et al. 1989; Rogers 1977).

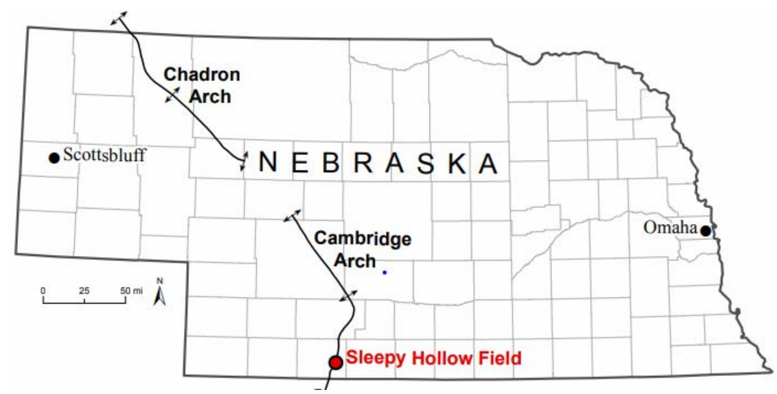

Figure 2.1. Location of the Sleepy Hollow Oil Field, and of the Cambridge Arch (Divine, Eversoll, and Howard 2018).

2.2 Storing CO_2 at the Sleepy Hollow field

Porous and permeable Paleozoic deep saline carbonate formations have been identified as potential geologic storage complexes at the Sleepy Hollow field.

2.2.1 Reservoir formations and confining units

At Sleepy Hollow Oil Field, deep saline CO_2 storage is being proposed and evaluated in four main lithostratigraphic groups of the Pennsylvanian system. They include the porous limestones of the Pleasanton-Marmaton and Lansing-Kansas City groups (A, D-F), and the sandstone intervals of the Shawnee-Douglas and the Wabaunsee groups (Figure 2.2). The deep saline storage zones are found at average depths ranging from 2,862 ft (872.3m) to 3,390 ft (1,000.33 m) (Duguid et al. 2020a).

Multiple overlying formations have been identified as potential sealing caprocks and are formed by shales, carbonates, and evaporites. These formations, deposited during the Late Pennsylvanian and Permian, include Admire Council Grove, Sumner, and Lower Nippewalla groups (Figure 2.2).

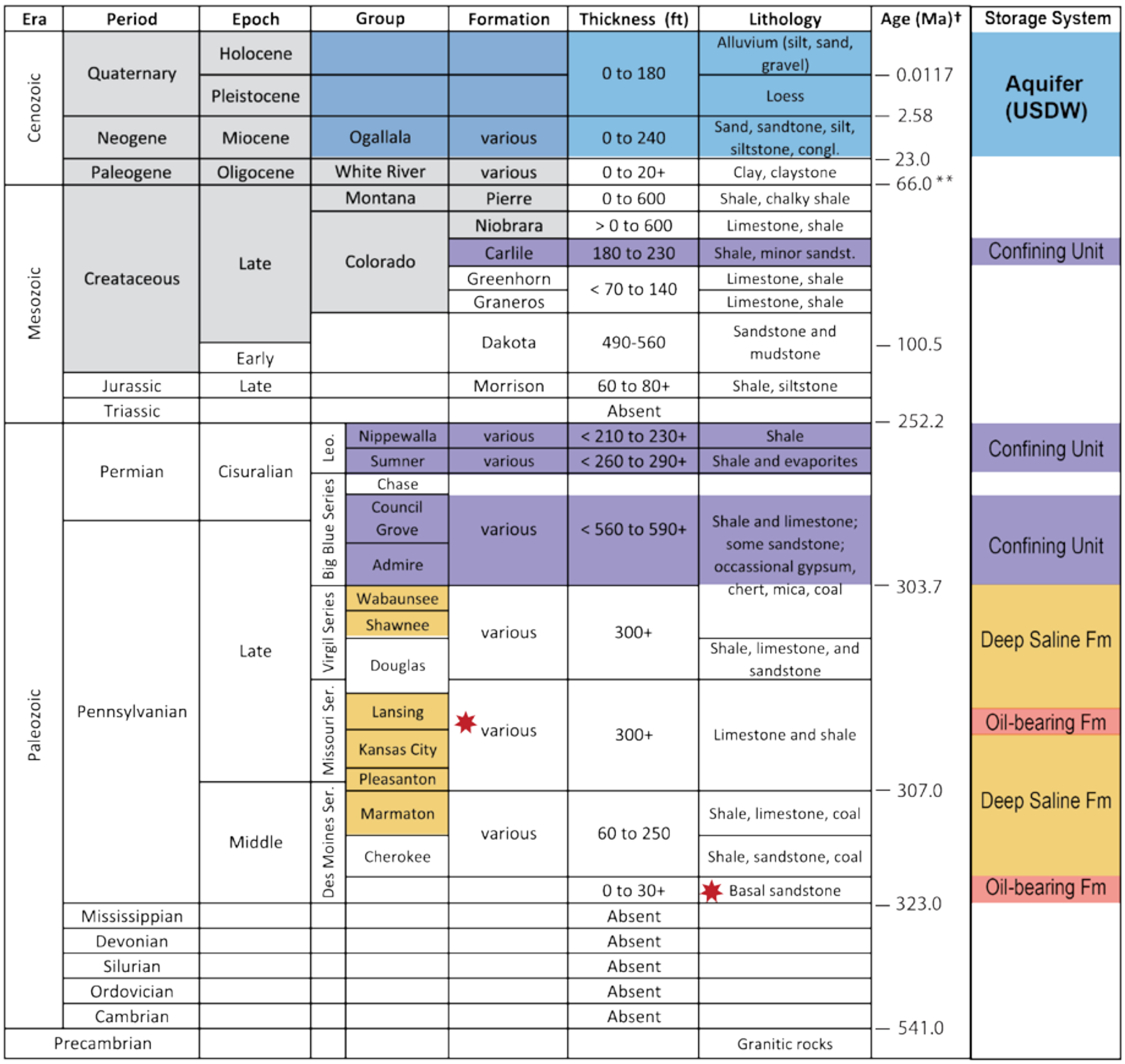

Era	Period	Epoch	Group	Formation	Thickness (ft)	Lithology	Age (Ma)†	Storage System
Cenozoic	Quaternary	Holocene			0 to 180	Alluvium (silt, sand, gravel)		Aquifer (USDW)
		Pleistocene				Loess	0.0117	
	Neogene	Miocene	Ogallala	various	0 to 240	Sand, sandtone, silt, siltstone, congl.	2.58	
	Paleogene	Oligocene	White River	various	0 to 20+	Clay, claystone	23.0	
Mesozoic	Createaceous	Late	Montana	Pierre	0 to 600	Shale, chalky shale	66.0 **	
			Colorado	Niobrara	> 0 to 600	Limestone, shale		
				Carlile	180 to 230	Shale, minor sandst.		Confining Unit
				Greenhorn	< 70 to 140	Limestone, shale		
				Graneros		Limestone, shale		
		Early		Dakota	490-560	Sandstone and mudstone	100.5	
	Jurassic	Late		Morrison	60 to 80+	Shale, siltstone		
	Triassic				Absent		252.2	
Paleozoic	Permian	Cisuralian	Leo. Nippewalla	various	< 210 to 230+	Shale		Confining Unit
			Leo. Sumner	various	< 260 to 290+	Shale and evaporites		
			Big Blue Series Chase					
			Big Blue Series Council Grove	various	< 560 to 590+	Shale and limestone; some sandstone; occassional gypsum, chert, mica, coal		Confining Unit
	Pennsylvanian	Late	Big Blue Series Admire				303.7	
			Virgil Series Wabaunsee	various	300+			Deep Saline Fm
			Virgil Series Shawnee					
			Virgil Series Douglas			Shale, limestone, and sandstone		
			Missouri Ser. Lansing	various	300+	Limestone and shale		Oil-bearing Fm
			Missouri Ser. Kansas City					
			Missouri Ser. Pleasanton				307.0	Deep Saline Fm
		Middle	Des Moines Ser. Marmaton	various	60 to 250	Shale, limestone, coal		
			Des Moines Ser. Cherokee			Shale, sandstone, coal		
					0 to 30+	Basal sandstone	323.0	Oil-bearing Fm
	Mississippian				Absent			
	Devonian				Absent			
	Silurian				Absent			
	Ordovician				Absent			
	Cambrian				Absent		541.0	
Precambrian						Granitic rocks		

† Million years ago

Figure 2.2. Complete stratigraphic section encountered at Red Willow County and the associated key stratigraphic units of the storage system evaluated (modified after Divine, Eversoll, and Howard (2018).

The formation tops identified in the SHRU-86A stratigraphic well drilled in June 2019 were used to build the stratigraphic column for the Sleepy Hollow Site. The storage reservoir formation tops are identified by the gamma ray log (Figure 2.3). The complex stratigraphy in Figure 2.2 was simplified for use in the NRAP-Open-IAM by defining one reservoir unit, two aquifer units, and three interspersed “shale” units. The term shale is somewhat a misnomer and is simply used to define a layer where fluid cannot leak to, as opposed to the Aquifer units that permit leakage.

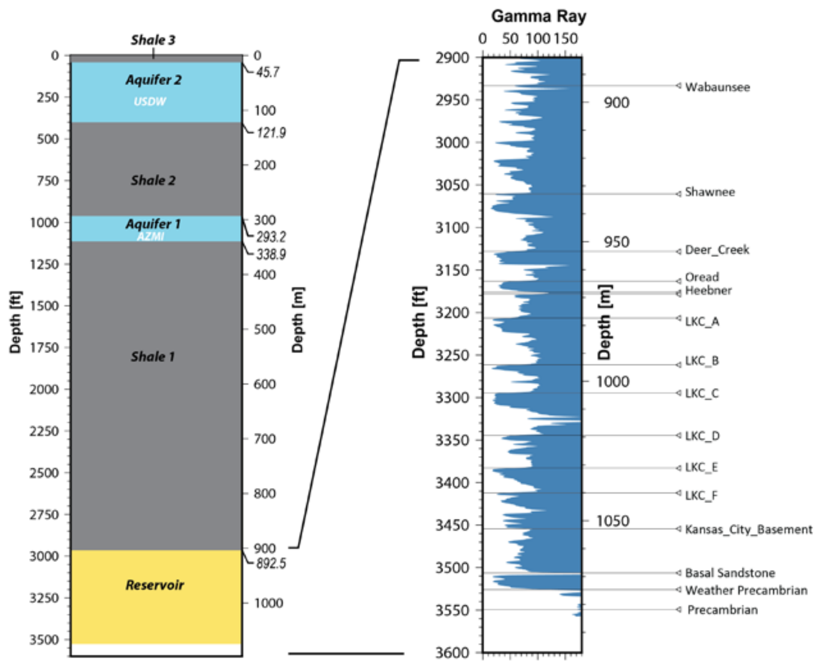

Figure 2.3. Simplified stratigraphic column of the storage complex used for NRAP-OPEN-IAM (left) and formation tops of the storage units revealed by the gamma ray log from the SHRU-86A (right).

2.2.2 Above Zone Monitoring Interval

For this exercise, we assume there is some porous and permeable subunit within the Cretaceous Dakota formation group that can serve as an Above Zone Monitoring Interval (AZMI), which is also called Aquifer 1 in the NRAP-Open-IAM.

2.2.3 Aquifers and Underground Sources of Drinking Water

The High Plains Aquifer is identified as a nationally important water resource that underlies about 174,000 mi^2 across eight states, including Nebraska and Kansas (Figure 2.4). The High Plains aquifers includes various geologic formations, although the Ogallala Formation in the main water-bearing formation. For this reason, the High Plain Aquifer is also referred to as the Ogallala Aquifer.

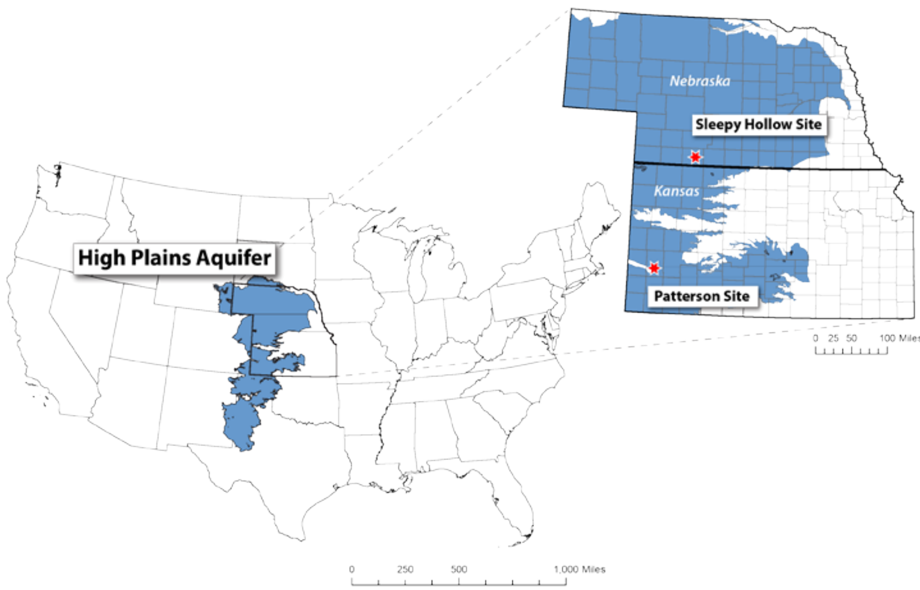

Figure 2.4. Extent of the High Plains Aquifer across the US (left) with a focus on Nebraska and Kansas (right).

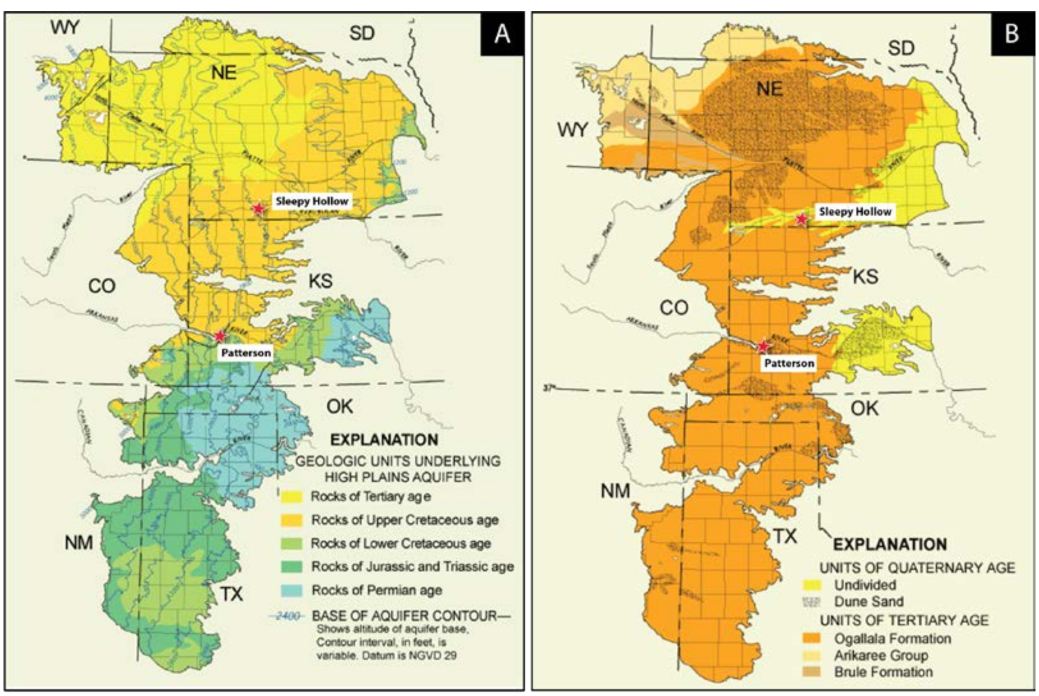

Figure 2.5. High Plains Aquifer: A) principal geologic units that constitute the High Plains aquifer B) age of the geologic units underlying the High Plains aquifer (http://ne.water.usgs.gov/ogw/hpwlms/hydsett.html, last accessed on 4/27/2020).

In Red Willow County, the aquifers are alluvial sand and gravel in the river and stream valleys and the High Plains aquifer, consisting mainly of the Ogallala Group and some Quaternary sand and gravels (Divine, Eversoll, and Howard 2018), as illustrated in Figure 2.5. According to the same authors, alluvial and High Plains aquifers appear connected in Red Willow County and are therefore considered as one aquifer. It constitutes the USDW. Depth to water ranges from zero to about 200 ft (61 m) in the county but can reach 250 ft (76 m). At the location of the Sleepy Hollow Field, this depth to water is expected to range from approximately 100 (30 m) to 150 ft (46 m).

The Cretaceous surface constitutes the base of the High Plains Aquifer. At the location of the Sleepy Hollow Field (SHRU-86A stratigraphic well), the elevation of the bedrock is estimated to reach 2,300 ft (701 m), which gives a depth of top of the Cretaceous of about 260 ft (79 m) below the ground surface. Unconformably overlying the Ogallala is a surficial mantle of Quaternary loess and alluvium.

2.3 Storage operations and reservoir parameters

An assessment conducted at the Sleepy Hollow field using the stratigraphic data from SHRU-86A well showed that storing 50 Mt of CO_2 over 30 years was not viable at the project site. Therefore, two stacked scenarios were evaluated as part of the recent dynamic modeling efforts (Duguid et al. 2020a): one with half the target injection amount (25 Mt) using four horizontal wells (scenario 1), and the other maximizing the injection amount using ten horizontal wells (scenario 2). Four formations were considered for CO_2 injection: Wabaunsee, Topeka, Oread and Deer Creek. While the formations from the Lansing-Kansas City group were initially considered as potential storage intervals, recent characterization efforts revealed that these formations have lower permeabilities and do not contribute significantly to total injection capability. For the NRAP-Open-IAM analysis an earlier version (i.e., before SHRU-86A was drilled) of the Sleepy Hollow reservoir simulation was used and is described in more detail in section 3.1.1.

2.3.1 Injection depth

The injection depth for each well of the two scenarios considered are provided in Table 2.2. These depths range from 2,956 ft (901 m) to 3,183 ft (970.2 m). This information will later be used to conduct the geomechanical risk analysis using SOSAT and corresponds to the depth where the analysis will be conducted (Table 4.1.).

2.3.2 Pore pressure

Four drill stim tests (DST) run in the SHRU-86A well confirmed that the injection intervals are under-pressured compared to the hydrostatic gradient. A pressure gradient of 0.3575 psi/ft was estimated in the dynamic modeling (Duguid et al. 2020a) and will be used in the geomechanical risk assessment study. Using the pore pressure gradient derived from measurements, the predicted fluid pressure in injector 1 of the first scenario (3,100 ft or 945 m) is 1,108 psi (7.64 MPa) (Table 2.1).

2.3.3 Maximum injection pressure

The maximum injection pressure is a parameter used in the fault activation probability calculations of SOSAT. As part of the dynamic modeling activities conducted to assess the feasibility of storing CO_2 at the Sleepy Hollow field reported in Duguid et al. (2020a), the maximum pressure was determined as being as 95% of the fracture pressure gradient, assumed by the dynamic modeling team to be 0.7 psi/ft (15.83 MPa/km). The corresponding maximum pressured allowed was calculated for each injection well and are reported in Table 2.1.

As a reminder, the Federal Requirements under the Underground Injection Control Program for Carbon Dioxide Geologic Sequestration Wells (75 FR 77230, December 10, 2010), referred to as the Class VI Rule, requires that injection pressure not exceed 90% of the fracture pressure of the injection zone(s) to ensure that CO_2 injection does not initiate new fractures or propagate existing ones [40CFR §146.88(a)].

Table 2.1. Injection depths considered for the two stacked scenarios evaluated, initial pore pressure and maximum injection pressure considered.

Scenarios 1	Injection formation	Depth at BHP* ft	Depth at BHP* m	Max. Injection Pressure** psi	Max. Injection Pressure** MPa	Pore pressure*** psi	Pore pressure*** MPa
Inj-1	Oread	3,100	945	2,062	14.21	1,108	7.64
Inj-2	Oread	3,067	935	2,040	14.06	1,096	7.56
Inj-3	Wabaunsee	2,938	896	1,954	13.47	1,050	7.24
Inj-4	Wabaunsee	3,053	931	2,030	14.00	1,091	7.53
Scenarios 2	**Injection formation**	**Depth at BHP* ft**	**Depth at BHP* m**	**Max. Injection Pressure** psi**	**Max. Injection Pressure** Mpa**	**Pore pressure*** psi**	**Pore pressure*** MPa**
Inj-1	Wabaunsee	2,956	901	1,966	13.55	1,057	7.29
Inj-2	Topeka	3053	931	2,030	14.00	1,091	7.53
Inj-3	Oread	3,086	941	2,052	14.15	1,103	7.61
Inj-4	Wabaunsee	3,051	930	2,029	13.99	1,091	7.52
Inj-5	Topeka	2,977	907	1,980	13.65	1,064	7.34
Inj-6	Oread	3,183	970	2,117	14.59	1,138	7.85
Inj-7	Deer Creek	3,167	965	2,106	14.52	1,132	7.81
Inj-8	Wabaunsee	2,937	895	1,953	13.47	1,050	7.24
Inj-9	Deer Creek	3,018	920	2,007	13.84	1,079	7.44
Inj-10	Oread	3,101	945	2,062	14.22	1,109	7.64

**BHP = Bottom Hole Pressure,*
***fracture pressure gradient: 0.7 psi/ft*
****pore pressure gradient: 0.3575 psi/ft*

2.4 Well locations

For this analysis the injection wells and any existing wells that penetrated the storage formation were considered as potential leak sources. The injection wells were those identified in the reservoir simulations (Table 2.2). The existing wells were identified using the Nebraska Oil and Gas Conservation Commission's well database (Ref. found at: http://www.nogcc.ne.gov/). The wells in the Sleepy Hollow (and not Sleepy Hollow NW) field were used. Wells with similar locations or that may be duplicated entries were removed and the result was 276 existing wells used in this study. Figure 2.6 shows a map with both the injection and existing wells.

Table 2.2. Injection well locations used in the reservoir simulations.

Injection well	X, m	Y, m
Inj-1	384,962	4,451,406
Inj-2	385,724	4,452,777
Inj-3	387,858	4,451,406
Inj-4	386,944	4,449,425
Inj-5	386,944	4,446,529
Inj-6	383,896	4,444548

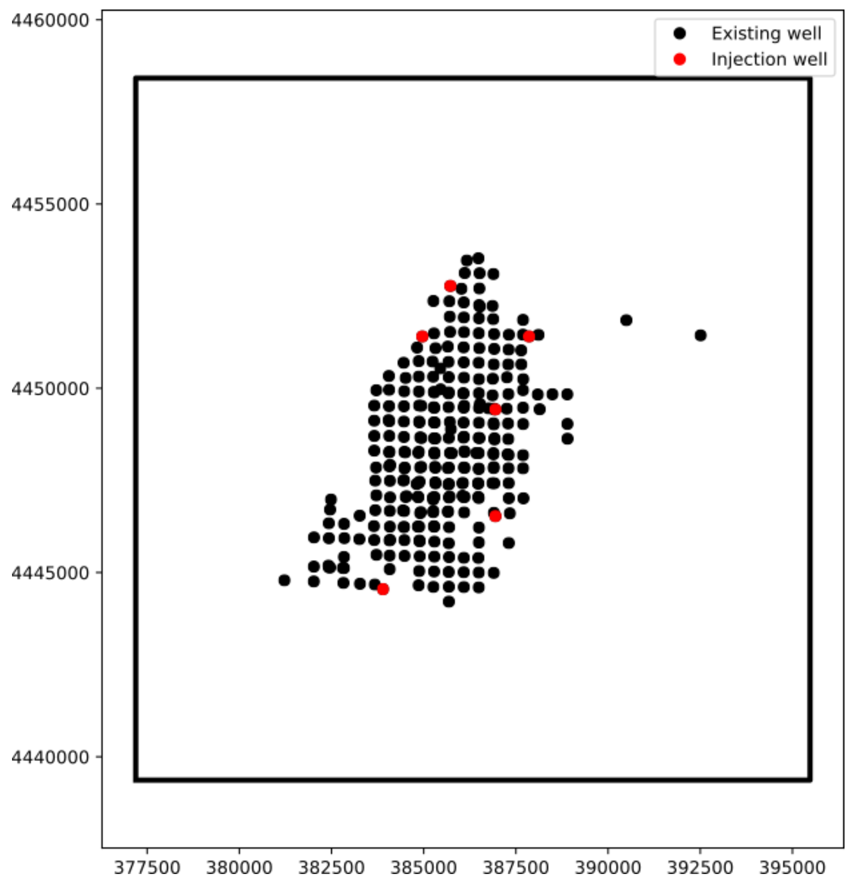

Figure 2.6. Map of the Sleepy Hollow field showing the locations of the 6 injection wells (red) and 276 existing wells (black).

2.5 In situ stress and regional stress observations

2.5.1 Overburden density and vertical stress determination

SOSAT requires the average overburden density as an input parameter, which is used to determine the magnitude of the vertical stress as a function of depth. It is assumed in this approach that one of the principal stresses is vertical such that the magnitude of the vertical stress S_v is determined as the weight of the overburden material given by:

$$S_v = \int_0^{z_0} \rho g dz \quad (1)$$

where z_0 is the depth of interest, ρ is the density, and g is the gravity acceleration.

Data from density logs collected in the SHRU-86A borehole are available from 1,606 to 3,600 ft bgs (489 to 1097 m). Between 0 and 1600 ft bgs (0 to 488 m), a linear gradient ranging from 2.2 to 2.3 g/cm^3 was assumed. Based on the density log, the average overburden density above the injection interval is 2.43 g/cm^3 (Figure 2.7). Although the vertical stress is directly computed in SOSAT, we determined and plotted the vertical stress profile by integrating the density log throughout the entire well (Figure 2.7). The values are taken as deterministic in SOSAT.

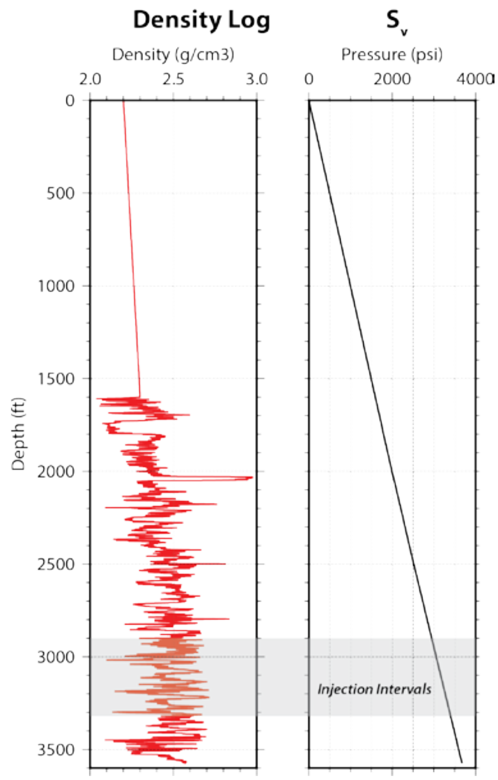

Figure 2.7. Density log (left) ad vertical stress profile Sv (right) calculated by integrating the density log from the SHRU-86A borehole. The average density above the injection intervals is 2.43 g/cm^3.

2.5.2 Regional observations of stress indicators

Figure 2.8 shows a map of the regional stress observations from the World Stress Map Database (Heidbach et al. 2018) that provides a global compilation of information on the current state of stress worldwide. This map clearly illustrates that very few data characterize the tectonic stress regime in this part of the continent where the two potential storage sites of the IMSCS-HUB are located. In the Midcontinent, a general east-west orientation of the maximum horizontal stress S_{Hmax} is observed.

A recent study from Lund Snee and Zoback (2020) mapped the evolution of the relative stress magnitudes throughout North America based on a compilation of stress indicators integrating new measurements (Figure 2.9). This map reveals a continent-scale transition from compression (strike-slip and or/reverse faulting) in eastern North American to strike-slip faulting in the midcontinent to primarily extension in western intraplate North America. This continent-scale interpretation of the stress field indicates that both Nebraska and Kansas are located at the transition between strike-slip regime (S_{Hmax}>S_v>S_{hmin}) and extensional regime (S_v >S_{Hmax} >S_{hmin}).

Earthquake moment tensor solutions can be used as indicators of current stress conditions. Crustal seismic events are expected to occur on preexisting faults, and resulting moment tensor solutions are therefore a function of the orientation of the pre-existing fault and of both the orientation and the relative magnitude of the principal stresses (M.L. Zoback et al. 1989). In order to get more indicators of the current stress field and reduce the uncertainty related to the stress regime, existing focal mechanisms in the region of the two targeted sites were plotted along the seismic event magnitudes in Figure 2.10. Earthquake moment tensor solutions were obtained from the Global Centroid-Moment-Tensor database[1] from January 1976 to February 2020 and from the Earthquake Center from Saint Louis University capturing events from 1962 to May 2020[2]. The catalogs from the National Earthquake Information Center[3] and from the Kansas Geological Survey[4] were used to compile events with magnitudes greater than 2.5 from 1980 to 2020.

Most of the focal mechanism solutions located in the northern part of Oklahoma and southern part of Kansas seem to confirm the presence of strike-slip faulting events, and also faults with components of normal and strike-slip. Pure normal slips are observed west of the Sleepy Hollow and PHH sites, in Colorado, while both strike-slip and normal faults are observed in Nebraska. The approximate stress province boundary differentiating the two regimes is therefore challenging to delineate. As of today, no stress measurements are available from well SHRU-86A and neighboring wells from the Sleepy Hollow field to assess the magnitude, or relative magnitude of the principal stresses. Analysis of image logs obtained in the SHRU-86A borehole can however help reduce some of the uncertainties. Two wellbore-failure features are commonly used as stress indicators: borehole breakouts (BO) and drilling-induced tensile fractures (DITF). No breakouts were observed either on the image or caliper logs. There are a few suspected drilling-induced tensile fractures (DITF) with E-W azimuth (suspected at 3074-3400 ft and 3398-3400 ft, 937.0-1036.3 m and 1035.7- 1036.3). DITFs open against the least principal stress, when the borehole is in tension, and propagate parallel to the direction of $S_{Hmax.}$ The presence of DITFs is often an indication of a large difference in magnitude between S_{hmin} and S_{Hmax}. Additionally, the sonic dispersion plot shows crossover at 1728.5ft, and indication of stress-induced anisotropy. However, the difference between the fast and slow shear waves is small. The sonic log shows minimal stress-induced anisotropy elsewhere in the well. This also indicates that the stress anisotropy is likely low. Both the suspected DITFs and sonic log polarization are consistent with a mostly E-W orientation of the maximum horizontal stress.

Based on the regional observations, the combination of lack of breakouts, minimal DITF, and very low shear wave splitting on the sonic logs, it is very likely, but not certain, that the Sleepy Hollow Field is not located in a strike-slip environment, and therefore that a normal faulting regime should be considered with a highest probability in the geomechanical risk analysis.

[1] https://www.globalcmt.org/CMTsearch.html, accessed on 3/1/2020
[2] http://www.eas.slu.edu/eqc/eqc_mt/MECH.NA/MECHFIG/mech.html, accessed on 5/21/2020
[3] https://earthquake.usgs.gov/earthquakes/search/ accessed on 3/13/2020
[4] http://www.kgs.ku.edu/Geophysics/Earthquakes/historic.html accessed on 3/12/2020

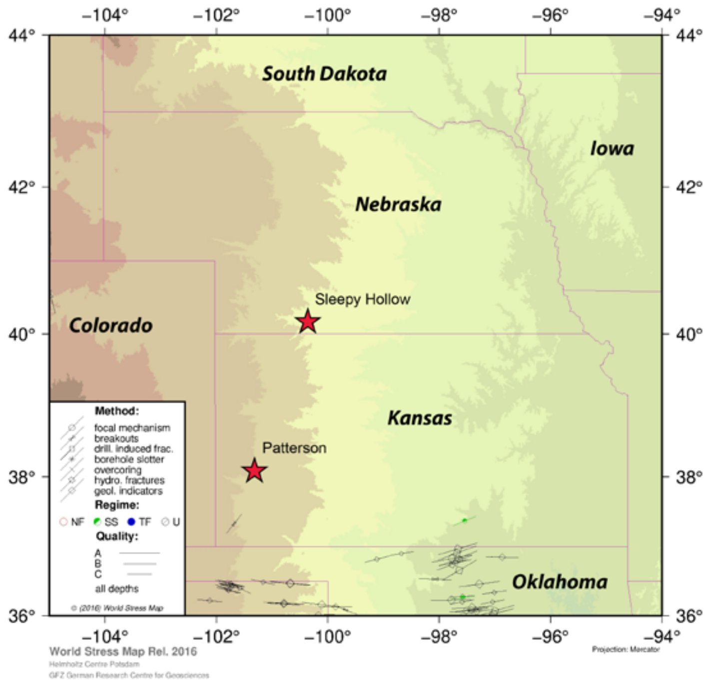

Figure 2.8. Plot of regional stress observations form the world stress map project (Heidbach et al. 2018).

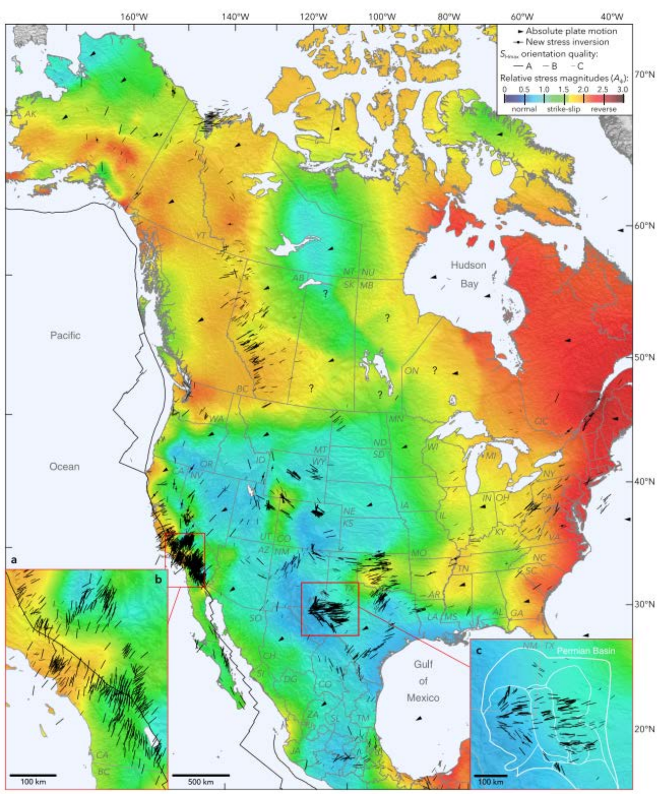

Figure 2.9. State of Stress in North America showing the relative stress magnitude (Lund Snee and Zoback 2020). Both Kansas and Nebraska states appear in the transition between strike-slip (green) and extensional faulting (blue) regimes.

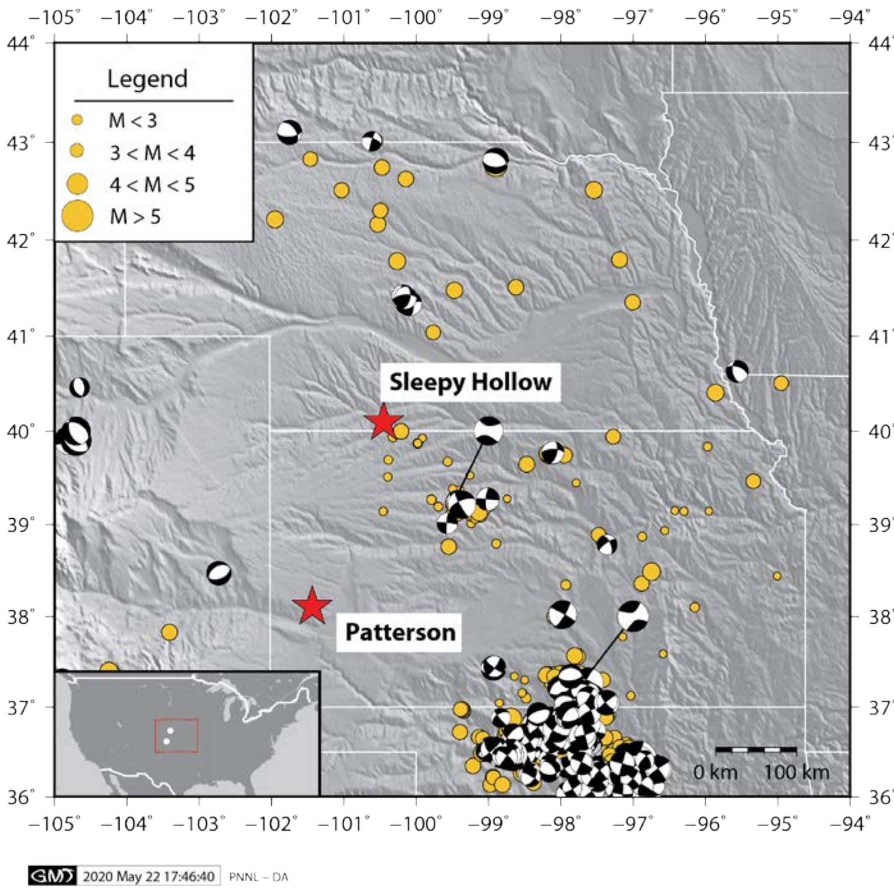

Figure 2.10. Seismic events (*M* > 2.5) and earthquake moment tensor solutions focal mechanisms identified in the area of the Sleepy Hollow and PHH fields.

2.5.3 Reservoir Stress Path Coefficient

Subsurface activities involving fluid injection or withdrawal cause perturbations in the pore pressure. In the context of CO_2 injection in a saline aquifer the pore pressure is expected to increase locally as CO_2 progressively displaces brine in the pore space. Increasing fluid pressures increases the likelihood of fault reactivation.

The two horizontal stresses S_{hmin} and S_{Hmax} arise from a combination of the Poisson effect resulting from overburden loading and the contribution of tectonic strains (Burghardt 2018). The evolution of the horizontal stresses during subsurface operations depends on several factors, including the initial state prior to operations and the distribution of poroelastic properties.

Over the last two decades, multiple studies related to field operations have demonstrated that the stress state within a reservoir is directly coupled to pore pressure changes resulting from fluid injection or withdrawal and that horizontal stresses evolve as pore pressure builds up (Vidal-Gilbert et al. 2010; Streit and Hillis 2004; R. Hillis 2000). This evolution of the stress state in the reservoir associated with subsurface operations is commonly referred to as the “stress path” (Addis 1997) or “pore pressure-stress coupling” (R.R. Hillis 2001). While a stress path could be defined for each principal stress (i.e., S_v, S_{hmin}, and S_{Hmax}), a reservoir is commonly assumed to behave under uniaxial strain conditions, which means that the total vertical stress is unaffected by changes in overpressure, and that there is no change in strain in the horizontal direction. This uniaxial strain assumption is a commonly used approximation, but because the pore pressure increases nonuniformly throughout the reservoir, uniaxial strain conditions are not fully representative of actual injection scenarios. Nonetheless, in the absence of numerical model predictions the uniaxial strain stress path estimate is a good starting point for estimation. Using the transversely isotropic vertical (TIV) elastic model assumed by Burghardt (2018), the resulting uniaxial strain stress path coefficient Γ_h is given by

$$\Gamma_h = \frac{\Delta S_h}{\Delta P_p} = \alpha_h(1 - \frac{C_{1133}}{C_{3333}}) \tag{2}$$

where

Γ_h = the horizontal stress path coefficient,
ΔS_h = the change in total horizontal stress,
α_h = the horizontal component of the Biot coefficient tensor, and
C_{1133} and C_{3333} = components of the fourth-order TIV stiffness tensor.

For an isotropic material, which is assumed for the Sleepy Hollow Field, the two components of the TIV stiffness tensor are given by

$$C_{1133} = \frac{E\nu}{(1+\nu)(1-2\nu)} \tag{3}$$

$$C_{3333} = \frac{E(1-\nu)}{(1+\nu)(1-2\nu)} \tag{4}$$

where E is Young's modulus and ν is Poisson's ratio. The stress path coefficient Γ_h can now be expressed as

$$\Gamma_h = \frac{\Delta S_h}{\Delta P_p} = \alpha_h(1 - \frac{\nu}{1-\nu}) \tag{1}$$

The coefficient $\Gamma_h$is now dependent on two parameters only, the Biot coeffcicient α_h and the Poisson’s ratio ν. The Biot coefficient can be measured in the laboratory using geomechanical tests performed on rock samples. No such data is available from core sample measurements, but it is generally assumed that the Biot’s coefficient ranges from 0.6 to 1. Based on the Poison’s ratio obtained in sonic logs from the SHRU-86A borehole, the minimum and maximum stress path coefficient (corresponding to a Biot coefficient of 0.6 and 1.0, respectively) was computed and plotted in Figure 2.11.

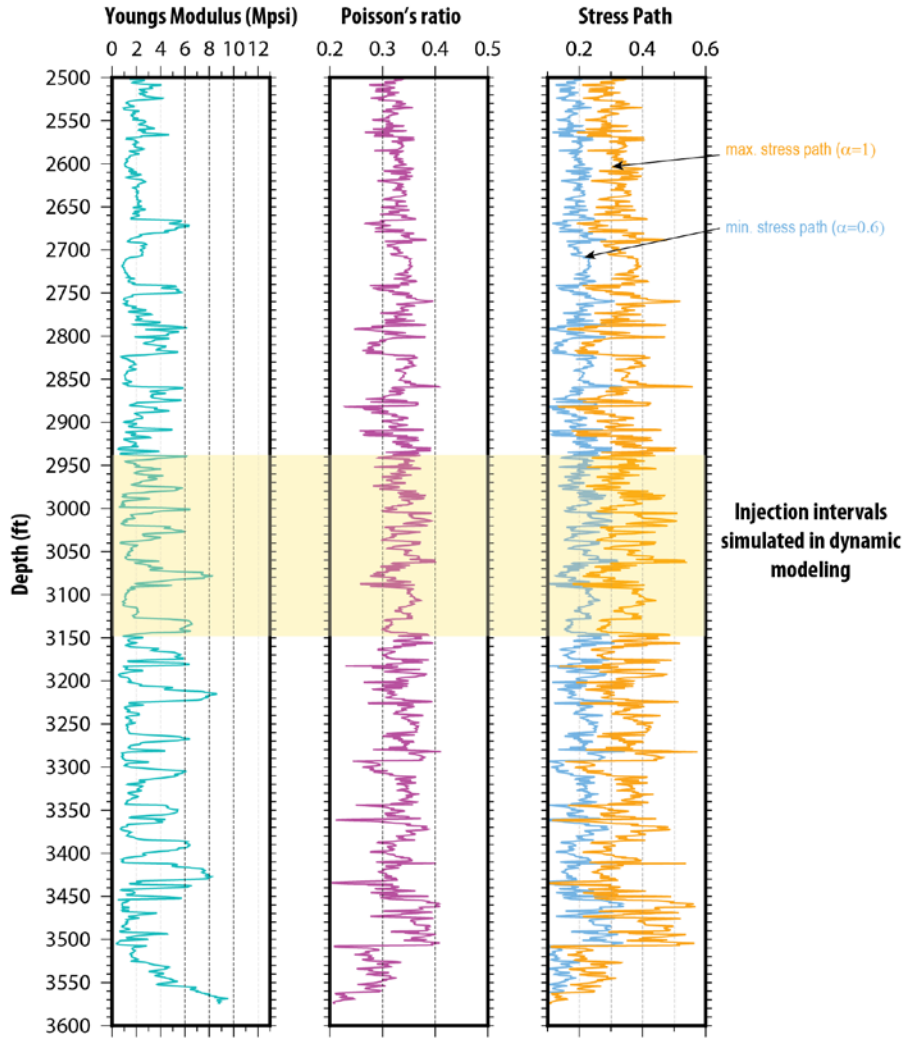

Figure 2.11. Static Young's modulus and Poisson's ratio from sonic logs from SHRU-86A borehole and computed minimum and maximum stress path.

For this range of values and based on Equation (1), the horizontal stress path coefficient Γ_h ranges from about 0.2 to 0.5 in the injection intervals. The stress path range determined from sonic logs is relatively low compared to what has been measured in field operations in different parts of the world, where the stress path coefficient usually ranges from 0.4 to 0.7, although values as low as 0.2 and as high as 1.18 have also been measured (R. Hillis 2000). This is primarily due the relatively high value of the Poisson's coefficient measured in the sonic logs. The provided sonic log interpretation assumed that, unlike the Young's modulus, the dynamic Poisson's ratio measured from the sonic logs would be the same as the quasi-static value, which is often not the case. Ideally the stress path should be estimated using parameters based on core measurements of elastic properties from the reservoir of interest and a numerical model that would account for the non-uniaxial strain that occurs during injection. Four triaxial compressive tests were conducted on SHRU-86A core samples. Three of these four samples are from the injection formations and indicates Poisson's ratios ranging from 0.13 to 0.18. Assuming a Biot's coefficient ranging from 0.6 to 1, the stress path ranges this time from 0.47 to 0.83.

In order to conduct the geomechanical analysis, and the absence of elastic properties measured from core samples, the minimum and maximum values of the stress path coefficient used to create a uniform distribution in SOSAT are chosen to vary from 0.2 to 0.6. This means that the total horizontal stresses are expected to increase by 20 to 60% of the increase in pore pressure associated with the injection.

3.0 Assessment of Leakage Risk at Sleepy Hollow with NRAP-Open-IAM

3.1 Approach

The NRAP-Open-IAM was used to estimate the risk of leakage for one scenario.

3.1.1 Reservoir simulation

The reservoir simulations used for this analysis were completed in January 2019 by project partners at the Energy & Environmental Research Center (Dalkhaa 2019) as a scoping exercise for Task 3 of the Phase II IMSCS-HUB CarbonSAFE project. The reservoir simulation was generated using Computer Modeling Group LTD's reservoir simulation software GEM. Additional Phase II simulation updates, which include the new characterization well data, occurred concurrently with this work (Duguid et al., 2020b) and could be used in future NRAP-Open-IAM analyses.

The model domain used was 19,312 m (12 miles) by 19,312 m (12 miles) in map view. Lateral grid size was 182.88 m (500 ft) by 182.88 m (500 ft) in the inner field area (8.2 km east to west and 13.1 km north to south) and 762 m (2,500 ft) by 762 m (2,500 ft) outside that.

The storage operations scenario was for a continuous injection period over 30 years with a total mass of CO_2 injected target of 50 million metric tons (Mt). The simulation calls for a total daily injection rate of 4,570 t/day split among the 6 possible injection wells. For this simulation injection well 2 was not utilized. The injection rate was controlled by a maximum bottom hole injection pressure of 13.789 MPa (2,000 psi). Injection occurs across multiple saline aquifers starting at the top of the Wabaunsee (2,900 ft deep). The initial reservoir pressure was assumed to be under pressured and was 16% depleted with respect to the hydrostatic gradient. Following completion of the injection period there was 10 years of post-injection simulation. Time points used in this study are 0, 1, 2, 3, 4, 5, 10, 15, 20, 25, 30, and 40 years.

The entire reservoir model consisted of 159 vertical layers. Layers 1 to 9 are considered as upper no flow boundaries and layers 156 to 159 are considered as lower no flow boundaries. The layers between 10 and 158 are considered as flow intervals. For the NRAP-Open-IAM analysis we used the upper-most flow interval (i.e., layer 10). Figure 3.1 shows the CO_2 saturation and pressure used to create the Sleepy Hollow lookup table component for NRAP-Open-IAM.

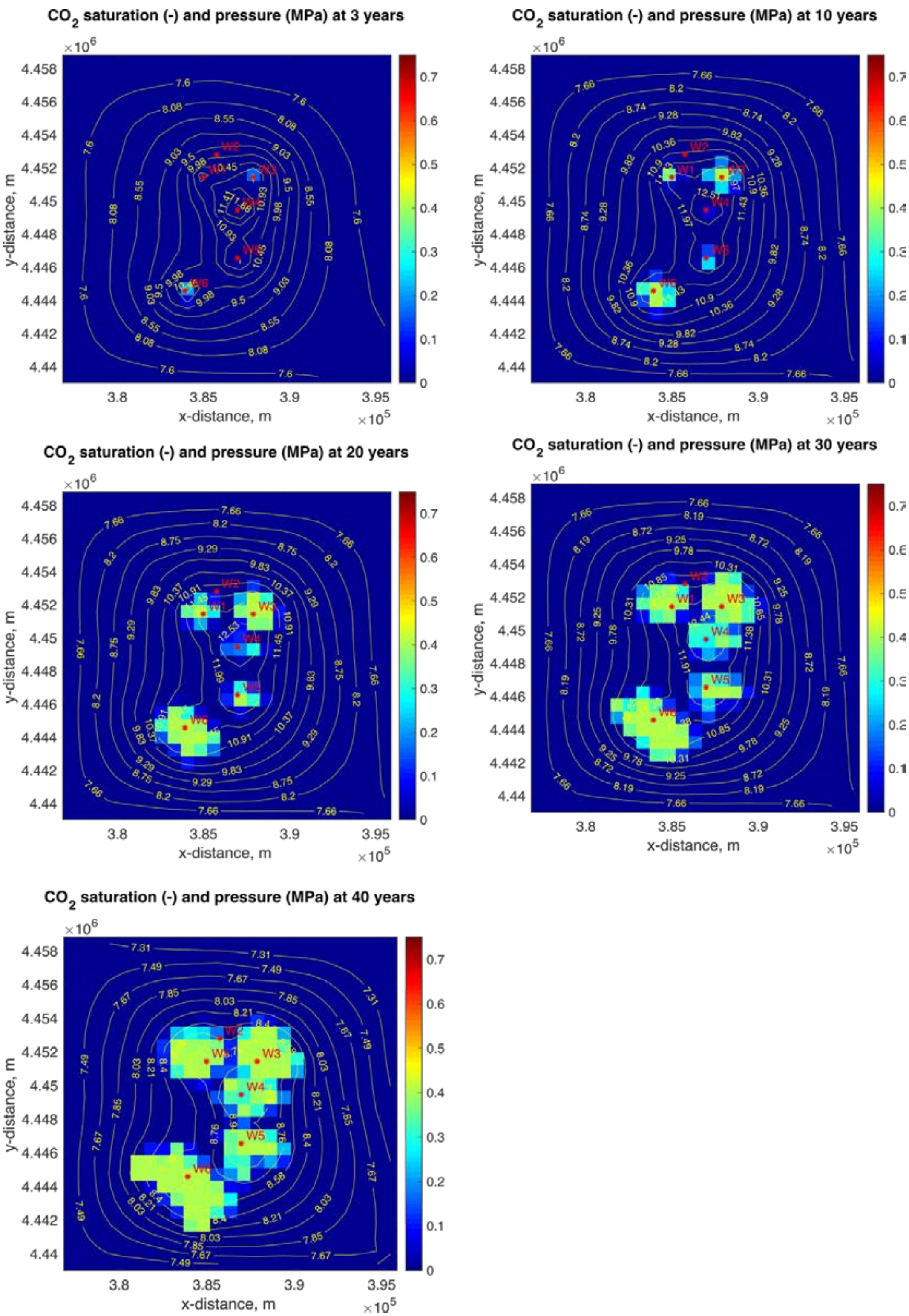

Figure 3.1. Pressure contours and saturation map for Sleepy Hollow reservoir simulation results for layer 10, which is the top of the Wabaunsee.

3.1.2 NRAP-Open-IAM Analysis of Risks of Leak through Well Annulus

Parameters used in the NRAP-Open-IAM were chosen based on available data from the Phase I and Phase II efforts.

Stratigraphy

Table 3.1 shows the model stratigraphy used in the NRAP-Open-IAM analysis. The stratigraphy is lumped into six units. Leakage occurs from the Reservoir, and through the overlying Aquifers and Shales. The stratigraphy was taken from the SH Reagan Unit 86A, Advanced Data Analysis report (Duguid et al., 2020a), and for uncertain parameters we used the NRAP-Open-IAM capabilities and limitations to inform. Specifically, the thickness of Aquifer 1 was held constant at 45.7 m.

Table 3.1. Stratigraphy and related rock properties for the Sleepy Hollow field used in the NRAP-Open-IAM. Note that blank cells imply parameter not used.

Unit	Depth to top, m	Depth to bottom, m	Thickness, m	Porosity, -	Horizontal permeability, $\log_{10}$ m^2	Anisotropy, -	Calcite volume fraction, -
Shale 3	0.0	45.7	45.7				
Aquifer 2 USDW	45.7	121.9	76.2	0.15	-12	0.3	0.1
Shale 2	121.9	293.2	171.3				
Aquifer 1 AZMI	293.2	338.9	45.7	0.1	-13	0.3	0.1
Shale 1	338.9	892.5	553.6				
Reservoir	892.5						

Inputs to the NRAP-Open-IAM Model

Table 3.1 and Table 3.2. have additional parameters used in the analysis. These parameters should be considered as uncertain and would need to be either better constrained by site-specific observations or included in a full uncertainty analysis to assess their impact.

The wellbore permeability along Shale 1 and Shale 2 was chosen to be randomly assigned using a uniform distribution to understand how permeability and distance from an injection well impacts leakage results (Figure 3.2).

Table 3.2. Static properties for the Sleepy Hollow field used in the NRAP-Open-IAM.

Parameter	Value
Brine density, kg/m^3	1,050
Well radius, m	0.015
Well leak-path permeability along Shale 1 and 2 ($\log_{10}$), m^2	-11 to -13
Well permeability along Shale 3 ($\log_{10}$), m^2	-17

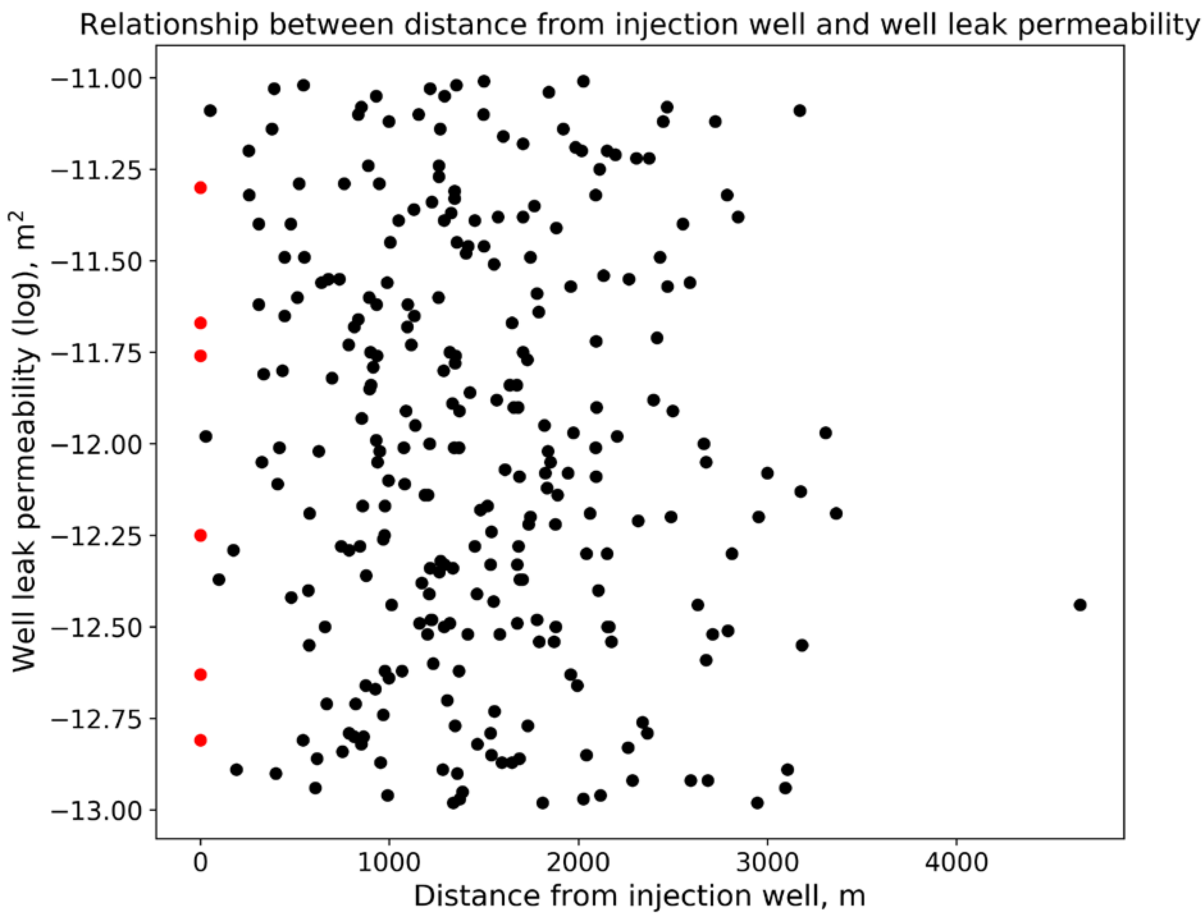

Figure 3.2. Well leak permeability plotted against distance from the nearest injection well. The red dots are injection wells (with distance of 0 meters) and the black dots are existing wells.

3.2 Results

Results are presented for one realization of the Sleepy Hollow field to describe features of the model output. Then the results for multiple realizations are compared to understand the impact of uncertainty on key metrics. A full risk assessment combines multiple realizations depending on uncertain parameters (e.g., well leak permeability) or the objective of the study (e.g., to inform the monitoring plan).

We present results for one realization of the NRAP-Open-IAM to illustrate features of the model. While this illustration shows well leakage fluxes and impacts for the wells at Sleepy Hollow, it should not be interpreted that this is a representation of the true risk at the site. To do a full risk assessment a stochastic approach would be utilized to account for uncertainties in parameters. To describe results, we present figures that show the behavior for individual wells (injection and existing) and summary percentiles (20, 50, 75, and 90 percentile).

3.2.1 Reservoir Pressure and CO_2 saturation at the wells

Pressure and saturation at the base of the wells drive brine and CO_2 leakage up a well and into aquifers. This data is interpolated from the reservoir lookup table at the well location over time. Figure 3.3 shows the pressure (left) and CO_2 saturation (right) during injection (0 to 30 years) and post-injection (30 to 40 years). The thin dashed colored lines represent the six injection wells, the thin solid lines are the existing wells, and the thick lines represent summary percentiles. Pressure for all wells increases for the first decade and then shallows out to a gentler increase until the end of injection. After injection stops at 30 years pressure rapidly decreases during the 10 years of post-injection time. CO_2 saturation increases over time for all wells that see CO_2 during the simulations. Unlike pressure, CO_2 saturation increases or remains constant for all well locations throughout the simulation.

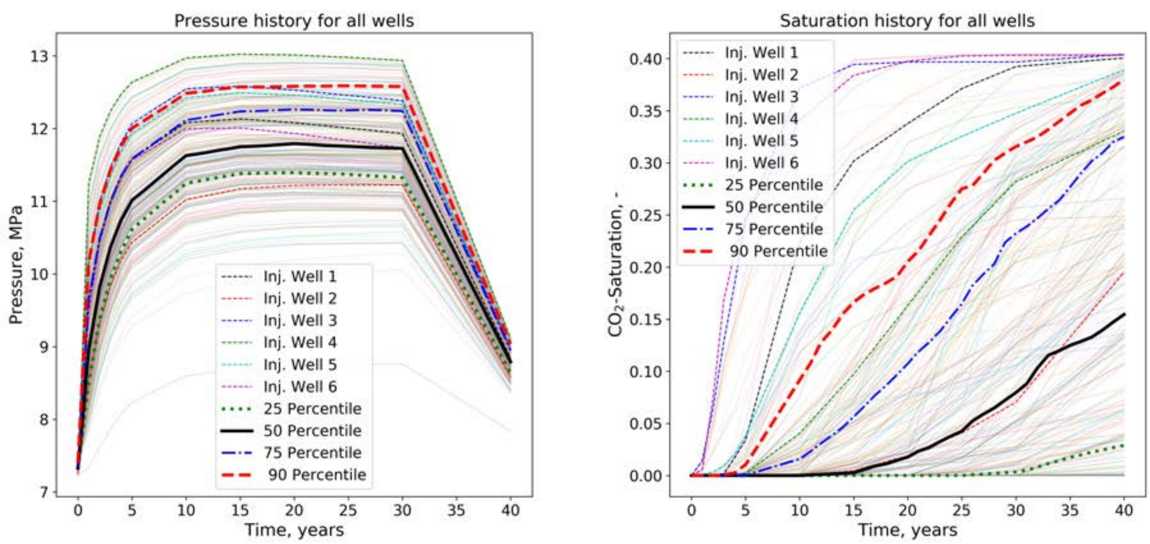

Figure 3.3. (left) Pressure history for all wells for one realization. (right) CO_2 saturation history for all wells for one realization. The thin dashed lines represent data for the six injection well locations and the thin solid lines represent values for the 276 existing wells. The thick lines represent percentiles for the entire dataset.

3.2.2 CO_2 and brine leakage flux and mass accumulation into aquifers and the atmosphere

Figure 3.4 shows the flux of CO_2 and brine into Aquifer 1, Aquifer 2, and to the atmosphere over time. The leak rate into the atmosphere is negligible given that we defined the permeability of the well above Aquifer 1 to be 1×10^{-17} m^2. For CO_2, the leak rate is greater into Aquifer 2 than Aquifer 1. For brine, the leak rate is greatest into Aquifer 1, then Aquifer 2. Leakage of CO_2 is higher than that of brine. Most of the wells show negligible leakage into either aquifer, as evidenced by the 50% percentile being at or near the horizontal intercept. There are a few outliers, notably the injection wells, which have the highest pressure.

Figure 3.5 shows the total mass of CO_2 and brine leaked into Aquifer 1 and Aquifer 2 over time. Most of the wells show negligible mass of either fluid leaked. As with the flux, most of the CO_2

accumulation occurs in Aquifer 2. It is important to note that even the few outlier wells leak significantly below 1% of the total amount injected.

3.2.3 Leakage impact into Aquifer 2 for key metrics

Figure 3.6 shows the diameter of impact for four metrics into Aquifer 2. Fluid pH and dissolved CO_2 have the largest impact but are still localized around the leaky well. Onset of a detectable leak is delayed by several years and the majority show no impact until around 10 years. This is an important finding when determining where a leak may be detected. TDS and pressure show little useful signal outside the immediate area of the leaky well.

Figure 3.7 shows the bulk volume of Aquifer 2 impacted for the four metrics. Similar to the diameter of impact, the largest metrics are dissolved CO_2 and pH. While some outlier wells have significant volumes impacted, most have a negligible impact.

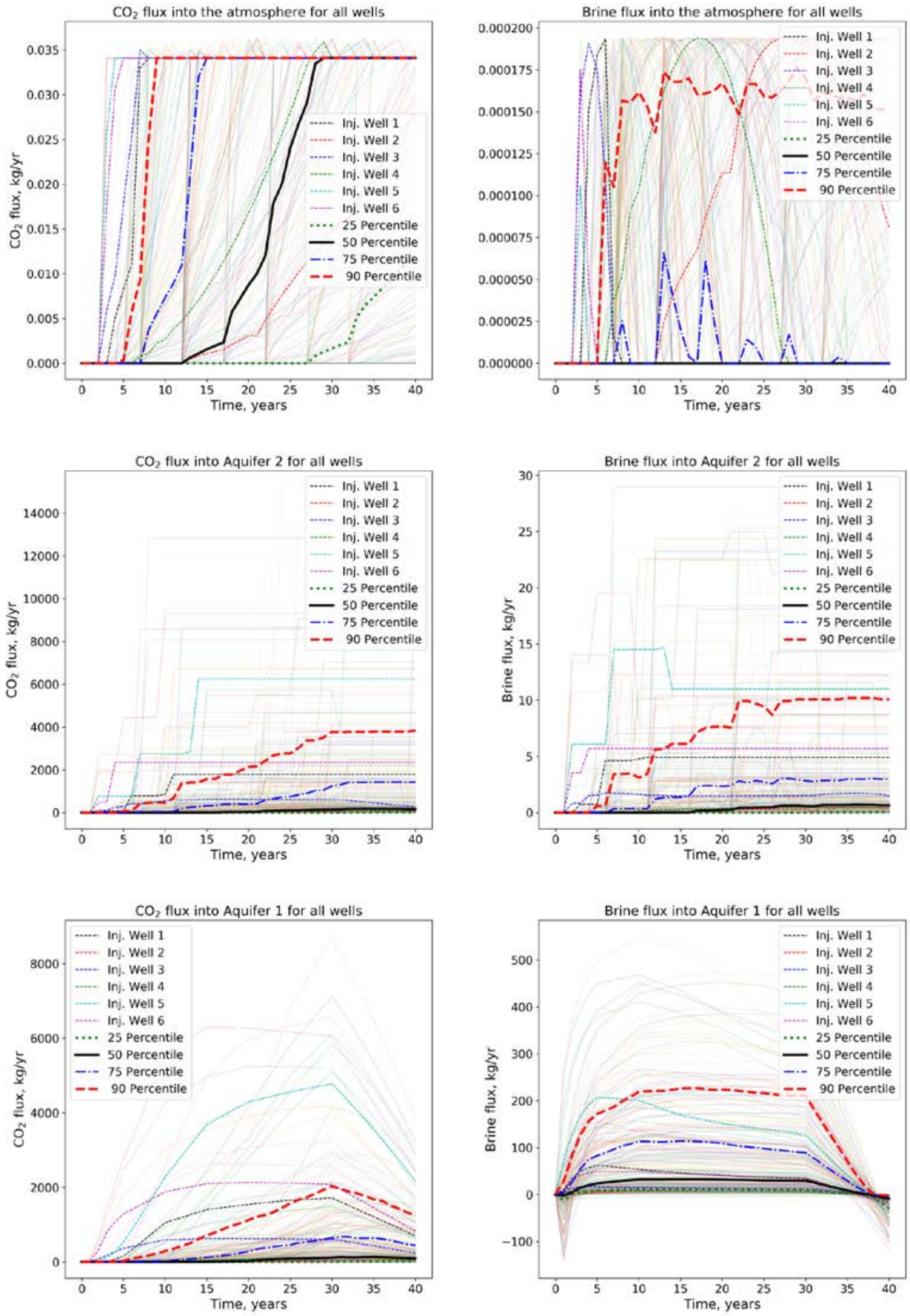

Figure 3.4. Flux histories for one realization. (top left) CO_2 flux into the atmosphere for all wells. (top right) Brine flux into the atmosphere for all wells. (middle left) CO_2 flux into Aquifer 2 for all wells. (middle right) Brine flux into Aquifer 2 for all wells. (bottom left) CO_2 flux into Aquifer 2 for all wells. (bottom right) Brine flux into Aquifer 2 for all wells. The thin dashed lines represent data for the six injection well locations and the thin solid lines represent values for the 276 existing wells. The thick lines represent percentiles for the entire dataset.

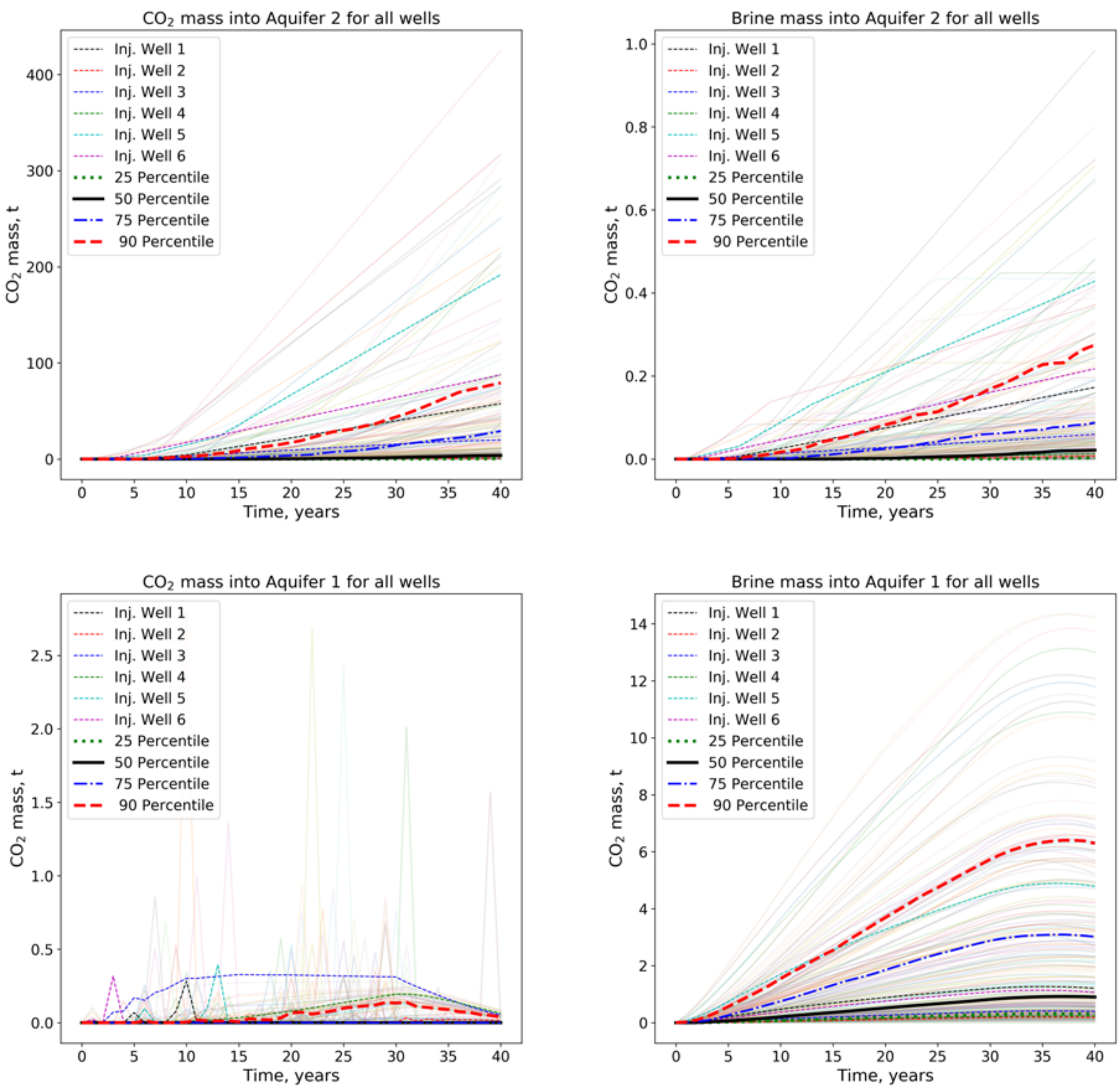

Figure 3.5. Total mass histories for one realization. (top left) Accumulated CO_2 mass into Aquifer 2 for all wells. (top right) Accumulated brine mass into Aquifer 2 for all wells. (bottom left) Accumulated CO_2 mass into Aquifer 1 for all wells. (bottom right) Accumulated brine mass into Aquifer 1 for all wells. The thin dashed lines represent data for the six injection well locations and the thin solid lines represent values for the 276 existing wells. The thick lines represent percentiles for the entire dataset.

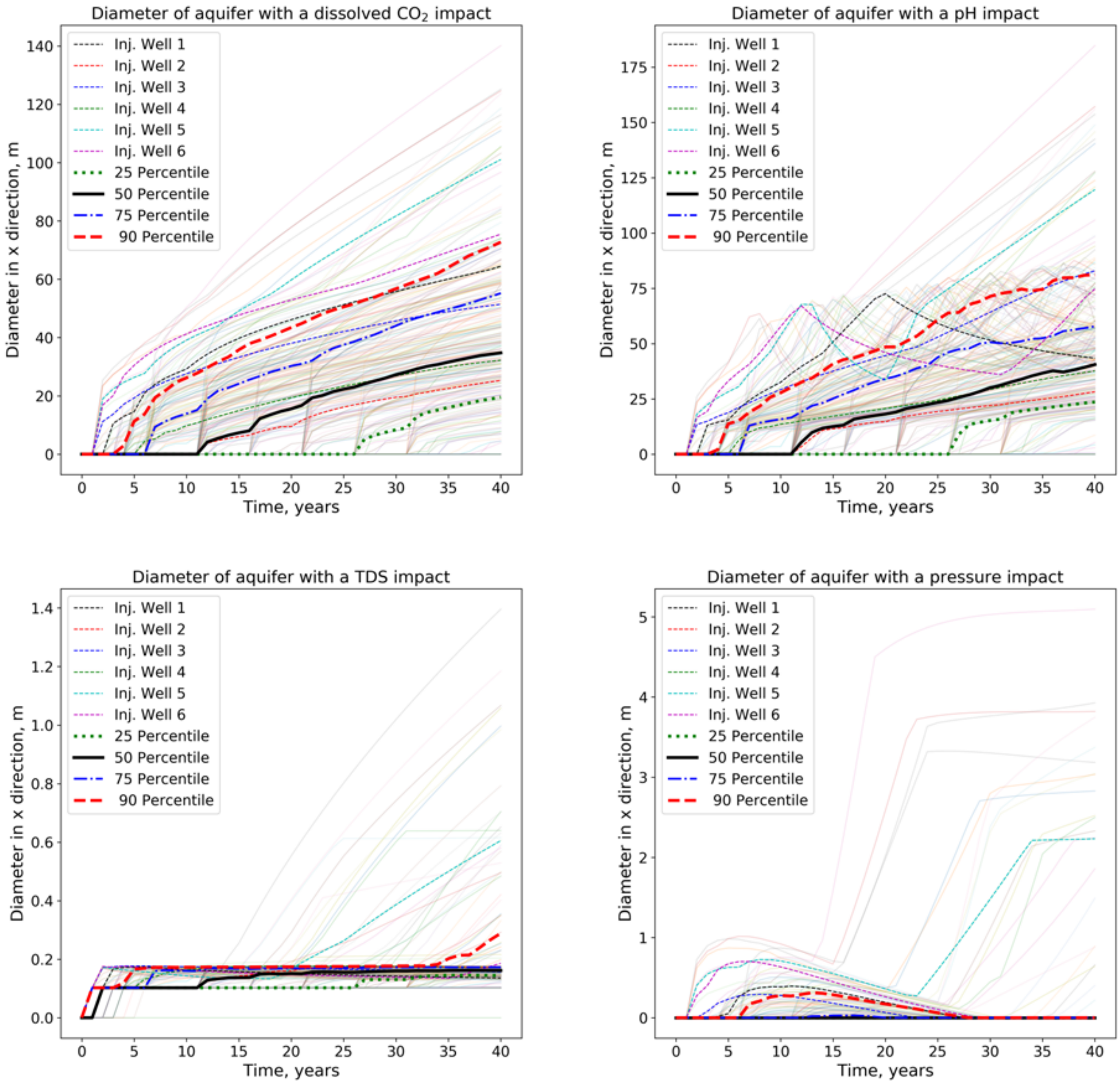

Figure 3.6. Diameter of leakage impact around wells in Aquifer 2. (top left) Change in dissolved CO_2 that causes an impact. (top right) Change in fluid pH that causes an impact. (bottom left) Change in fluid TDS that causes an impact. (bottom right) Changes in pressure that causes an impact. The thin dashed lines represent data for the six injection well locations and the thin solid lines represent values for the 276 existing wells. The thick lines represent percentiles for the entire dataset.

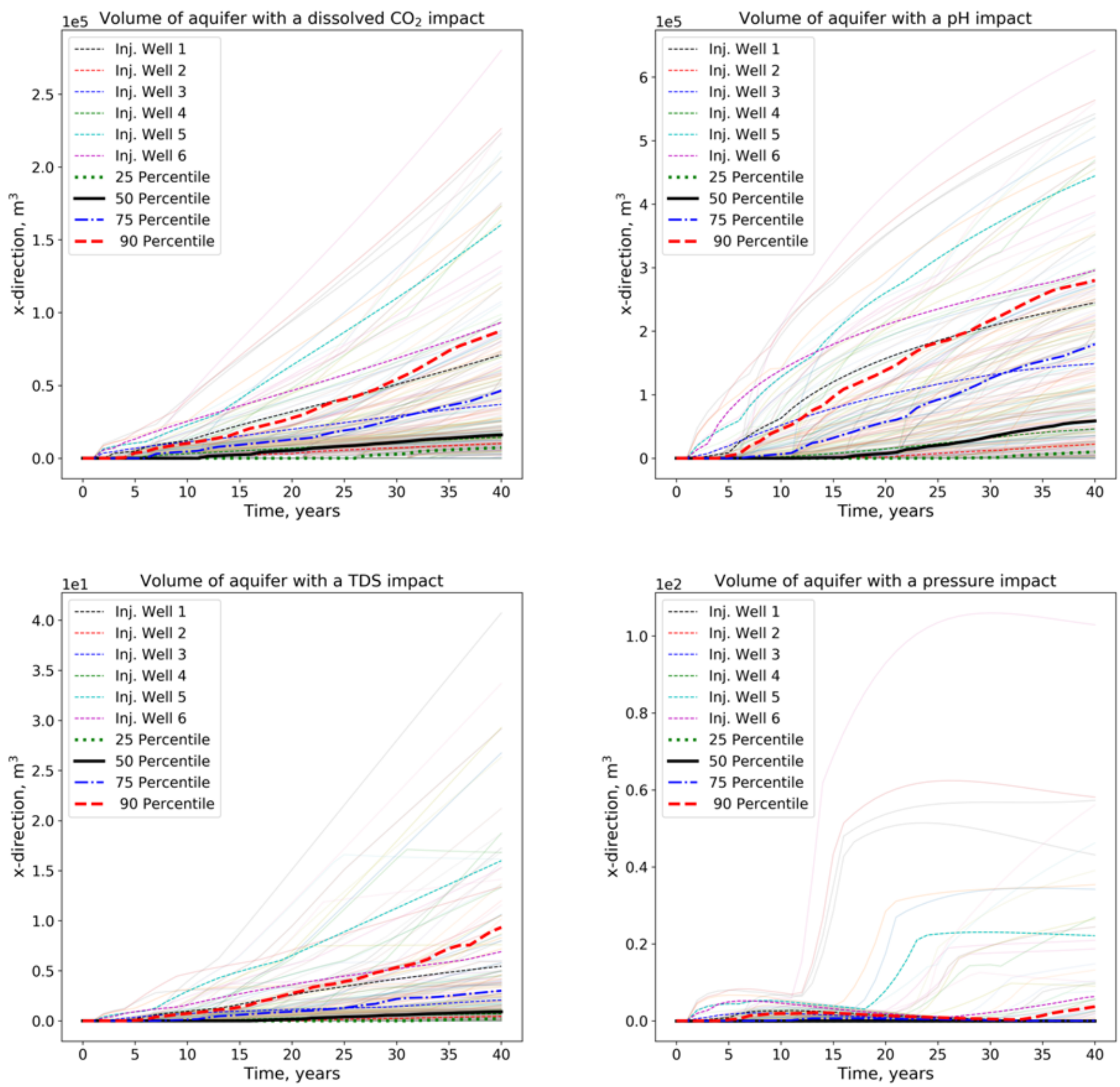

Figure 3.7. Volume of impact around each well in Aquifer 2 for a given parameter (top left) dissolved CO_2 impact, (top right) pH impact, (bottom left), TDS impact (bottom right), pressure impact. Note that in this figure the vertical axis is in scientific notation, with the exponent at the top left of the axis for a given plot.

4.0 Assessment of Geomechanical risks at Sleepy Hollow Site

The knowledge of any site proposed for fluid injection relies on quantitative and qualitative information, regional observations and site-specific measurements. Estimates of the state of stress derived from numerical models are commonly deterministic. While the estimates derived from these models can be correct, there is no information about the certainty of the prediction. What makes SOSAT a unique tool is that parameters relevant to a geomechanical analysis to estimate the state of stress can be expressed in statistical rather than deterministic terms. Based on the degree of uncertainty proper to some parameters, SOSAT evaluates a probability distribution for in situ stress at a given depth.

In this study, the top of the shallowest CO_2 injection interval of the first injection scenario considered (i.e., Injector 1 in the Oread Formation) was chosen to demonstrate the methodology. The same approach can be used in any desired locations to evaluate the state of stress and the geomechanical risks at different desired levels, including sealing formations or basement. The goal of the application of SOSAT to the Sleepy Hollow Site in this study is not to provide an exhaustive geomechanical analysis, but is aimed to highlight how uncertainties can affect how risks are perceived at a given site, and how this could impact decision making (e.g, site screening, characterization activities, injection operations, etc.). The tool can also be used to perform a value of information analysis to strategically focus further characterization efforts in ways most likely to offer significant reductions in uncertainty.

As described in Section 1.2.2, the parameters used to estimate the state of stress can be expressed either as a probability distribution reflecting the degree of certainty with which the parameters are known or as deterministic parameters. Based on the input parameters provided in SOSAT and listed in Table 4.1, the probability distribution of the state of stress is calculated and the probability of activating a critically oriented fault at a specified range of pore pressures is determined. The approach is conservative as it assumed that a critically oriented fault exists. Including this possibility is also part of the risk evaluation and should not be dismissed since it is generally not possible to rule out the existence of such a fault since they are not always identifiable from geophysical surveys. SOSAT outputs can subsequently be used to evaluate the risk of unintentional hydraulic fracturing.

Table 4.1. List of parameters required in SOSAT, their requested degree of certainty, and their main purpose in the geomechanical risk assessment.

Parameters	Degree of Certainty	Purpose
Reservoir Properties		
Friction coefficient (mean/ standard deviation/ maximum possible)	Probability distribution (log normal distribution)	Constrain the stress difference for each faulting regime (stress polygon approach from (M. D. Zoback et al. 2003)
Reservoir depth	Deterministic parameter	Analyze of the state of stress in SOSAT at this given depth (true vertical depth)
Pore pressure gradient	Deterministic parameter	Determination of state of stress

Parameters	Degree of Certainty	Purpose
(expected pore pressure at a given depth, divided by the depth)		
Average overburden density	Deterministic parameter	Determination of the vertical principal stress (S_v)
Maximum injection pressure	Deterministic parameter	Maximum pore pressure that will be used in the fault activation probability calculations.
Regional Stress Information		
Faulting regime weight/ faulting regime transition parameters	Probability distribution	Relative weight assigned to the three faulting regimes. Allows expression of the stress state as a probability distribution using a superposition of two logistic functions. Transition parameters control how gradual the transition between the different faulting regimes is.
Stress Measurements (optional)		
Minimum principal stress (mean/standard deviation)	Probability distribution (normal distribution)	Used to better constrain the posterior distribution of horizontal stresses
Calculation and Plot		
Number of trial stress states	Deterministic – user-defined value	Control the rejection sampling algorithm used to generate a representative sample of stress states from the posterior distribution.
Minimum and maximum values of the stress path coefficient	User-defined value	Used to create a uniform distribution for the stress path coefficient (ratio of the change in the total minimum principal stress, resulting from a change in the pore pressure). Defined using elastic properties from core measurements from the reservoir.
Stress grid size	User-defined value	Control the resolution of the grid used to discretize the joint distribution of principal stresses.
Minimum stress to plot	User-defined value	Control the ranges of the stresses plotted on the posterior stress distribution plot.
Number of injection pressures to evaluate	User-defined value	Control how the fault activation probability curve is plotted. Specify the number of pore pressures between the initial pore pressure and the maximum injection pressure.

4.1 SOSAT inputs: Summary of parameters

Input parameters to be used in SOSAT are based on the site-specific data acquired at the Sleepy Hollow Field and described in section 2.0. Some deterministic parameters such as the parameters related to reservoir conditions (i.e., pore pressure, injection depth) or operation conditions (i.e., injection pressure) are taken as deterministic. Other parameters that should be provided with the degree of certainty with which they are known are further described below.

All the parameters used to run SOSAT using this scenario are summarized in Table 4.2.

4.1.1 Fault Regime weights

In SOSAT, the regional stress information is expressed with a probability distribution function describing the regional stress information. The calculated probability distribution is constructed using a superposition of two logistic functions (explained by in (Burghardt 2018)), that allows the user to assign a weight to the different stress regimes and to set transition parameters specific to the sigmoid functions referred to as K-thrust and K-SS, that control the width of the sigmoid transitions between the three faulting regimes (i.e., how smooth is the transition). The larger the value, the more abrupt the transition.

In the absence of in-situ stress measurements, the evaluation of the regional stress data, earthquake moment tensor solutions, image and sonic logs from the SHRU-86A borehole suggest that the stress regime at the location of the Sleepy Hollow site is most likely normal faulting. The regional presence of strike-slip indicators in the area does not allow to totally rule out the potential for strike-slip faulting regime. It is therefore reasonable to assign a conservative probability of normal faulting greater than a strike-slip faulting state, while the probability of reverse faulting is approaching zero (a zero value is not a possible option in the current version of SOSAT).

A weight of 85 was then assigned to the normal stress state, and respective weights of 14 and 1 were given to the strike-slip and reverse faulting regimes. Additional parameters specific to the sigmoid functions, referred to as K-thrust and K-SS, control the width of the sigmoid transition between the different faulting regimes. K-thrust and K-SS were respectively chosen to be 300 and 50, leading to a smooth transition between the thrust faulting and the strike-slip faulting regimes, and an abrupt transition between the strike-slip and the very low probability normal faulting state. The resulting probability distribution for g_θ is shown in Figure 4.1. In this plot, the parameter g_θ is a result of the specific coordinate system defined by Burghardt (2018). In this coordinate system, the thrust faulting states lie between $-1 \leq g_\theta < -\frac{\sqrt{2}}{2}$, strike-slip states lie between $-\frac{\sqrt{2}}{2} \leq g_\theta < \frac{\sqrt{2}}{2}$, and the normal faulting state lies between $\frac{\sqrt{2}}{2} \leq g_\theta < 1$.

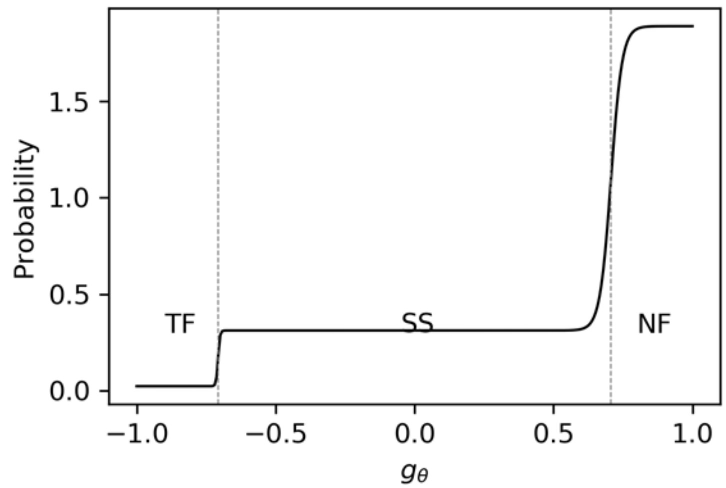

Figure 4.1. Plot of the probability distribution expressing the regional stress state information, with weight thrust fault (TF) = 1, weight strike-slip (SS) = 14, weight normal fault (NF) = 84, reverse thrust (K-thrust) = 300, and reverse strike-slip (K-SS) = 50.

4.1.2 Friction Coefficient

Information related to the fault friction coefficient is provided in SOSAT with the parameters defining a lognormal distribution (i.e., median fault friction coefficient and standard deviation). The frictional properties of these planes of weakness will constrain the possible states of stress.

Despite the importance of these parameters, it is generally not feasible to collect the frictional properties of specific faults and fractures present at a given site. However, frictional properties have been measured in laboratory and field studies and have shown that coefficients of friction between 0.6 and 1.0 (Jaeger and Cook 1979) were applicable to the crust, although typical values generally range from 0.6 to 0.7.

For the Sleepy Hollow field, a lognormal distribution with a mean μ_0 of 0.7 and standard deviation σ_μ of 0.15 was chosen and is plotted in Figure 4.2. These correspond to the default parameters proposed in SOSAT.

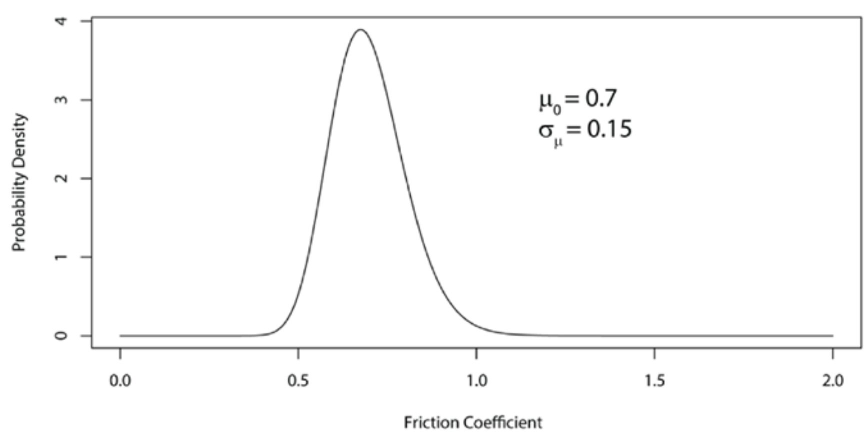

Figure 4.2. Lognormal probability density distribution for friction coefficient having a mean of 0.7 (μ_0) and a standard deviation of 0.15 (σ_μ).

4.1.3 Summary of input parameters

The summary of the input parameters for SOSAT are provided in the table below.

Table 4.2. Summary of the reservoir properties and stress observations input parameters for SOSAT.

Parameters	Values
Reservoir Parameters	
Median Friction Coefficient	0.7 (default)
Standard deviation of logarithm of fault friction coefficient	0.15 (default)
Maximum possible friction coefficient	1.5 (default)
Reservoir depth	3,100 ft *(944.88 m)*
Pore pressure gradient	0.3375 psi/ft *(7.63 MPa/km)*
Average overburden density	2.43 g/cm^3
Maximum injection pressure	2,062 psi *(14.22 MPa)*
Regional Stress Info	
Normal faulting weight	85
Strike-slip faulting weight	14
Thrust-faulting weight	1
Maximum possible friction coefficient	1.5 (default)
K-thrust	300
K-SS	50
Stress Measurement	
Mean of minimum principal stress measurement	-
Standard deviation of minimum principal stress measurement	-
Stress Path	
Minimum value of the stress path coefficient	0.2
Maximum value of the stress path coefficient	0.6

4.2 Stress distribution and risk of induced shear failure

The posterior stress distribution presented in Figure 4.3 represents the probability density (shown in grayscale) for combinations of minimum and maximum horizontal stress values. The results demonstrate the high degree of uncertainty on the magnitude of both the minimum and maximum horizontal stresses. The maximum value possible for the maximum horizontal stress is limited by the normal-faulting conditions and is approximately 22 MPa. For the two horizontal stresses, possible magnitudes range from about 10 MPa to 22 MPa.

The total probability of induced shear failure as a function of pore pressure change is determined in SOSAT and plotted in Figure 4.4. This plot shows that the probability that the injection zone was initially critically stressed is relatively high as indicated by the value of 22%.

When the pore pressure increases to 14.2 MPa (2,063 psi), determined to be the maximum allowable pressure based on the dynamic modeling, the risk of shear failure approaches a probability of 45%. This high range of probabilities reflects the dearth of information available on the geomechanical conditions in this part of Nebraska. The ranges are caused primarily by a lack of characterization of the minimum and maximum horizontal stress, where no direct stress measurements are available. This uncertainty could be dramatically decreased with mini-frac/DFIT stress measurements.

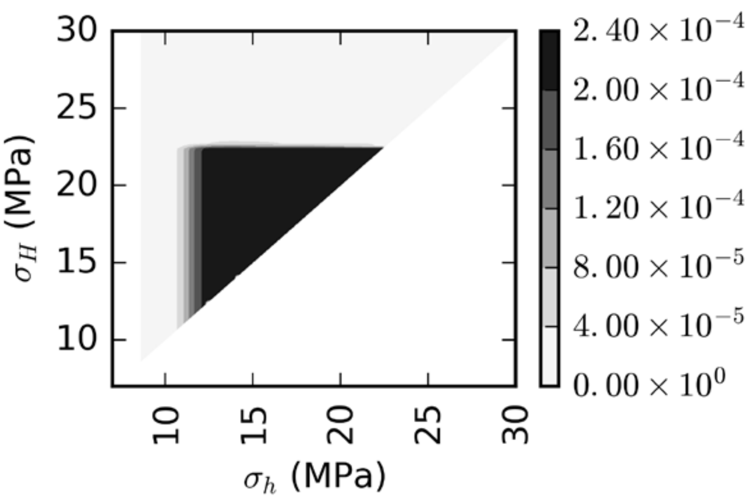

Figure 4.3. Posterior Stress Distribution Plot at the Sleepy Hollow field.

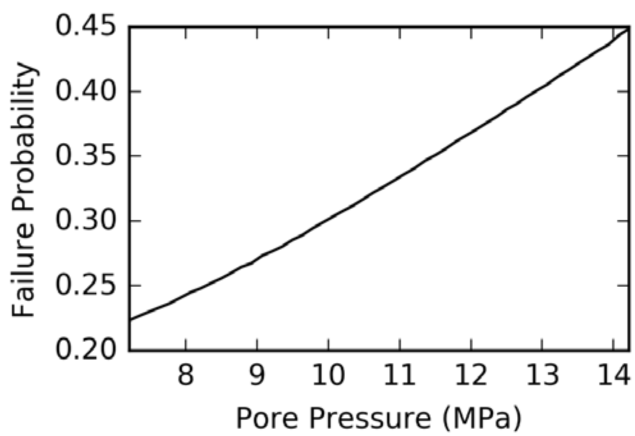

Figure 4.4. Probability of inducing shear failure on a critically oriented fault plane for a given pore pressure at the Sleepy Hollow Site.

4.3 Risk of unintentional hydraulic fracturing

The risk of unintentional hydraulic fracturing was also evaluated. To prevent the initiation of hydraulic fractures, the injection pressure must remain smaller than the minimum principal stress. Three scenarios were evaluated, assuming that either a 1%, 5%, or 10% risk of fracturing was acceptable. Based on the cumulative probability distribution obtained from the posterior stress distribution calculated with SOSAT (Figure 4.5), the maximum allowable pressure under initial reservoir conditions was obtained for the three scenarios (Figure 4.6). Under the 1% probability threshold (i.e., 99% of the possible stress states would not produce a hydraulic fracture), an injection pressure of 10.88 MPa was found, whereas 11.72 MPa and 12.35 MPa were respectively determined for a 5% or 10% risk of fracturing. These results are based on the high level of uncertainty in some of the parameters provided, as described above. In addition, the Sleepy Hollow Field is currently undergoing waterflooding and no induced hydraulic fractures have been reported. The availability of stress measurements would greatly help reduce this uncertainty (See section 4.4.1).

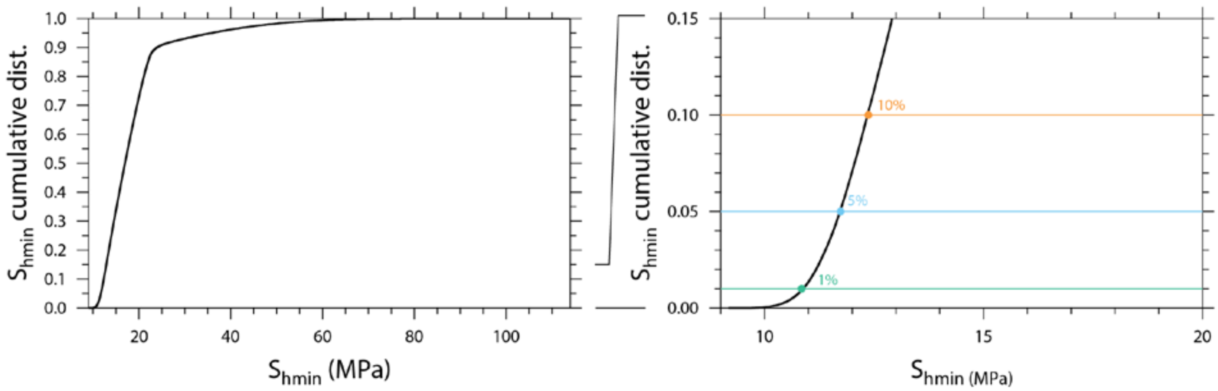

Figure 4.5. Cumulative distribution of the minimum horizontal stress (S_{hmin}) as determined by SOSAT (left) and the determination of the maximum allowable injection pressure under initial reservoir conditions corresponding to a 1%, 5%, and 10% risk of hydraulic fracturing (right).

In Section 2.5.3, the values for the stress path Γ_h coefficient were determined to conservatively range from 0.2 to 0.6. To demonstrate how SOSAT can be applied to the Sleepy Hollow Site, a value of 0.45 of potential pore pressure increase was taken to evaluate the risk of hydraulic fracturing. Using this reservoir stress path coefficient, the maximum safe injection pressure will increase by 45% of the average pore pressure increase. In other words, while the reservoir pressure increase progressively during CO_2 injection, the injection pressure can be increased over time without increasing the risk of hydraulic fracturing within the reservoir (Burghardt 2018).

Figure 4.6 presents a plot of the maximum allowable injection pressure that would result in either a 1%, 5%, or 10% risk of hydraulic fracturing as a function of average reservoir pore pressure. This plot shows that once the pore pressure builds up in the reservoir, the injection pressure can be slightly increased while maintaining the same probability of inducing hydraulic fracturing. This increase in the same injection pressure does not apply to the risk of induced seismicity. Based on the assumptions taken here for the stress path coefficient, the risk to create hydraulic fracturing can be substantial depending on the injection pressure. Based on the current state of knowledge about the state of stress it would be inadvisable to inject at the proposed injection pressure of 14.22 MPa since this would exceed the 10% probability threshold for hydraulic fracture initiation. Again, this is due to the lack of direct measurement of the minimum principal stress, and this risk could almost certainly be reduced substantially if a stress measurement were made. The safety of potential CO_2 injection is further evidenced by the fact that the field is currently undergoing waterflooding without incident.

The same analysis could be conducted with higher value for the stress path coefficient, which would be less conservative. This approach to analyzing this risk does not consider the risk of fracturing outside of the reservoir. For example, if the pore pressure remains low in the caprock it would still be risky to inject at a pressure exceeding the minimum principal stress in the caprock, even if this value would be below the elevated stress state in the reservoir. A coupled reservoir/geomechanical model would be required to evaluate this risk, and so it would be inadvisable based only on the current level of uncertainties revealed by this analysis to plan to increase the pore pressure beyond the initial thresholds. Stress measurements within the caprock formations would be very helpful to better quantify this risk.

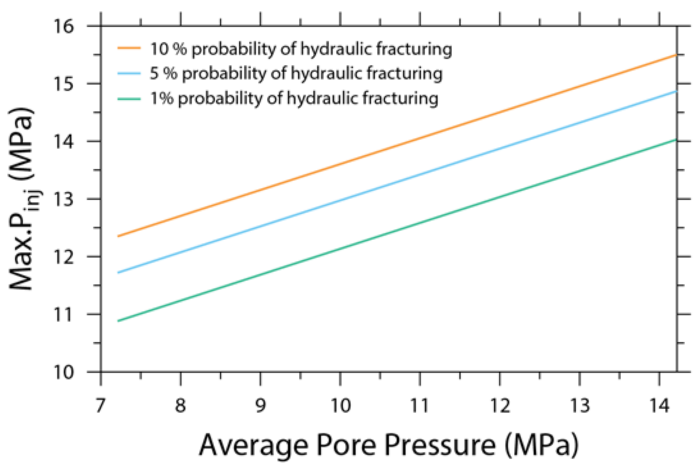

Figure 4.6. Injection pressure that would produce a 1% (orange), 5% (blue), and 10% (green) probability of hydraulic fracturing as a function of reservoir pore pressure.

4.4 Effects of parameters on perceived risks

4.4.1 Effect of stress measurement

As discussed above, to our knowledge, no stress measurements are available in the injection formation. To demonstrate how stress measurements could considerably add value to the analysis and could change the perception of risk, it was assumed that a measurement of the minimum horizontal stress was performed, leading to a value of 14.3 MPa with a standard deviation of 0.8 MPa. The same analysis is performed with SOSAT, using the same parameters as the one listed in Table 4.2, but with this additional parameter. The new distribution of horizontal stresses is shown in Figure 4.7, along with the probability of inducing shear failure on a critically oriented fault.

In contrast to the analysis where no stress measurements are available, with this hypothetical measurement, the risk that the reservoir was initially critically stressed in now only of approximately 6% to be compared to 22% without measurements. The risk of unintentional hydraulic fracturing would likewise decrease dramatically below the measured fracture pressure. In other words, the analysis presented here highlights the perception of the risk based on the information available: stress measurements would significantly reduce the uncertainty and allow for injection rates to be safely increased.

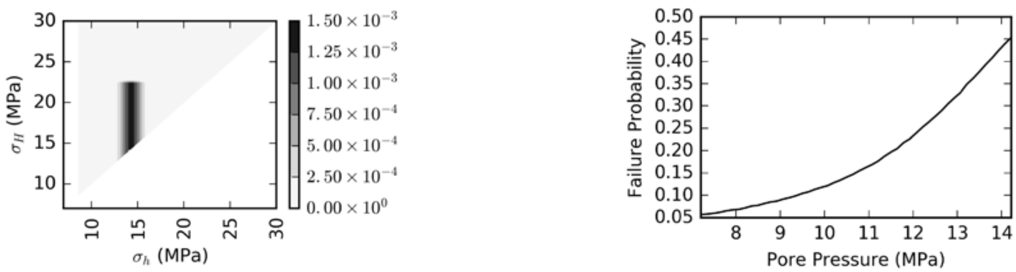

Figure 4.7. Horizontal stress distribution after a hypothetical measurements of the minimum horizontal stress (right) and probability of inducing shear failure on a critically oriented fault (left).

4.4.2 Effect of Stress Regime Observations

In the initial analysis, we assume that the faulting regime was very likely a normal faulting regime, without dismissing the probability of a strike-slip faulting regime (respective weights of 84, 14 and 1 were considered for normal faulting, strike-slip and reverse faulting). To evaluate the value of regional or site-specific observations, those weights are now considered to be respectively 60, 40 and 1. The higher probability of having a strike-slip faulting regime leads naturally to a higher uncertainty on the range of possible values for the maximum horizontal stress (Figure 4.8).

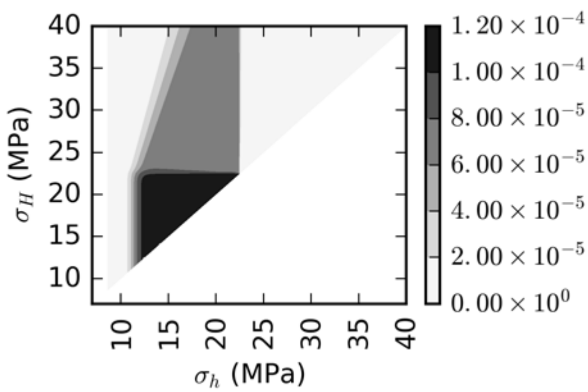

Figure 4.8. Horizontal stress distribution after changing the weight assigned the faulting regime horizontal stress.

5.0 Overview of PHH Site, KS

5.1 Setting and field history

The PHH site, located in Kearny County, southwestern Kansas (Figure 5.1), is composed of three oilfields (Patterson, Heinitz and Hartland) aligned on a geologic structure, covering an area of 36 mi^2. A total of 7.3 million barrels of oil have been produced from the Mississippian, Morrow sandstone, and Chester sandstone zones of these three fields through August 2018 (Holubnyak et al., 2020).

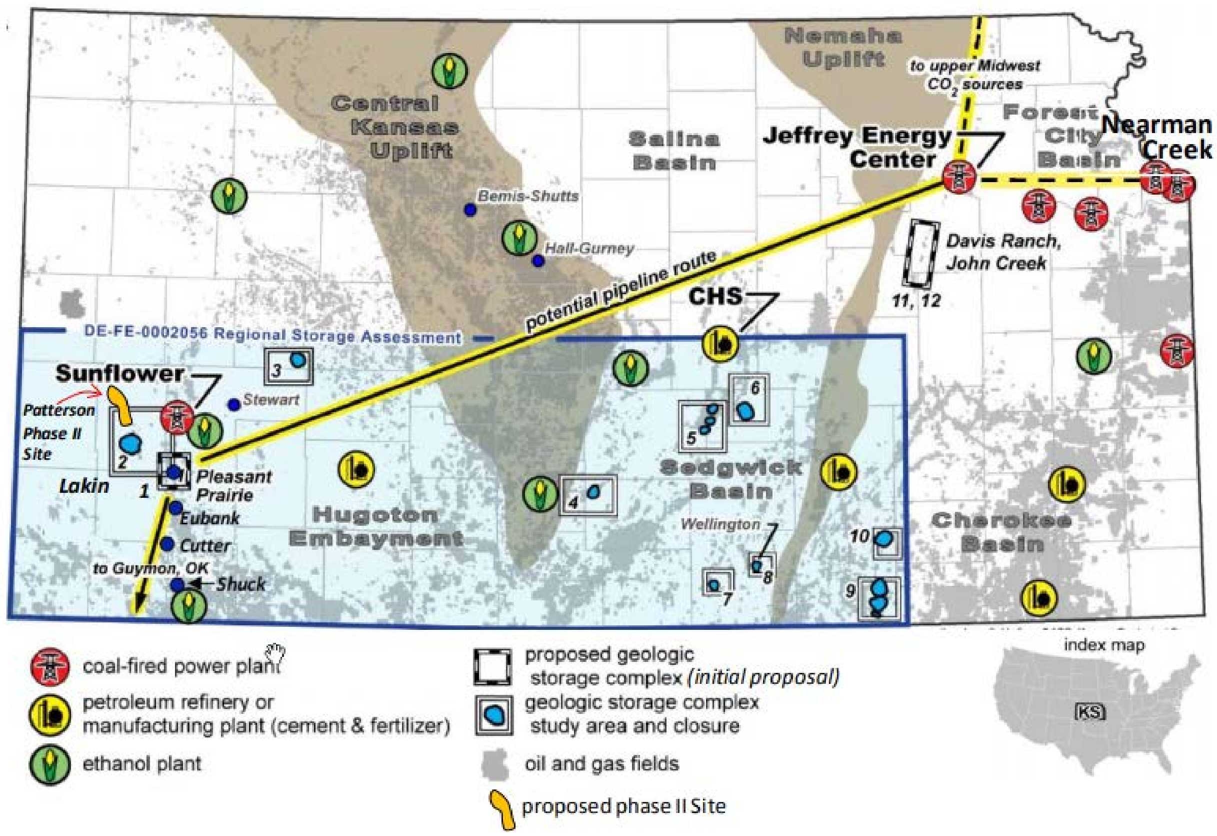

Figure 5.1. Kansas map showing location and general regional structure province from the PHH site (Holubnyak et al. 2018).

5.2 Storing CO_2 at the PHH Field

5.2.1 Reservoir Formations and Confining Units

Three deep saline storage intervals are considered for CO_2 storage: the Mississippian Osage, Middle-Ordovician Viola, and Cambro-Ordovician Arbuckle (Figure 5.2). These three formations are thick, laterally extensive, and present at depths ranging from 5,310 ft to 5,800 ft and are separated carbonate and shales formations (Meramec, Kinderhook, and Simpson dense carbonate and thin shales).

The Morrow shale (Pennsylvanian) on top of the Meramec (Mississippian) forms the primary confining unit at the PHH site, while numerous shale units in the Atoka and the Cherokee formations have also confining properties to ensure the containment of injected CO_2. The lateral continuity of the Morrow shale throughout the PHH site was confirmed recently with the interpretation of newly acquired seismic data under the IMSCS-HUB project (Duguid et al., 2020a).

Additionally, multiple Pennsylvanian shale units form other confining units. The evaporites of the Upper Permian Sumner and Nippewalla Groups are also considered as extensive confining layers that also contribute to protecting the High Plains Aquifer from the oil and gas operations.

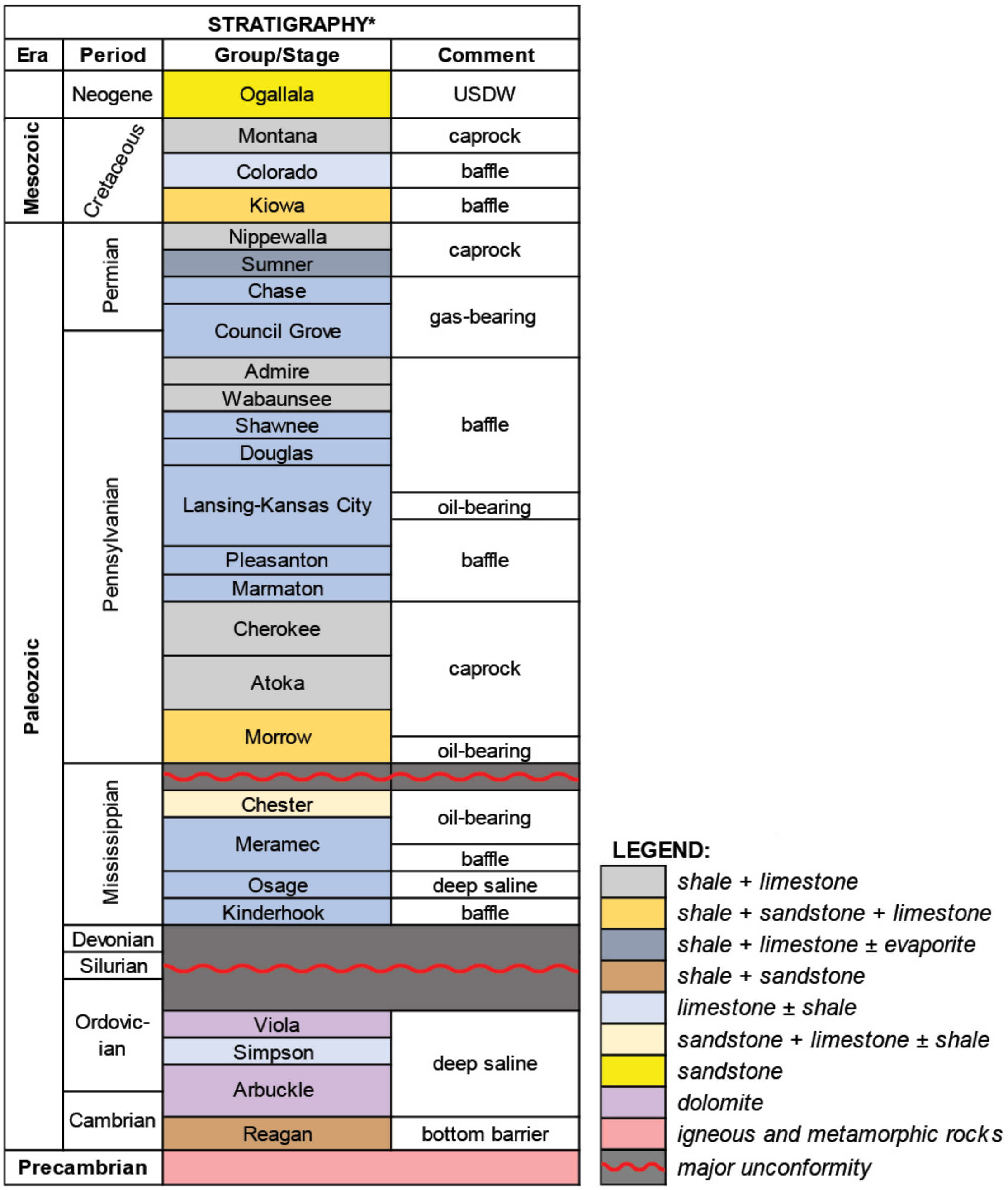

Figure 5.2. General stratigraphic chart of the PHH Site (Holubnyak et al., 2018; 2020).

5.2.2 Aquifers and Underground Sources of Drinking Water

The PHH site is located on the very edge of the same major source of irrigation and drinking water (i.e., High Plains Aquifer). Based on measurements provided by the Kansas Geological Survey and plotted in Figure 5.3 and Figure 5.4 the depth to water is ranging from 190 to 250 ft (58 to 76 m) in the nearest wells to the PHH site, although an important decrease was observed in the eastern part of the site (well 380057101181401).

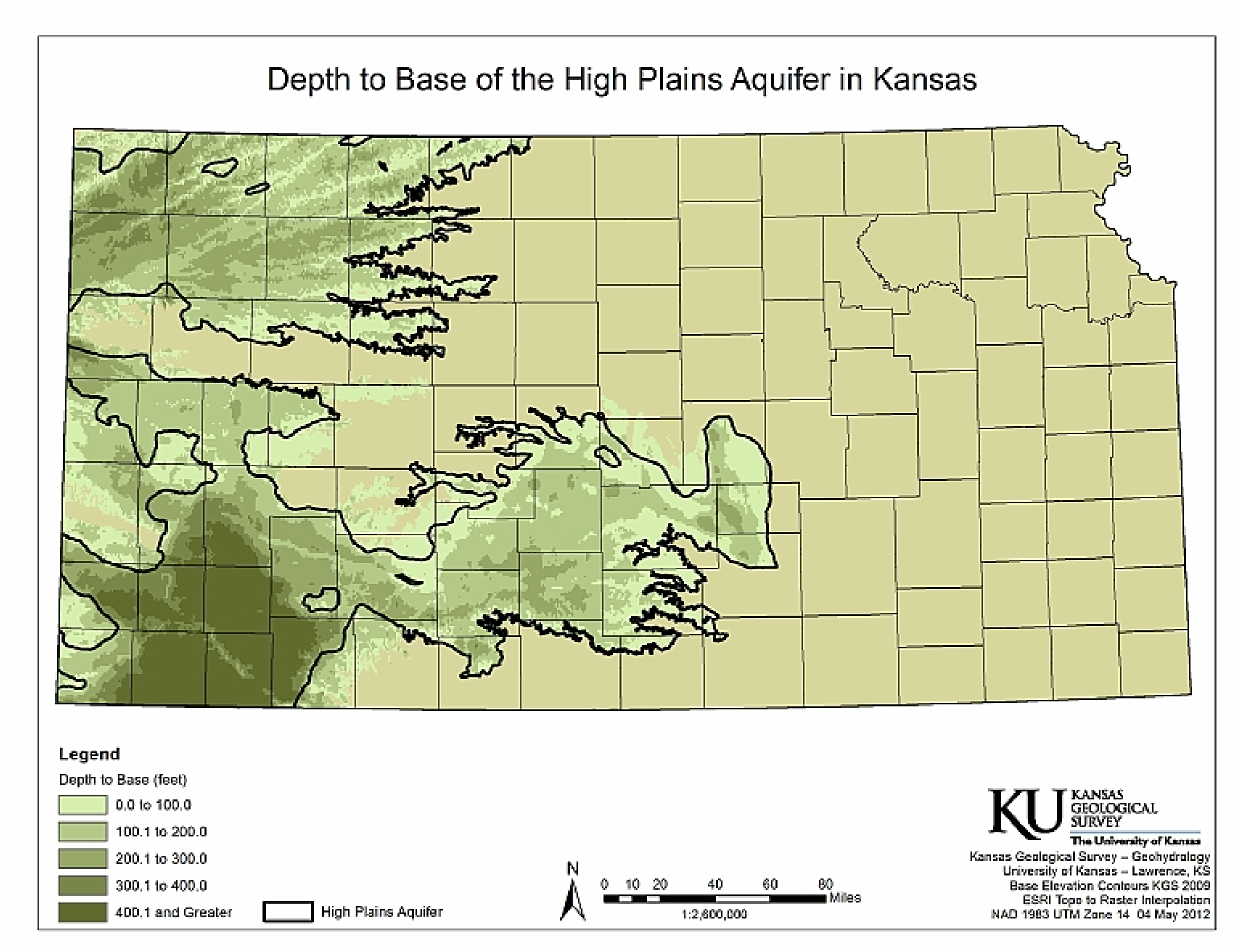

Figure 5.3. Depth to Base of the High Plain Aquifer in Kansas[1]

---

1 http://www.kgs.ku.edu/HighPlains/HPA_Atlas/Aquifer%20Basics/index.html#Depth_to_Base_of_HPA.jpg, last accessed on 6/22/2020

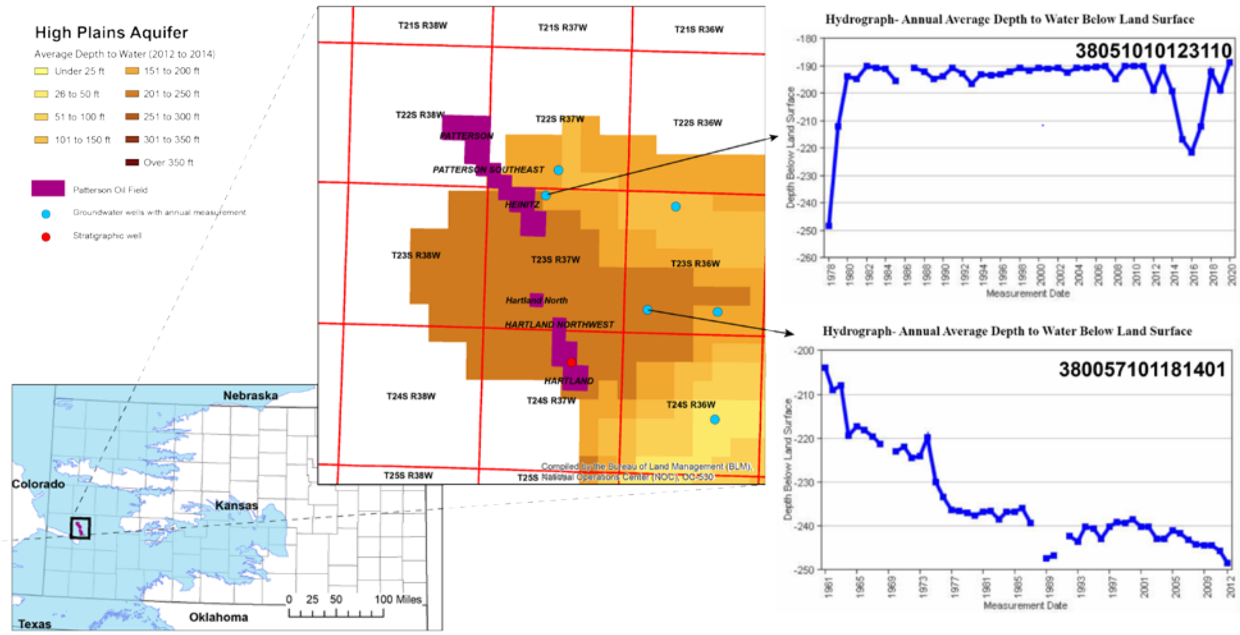

Figure 5.4. Average Depth to water of the High Plain Aquifer in the vicinity of the PHH Oil Field[1].

5.2.3 Above Zone Monitoring Interval

Besides the USDW (denoted as Aquifer 2) at the top, another aquifer (denoted as Aquifer 1) may exist between the USDW and the reservoir and may be used as an AZMI. More details of Aquifer 1 (aka AZIMI) are given in Section 6.1.2.

5.3 Storage operations and reservoir parameters

5.3.1 Injection depth

For the first set of simulations performed for the evaluation of the suitability of the site, the Osage formation was encountered between the depth of 5,260 and 5,400 ft, the Viola Formation between 5,500 and 5,700 ft (1,676 and 1,737 m) and the Arbuckle Group between 5,740 and 6,340 ft (1,676 m and 1932 m) (Table 5.1.). While two new wells Hartland KGS 6-10 and Patterson KGS 5-25 were recently drilled providing additional information on the local stratigraphy, these ranges of depths are the ones chosen to conduct the geomechanical analysis for consistency with the dynamic simulations.

5.3.2 Pore pressure

The initial static pressure in the injection zones used in the simulation, provided in Table 5.1. ranges from 1,615 psi (11.14 MPa) in Osage to 1,780 psi (12.27 MPa) in the Arbuckle Group. The pore pressure information will later be used in SOSAT to assess the geomechanical risks associated with CO_2 injection. The information is provided in the tool by defining a “pore pressure gradient”, which may be misleading. The pore pressure gradient, as defined in

[1] http://www.kgs.ku.edu/HighPlains/HPA_Atlas/InteractiveAtlas.html

SOSAT, corresponds to the pore pressure divided by the depth and is not the derivative of pore pressure with respect of depth.

5.3.3 Maximum injection pressure

As part of the dynamic modeling conducted to assess the feasibility of storing CO_2 at the PHH site, the well operating conditions are assumed to be 500 psi higher than the ambient pressure, leading to values ranging from 2,115 psi (14.6 MPa) to 2,280 psi (17.7 MPa) (Table 5.1.).

Table 5.1. Reservoir Formation Properties.

Formation	Depth	Depth	Reservoir Pressure	Reservoir Pressure	Pore pressure gradient*	Pore pressure gradient*	Max. injection pressure	Max. injection pressure
-	ft	m	psi	MPa	psi/ft	MPa/km	psi**	MPa**
Osage-Warsaw	5,260 to 5,400	1603 to 1646	1,615	11.13	0.307	6.9	2,115	14.6
Viola	5,500 to 5,700	1676 to 1737	1,720	11.86	0.313	7.1	2,220	15.3
Arbuckle Group	5,740 to 6,340	1750 to 1932	1,780	12.27	0.310	7.0	2,280	15.7

**As defined in SOSAT (i.e., pressure/depth)*
*** 500 psi higher than initial pressure*

5.4 In-situ stress measurements and regional observations

5.4.1 Average overburden density

Data from density logs collected in the Longwood GU#2 borehole were used to determine the average overburden density above the injection zone. Between 0 and 1642 ft bgs (0 and 500 m), where data were not available, a linear gradient ranging from 2.3 to 2.4 g/cm^3 was assumed. Based on the density log from the well, the resulting average overburden density above the injection interval (i.e., 5300 ft) is 2.43 g/cm^3 (Figure 5.5).

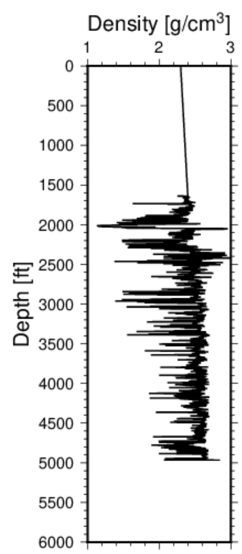

Figure 5.5. Density Log (RHOB) and associated Lithostatic Pressure Evolution with Depth for Longwood GU#2 (API# 15-093-20815).

5.4.2 Regional Stress Observations and stress indicators

The discussion presented for the Sleepy Hollow site related to the regional stress observations from the World Stress Map database, regional seismicity and identified focal mechanisms also applies for the PHH site (2.5.2). In this part of the midcontinent where the PHH site is located, stress measurements and stress indicators are also very limited. In the stress assessment conducted as part of the Integrated CCS for Kansas project and documented in Holubnyak et al. (2018), a strike-slip faulting regime was assumed, but as of today, no in-situ stress measurements have been performed to confirm this assumption. The stress regime at the site is likely to be at the transition between a strike-slip faulting regime and an extensional regime.

Multiple drilling induced tensile fractures (DITF) were identified in the image logs obtained from boreholes Hartland KGS 6-10 and Patterson KGS 5-25, while no breakouts were observed. In borehole Patterson KGS 5-25, the DITF are very consistent in the E-W direction, indicating the direction of the maximum horizontal stress (Figure 5.6 left). In the Hartland KGS 6-10 borehole, the directions of DITFs are mostly E-W, with some sections where a N-NE/S-SW trend is observed. Some of the DITFs appear also with en-echelon fractures (Figure 5.6 left, right), which indicates that the principal stresses are not aligned with the well at those locations.

The formation of DITFs is dependent on the relative magnitude of the two principal horizontal stresses, drilling mud pressure and temperature, formation temperature, and tensile strength. DITFs occur when the borehole wall goes into tension, which is often the case when there is a large difference between the two horizontal stresses because of the stress concentration that occurs due to the borehole. The formation of DITFs in the absence of substantial drilling mud losses indicates that the tensile stress state is local to the near wellbore region. The multiple DITFs observed in these two boreholes are also consistent with what has been reported in the area of the North Hugoton Storage Complex in Holubnyak et al. (2018), the stress regime is more likely a strike-slip faulting regime, although a normal faulting regime cannot be excluded and should therefore be considered for the probability distribution of the horizontal stresses.

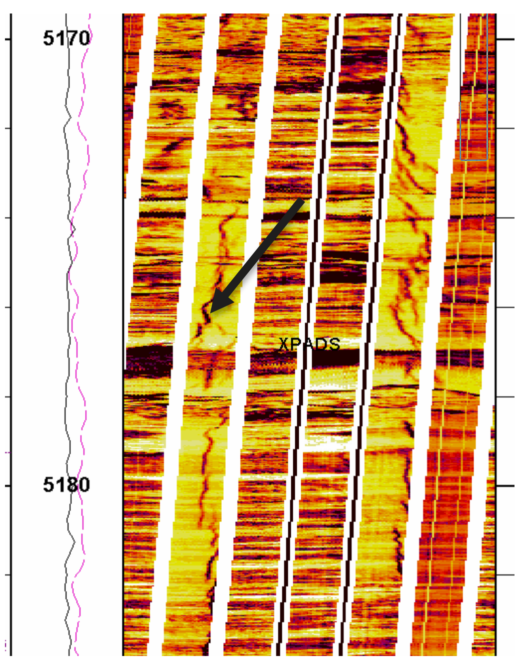

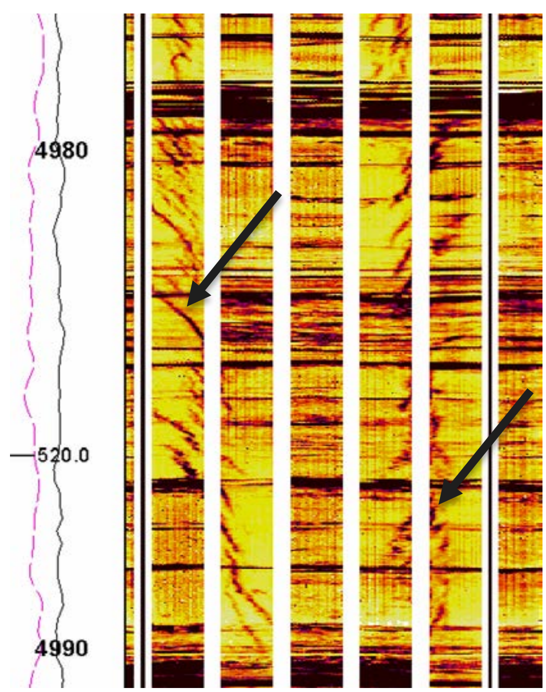

Figure 5.6. Left- Example of Drilling Induced Tensile Fracture (DITF) with E-W direction observed in Patterson KGS 5-25 borehole – Right: example of DITF observed in Hartland KGS 6-10 borehole. Here, en-echelon fractures are observed, indicating that the principal stresses are not aligned with the well at this location. DITFs are identified with black arrows.

5.4.3 Reservoir stress path coefficient

Data provided by the Kansas Geological Survey indicate that the Poisson's coefficient for the three injection intervals ranges from 0.222 to 0.227, which will therefore be considered as representative range for this study although for a complete analysis, additional core measurements will be available later in this phase of the project. Modeling using these data will refine results. These values are slightly lower than the range of the Poisson's ratio derived from the sonic logs, approximately ranging from 0.2 to 0.3 for the reservoir formations.

In the absence of measurements of the Biot's coefficient, a similar range of possible value as for the Sleepy Hollow analysis will be assumed (0.6 to 1.0).

Based on these assumptions, the stress path coefficient is expected to range from 0.43 to 0.72, which is very representative of what has been measured in field operations in different parts of the world.

5.4.4 Structural Framework

Recent interpretation of 3D seismic data acquired on the three oil fields forming the PHH site revealed the existence of two reverse faults perpendicular to each other that penetrate the reservoir and seal intervals (Duguid et al. 2020b). Fault offsets are maximum in the Precambrian basement and decrease upward. The first fault strikes N. 33°W and dips at 60-65° to the northeast, and the second strikes 40°E and dips at 55-65°.

The presence of the structural features justifies furthermore the critical need to assess the potential for faults reactivation in response to pore fluid pressure change associated with CO_2 injection.

6.0 Assessment of Leakage Risk at PHH with NRAP-Open-IAM

This section summarizes the application of the NRAP-Open-IAM to evaluate the risks of CO_2, and brine leakage, and their impacts to the USDW and the AZMI at the PHH site. The risk analysis was based on the reservoir simulation results for CO_2 injection and post-injection. The reservoir simulation used in this analysis was the one named “Perm5X_Model.” Additional Phase II simulation updates occurred concurrently with this work (Duguid et al., 2020b) and could be used in future NRAP-Open-IAM analyses.

6.1 Approach

First, the reservoir simulation was converted into a series of lookup tables, one table per layer. For the Perm5X_Model, there were 54 layers and hence 54 lookup tables were produced. One or more of the tables can be used for leakage risk analysis using the NRAP-Open-IAM.

Then a geological model that was composed three shale layers and two aquifers was established. After that, all the potential leak pathways (e.g, the injection wells and abandoned wells) were identified. For the PHH site, there were 6 injection wells. 19 abandoned wells that penetrated into the reservoir were identified.

Finally, NRAP-Open-IAM simulations were conducted to model the risk of the risks of leaks of CO_2, brine, and their impacts to the USDW and the AZMI for all the pathways to the overlying aquifers. Each of these steps is described in detail for the PHH site below.

6.1.1 Reservoir simulation

The CO_2 injection was implemented with 6 injection wells (Figure 6.1) under constant injection pressures for 25 years. The well bottom-hole pressure was kept constant at 500 psi above the reservoir pressure. The reservoir simulation was composed of a 25-year injection period and a 25-year post-injection period. As an example, the spatial distribution pressure and of CO_2 saturation at layer 11 at the end of injection (25 years) is shown in Figure 6.2. This study found 11 wells that penetrated the storage complex (reservoir), assuming the ground surface and the top of the reservoir are perfectly leveled. Because the elevations of these surfaces vary spatially, to be conservative, an additional 8 wells that are within 70 ft to the top of the reservoir were also included. Hence, the number of wells penetrating considered in this study is higher than the number found by Duguid et al. (2020c) who determined well penetrations using published geologic tops.

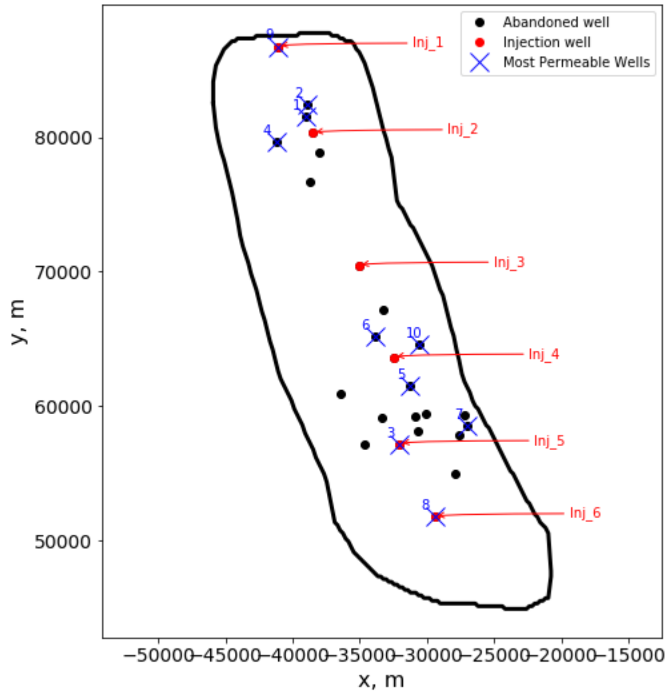

Figure 6.1. The 6 injection wells and the 19 existing wells that intersect the storage complex. The 10 most permeable well pathways are labeled by their permeability rank in decreasing order (e.g., rank 1 denotes for the most permeable well pathway).

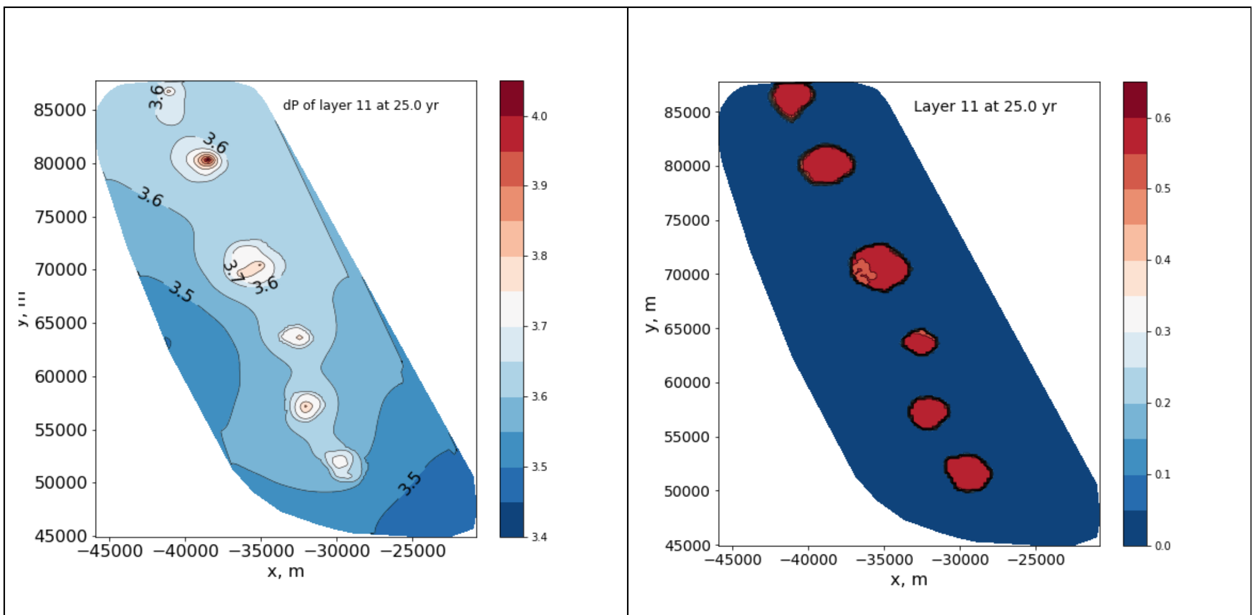

(a) Pressure Differential | (b) CO_2 Saturation

Figure 6.2. The distribution of gas pressure differential and CO_2 saturation at layer 11 at the end of CO_2 injection (25 years).

6.1.2 NRAP-Open-IAM analysis of risks of leak through well annulus

Stratigraphy

The stratigraphy of the PHH site is shown in Figure 5.2. Besides the USDW (denoted as Aquifer 2) at the top, another aquifer (denoted as Aquifer 1, aka, the AZMI) may exist between the USDW and the reservoir but there is no quantitative information to determine it. Hence, in NRAP-Open-IAM analysis, it was assumed that the thickness and depth of Aquifer 1 were uncertain. To address this uncertainty, three thicknesses, i.e., 800, 400, and 200 ft were conceptualized for Aquifer 1 (Figure 6.3), and their depths roughly correspond to the Lansing-Kansas City formation (Figure 5.2). Because the IAM tool requires at least three shale layers, a hypothetical Shale 3 was added above Aquifer 3 (Figure 6.3). This addition has negligible effect on the NRAP-Open-IAM analysis results for Aquifer 1 and Aquifer 2.

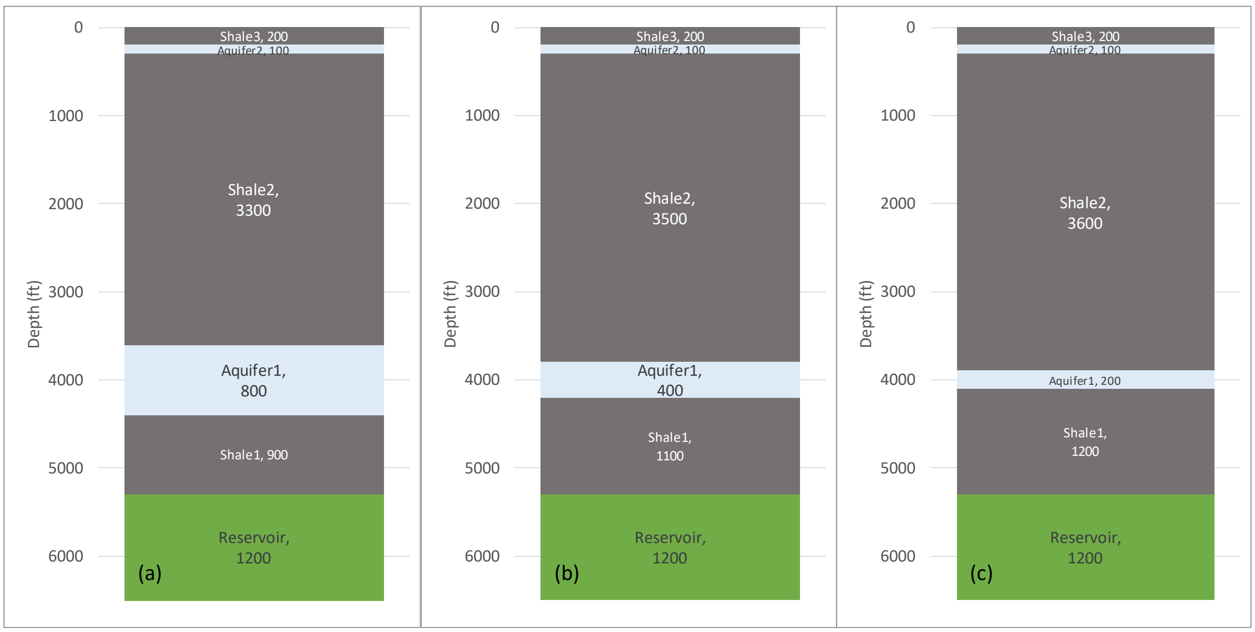

Figure 6.3. Three conceptual models composed of three shale layers and two aquifers for the NRAP-OPEN-IAM analysis representing for an aquifer (Aquifer 1, or AZMI) of a) large, b) intermediate, and c) small thickness. The numbers after the layer names are the thickness of the layer in feet.

Inputs to the NRAP-Open-IAM Model

Due to the lack of characterization data, hypothetical inputs were used in the analysis. The physical properties of the aquifers are summarized in Table 6.1. 19 legacy wells that occur in the simulation domain and penetrate to the reservoir were selected (Figure 6.1). Together with the 6 injection wells, there were 25 potential pathways for leakage. The permeability of these 25 well pathways were unknown and hence were generated randomly between the logk range of -13 and -11 (about 0.1 and 10 Darcy) and are shown in Figure 6.4. It was expected that the pathways with high permeability will be of the most concern, and hence the permeability rank of each pathway in descending order is also marked in Figure 6.4.

The NRAP-Open-IAM model also needs inputs, i.e., CO_2 saturation (S_g) and pressure (P) from the reservoir simulation at different times from the start of CO_2 injection to the end of post-injection. The pressure is the driving force for brine migration, while the quantity of CO_2 is of concern.

The distribution of S_g and P of one layer of the reservoir model was needed as input to the IAM model. The vertical distribution of reservoir was not linear (Figure 6.5) possibly because of the layering structure of the stacked reservoir. The bottom-most layer 54 shows exceptionally higher pressure than what the trend line would predict (Figure 6.5). As a result, the pressure in this layer poses the highest risk to drive brine along any leak pathways. However, the CO_2 saturation at this layer was very low (<0.00012). Layer 11 had higher CO_2 saturation (up to approximately 0.7, Figure 6.2) than other layers. Hence, the leak risk from both layers 54 and 11 were investigated.

Table 6.1. Aquifer properties at the PHH Site.

Parameters	Aquifer 1	Aquifer 2
Porosity	0.10	0.15
Log-Permeability (m^2)	-13.39	-11.92
Log-Anisotropy	0.30	0.30
Volumetric Fraction of Calcite	0.1	0.1

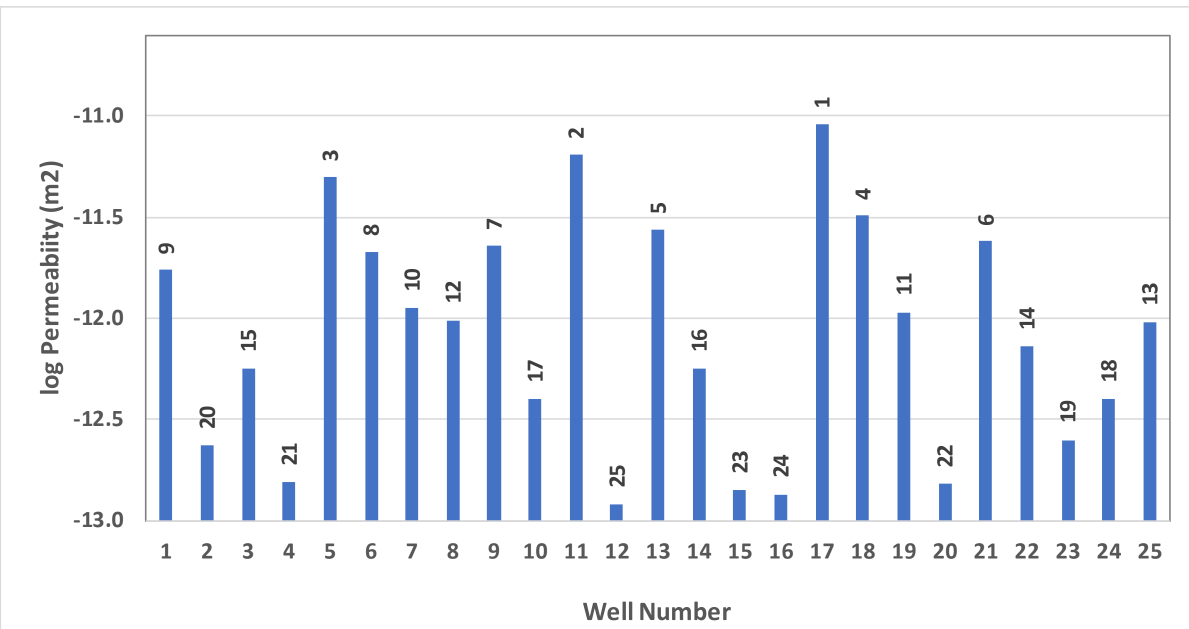

Figure 6.4. Log-permeability of the 25 well pathways. The labels denote the permeability rank from largest to the smallest.

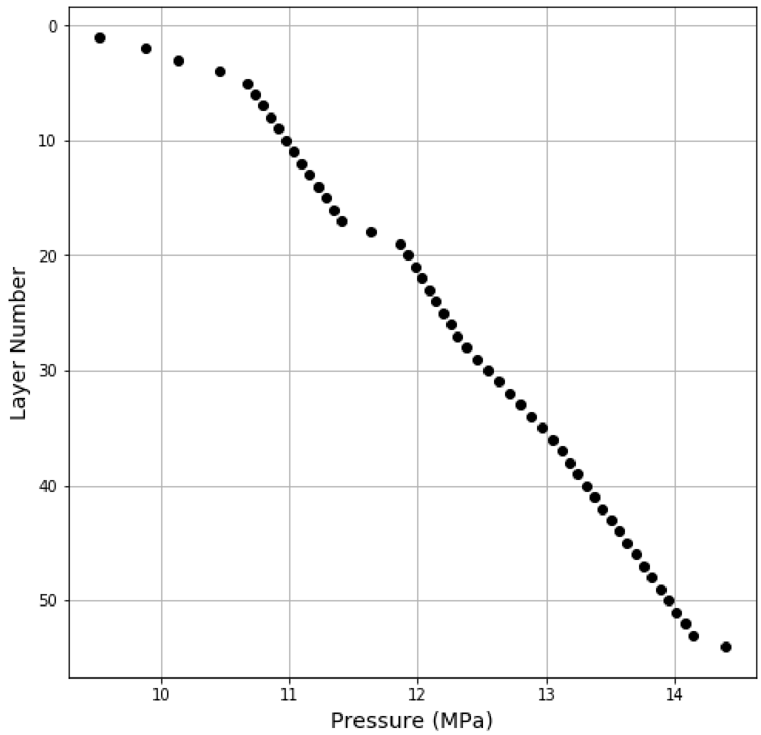

Figure 6.5. The initial pressure distribution in the reservoir.

6.2 Results

Because the reservoir is under pressured, the IAM analysis using the reservoir simulation results of Layer 11 produced zero leakage for both CO_2 and brine and hence had no impact on the overlying aquifers. The results using Layer 11 will not be discussed further and the results using Layer 54 will be discussed in detail below.

Although the three sets of NRAP-Open-IAM analysis were conducted for the thick, intermediate, and think thickness of Aquifer1, the thick aquifer case (Case a in Figure 6.3**Error! Reference source not found.**) poses the most risk. Hence, here we focus on this case, while the complete results for all the three cases are given in Appendices C, D, and E, respectively.

6.2.1 Reservoir pressure

Figure 6.6 shows the pressure variation with time for all 25 wells for the case of thick Aquifer1 along with four percentile lines. The pressure increased with time during the CO_2 injection period (0 to 25 years) but kept relatively stable during the post injection period (25 to 50 years). The pressure in some wells were much higher than that of others. At the end of injection, the pressure at the 95th percentile was approximately 0.7 MPa higher the that at the 50th percentile, indicating some wells pose much higher risks than others.

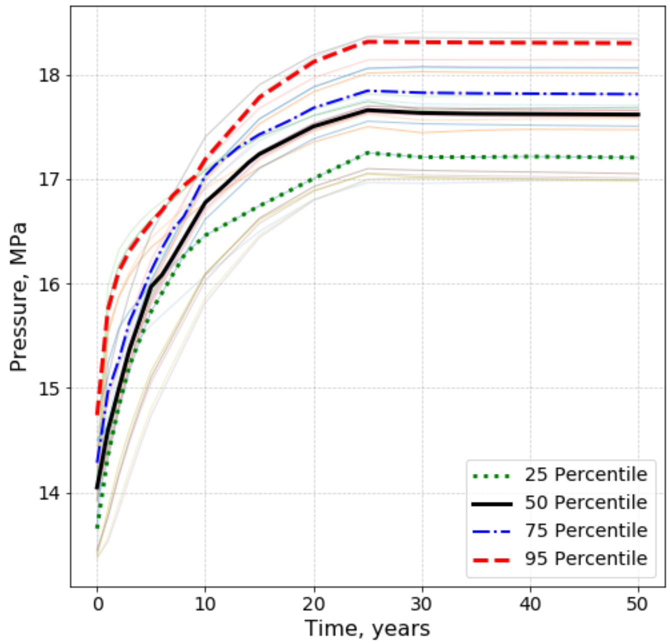

Figure 6.6. The pressure variation with time for all 25 wells for the case of a thick Aquifer 1 (thin lines). The thick lines denote the selected percentiles.

6.2.2 CO_2 leak to aquifers

Figure 6.7 shows CO_2 leakage rates for all 25 wells to Aquifer 1 and Aquifer 2. The leakage rates generally increased with time till the end of injection at 25 years. Then the leakage rates remained relatively stable. The leakage rate was very small (no more than 5.3 kg/yr). Figure 6.8 shows the leaked mass to Aquifer 1 and Aquifer 2. The quantity of CO_2 leaked to Aquifer 2 was over one order of magnitude larger than that to Aquifer 1. The reason was that Aquifer 2 had larger permeability than Aquifer 1 (Table 6.1).

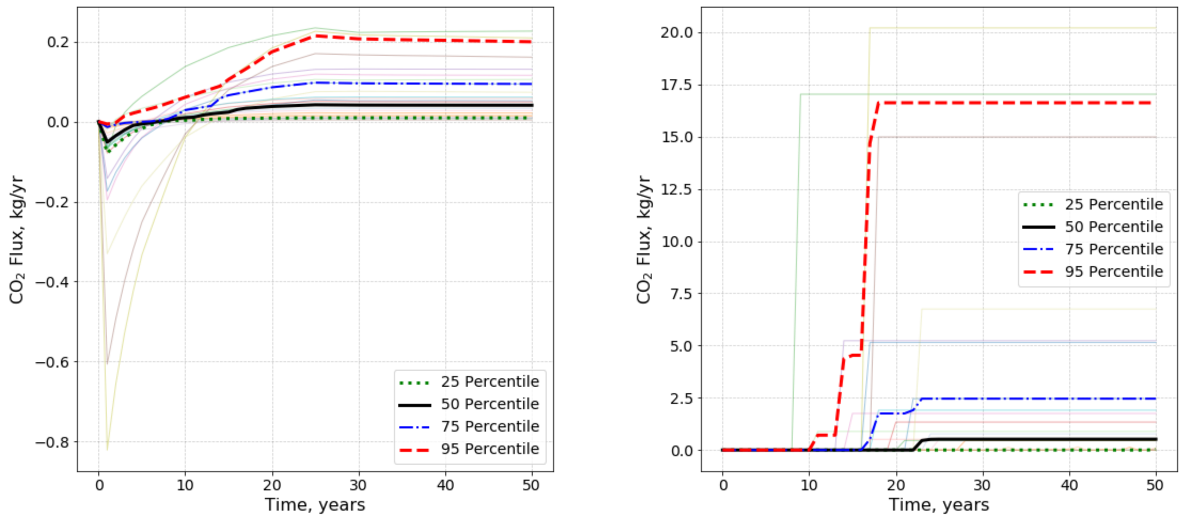

(a) (b)

Figure 6.7. CO_2 leakage rate (a) Aquifer 1 and (b) Aquifer 2 for all the wells. The thick lines denote the selected percentiles.

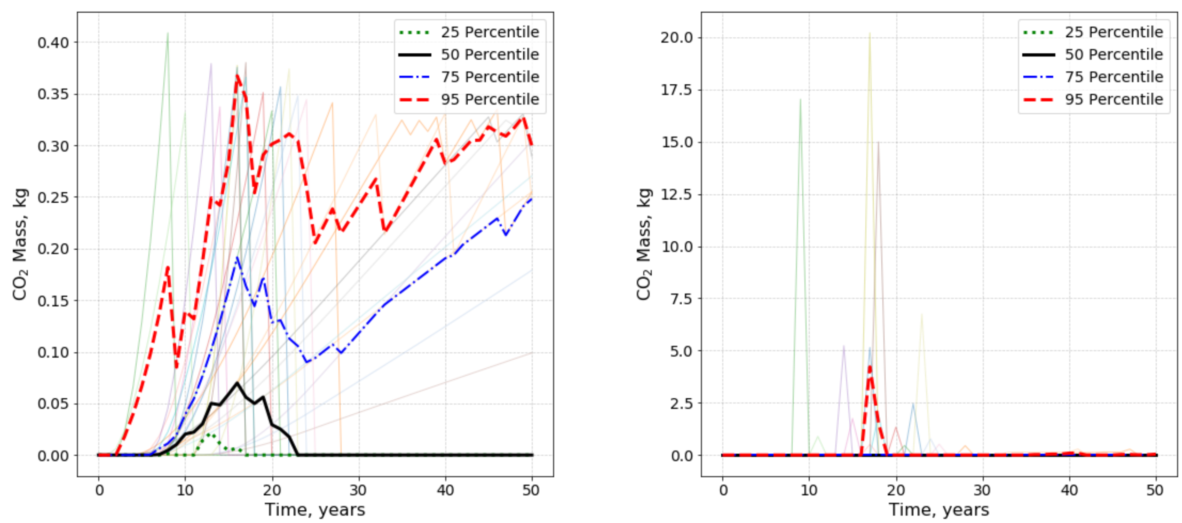

(a) (b)

Figure 6.8. CO_2 mass to (a) Aquifer 1 and (b) Aquifer 2 for all the wells. The thick lines denote the selected percentiles.

6.2.3 Brine leak to aquifers

Figure 6.9 shows the brine leakage rate to Aquifer 1 and Aquifer 2 for all the 25 wells. Generally, the leakage rates were either negative or near zero, meaning the reservoir pressure was insufficient to cause any significant brine leak.

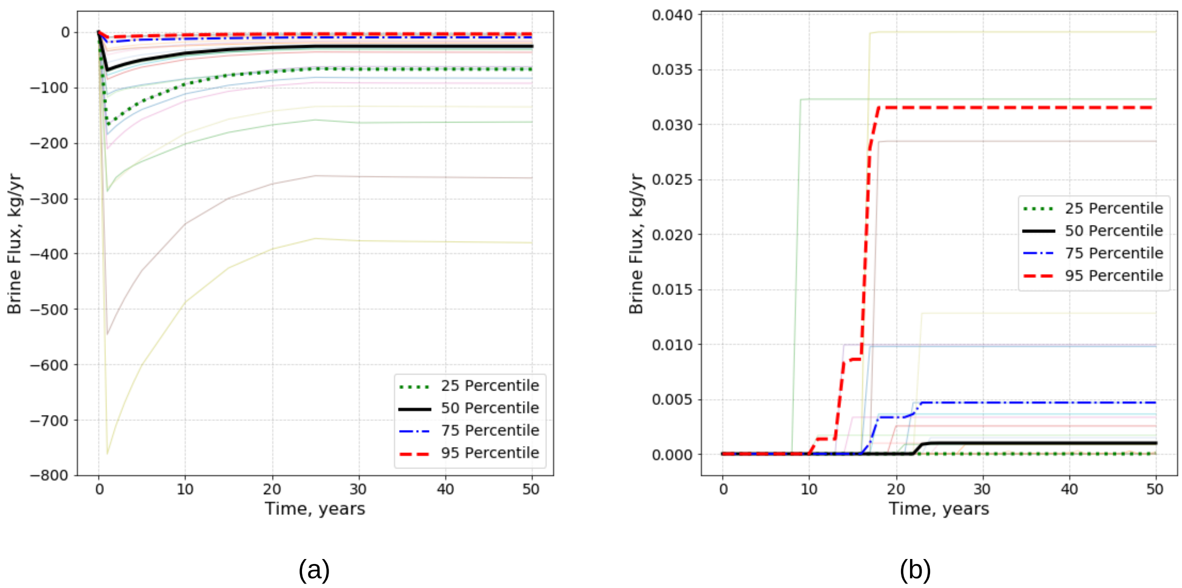

Figure 6.9. Brine leakage rate to (a) Aquifer 1 and (b) Aquifer 2 for all the 25 wells. The thick lines denote the selected percentiles.

6.2.4 Impacts of leaks to the USDW (Aquifer 2)

Figure 6.10 shows the impact of CO_2 leakage to the USDW expressed as the volume of the aquifer because of pH change or the increased concentration of dissolved CO_2. The pH impact was up to hundreds of cubic meters and the dissolved CO_2 was up to thousands of cubic meters of Aquifer 2. However, these impacts appeared to be short-lived and disappeared in one time-step (i.e., 1 year) of the model. The increase of the reservoir pressure and TDS had no impact to the USDW.

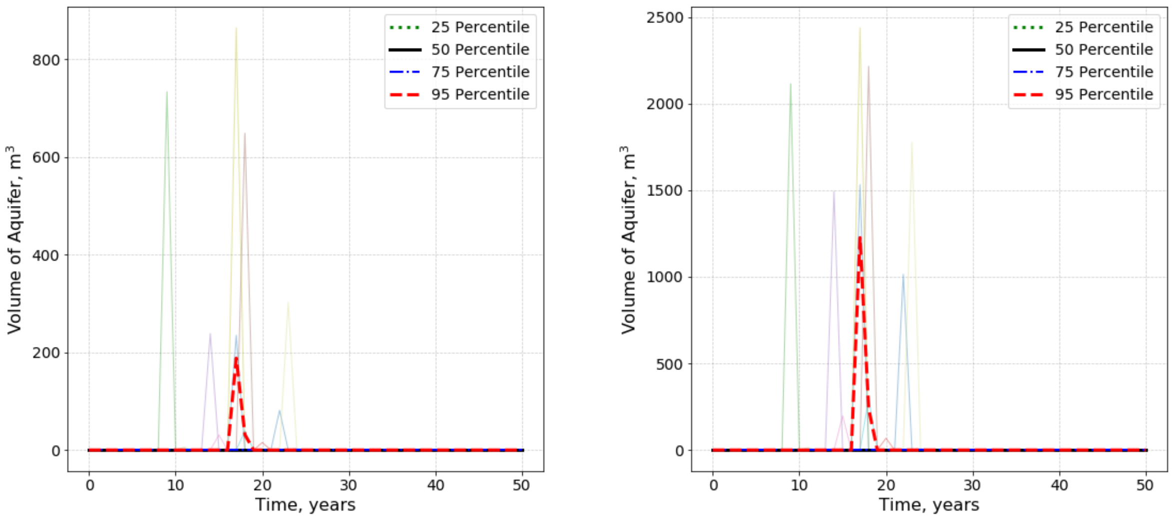

(a) pH Impact (b) Dissolved CO_2 Impact

Figure 6.10. The impact of CO_2 leakage to Aquifer 2.

6.2.5 Permeability effects on CO_2 leak

Table 6.2 tabulates the maximal values of the evaluation variables, the permeability rank of the well pathway through which the maximum leakage occurred, and the occurrence time. With one exception, the peak values occurred in the two wells, with permeability ranks of 1 and 3 (corresponding to Wells #7 and #5, respectively, Figure 6.4). However, the well with permeability rank 2 does not show up in the table. From Figure 6.1, we can see the rank 1 well is very close to injection well #1, while the rank 3 well actually is the injection well #5. These results indicate that both the well permeability and the distance to an injection well affect the risk of CO_2 leakage.

Table 6.2. The maximal values, the permeability rank of the well, and occurrence time during the injection and post-injection period.

	(a) Thick Aq1			**(b) Intermediate Aq1**			**(c) Thin Aq1**		
Variable Name	Well Rank	Max Value	Time (yr)	Well Rank	Max Value	Time (yr)	Well Rank	Max Value	Time (yr)
Aq1 CO_2 Flux, kg/yr	3	0.2	25	3	0.2	25	3	0.2	25
Aq2 CO_2 Flux, kg/yr	1	5.3	50	1	26.8	50	1	20.2	50
Aq1 CO_2 Mass, kg	7	1.4	49	1	0.8	21	3	0.4	8
Aq2 CO_2 Mass, kg	1	5.3	36	1	26.8	22	1	20.2	17
pH Impact Volume, m3	1	241.0	36	1	1131.8	22	1	864.6	17
Dissolved CO_2 Impact Volume, m^3	1	1866.8	36	1	2816.5	22	1	2436.7	17

7.0 Assessment of Geomechanical Risks at PHH

The state of stress assessment was conducted using SOSAT in the shallowest CO_2 injection interval considered at the PHH site (i.e., Osage formation, Table 7.1), chosen to demonstrate the methodology. As stated in the objectives of the analysis in Section 1, the goal of this study is not to provide an exhaustive geomechanical analysis at the PHH site but is clearly meant to highlight how uncertainties can affect the degree of which risks are perceived at the site and how this could subsequently affect decision making.

7.1 SOSAT inputs: Summary of parameters

The required and optional parameters of SOSAT described in Section 1.2.2 and listed in Table 4.1) were determined based on the current knowledge of the site. The probability distribution of the state of stress is calculated and the probability of activating a critically-oriented fault at a specified range of pore pressures is determined. As already stated earlier, the approach is conservative as it assumed that a critically-fault exists.

7.1.1 Fault regime weights

In the absence of in-situ stress measurements, the evaluation of the regional stress data, earthquake moment tensor solutions, image and sonic logs from the KGS-5-25 and KGS 6-10 boreholes suggest that the stress regime at the location of the PHH site is most likely strike-slip faulting regime with a lower probability for a normal faulting regime. The location of the boundary between extensional and strike-slip faulting regimes is not well defined. It is therefore reasonable to assign a conservative probability of strike-slip faulting regime greater than a normal faulting state, while the probability of reverse faulting is approaching zero (a zero value is not a possible option in the current version of SOSAT).

A weight of 85 was then assigned to the strike-slip state, and respective weights of 14 and 1 were given to the normal and reverse faulting regimes. Respective values of 50 and 300 were assigned to K-thrust and K-SS, leading to a smooth transition between the normal faulting and strike-slip faulting regimes, and an abrupt transition between the strike-slip. The resulting probability distribution for g_θ is shown in Figure 7.1 (see Burghardt (2018) and section 4.1.1).

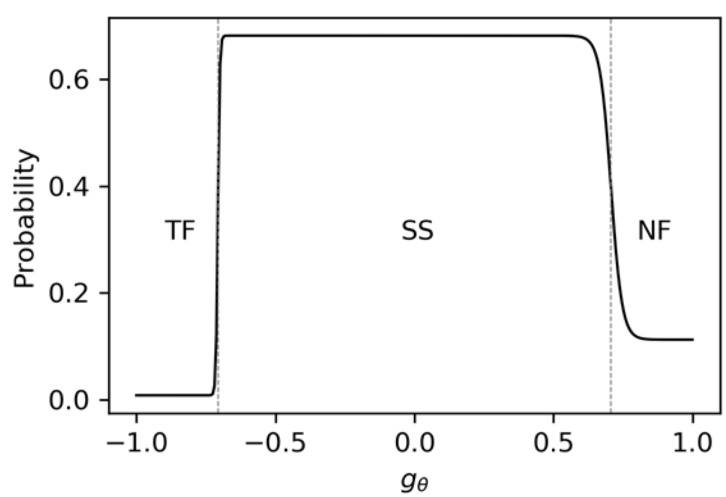

Figure 7.1. Plot of the probability distribution expressing the regional stress state information, with weight TF = 1, weight SS = 84, weight NF = 14, K-thrust = 300, and K-SS = 50.

7.1.2 Friction coefficient

Similarly to the Sleepy Hollow field, the friction coefficient was defined as a lognormal distribution with a mean μ_0 of 0.7 and standard deviation σ_μ of 0.15 for the PHH field (see Figure 4.2 for reference).

7.1.3 Summary of input parameters

The resulting parameters determined for the needs of SOSAT are listed in Table 7.1 for the three targeted formations, although the analysis was performed in the first injection interval (Osage). In the absence of in situ stress measurements and formation-specific elastic properties, conducting an analysis for each of the targeted reservoirs would not add any value.

Table 7.1. Summary of the reservoir properties and stress observations input parameters for SOSAT.

Parameters	Osage	Viola	Arbuckle
Reservoir Parameters			
Median Friction Coefficient	0.7 (default)	0.7 (default)	0.7 (default)
Standard deviation of logarithm of fault friction coefficient	0.15 (default)	0.15 (default)	0.15 (default)
Maximum possible friction coefficient	1.5 (default)	1.5 (default)	1.5 (default)
Reservoir depth (ft)	5,260 ft *(1603.2 m)*	5,500 ft *(1676.4 m)*	5,740 *(1749 m)*
Pore pressure gradient[1]	0.307 psi/ft *(6.92 MPa/km)*	0.313 psi/ft *(7.08 MPa/km)*	0.310 psi/ft *(7.01 MPa/km)*
Average overburden density	2.43 g/cm^3	2.43 g/cm^3	2.43 g/cm^3
Maximum injection pressure	2,250 psi *(15.5 MPa)*	2,300 psi *(15.85 MPa)*	2,400 psi *(16.55 MPa)*
Regional Stress Info			
Normal faulting weight	14	14	14
Strike-slip faulting weight	85	85	85
Thrust-faulting weight	1	1	1
Maximum possible friction coefficient	1.5 (default)	1.5 (default)	1.5 (default)
K-thrust /K-SS	50 / 300	50 /300	50 / 300
Stress Measurement			
Mean of S_{hmin}	-	-	-
Standard deviation of S_{hmin}	-	-	-
Stress Path			

[1]as defined in SOSAT (pore pressure at the a given depth, divided by the total vertical depth).

Minimum value of the stress path coefficient	0.43	0.42	0.42
Maximum value of the stress path coefficient	0.72	0.72	0.72

7.2 Stress distribution and risk of induced shear failure

The posterior stress distribution presented in Figure 7.2 represents the probability density (shown in grayscale) for combinations of minimum and maximum horizontal stress values. The results demonstrate the extremely high degree of uncertainty on the magnitude of the maximum horizontal stress, due to the stress faulting regime assumed (strike-slip faulting conditions). While possible magnitudes ranges from about 20 MPa to 40 MPa for the minimum horizontal stress, the possible magnitude for the maximum horizontal stress ranged from 40 MPa to more than 100 MPa. This high range of probabilities for both horizontal stresses reflects the current state of information available on the geomechanical conditions in this part of Kansas, and highlights the crucial need to obtain in situ stress measurements to reduce uncertainties.

The total probability of induced shear failure as a function of pore pressure change is determined in SOSAT and plotted in Figure 7.3. This plot shows that the probability that the injection zone was initially critically stressed is relatively high as indicated by the value of about 23%. When the pore pressure increases to 15.5 MPa (2,250 psi), determined to be the maximum allowable pressure based on the dynamic modeling, the risk of shear failure approaches a probability of 28%. As with the Sleepy Hollow site, this risk is primarily driven by large uncertainties in the in situ state of stress cause by the lack of direct measurements. These uncertainties could be substantially reduced with direct stress measurements. In the case of the PHH site, special effort should be made to infer the maximum horizontal stress since a strike-slip faulting regime is likely to prevail at this site. Methods such as sleeve fracture re-opening and careful analysis of the DITFs and breakouts together with mud pressure/temperature measurements and core-based strength measurements are suggested.

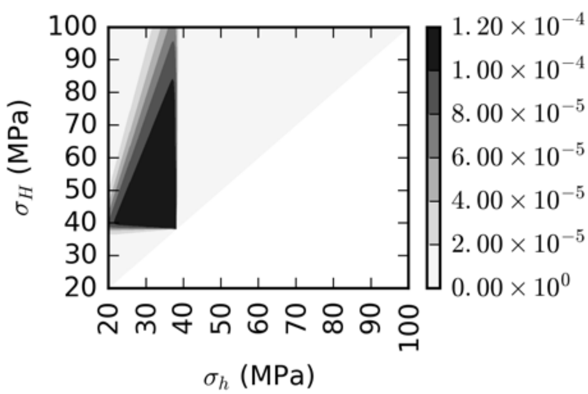

Figure 7.2. Posterior Stress Distribution Plot at the PHH field.

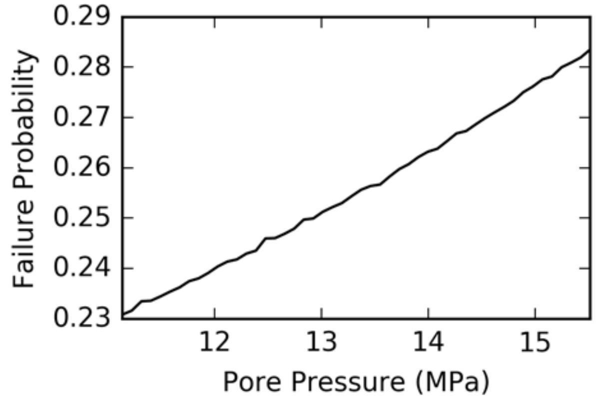

Figure 7.3. Probability of inducing shear failure on a critically oriented fault plane for a given pore pressure at the Sleepy Hollow Site.

7.3 Risk of unintentional hydraulic fracturing

The same type of analysis as the one conducted on Sleepy Hollow was performed to evaluate the risk of unintentional hydraulic fracturing. As stated before, the injection pressure must remain smaller than the minimum principal stress to prevent the initiation of hydraulic fractures. Three scenarios were evaluated, assuming that either a 1%, 5%, or 10% risk of fracturing was acceptable. Based on the cumulative probability distribution obtained from the posterior stress distribution calculated with SOSAT (Figure 7.1), the maximum allowable pressure under initial reservoir conditions was obtained for the three scenarios (Figure 4.6). Under the 1% probability threshold (i.e., 99% of the possible stress states would not produce a hydraulic fracture), an injection pressure of 19.37 MPa was determined, whereas 22.11 MPa and 24.11 MPa were respectively determined for a 5% or 10% risk of fracturing.

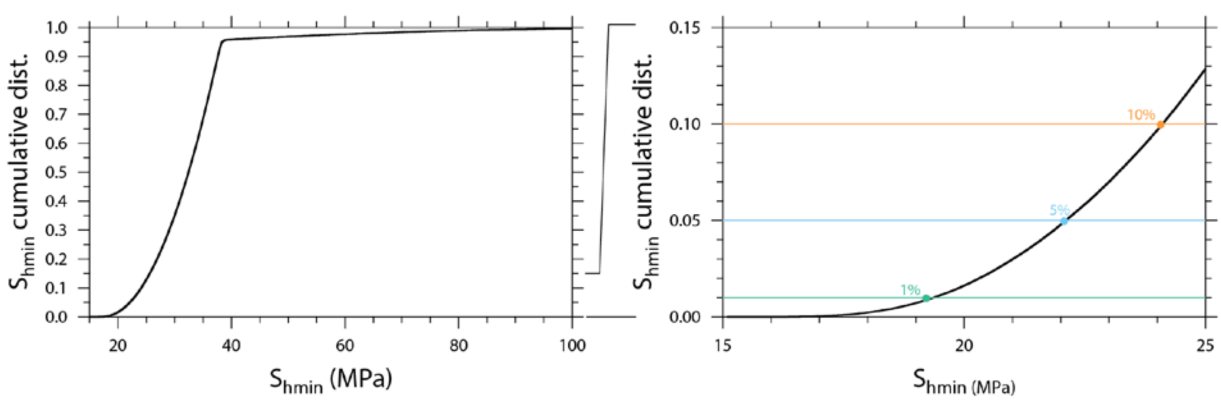

Figure 7.4. Cumulative distribution of the minimum horizontal stress ($S_{hmin)}$ as determined by SOSAT (left) and the determination of the maximum allowable injection pressure under initial reservoir conditions corresponding to a 1%, 5%, and 10% risk of hydraulic fracturing (right).

The stress path Γ_h coefficient was determined to conservatively range from 0.42 to 0.73. To demonstrate how SOSAT can be applied to the Sleepy Hollow Site, a value of 0.57 of potential pore pressure increase was assumed to evaluate the risk of hydraulic fracturing. Using this reservoir stress path coefficient, the maximum safe injection pressure will increase by 57% of the average pore pressure increase.

Figure 7.5 presents a plot of the maximum allowable injection pressure that would result in either a 1%, 5%, or 10% risk of hydraulic fracturing as a function of average reservoir pore pressure. This plot shows that once the pore pressure builds up in the reservoir, the injection pressure can be slightly increased while maintaining the same probability of inducing hydraulic fracturing. Based on the assumptions taken here for the stress path coefficient, the risk to create hydraulic fracturing with the injection pressure assumed (15.5 MPa) is limited.

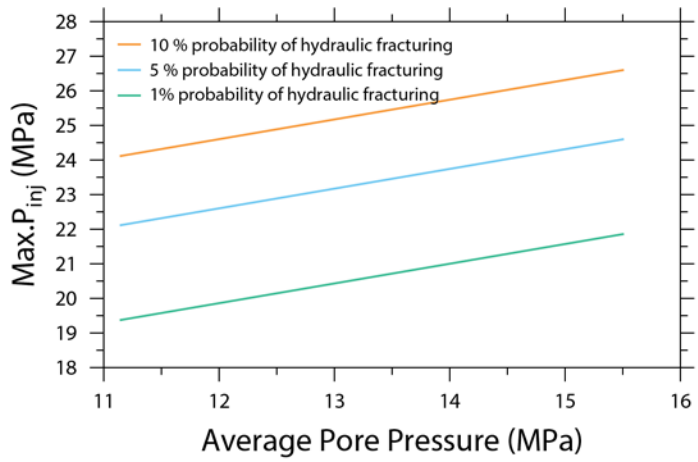

Figure 7.5. Injection pressure that would produce a 1% (orange), 5% (blue), and 10% (green) probability of hydraulic fracturing as a function of reservoir pore pressure.

8.0 Discussion

8.1 NRAP-Open-IAM

8.1.1 Sleepy Hollow and PHH

Sleepy Hollow Field

Application of the NRAP-Open-IAM to the Sleepy Hollow Field showed that while every well was allowed to leak with some permeability, most of the fluxes, amount leaked, and resulting impacts were negligible. Leakage of CO_2 into the USDW (Aquifer 2) was most impactful but monitoring should be conducted near injection wells as the diameter of impact is at most 10s of meters. In these studies, pressure was less impacted than geochemical indicators (i.e., pH and dissolved CO_2). The leakage impact signal was also significantly delayed, often by years or even a decade, so monitoring may be justifiably deployed over extended time and with semi-annual sampling frequency unless a problem is detected early.

More parameter characterization and uncertainty quantification is needed before such results could be used to support a Corrective Action or Monitoring plan, which are required components of a Class VI UIC injection well permit, but this tool does have the capability to support those plans if more data is collected for that effort.

PHH Field

The NRAP-Open-IAM was used to evaluate the risks of leaks of CO_2, brine, and their impacts to the USDW and the AZMI at the PHH site. The risk analysis was based on the reservoir simulation results of 25-years of CO_2 injection and a 5-year post-injection period. In the IAM analysis, it was assumed that the thickness and depth of Aquifer1 were uncertain. To address this uncertainty, three thicknesses, i.e., 800, 400, and 200 ft were conceptualized. The leakage risk from 6 injection wells and 19 legacy wells that occur in in the simulation domain and penetrate to the reservoir were selected were investigated. Due to the lack of characterization data, hypothetical inputs were used in the analysis. The leakage risk from two reservoir layers was evaluated, i.e., layer 54 with the exceptionally higher pressure than what the trend line would predict and layer 11 with the highest CO_2 saturation. There was no leakage of CO_2 or brine from layer 11 because the layer was considerably under-pressured. For layer 54, the main findings are summarized below.

- The CO_2 injection caused pressure increase did not cause any brine leakage to the overlying aquifer, while a small amount of CO_2 leaked to Aquifer 1 and Aquifer 2.
- The CO_2 leakage rates generally increased with time until the end of injection at 25 years. Then the leakage rates remained relatively stable. The leakage rate was very small (no more than 5.3 kg/yr). The quantity of CO_2 leaked to Aquifer 2 was over one order of magnitude larger than that to Aquifer 1.
- The pH impact was up to hundreds of cubic meters and the dissolved CO_2 was up to thousands of cubic meters of Aquifer 2. However, these impacts appeared to be short-lived and disappeared in one time-step (i.e., 1 year) of the model.

- With one exception, the peak values of investigated variables occurred in the two wells, with permeability rank of 1 and 3. Both the well permeability and the distance to an injection well affect the risk of CO_2 leakage.

8.1.2 Feedback on application of NRAP-Open-IAM

Some observations on applying the tools to the sites are:

- The Graphical User Interface (GUI) version of the NRAP-Open-IAM is currently too simplistic to deploy at an actual site. The GUI version should either be expanded in robustness or should be used as a training tool to understand the NRAP-Open-IAM.

- We were unable to use the permeability generator for well properties as we needed to visualize the realized permeabilities in the context of their well number and distance from an injector. The code should be updated to take in either external permeability files or functions and to export the realizations for post-processing analysis.

- We used an augmented version of the multisegmented well model that has the brine and CO_2 accumulator built in (Lackey et al. 2019). We recommend building this capability in to the main version. We wanted to use for this analysis but did not because it was not in the officially supported version.

- There should be an ability to plot the pressure, saturation, and pressure differential maps as a function of time with well locations as part of the standard capabilities.

8.2 Estimation of Geomechanical Risks with SOSAT

8.2.1 Sleepy Hollow and PHH sites

The methodology proposed in SOSAT was followed to evaluate the state of stress and the probability of reactivating critically oriented faults or potentially creating new hydraulic fractures in one of the injection intervals proposed for each site. The input parameters required in SOSAT include initial reservoir conditions, such as pore pressure, depth, and pressure of planned injection, as well as optional information about the regional stress state. While the deterministic parameters related to the reservoir conditions were relatively easily accessible for both sites, significant uncertainties remain for some critical parameters needed to decrease the perception of the risk at both sites (i.e., in situ stress measurements, and elastic properties).

Recently, a 3D numerical modeling approach was performed by Schlumberger to assess the geomechanical risk associated with CO_2 injection at the Sleepy Hollow site using an uncalibrated stress model. Preliminary results were shared with the project team. As discussed above, while this approach is commonly performed in industry, such an analysis relies on unvalidated assumptions. The limitations and reliability of uncalibrated stress models were highlighted by the modelers themselves: some of the model parameters are based on regional knowledge, the elastic model predicted is based on wireline measurements, and the model is not calibrated. As described in Thiercelin and Plumb (1994), such uncalibrated models seem to be a reasonable approach in regions that are not tectonically active, such as the Gulf of Mexico where there is minimal tectonic loading. However, these models are not satisfactory in most cases where rocks have undergone tectonic deformations, loading, compaction, or heating, over millions of years. Based on available data, the assumed initial stress field used in the dynamic geomechanical model are plausible, but represent only one such plausible scenario. Therefore, the results of the model are not comprehensive or conservative in terms of geomechanical risks.

The initial results of the 3D geomechanical modeling of the storage complex concluded that the stress conditions are far from both shear and tensile failure envelopes. We demonstrated with SOSAT that with the current degree of knowledge of the site-specific conditions, these statements cannot be confirmed without including a degree of uncertainty. Both studies agreed on the critical need to acquire in-situ stress measurements and perform geomechanical characterization of the elastic properties on keys rocks of the storage complex to significantly decrease the uncertainties.

8.2.2 About the importance of reducing uncertainties with more characterization

For both sites, there is a critical lack of characterization of the magnitude of the horizontal stresses. Measurements of the minimum horizontal stress via mini-frac measurements would significantly decrease the perception of the risk, and more specifically the potential for reactivation of a potential critically oriented fault, currently greater than 22% for both sites. Because characterization activities revealed the presence of two preexisting faults in the PHH site, it is particularly fundamental to evaluate the risk of reactivation of those faults, and thus to obtain site specific data to refine the geomechanical analysis.

Based on the stress path coefficients assumed for both sites to perform the evaluation of the risk of unintentional hydraulic fracturing, it was concluded that the risk of unintentional hydraulic fracturing is substantial at the Sleepy Hollow site, but limited at the PHH site with the maximum injection pressures considered. This conclusion would require to be verified with the integration of elastic properties for each formation measured in the laboratory to determine stress path coefficients with a high level of confidence.

New data resulting from the characterization activities performed in the new boreholes drilled during the spring of 2020 in Kansas could bring additional valuable information. If new data relevant to the geomechanical analysis are obtained, new analyses could be performed to evaluate how the risk perception evolves.

8.2.3 Feedback on application of SOSAT

From a user perspective, and compared to any dynamic stress simulation modeling, SOSAT provides a very intuitive user interface that could be accessible to any operators or regulators desiring to evaluate in situ stress conditions and geomechanical risks associated to CO_2 injection operations. Such an analysis performed during the site screening phase could be of high value to identify the critical parameters needed, and the subsequent characterization activities to be performed to obtain these parameters and establish a given site with quantified uncertainties.

The determination of some of the parameters to run SOSAT could require significant effort, especially if the analysis is conducted in multiple intervals presenting different elastic properties (which will likely be the case). However, once all parameters are determined, running SOSAT and obtaining the output plots and data takes only few minutes.

To conclude, the state of stress and geomechanical risk assessment on both sites was performed using the current and unique version of SOSAT available at https://edx.netl.doe.gov/nrap_wpsandbox/state-of-stress-analysis-tool-sosat/. It must be noted that Jeff Burghardt, author of the probabilistic approach integrated in SOSAT, developed a new probabilistic approach that takes into account the existence (or absence) of breakouts and DITFs. While this approach will not be described further, using it for future analyses could significantly decrease the degree of uncertainty on the magnitude of the maximum horizontal stress. Using such an approach on Sleepy Hollow where no breakouts and DITFs were observed would probably have decreased the uncertainty on the state of stress.

9.0 References

Addis, M. A. 1997. “The Stress-Depletion Response Of Reservoirs.” SPE Annual Technical Conference and Exhibition, San Antonio, Texas, 1997/1/1/. https://doi.org/10.2118/38720-MS.

Bacon, D. H., D. Blankenau, D. Divine, A. Duguid, I. Fukai, J. Glier, J. Hawkins, M. Jimenez, R. M. Joeckel, S. McDonald, R. Middleton, R. Peterson, M. Scharenberg, V. Smith, S. K. White, and S. P. Yaw. 2018. *Integrated mid-continent stacked carbon storage hub, Phase I Final Report.* ; Battelle Memorial Inst., Columbus, OH (United States) DOE-BMI-29264 United States 10.2172/1478726 NETL English. https://www.osti.gov/servlets/purl/1478726.

Bacon, D. H., C. M. R. Yonkofski, C. F. Brown, D. I. Demirkanli, and J. M. Whiting. 2019. “Risk-based post injection site care and monitoring for commercial-scale carbon storage: Reevaluation of the FutureGen 2.0 site using NRAP-Open-IAM and DREAM.” *International Journal of Greenhouse Gas Control* 90: 102784. https://doi.org/10.1016/j.ijggc.2019.102784.

Burghardt, J. 2018. “Geomechanical Risk Assessment for Subsurface Fluid Disposal Operations.” *Rock Mechanics and Rock Engineering* 51 (7): 2265-2288. https://doi.org/10.1007/s00603-018-1409-1.

Carlson, M., U. o. N.-.-L. Conservation, S. Division, N. G. Survey, N. Oil, and G. C. Commission. 1989. *Oil in Nebraska: 50 Years of Production, 100 Years of Exploration, 500 Million Years of History*. Nebraska Geological Survey, Conservation and Survey Division, Institute of Agriculture and Natural Resources, University of Nebraska--Lincoln.

Christopher, C. A., T. J. Clark, and D. H. Gibson. 1988. “Performance and Operation of a Successful Polymer Flood in the Sleepy Hollow Reagan Unit.” SPE Enhanced Oil Recovery Symposium, Tulsa, Oklahoma, 1988/1/1/. https://doi.org/10.2118/17395-MS.

Dalkhaa, C., Burton-Kelly, M., Klenner, R., Wildgust, N. January, 2019 2019. *Dynamic Simulation study IMSCS Hub Phase 2 Task 3.*

Divine, D., D. Eversoll, and L. Howard. 01/01 2018. *The Groundwater Atlas of Red Willow County, Nebraska.* University of Nebraska—Lincoln,Conservation and Survey Division.

Duguid, A., Bidgoli, T., Blankenau, D., Divine, D., Fukai, I., Grove, B., Hasiuk, F., Hollenbach, J., Holubnyak, E., Joeckel, R.M., Keister, L., Main, J., Meng, J., Polun, S., Scharenberg, M., Smith, V., Walker, J. (2020a). *Integrated Mid-Continent Stacked Carbon Storage Hub Project Phase II. Topical Report: Advanced Data Analysis. Task 5 Storage Complex Analysis and Modeling.* Battelle Memorial Inst., Columbus, OH (United States).

Duguid, A., D. Blankenau, N. W. Bosshart, M. E. Burton-Kelly, C. Dalkhaa, A. B. Djezzar, D. Divine, F. Hasiuk, J. Hollenbach, E. Holubnyak, T. Jiang, R. M. Joeckel, L. Keister, S.-Y. Lee, J. Main, J. Meng, A. Y. Salaza, M. Scharenberg, V. Smith, J. A. Sorensen, J. Walker, and M. K. Valluri. (2020b). *Integrated Mid-Continent Stacked Carbon Storage Hub Project Phase II - Topical Report: Storage Complex Geologic and Reservoir Modeling - Task 5 Storage Complex Analysis and Modeling.* Battelle Memorial Inst., Columbus, OH (United States).

Heidbach, O., M. Rajabi, X. Cui, K. Fuchs, B. Müller, J. Reinecker, K. Reiter, M. Tingay, F. Wenzel, F. Xie, M. O. Ziegler, M.-L. Zoback, and M. Zoback. 2018. “The World Stress Map database release 2016: Crustal stress pattern across scales.” *Tectonophysics* 744: 484-498. https://doi.org/https://doi.org/10.1016/j.tecto.2018.07.007.

Hillis, R. 2000. “Pore Pressure/Stress Coupling and its Implications foDr Seismicity.” *Exploration Geophysics* 31 (1-2): 448-454. https://doi.org/10.1071/EG00448.

Hillis, R. R. 2001. “Coupled changes in pore pressure and stress in oil fields and sedimentary basins.” *Petroleum Geoscience* 7 (4): 419-425. https://doi.org/10.1144/petgeo.7.4.419.

Holubnyak, Y. E., M. Dubois, T. Bidgoli, D. Wreath, L. Watney, S. Stover, D. Newell, F. M. Fazelalavi, A. Hollenbach, J. Jennings, C. Steincamp, J. Schremmer, B. Jordan, B. Crabtree, J. Christensen, D. McFarlane, J. Doveton, K. Krishnamurthy, M. Byron, and K. Watts. 2018. *Integrated CCS for Kansas (ICKan) Final Technical Report.* ; Kansas Geological Survey; University of Kansas Center for Research DOE-ICKan-29474; Other: DUNS 076248616 United States 10.2172/1491482 Other: DUNS 076248616 NETL English. https://www.osti.gov/servlets/purl/1491482.

Jaeger, J. C., and N. G. W. Cook. 1979. *Fundamentals of Rock Mechanics, Third ed.* London: Chapman and Hall.

Lackey, G., V. S. Vasylkivska, N. J. Huerta, S. King, and R. M. Dilmore. 2019. “Managing well leakage risks at a geologic carbon storage site with many wells.” *International Journal of Greenhouse Gas Control* 88: 182-194. https://doi.org/10.1016/j.ijggc.2019.06.011.

Langenbruch, C., and M. D. Zoback. 2016. “How will induced seismicity in Oklahoma respond to decreased saltwater injection rates?” *Science Advances* 2 (11): e1601542. https://doi.org/10.1126/sciadv.1601542.

Lund Snee, J.-E., and M. D. Zoback. 2020. “Multiscale variations of the crustal stress field throughout North America.” *Nature Communications* 11 (1): 1951. https://doi.org/10.1038/s41467-020-15841-5.

Nicol, A., R. Carne, M. Gerstenberger, and A. Christophersen. 2011. “Induced seismicity and its implications for CO2 storage risk.” *Energy Procedia* 4: 3699-3706. https://doi.org/https://doi.org/10.1016/j.egypro.2011.02.302.

Nordbotten, J. M., M. A. Celia, and S. Bachu. 2004. “Analytical solutions for leakage rates through abandoned wells.” *Water Resources Research* 40 (4). https://doi.org/http://dx.doi.org/10.1029/2003wr002997.

Nordbotten, J. M., M. A. Celia, S. Bachu, and H. K. Dahle. 2005. “Semianalytical solution for CO2 leakage through an abandoned well.” *Environmental Science & Technology* 39 (2): 602-611. https://doi.org/DOI 10.1021/es035338i.

Nordbotten, J. M., D. Kavetski, M. A. Celia, and S. Bachu. 2009. “Model for CO2 Leakage Including Multiple Geological Layers and Multiple Leaky Wells.” *Environmental Science & Technology* 43 (3): 743-749. https://doi.org/http://dx.doi.org/10.1021/es801135v.

Rogers, J. P. 1977. “Genesis and Distribution of Desmoinesian (Pennsylvanian) Sandstone Reservoir, Sleepy Hollow Field, Red Willow County, Nebraska1.” *AAPG Bulletin* 61 (7): 1029-1044. https://doi.org/10.1306/c1ea43bf-16c9-11d7-8645000102c1865d.

Streit, J. E., and R. R. Hillis. 2004. “Estimating fault stability and sustainable fluid pressures for underground storage of CO2 in porous rock.” *Energy* 29 (9): 1445-1456. https://doi.org/https://doi.org/10.1016/j.energy.2004.03.078.

Thiercelin, M. J., and R. A. Plumb. 1994. “A Core-Based Prediction of Lithologic Stress Contrasts in East Texas Formations.” *SPE Formation Evaluation* 9 (04): 251-258. https://doi.org/10.2118/21847-PA.

Vidal-Gilbert, S., E. Tenthorey, D. Dewhurst, J. Ennis-King, P. Van Ruth, and R. Hillis. 2010. “Geomechanical analysis of the Naylor Field, Otway Basin, Australia: Implications for CO2 injection and storage.” *International Journal of Greenhouse Gas Control* 4 (5): 827-839, http://www.sciencedirect.com/science/article/B83WP-50G75PJ-1/2/a6bcae373c2bdf0710ffd8be6cdc9732.

Walsh, F. R., and M. D. Zoback. 2015. *Oklahoma’s recent earthquakes and saltwater disposal*. Journal Article. Vol. 1. Vol. 5.

White, J., W. Foxall, C. Bachmann, T. M. Daley, and L. Chiaramonte. 2016. *Induced Seismicity and Carbon Storage: Risk Assessment and Mitigation Strategies.* U.S. Department of

Energy, National Energy Technology Laboratory NRAP-TRS-II-005-2016. Morgantown, WV.

Zoback, M. D., C. A. Barton, M. Brudy, D. A. Castillo, T. Finkbeiner, B. R. Grollimund, D. B. Moos, P. Peska, C. D. Ward, and D. J. Wiprut. 2003. “Determination of stress orientation and magnitude in deep wells.” *International Journal of Rock Mechanics and Mining Sciences* 40 (7–8): 1049-1076. https://doi.org/10.1016/j.ijrmms.2003.07.001.

Zoback, M. D., and S. M. Gorelick. 2012. “Earthquake triggering and large-scale geologic storage of carbon dioxide.” *Proceedings of the National Academy of Sciences* 109 (26): 10164-10168. https://doi.org/10.1073/pnas.1202473109.

Zoback, M. L., M. Zoback, J. Adams, M. Assumpcao, S. Bell, E. Bergman, P. Blümling, N. R. Brereton, D. Denham, and J. Ding. 1989. “Global patterns of tectonic stress.”

Appendix A – CO_2 Saturation Contour Plots of Layer 54 of the Reservoir at Different Times at the PHH Site

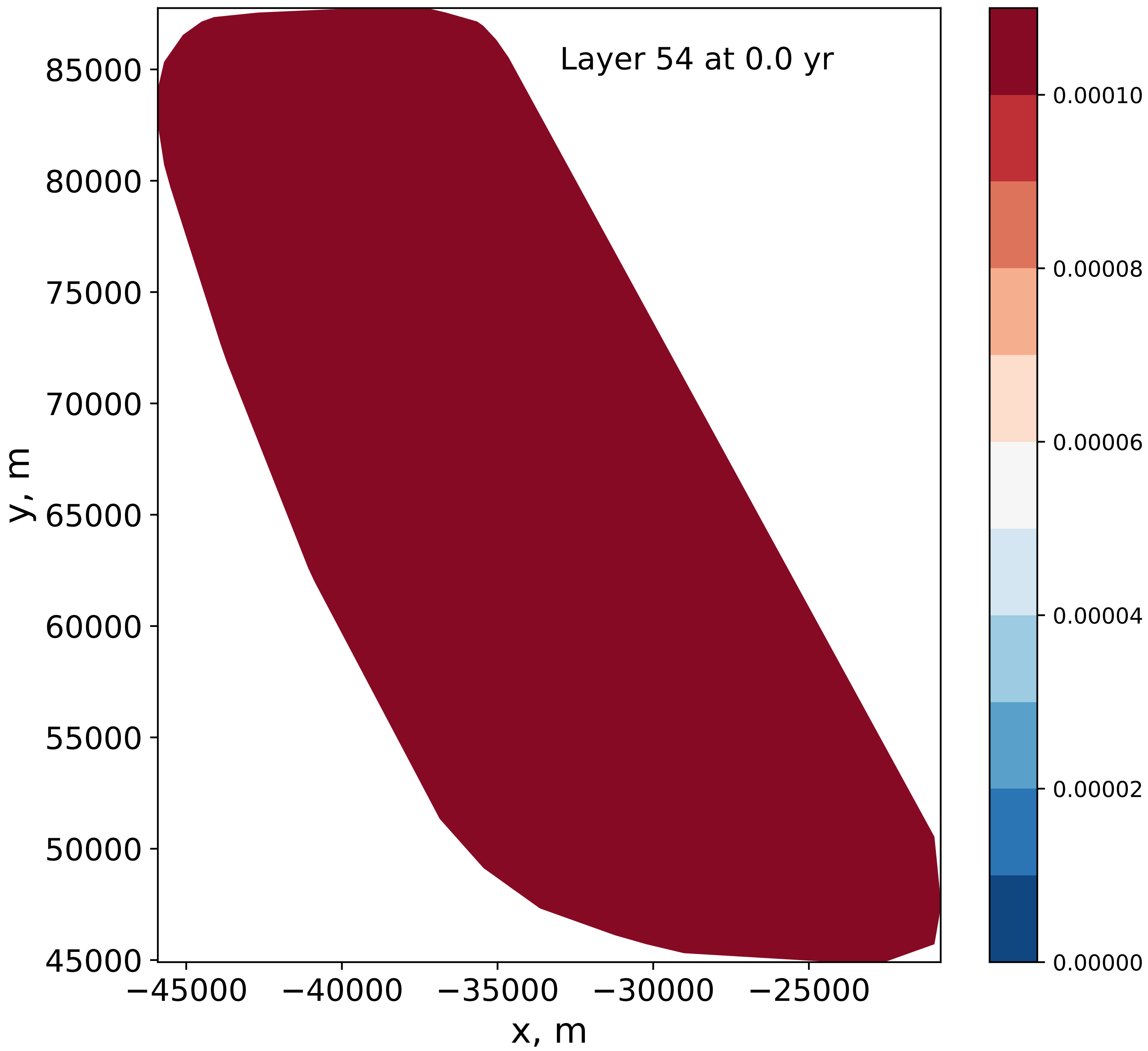

A-1. Reservoir CO_2 Saturation at 0.0 year

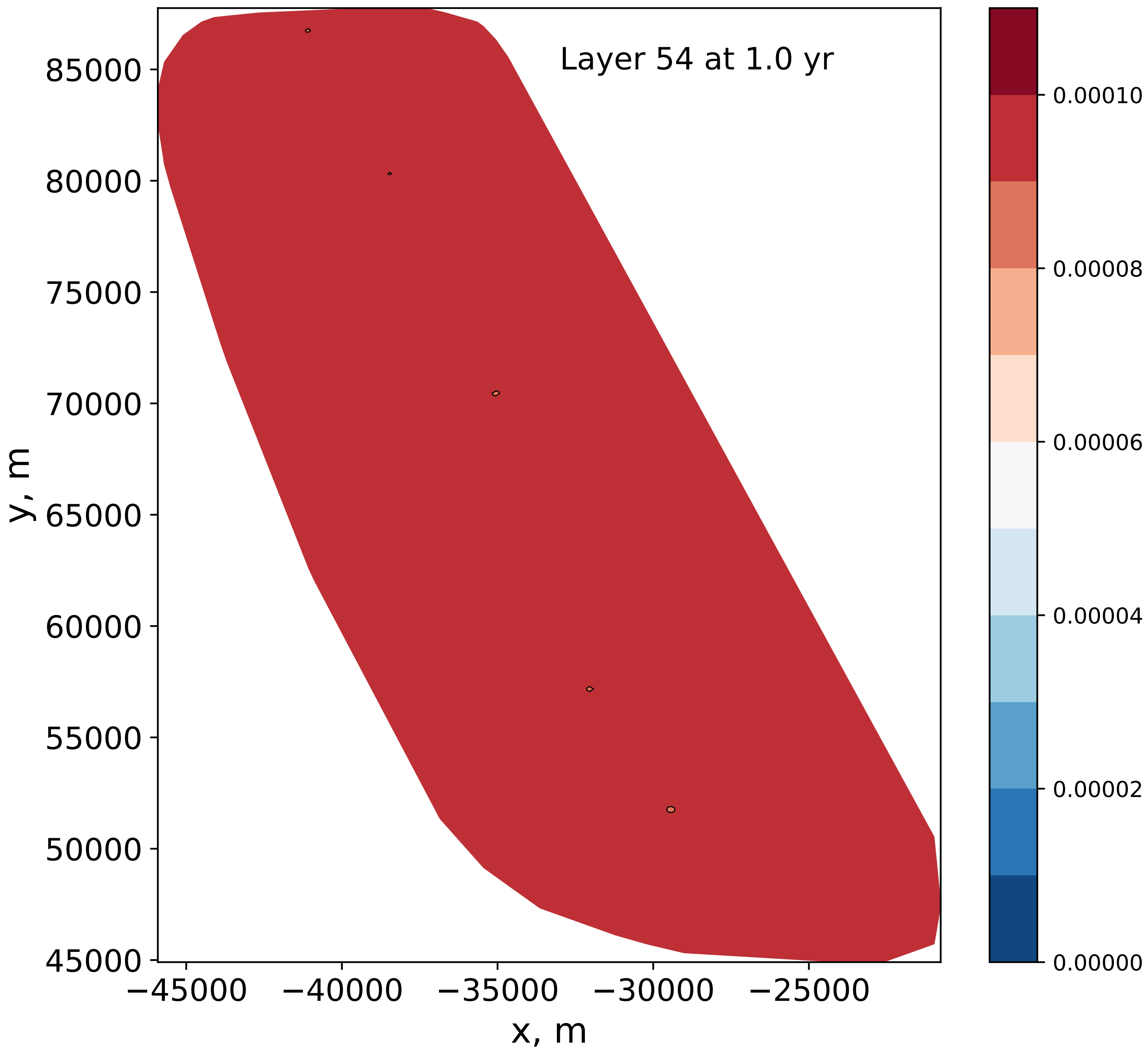

A-2. Reservoir CO_2 Saturation at 1.0 year

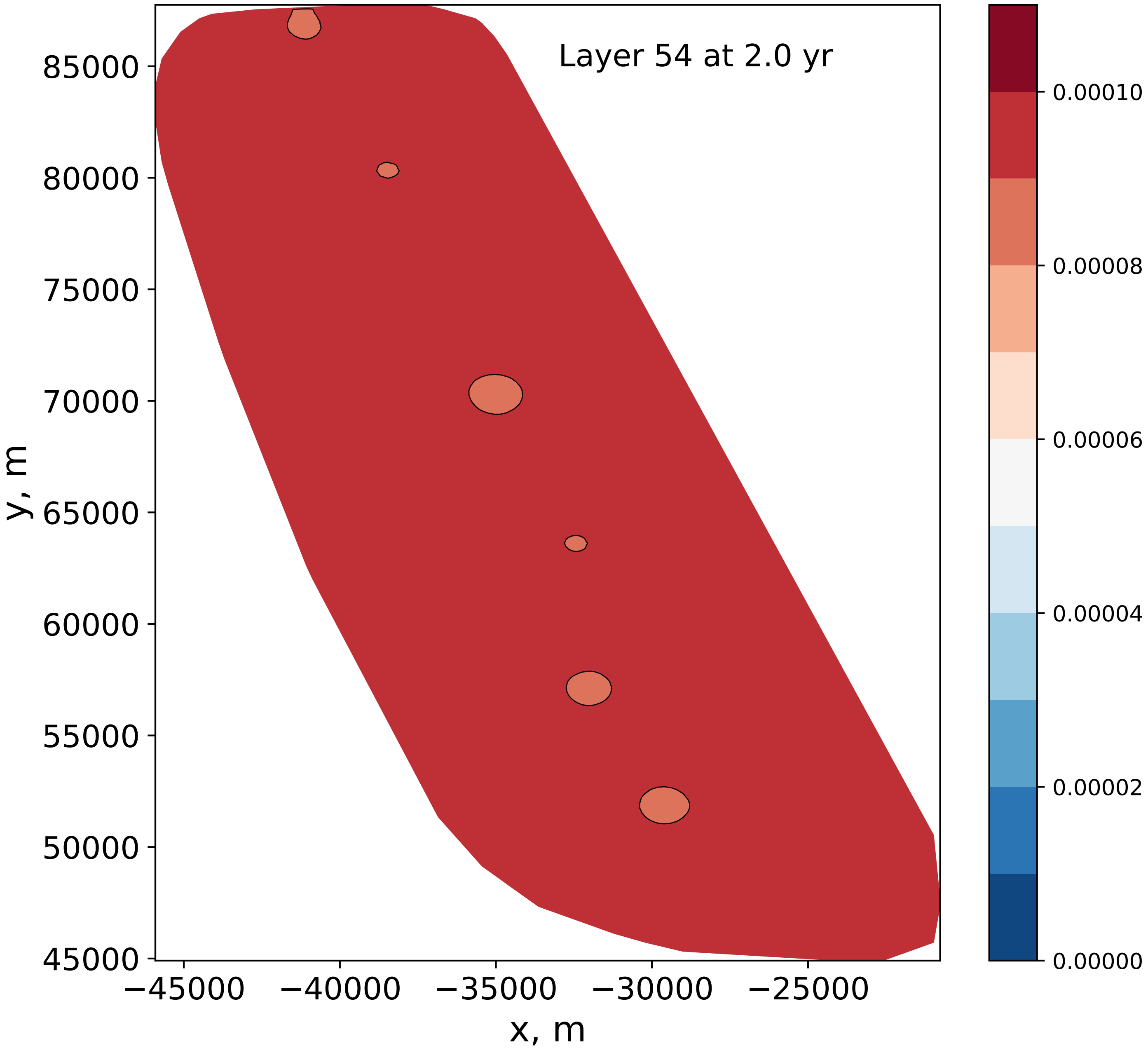

A-3. Reservoir CO_2 Saturation at 2.0 year

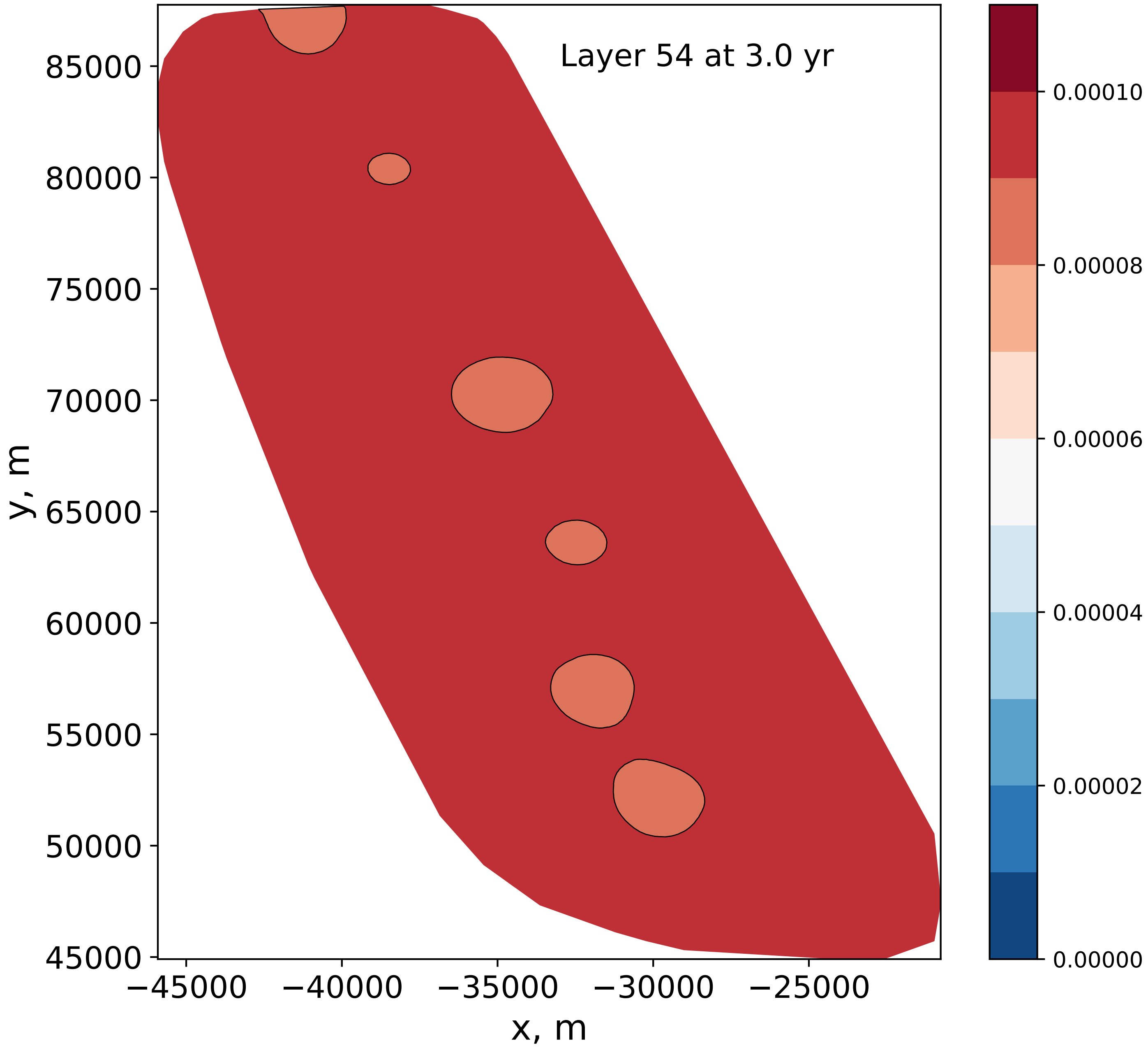

A-4. Reservoir CO_2 Saturation at 3.0 year

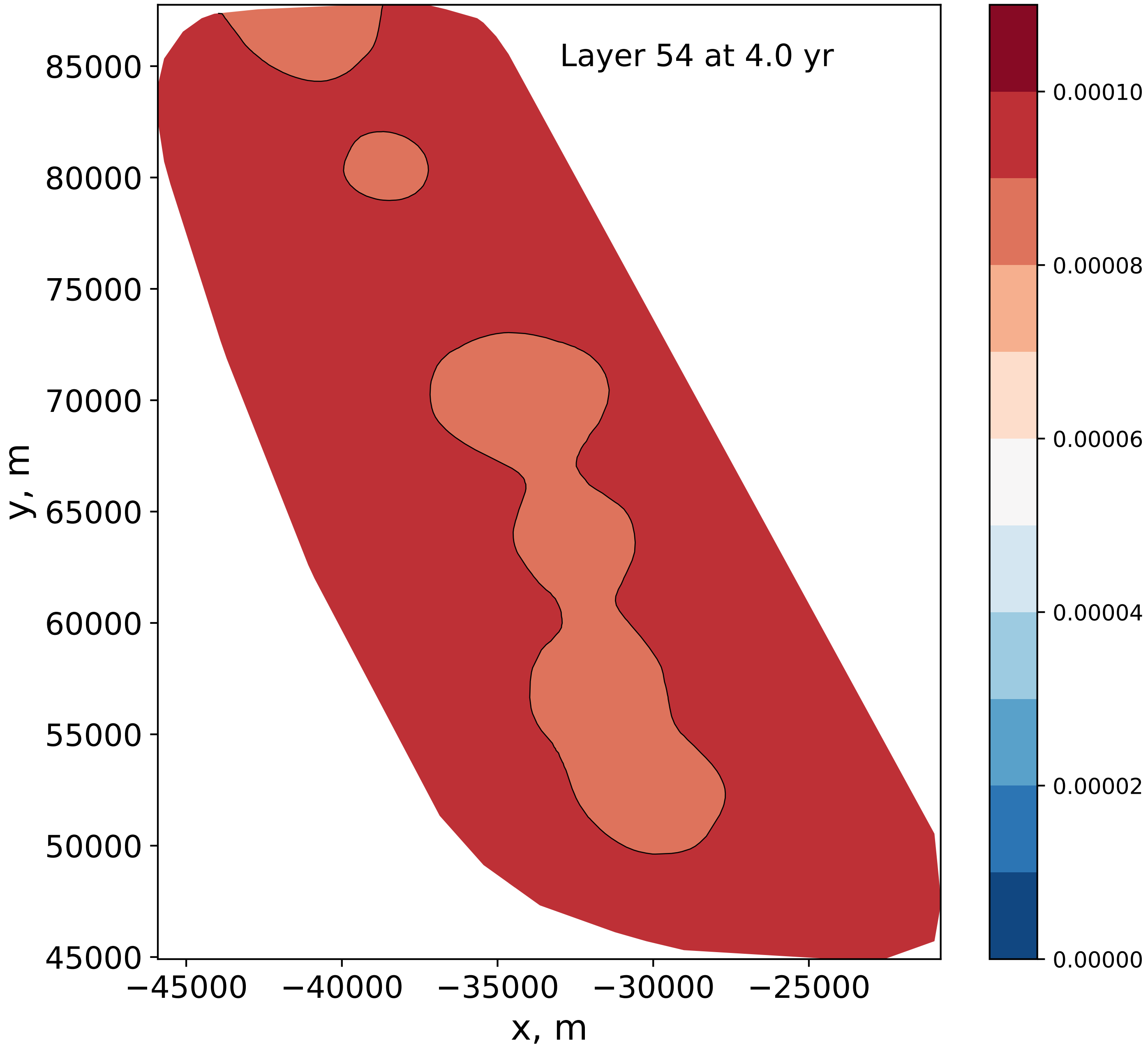

A-5. Reservoir CO_2 Saturation at 4.0 year

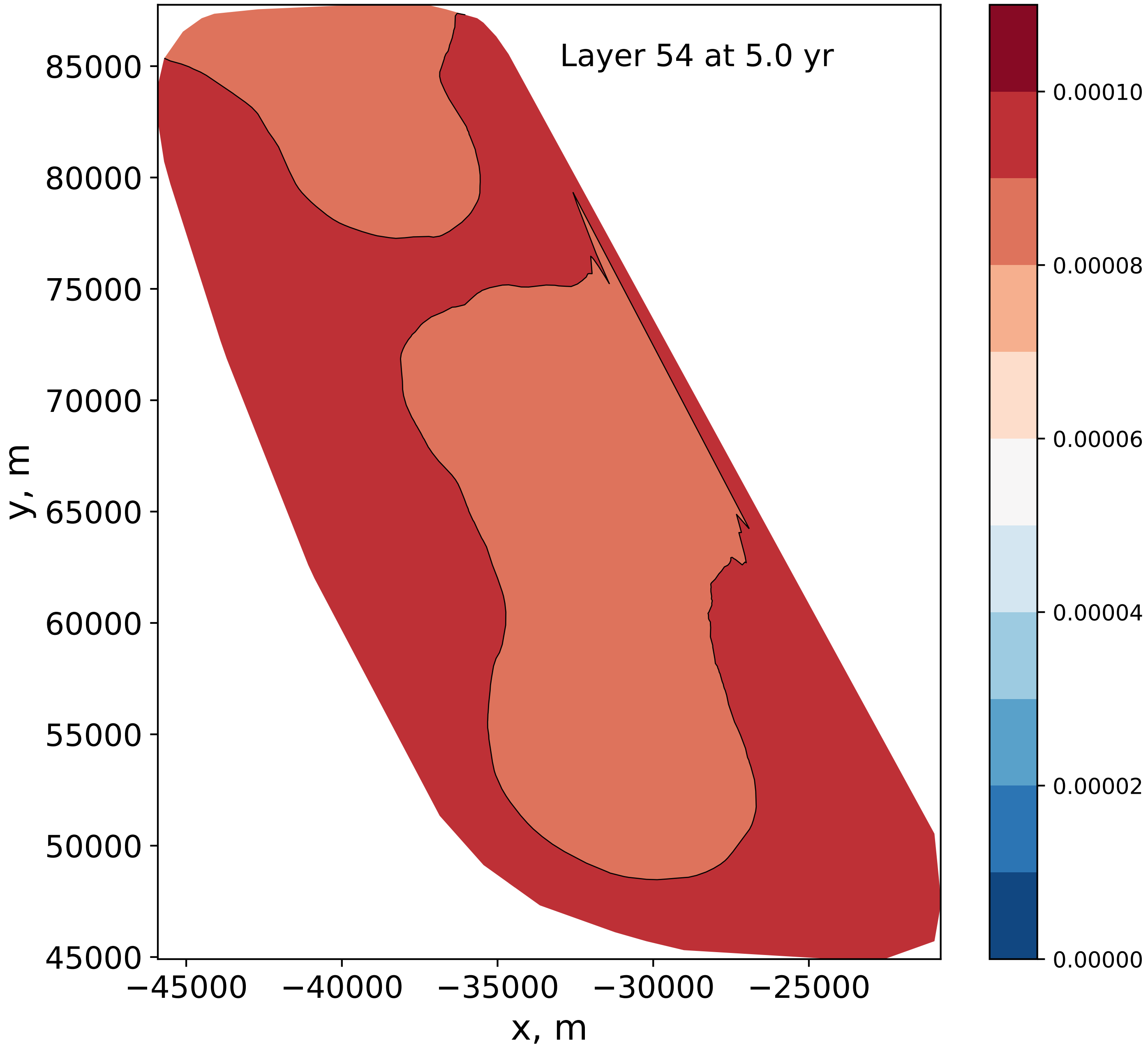

A-6. Reservoir CO_2 Saturation at 5.0 year

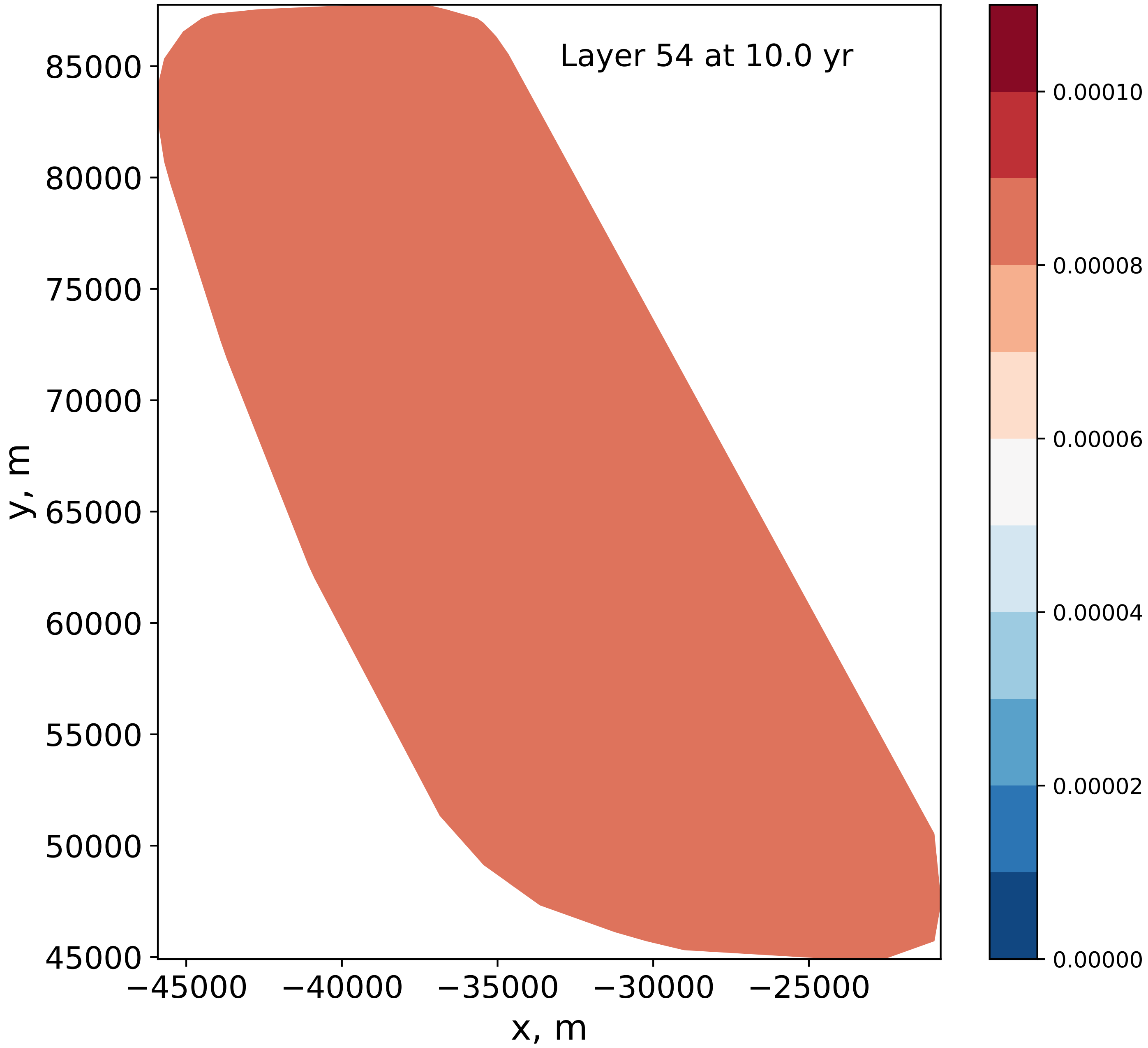

A-7. Reservoir CO_2 Saturation at 10.0 years

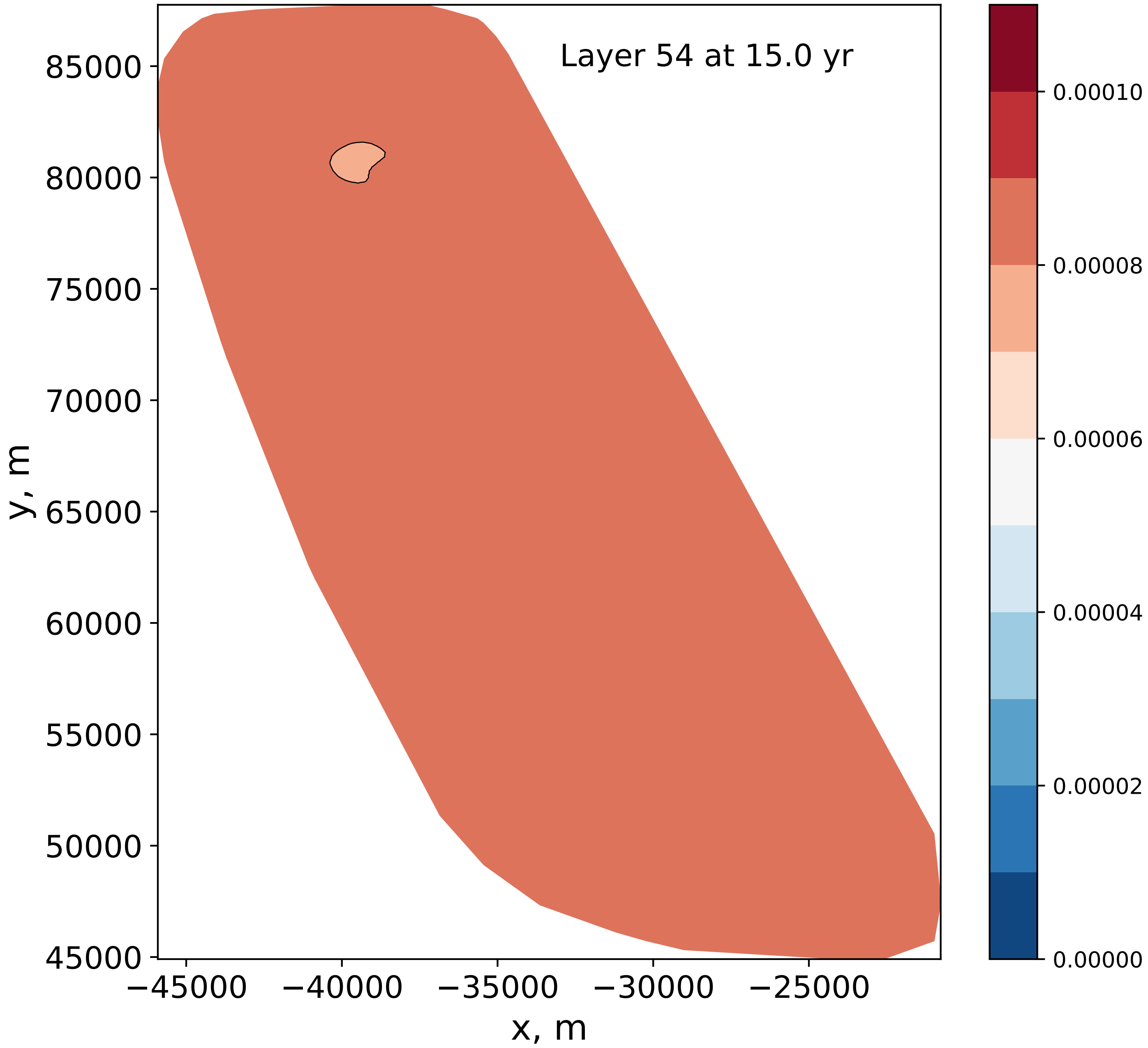

A-8. Reservoir CO_2 Saturation at 15.0 years

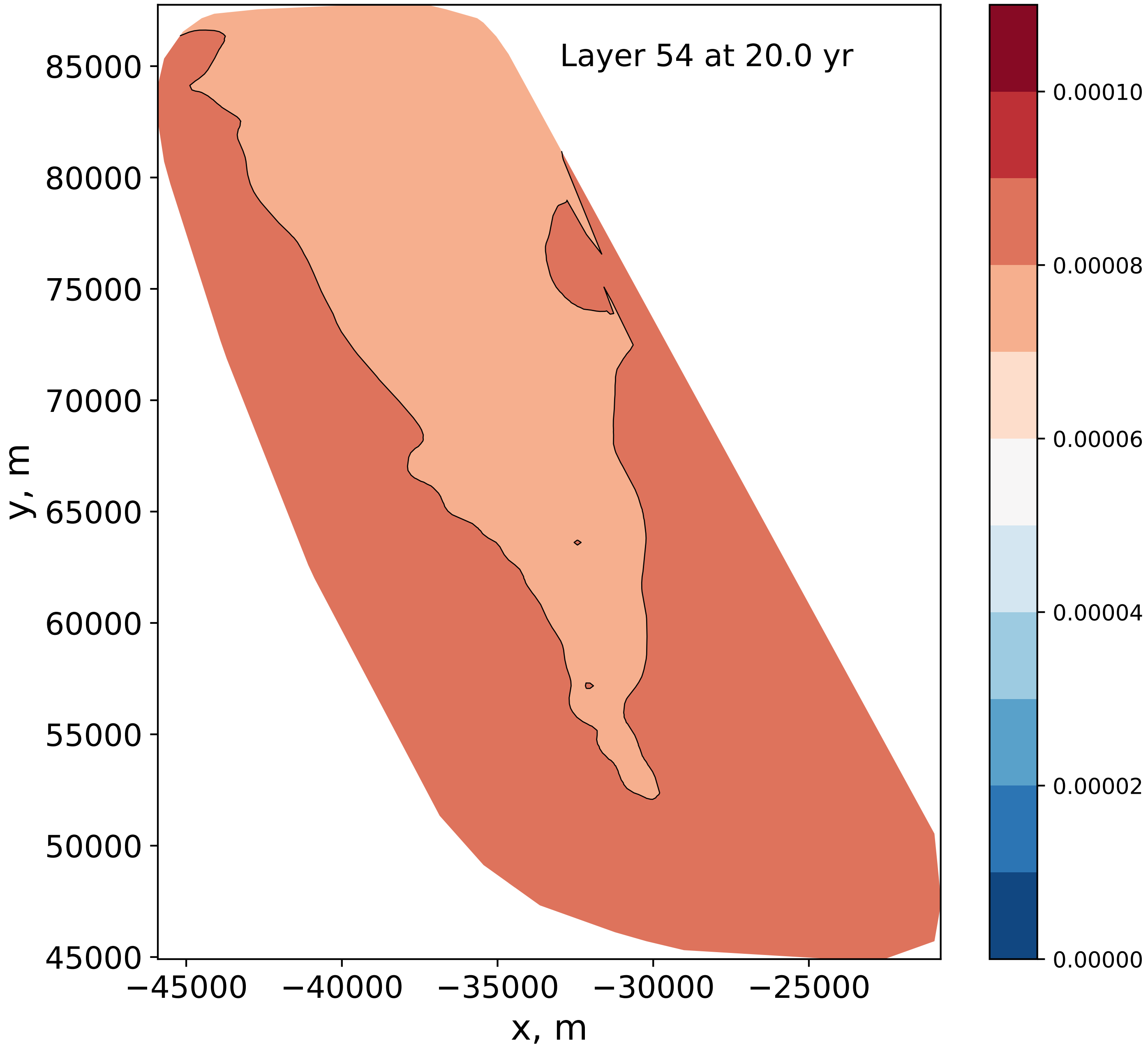

A-9. Reservoir CO_2 Saturation at 20.0 years

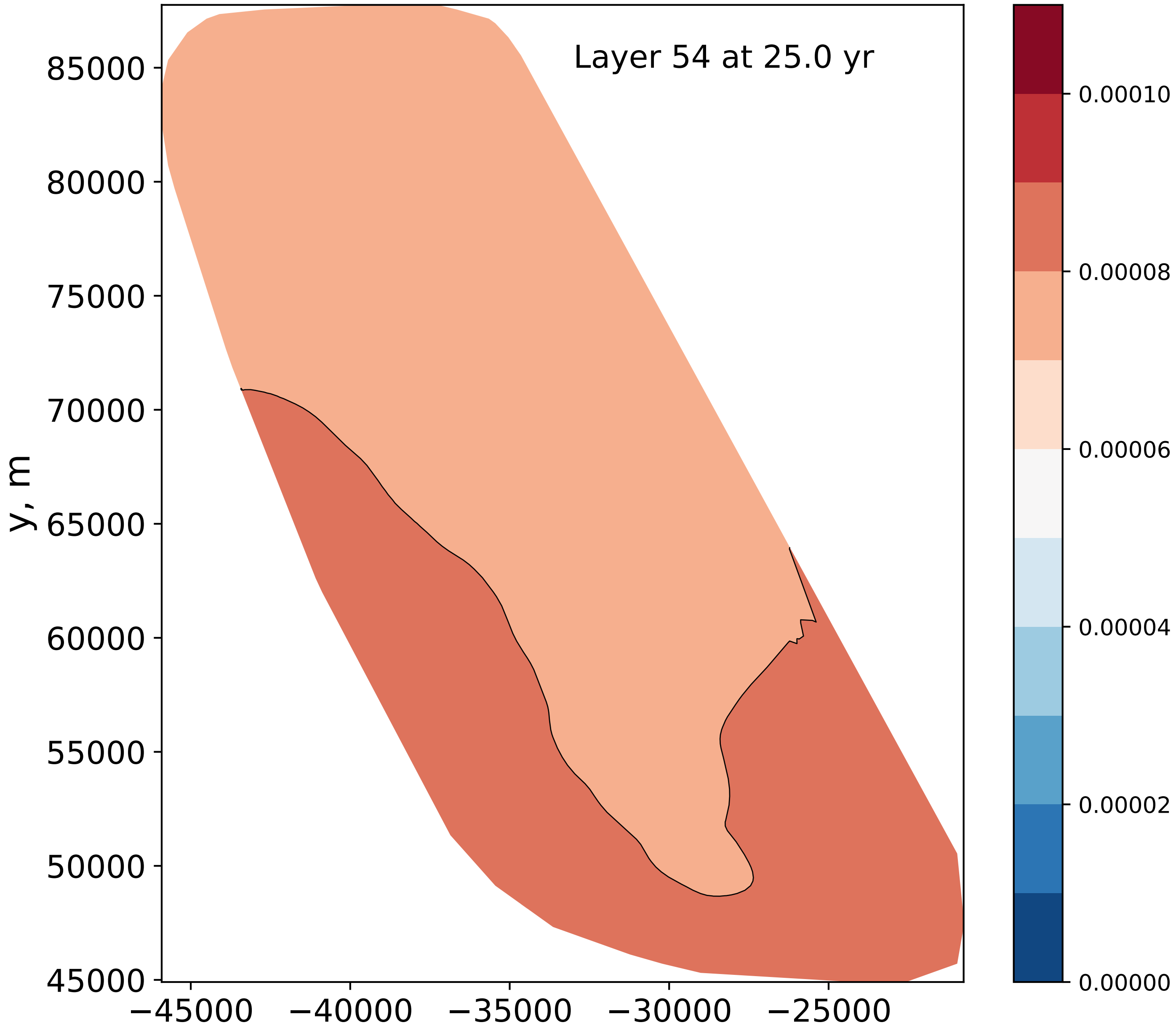

A-10. Reservoir CO_2 Saturation at 25.0 years

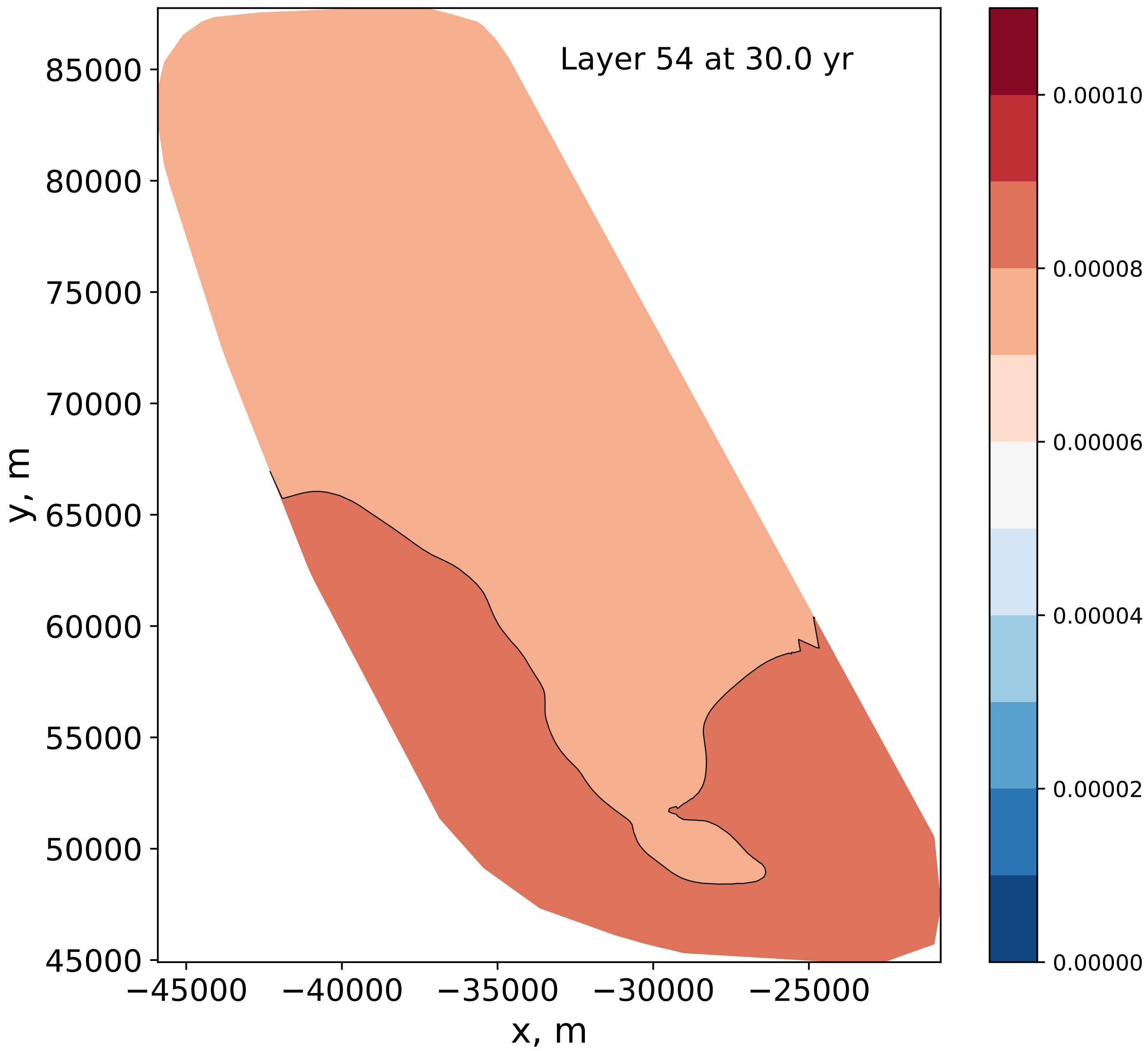

A-11. Reservoir CO_2 Saturation at 30.0 years

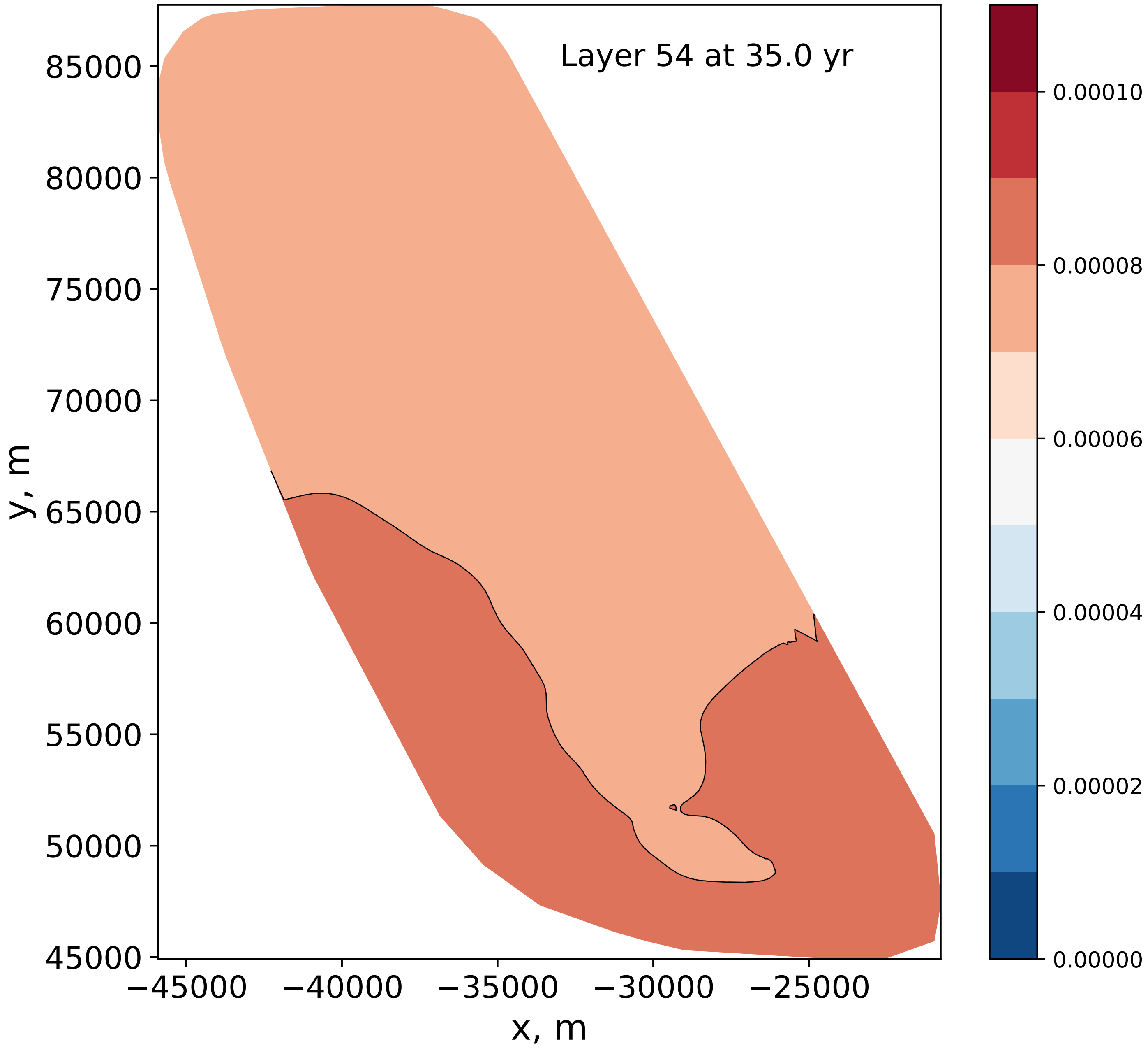

A-12. Reservoir CO_2 Saturation at 35.0 years

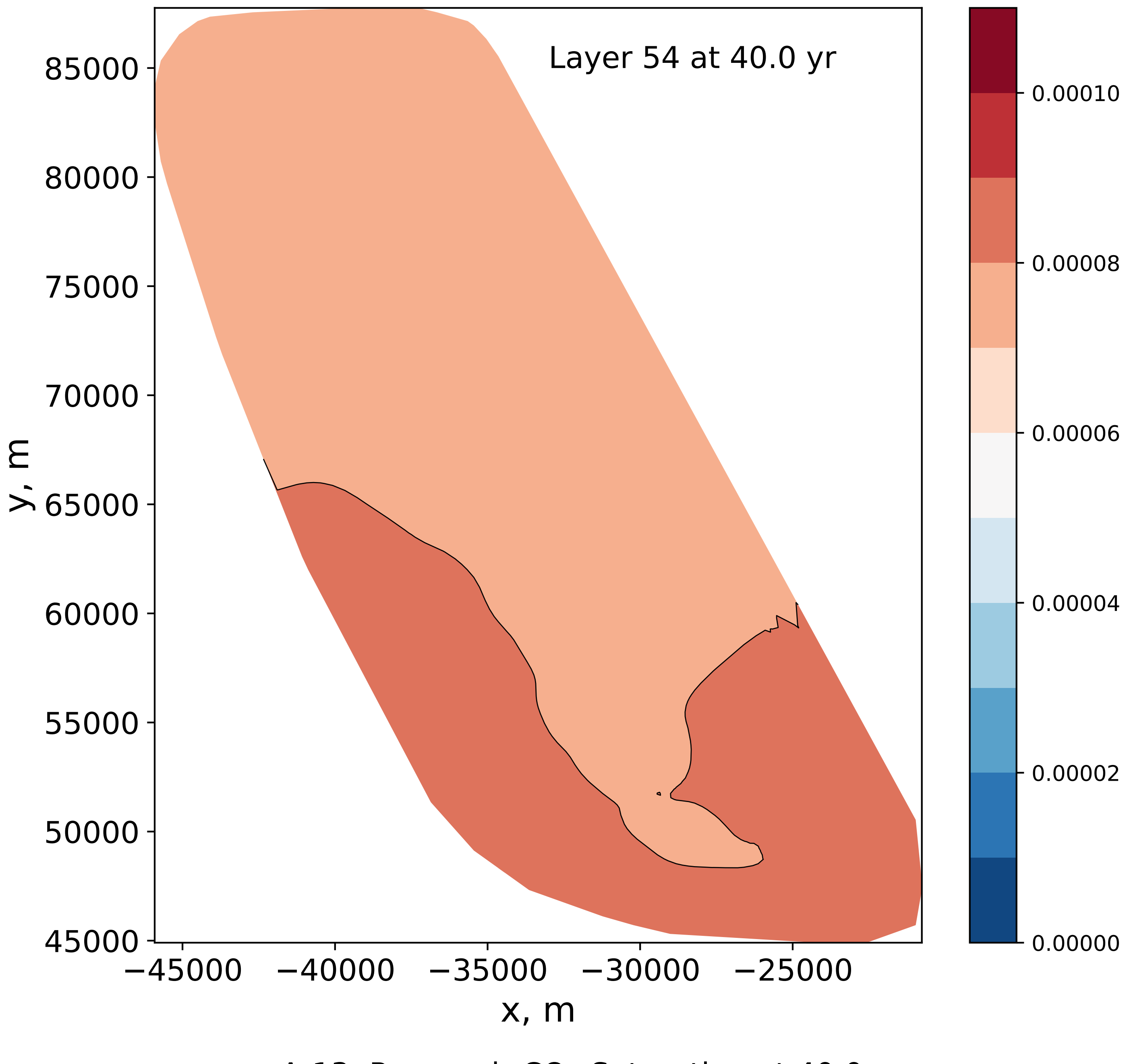

A-13. Reservoir CO_2 Saturation at 40.0 years

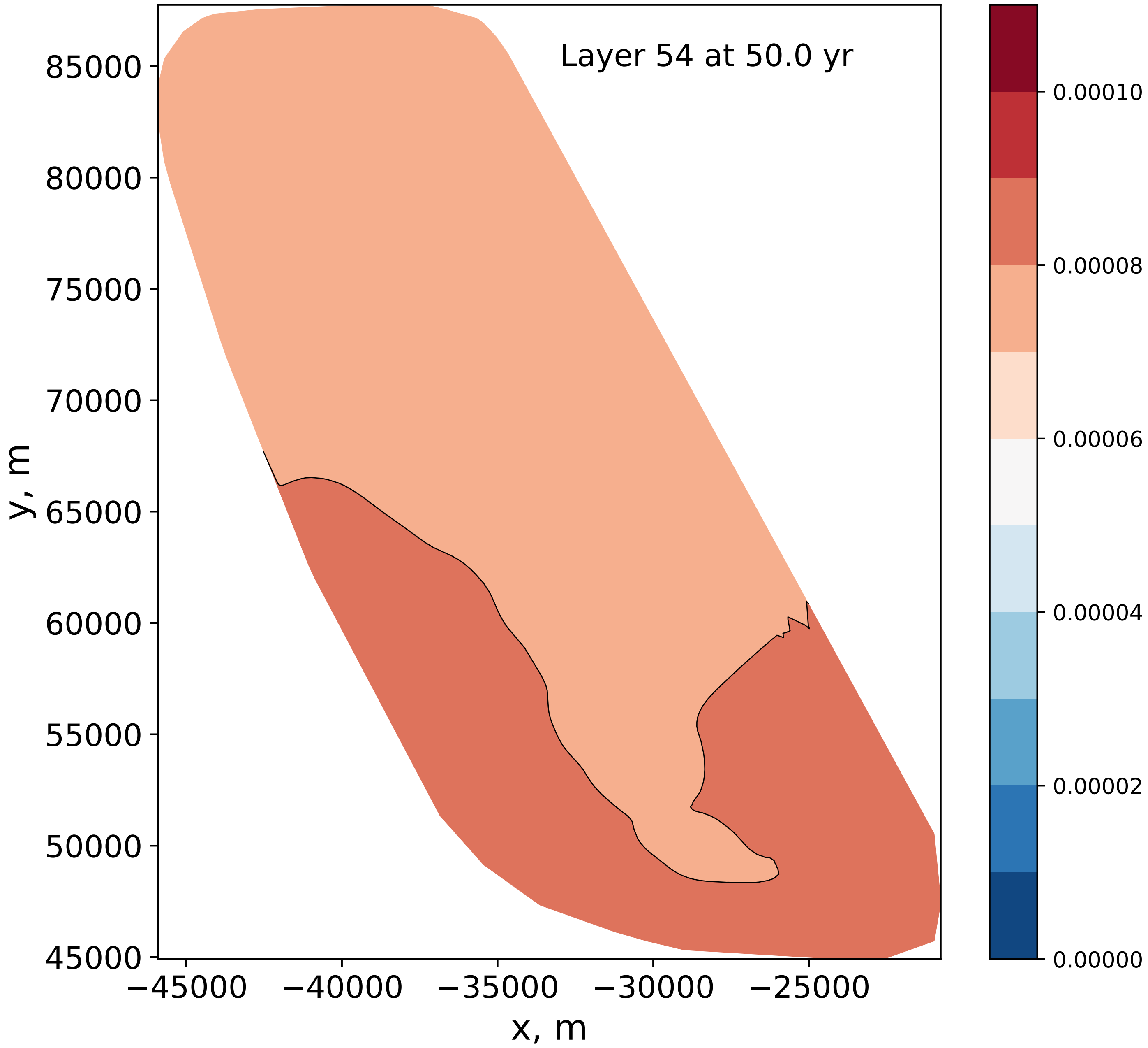

A-14. Reservoir CO_2 Saturation at 50.0 years

Appendix B – Gas Pressure Differential Contour Plots of the Layer 54 of the Reservoir at Different Times at the PHH Site

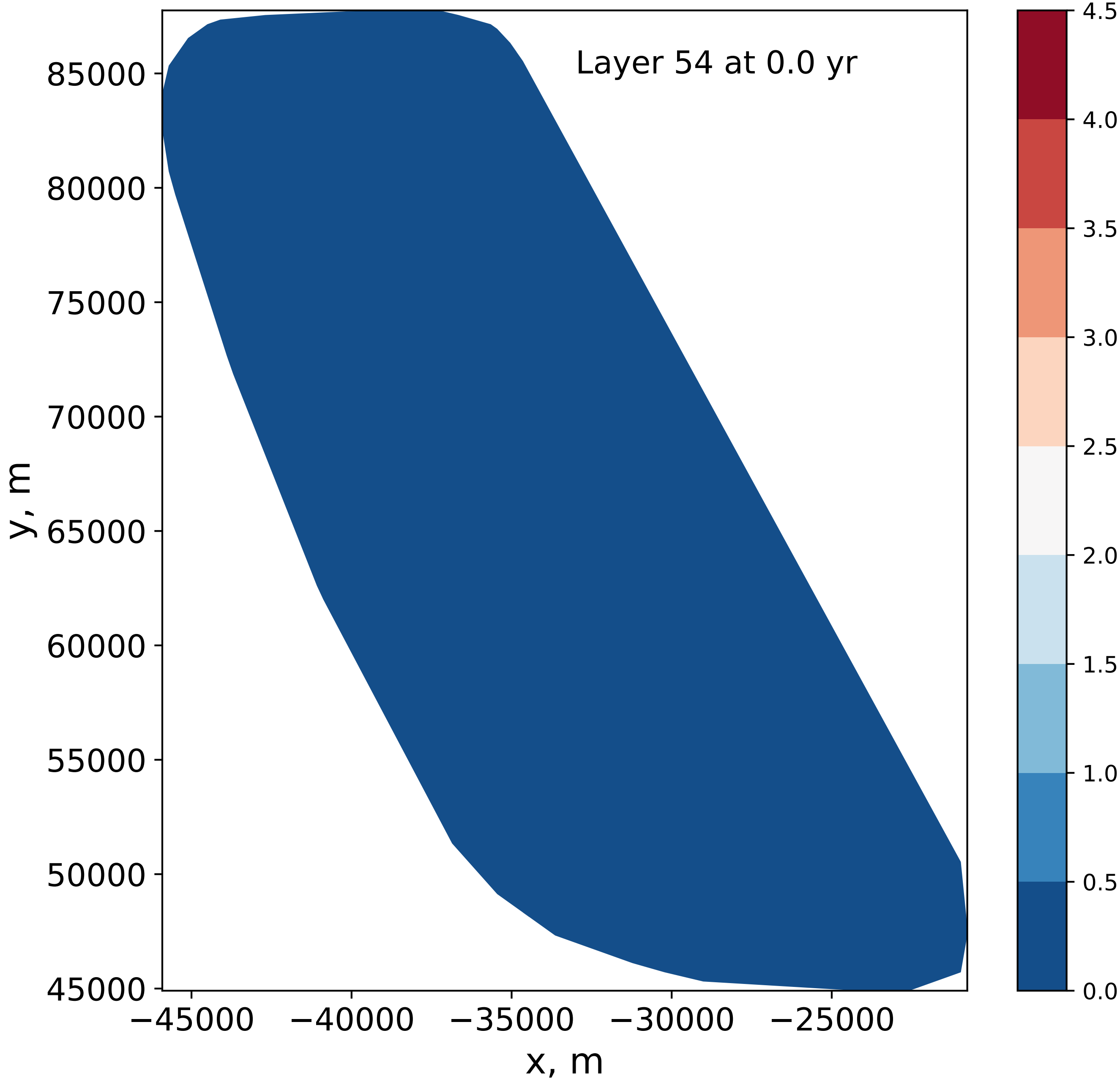

B-1. Reservoir Pressure Differential (MPa) at 0.0 year

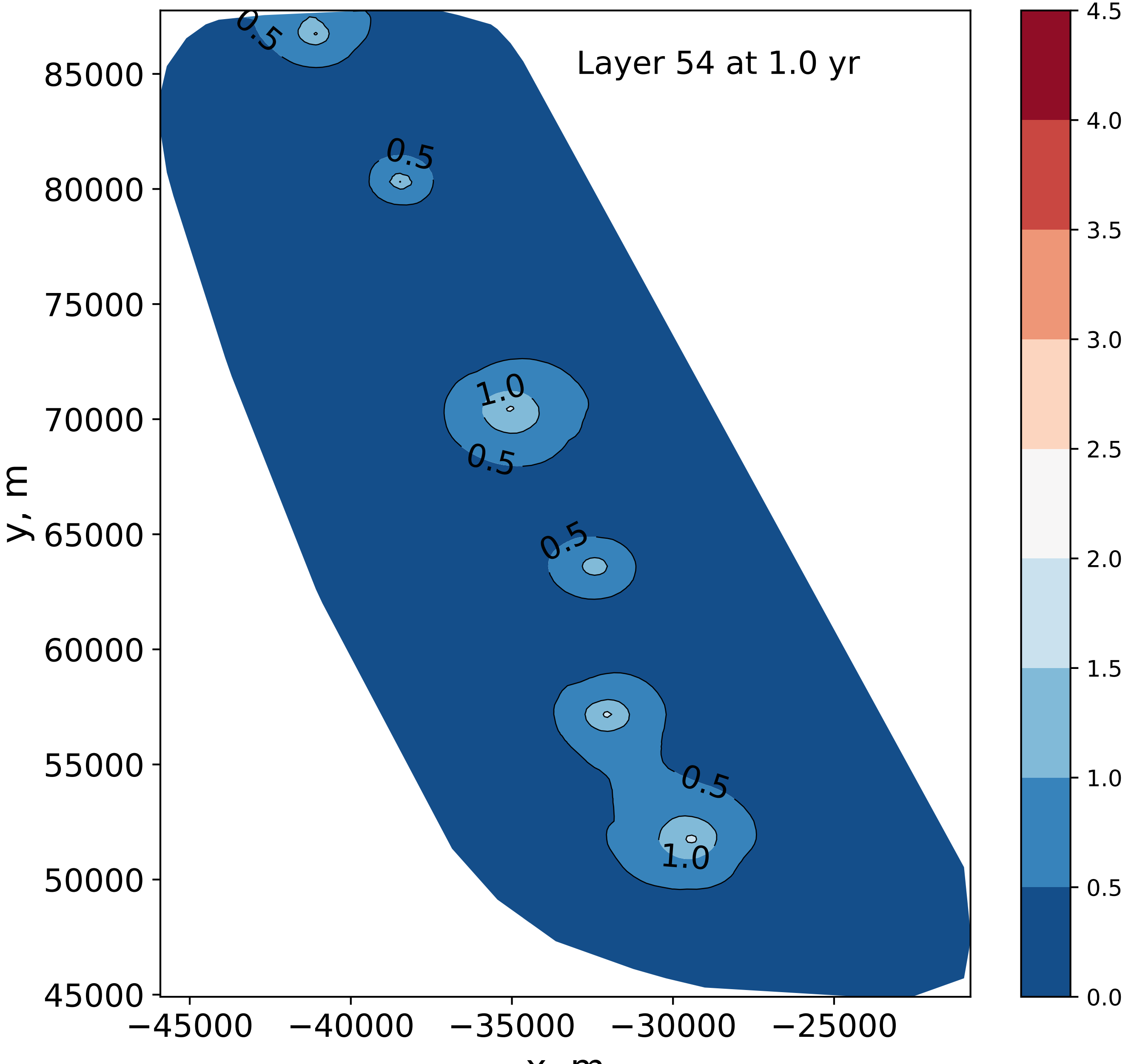

B-2. Reservoir Pressure Differential (MPa) at 1.0 year

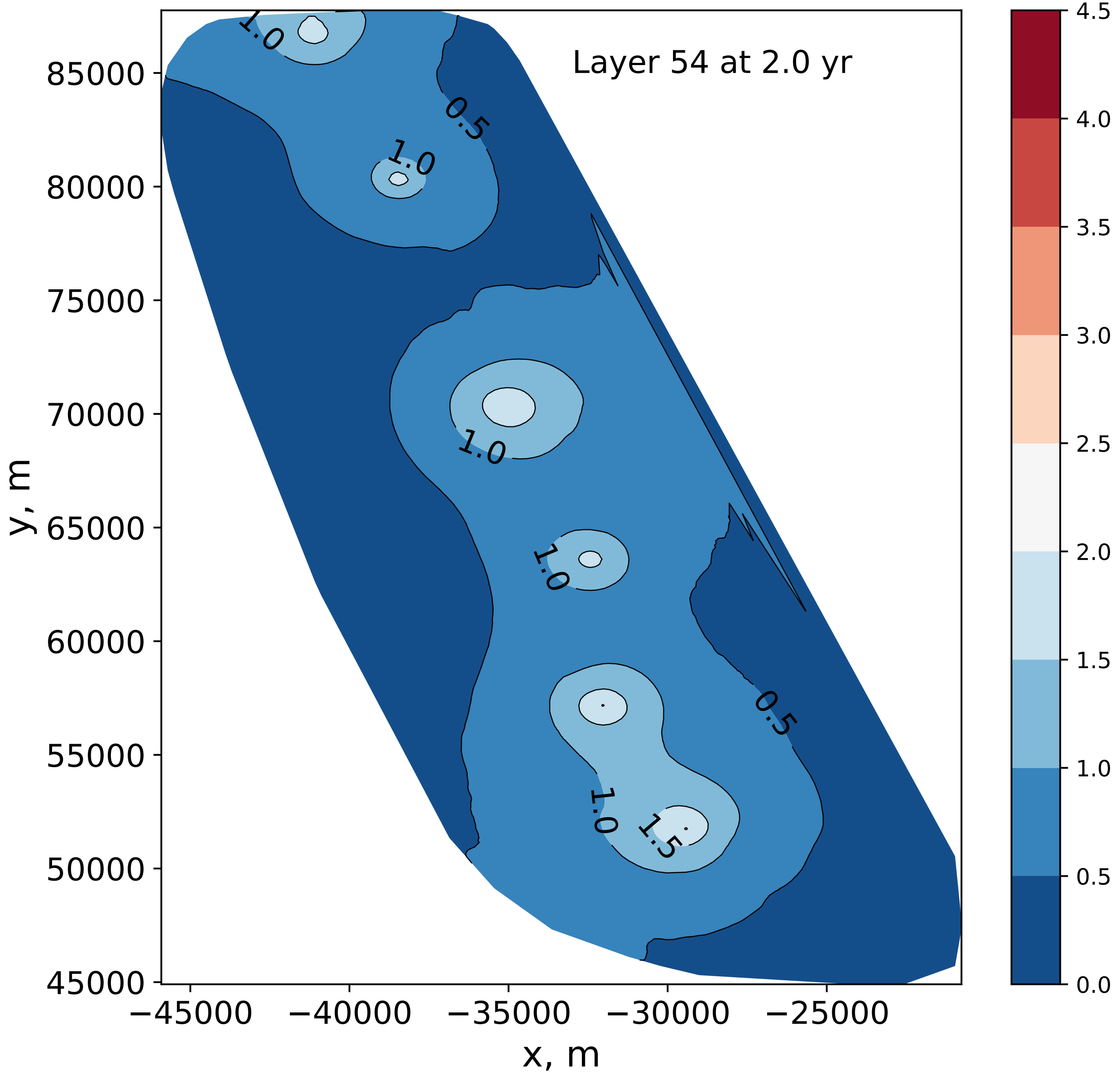

B-3. Reservoir Pressure Differential (MPa) at 2.0 year

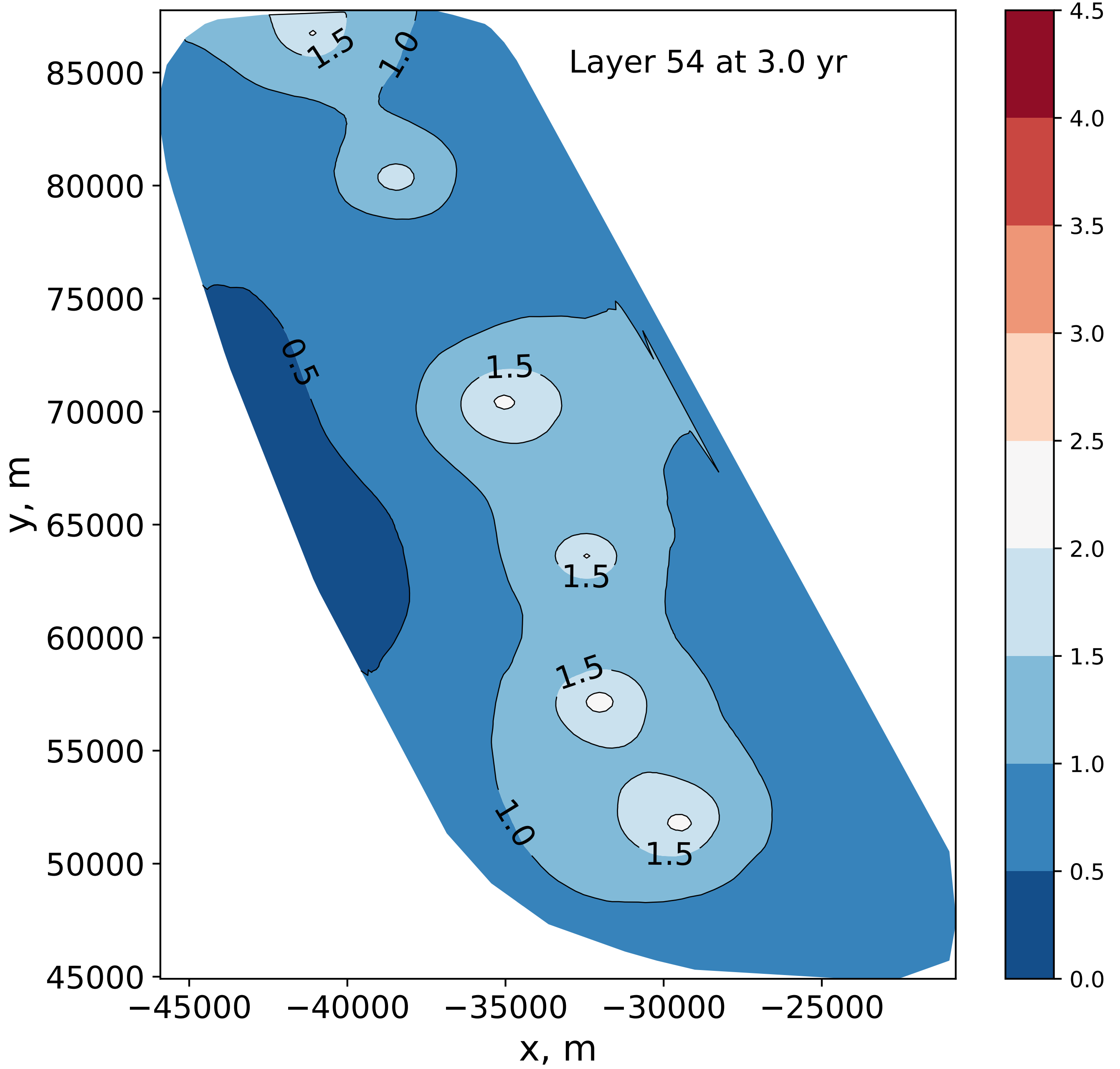

B-4. Reservoir Pressure Differential (MPa) at 3.0 year

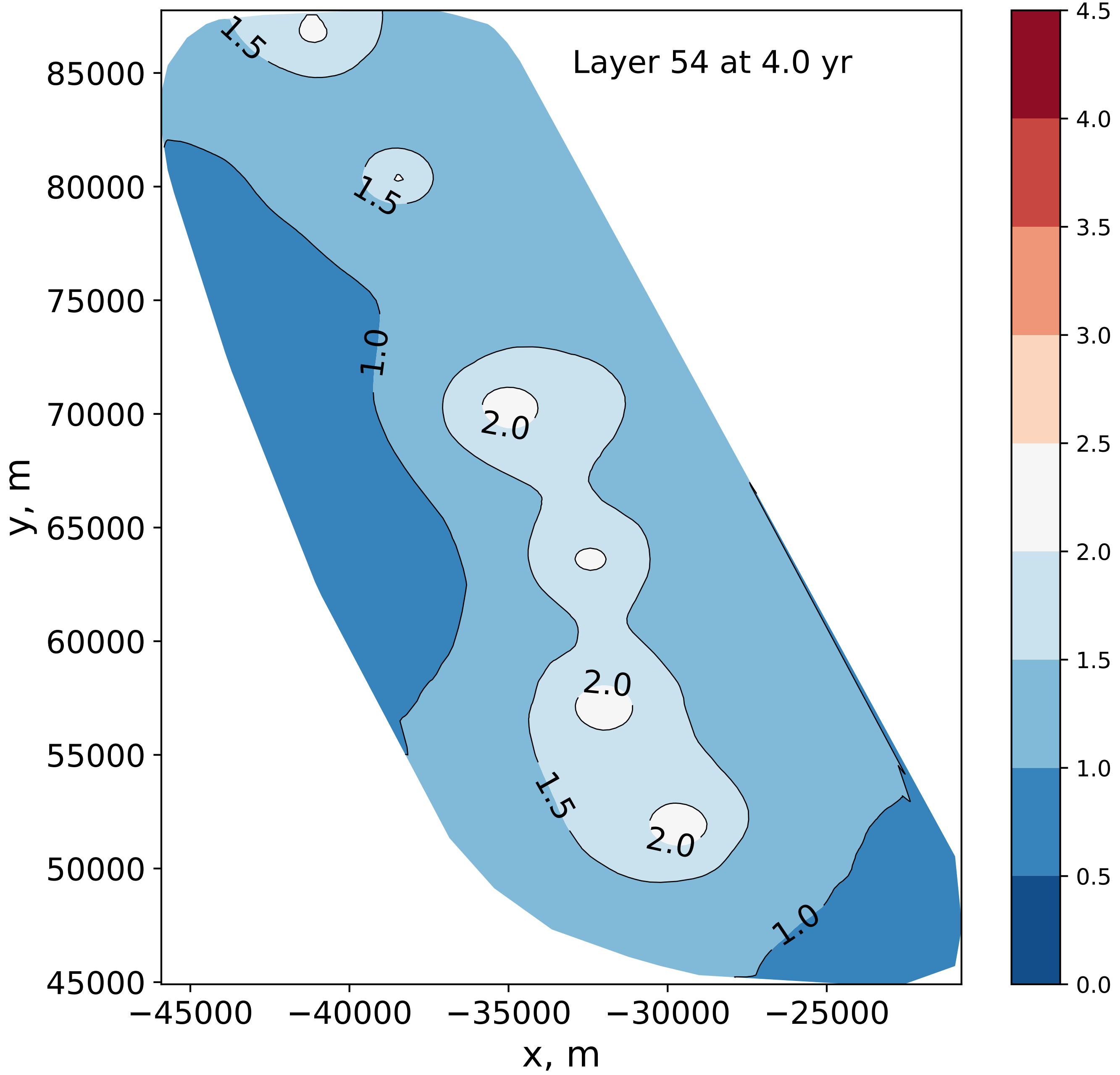

B-5. Reservoir Pressure Differential (MPa) at 4.0 year

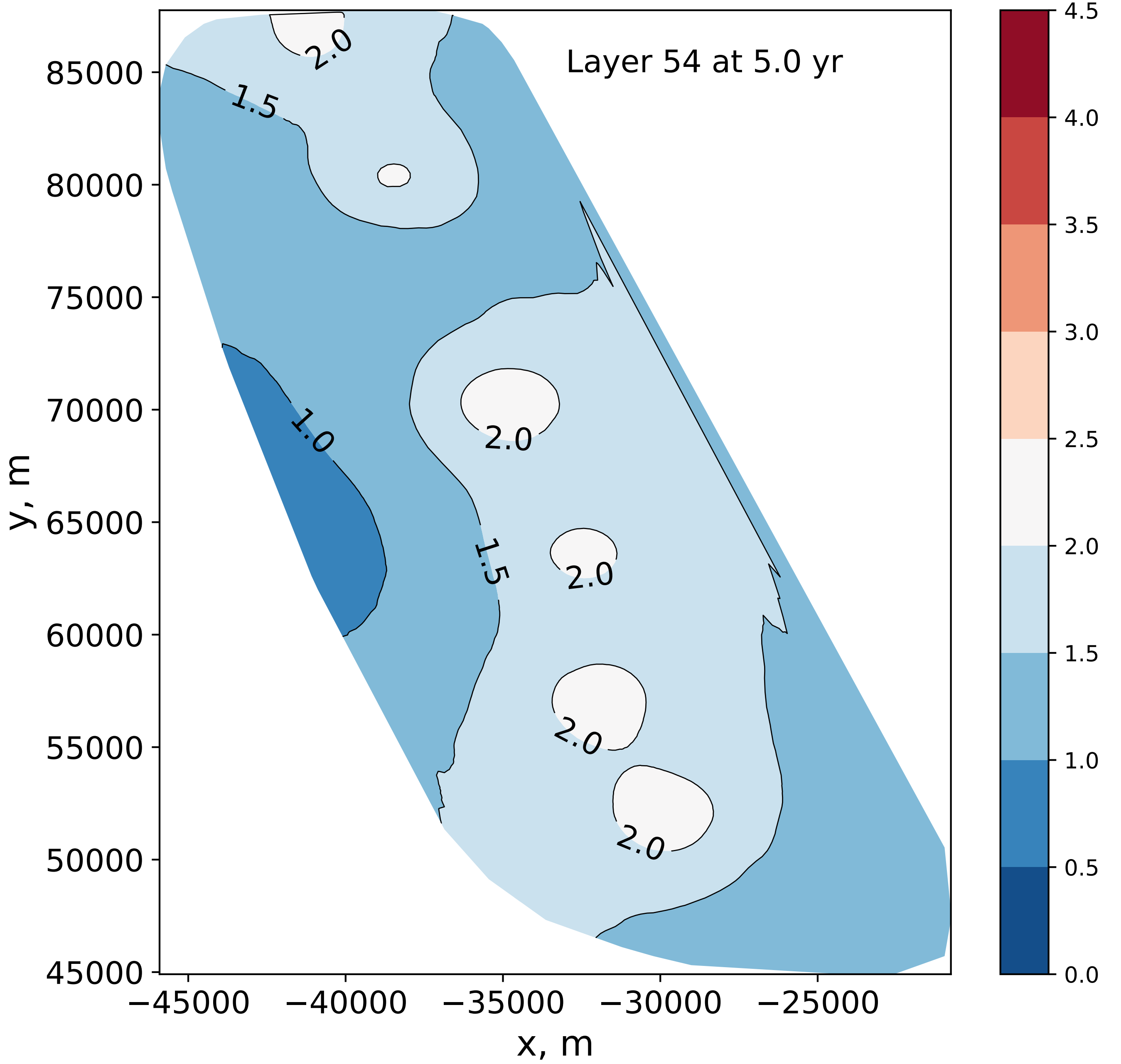

B-6. Reservoir Pressure Differential (MPa) at 5.0 year

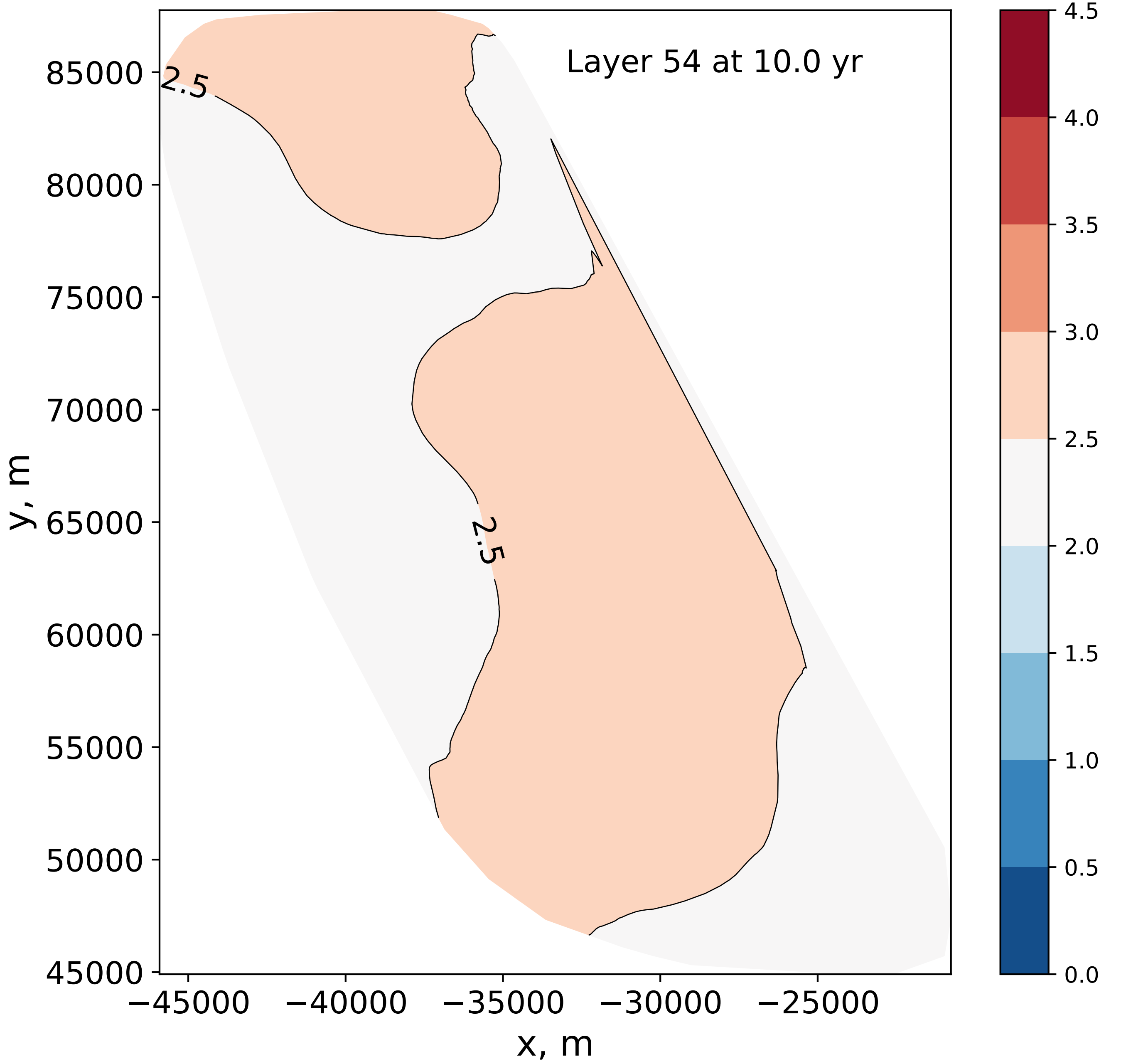

B-7. Reservoir Pressure Differential (MPa) at 10.0 years

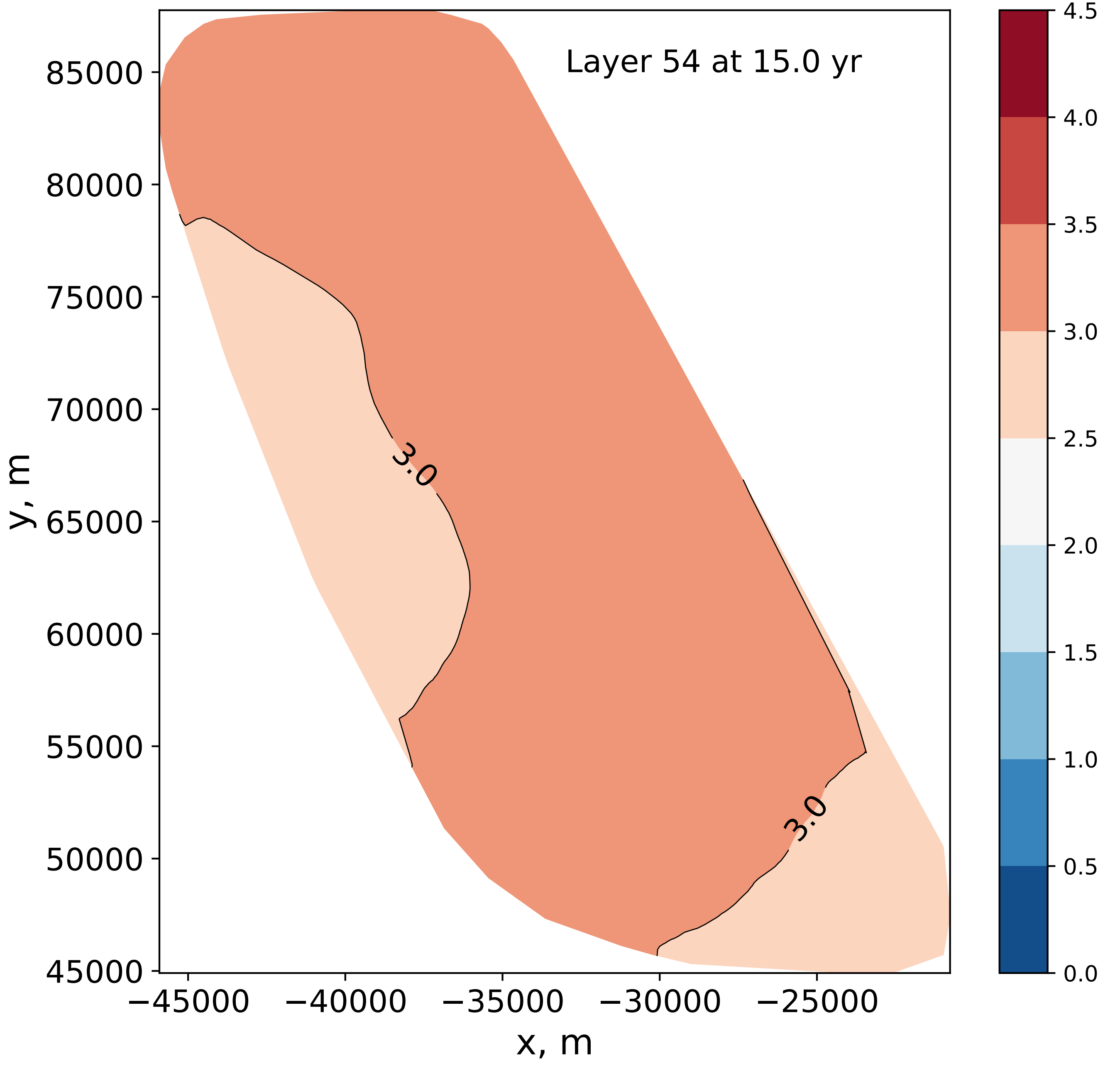

B-8. Reservoir Pressure Differential (MPa) at 15.0 years

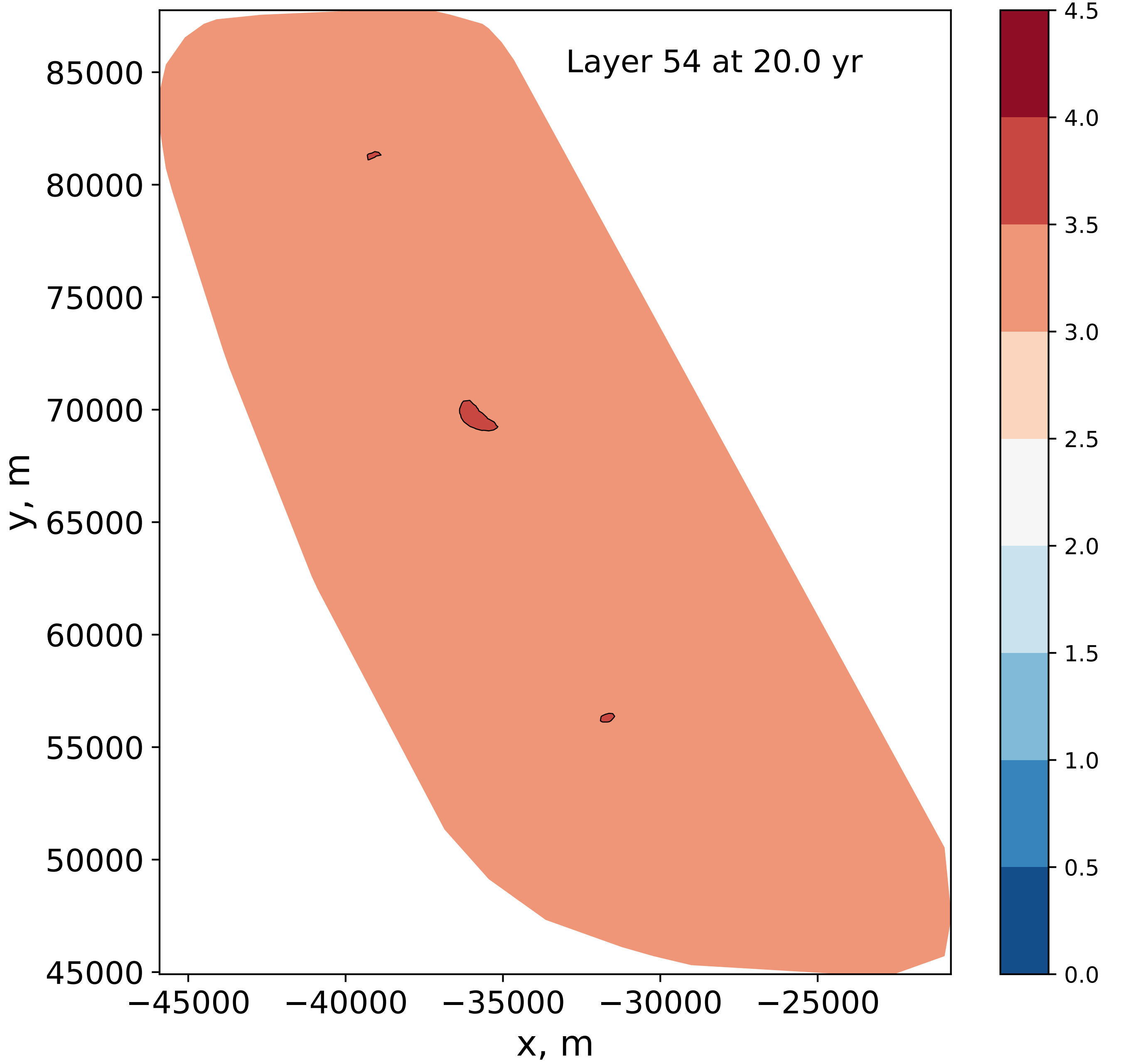

B-9. Reservoir Pressure Differential (MPa) at 20.0 years

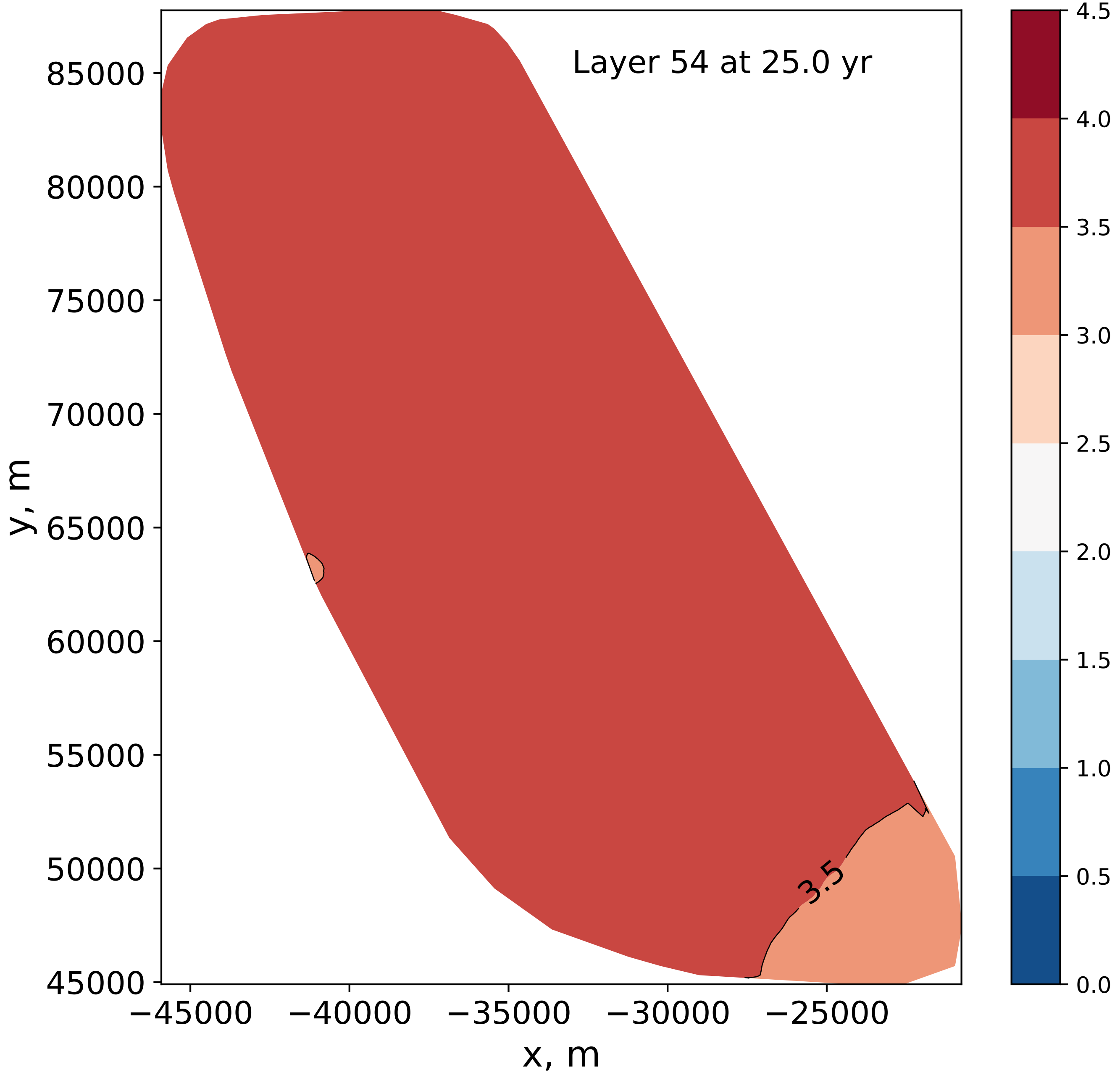

B-10. Reservoir Pressure Differential (MPa) at 25.0 years

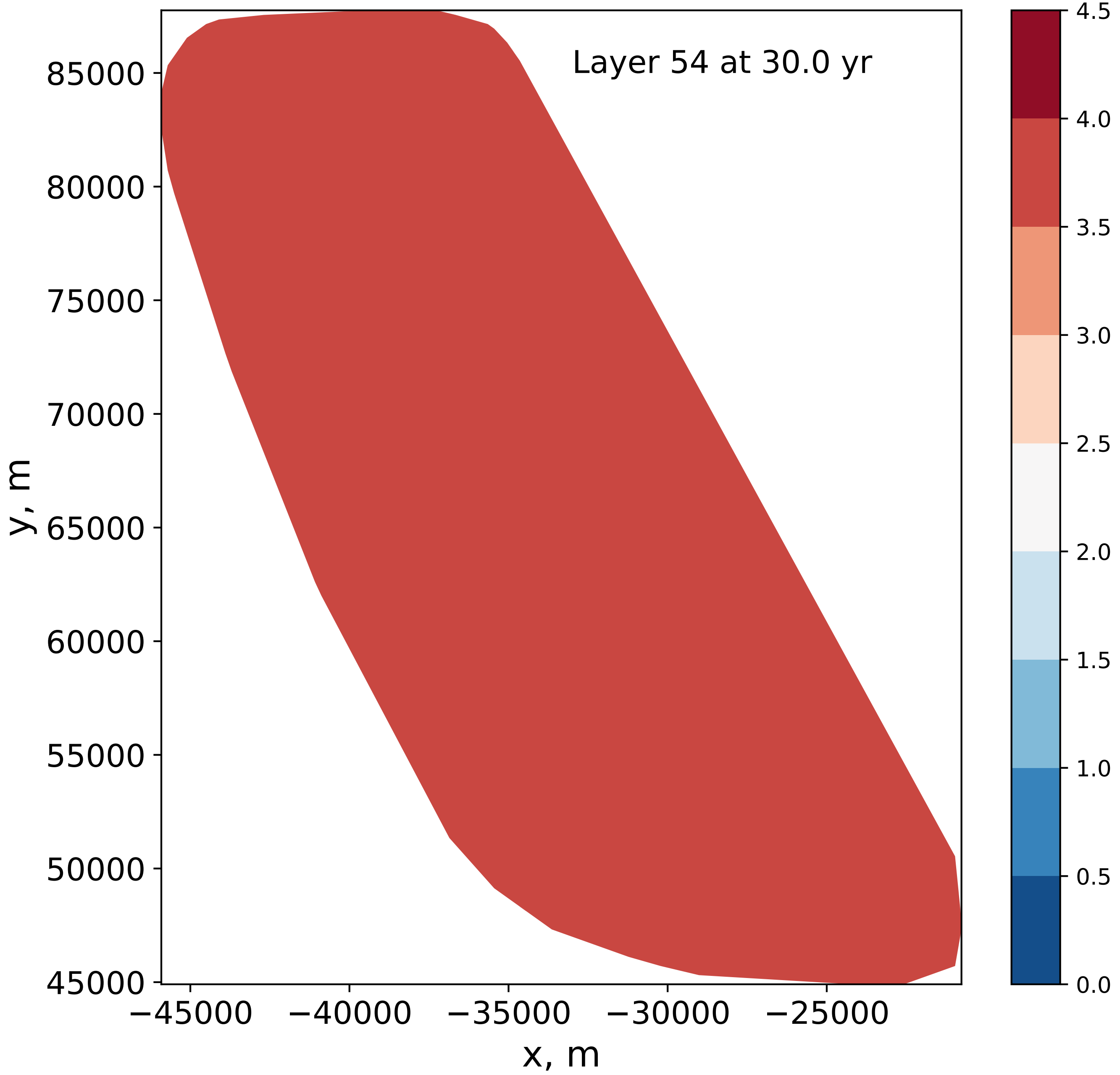

B-11. Reservoir Pressure Differential (MPa) at 30.0 years

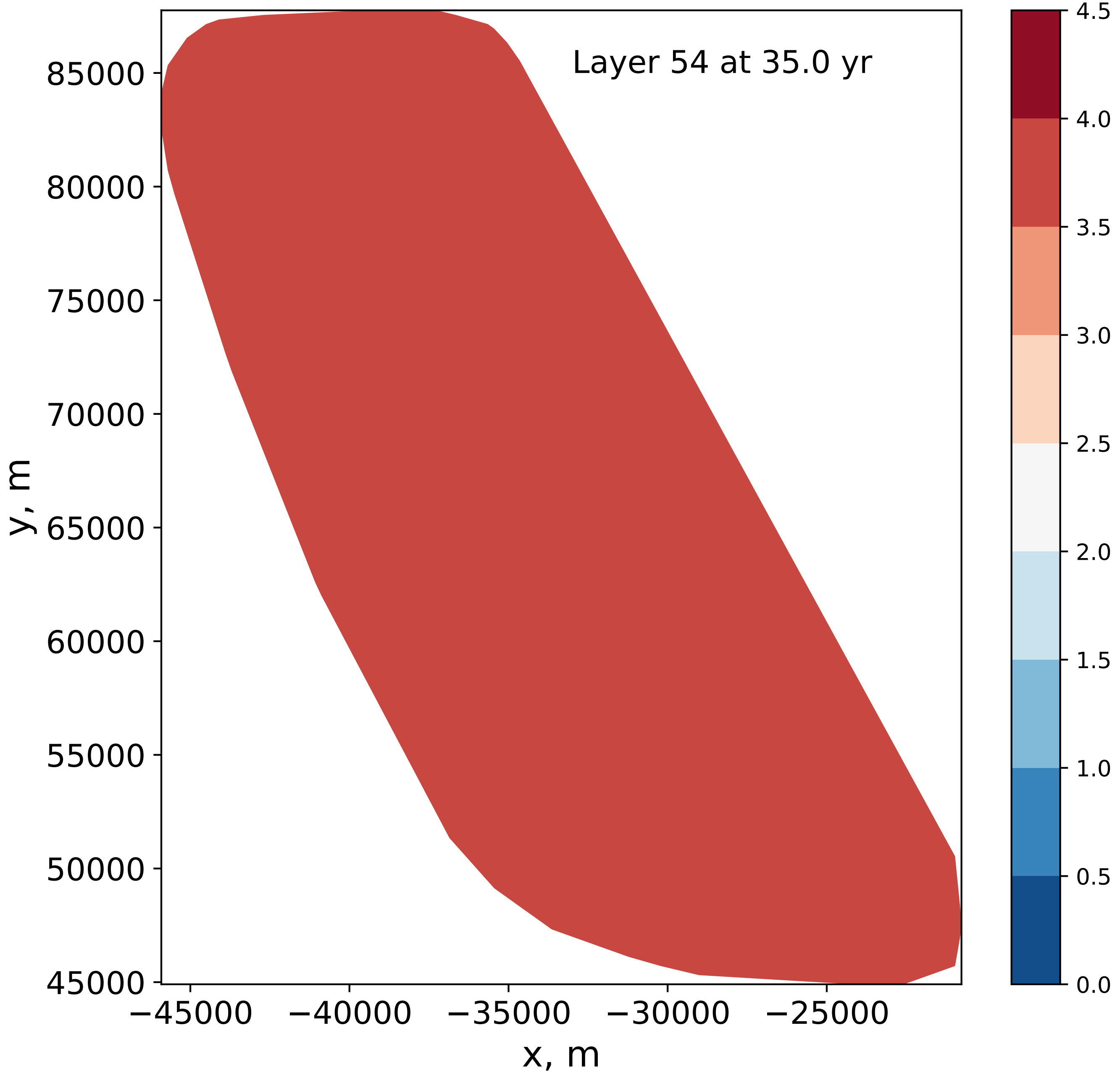

B-12. Reservoir Pressure Differential (MPa) at 35.0 years

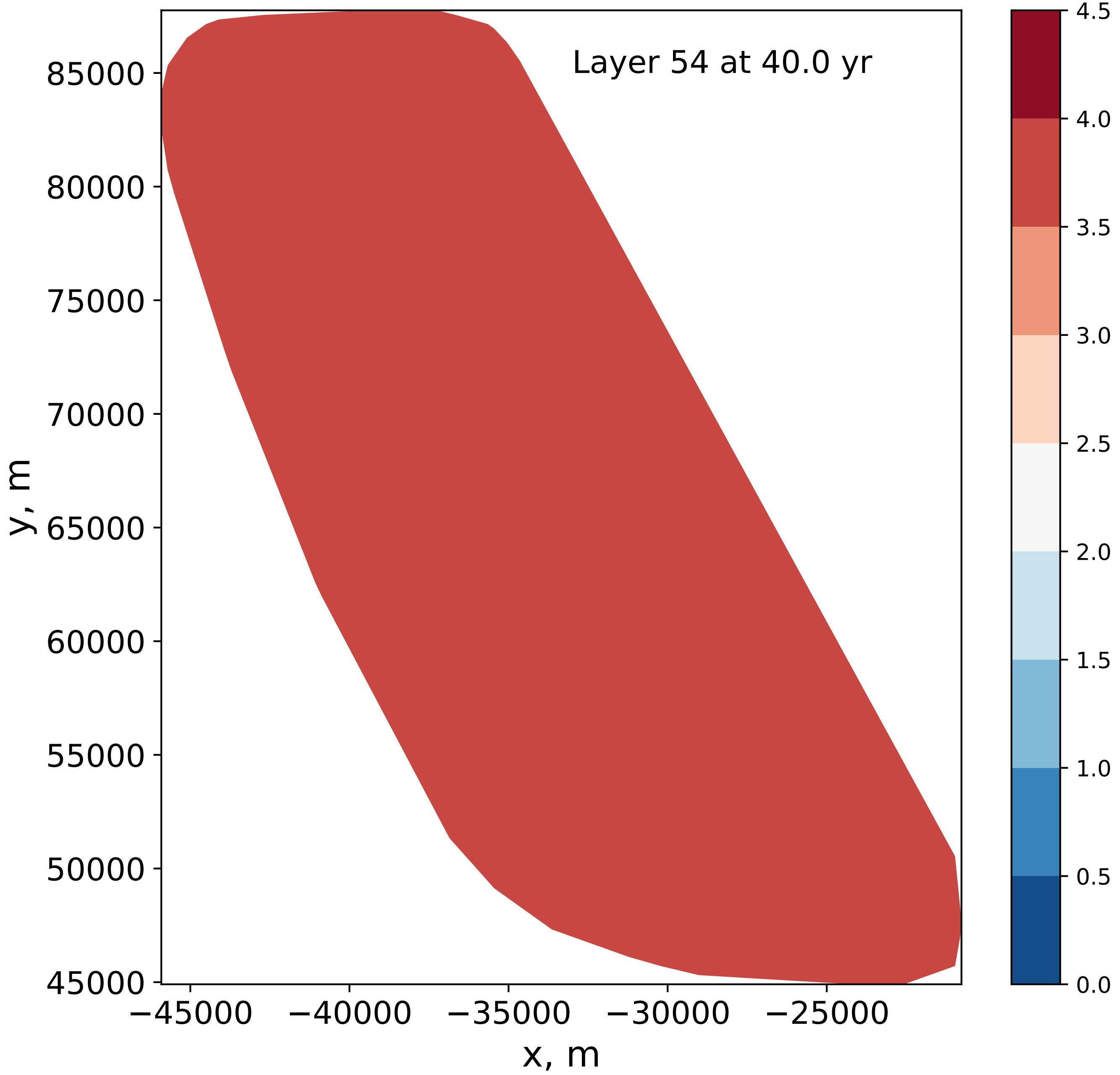

B-13. Reservoir Pressure Differential (MPa) at 40.0 years

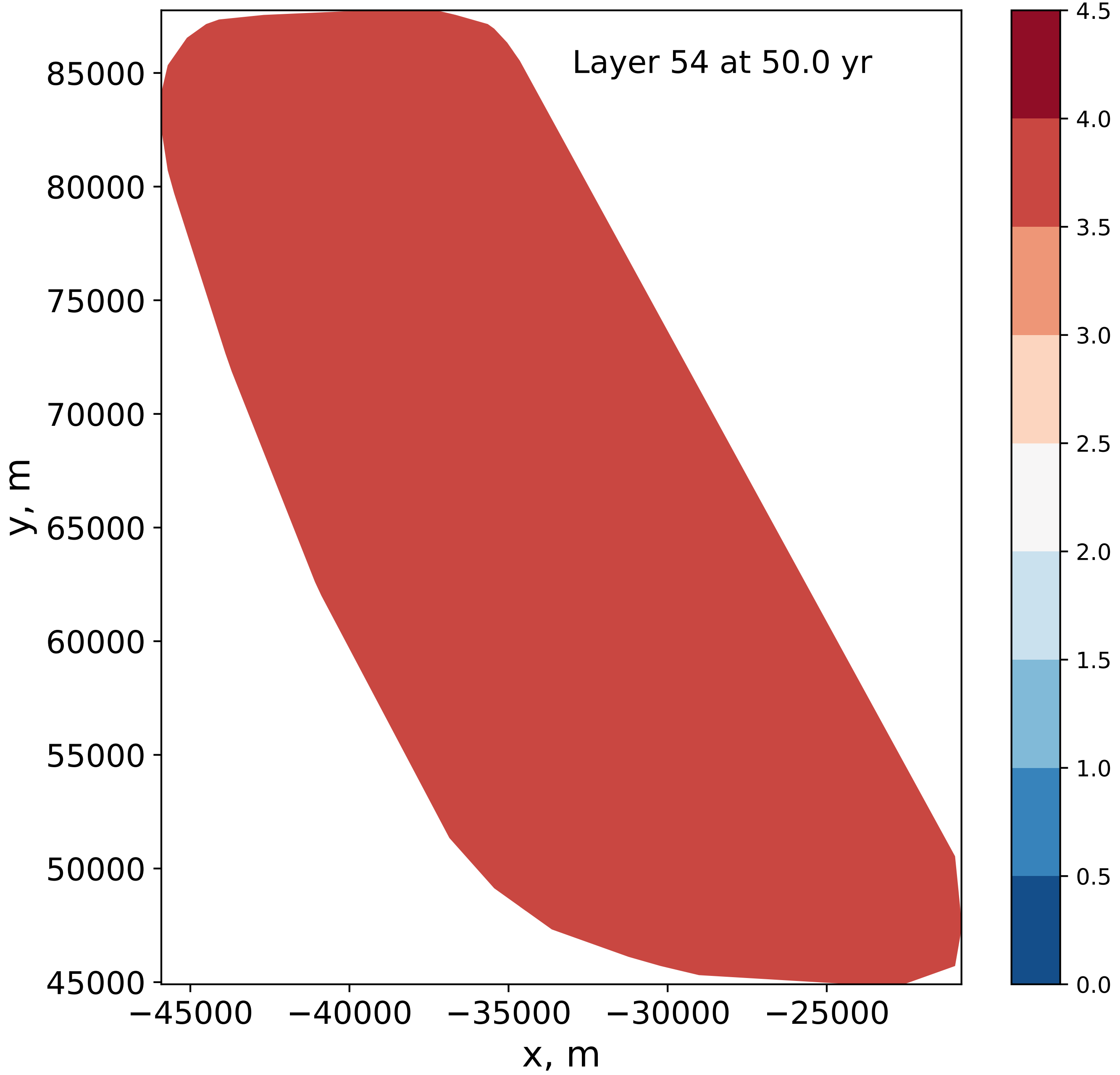

B-14. Reservoir Pressure Differential (MPa) at 50.0 years

Appendix C – NRAP-Open-IAM Results for Conceptual Model with a Large Thickness of Aquifer 1 at the PHH Site Based on the Reservoir Simulation Results of Layer 54

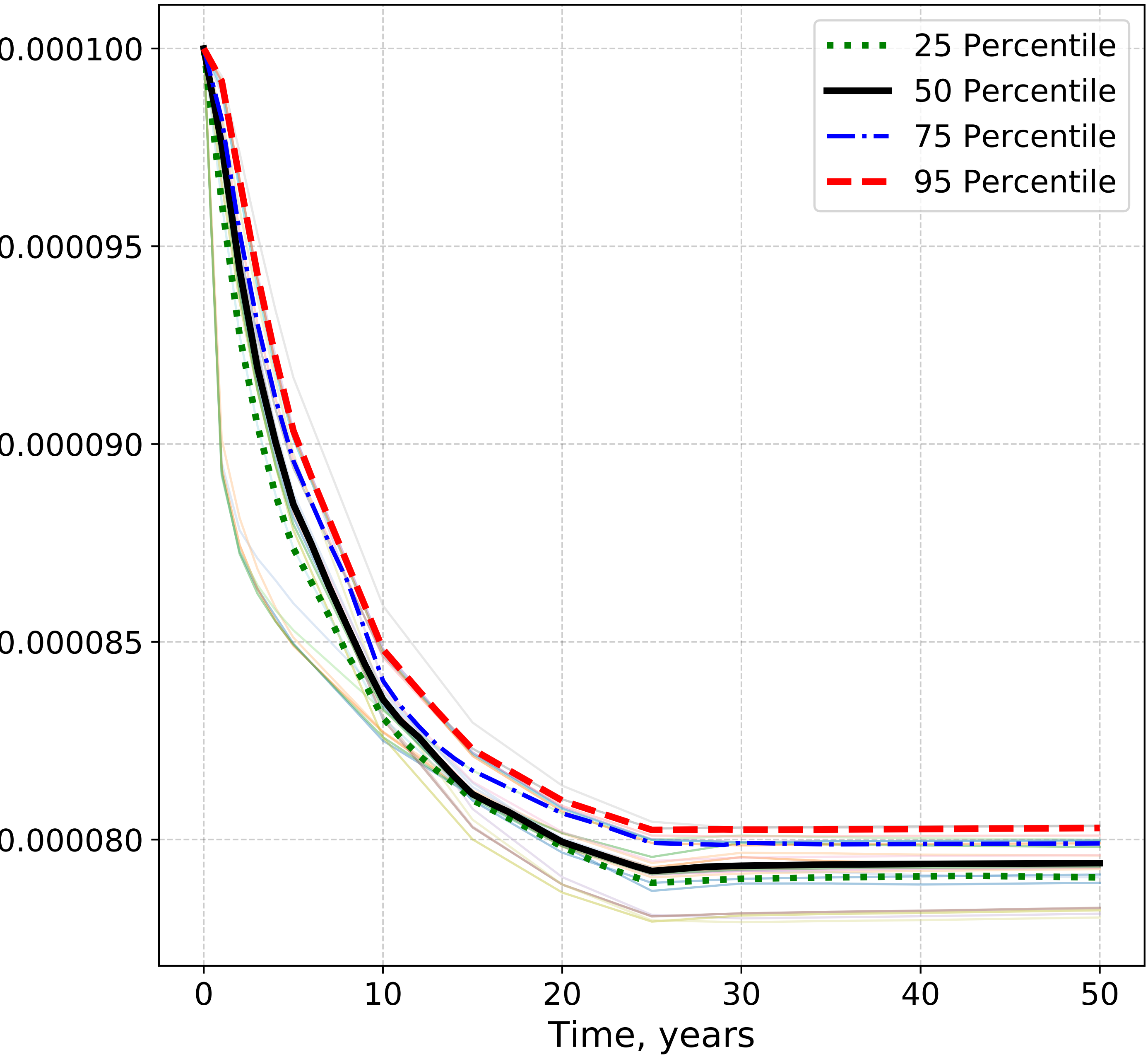

Figure C-1. Saturation History. Layer 54 of the reservoir simulation was used in the IAM analysis.

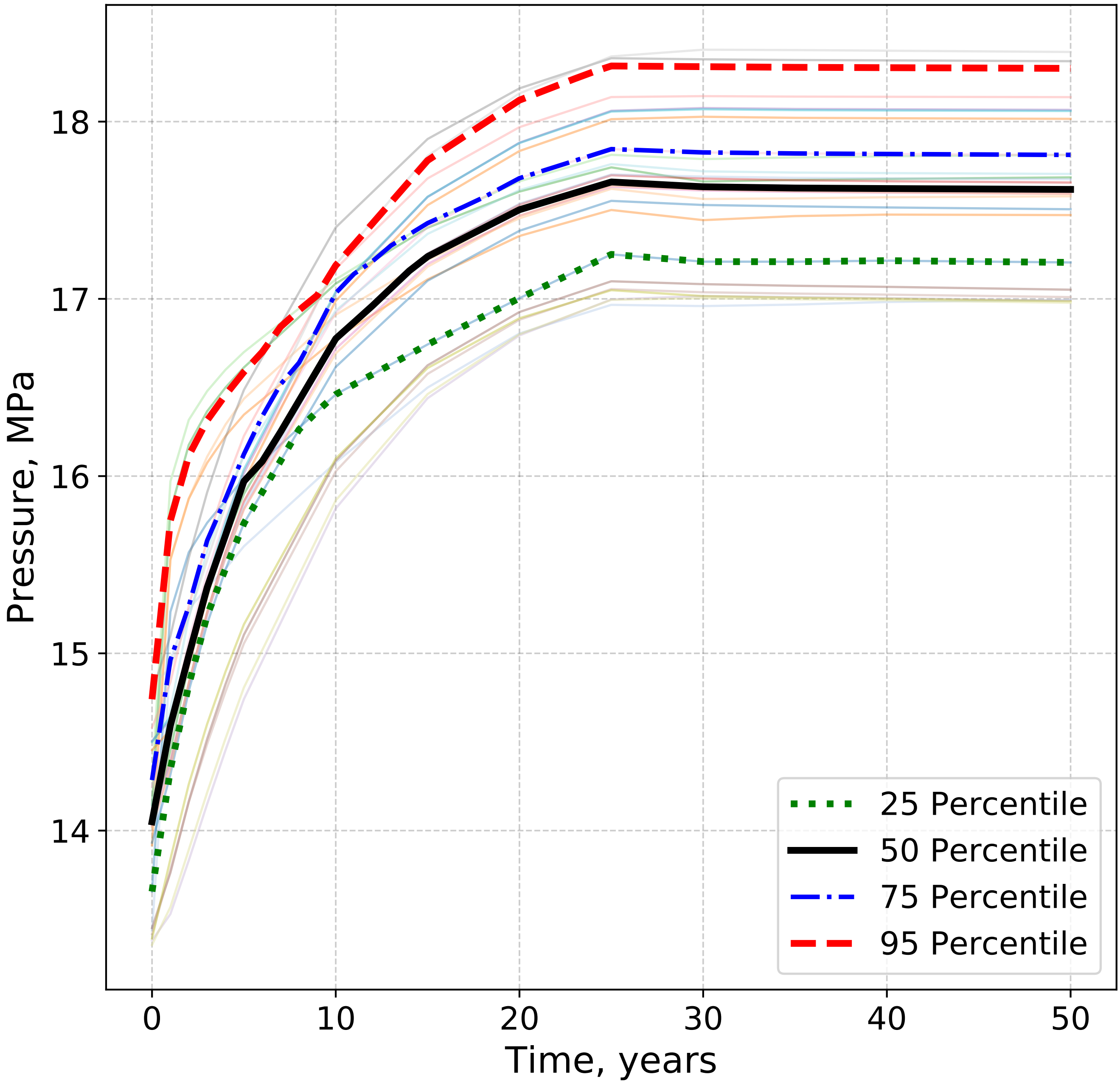

Figure C-2. Pressure History. Layer 54 of the reservoir simulation was used in the IAM analysis.

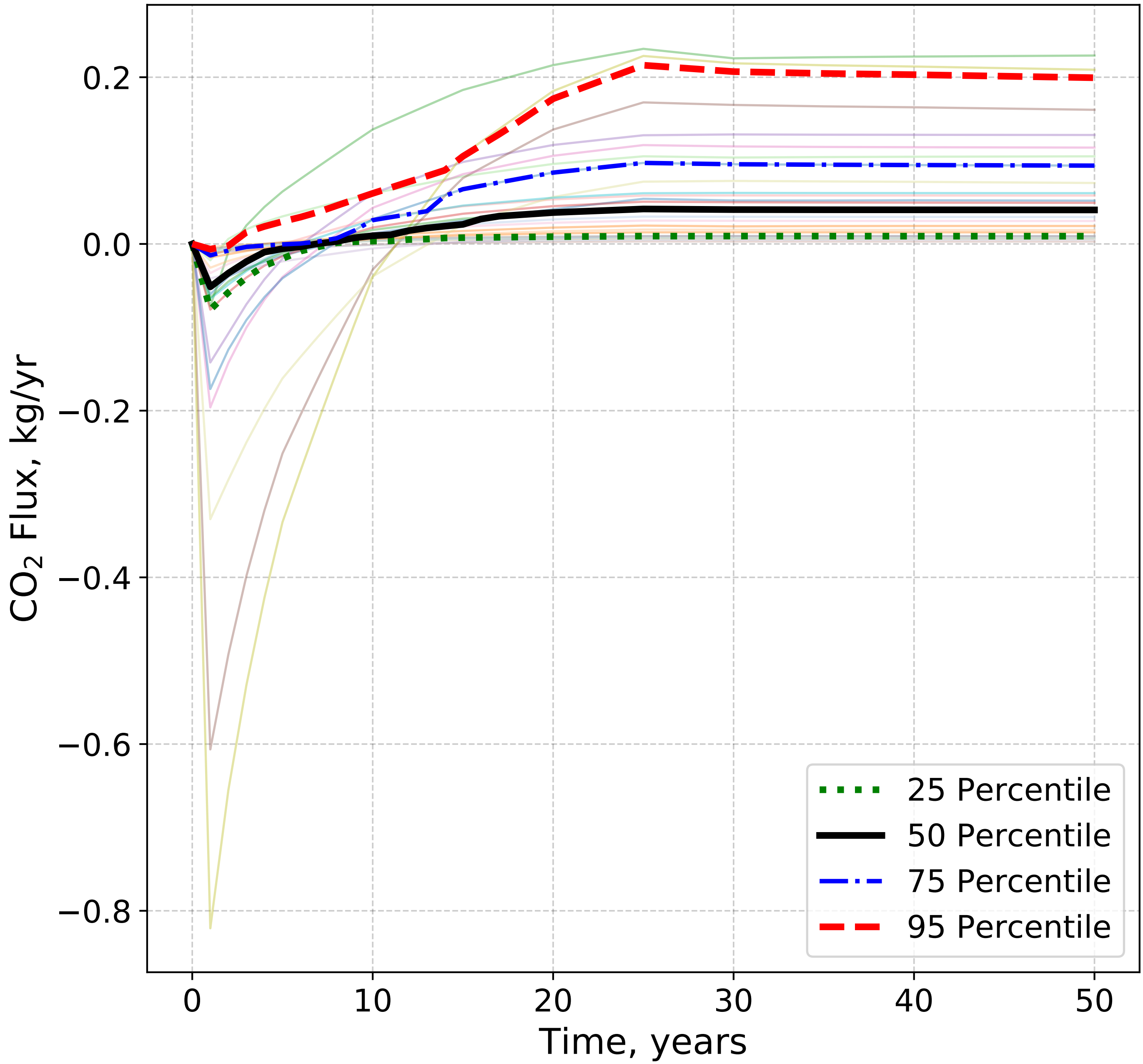

Figure C-3. CO_2 Flux to Aquifer 1. Layer 54 of the reservoir simulation was used in the IAM analysis.

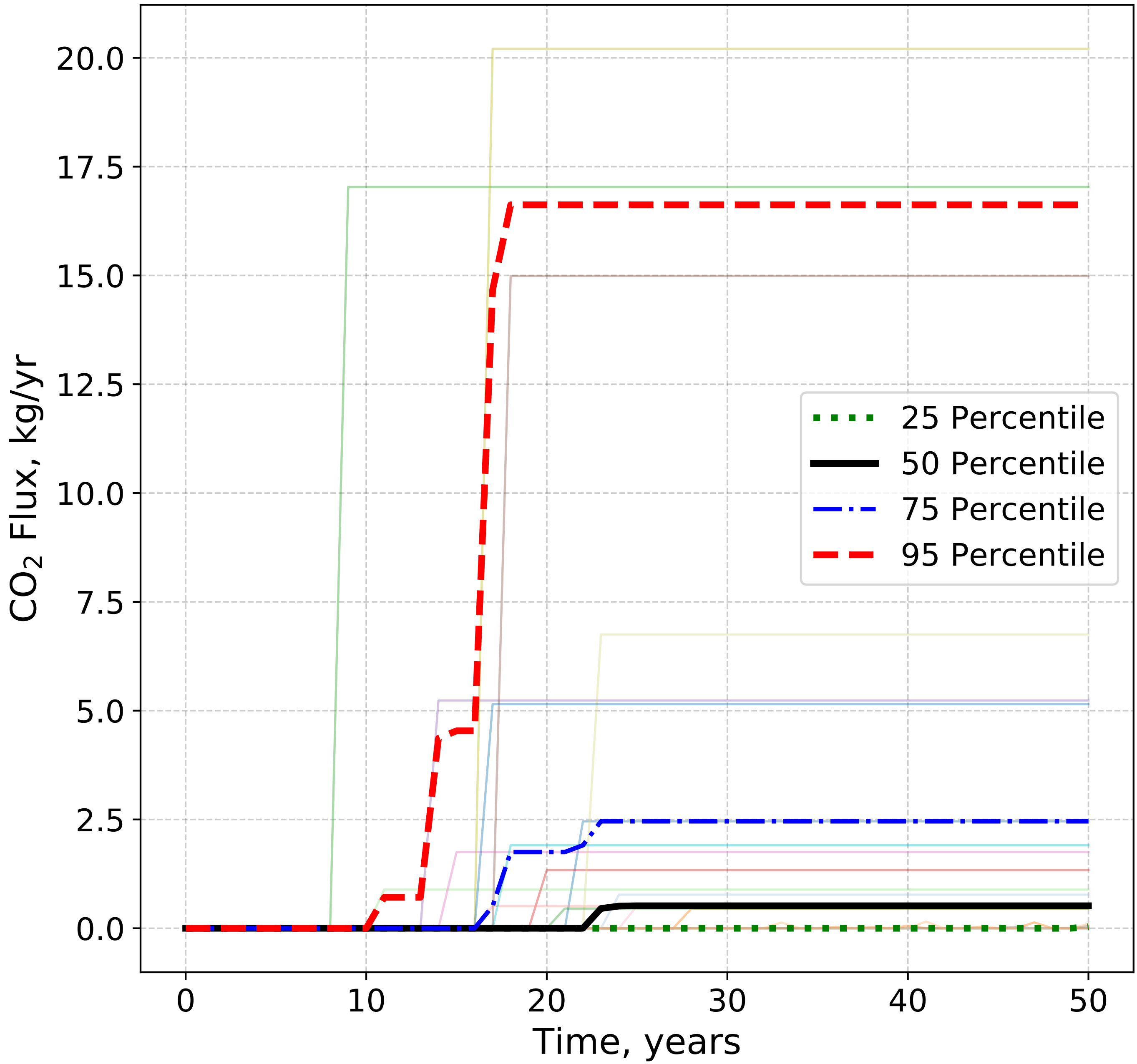

Figure C-4. CO_2 Flux to Aquifer 2. Layer 54 of the reservoir simulation was used in the IAM analysis.

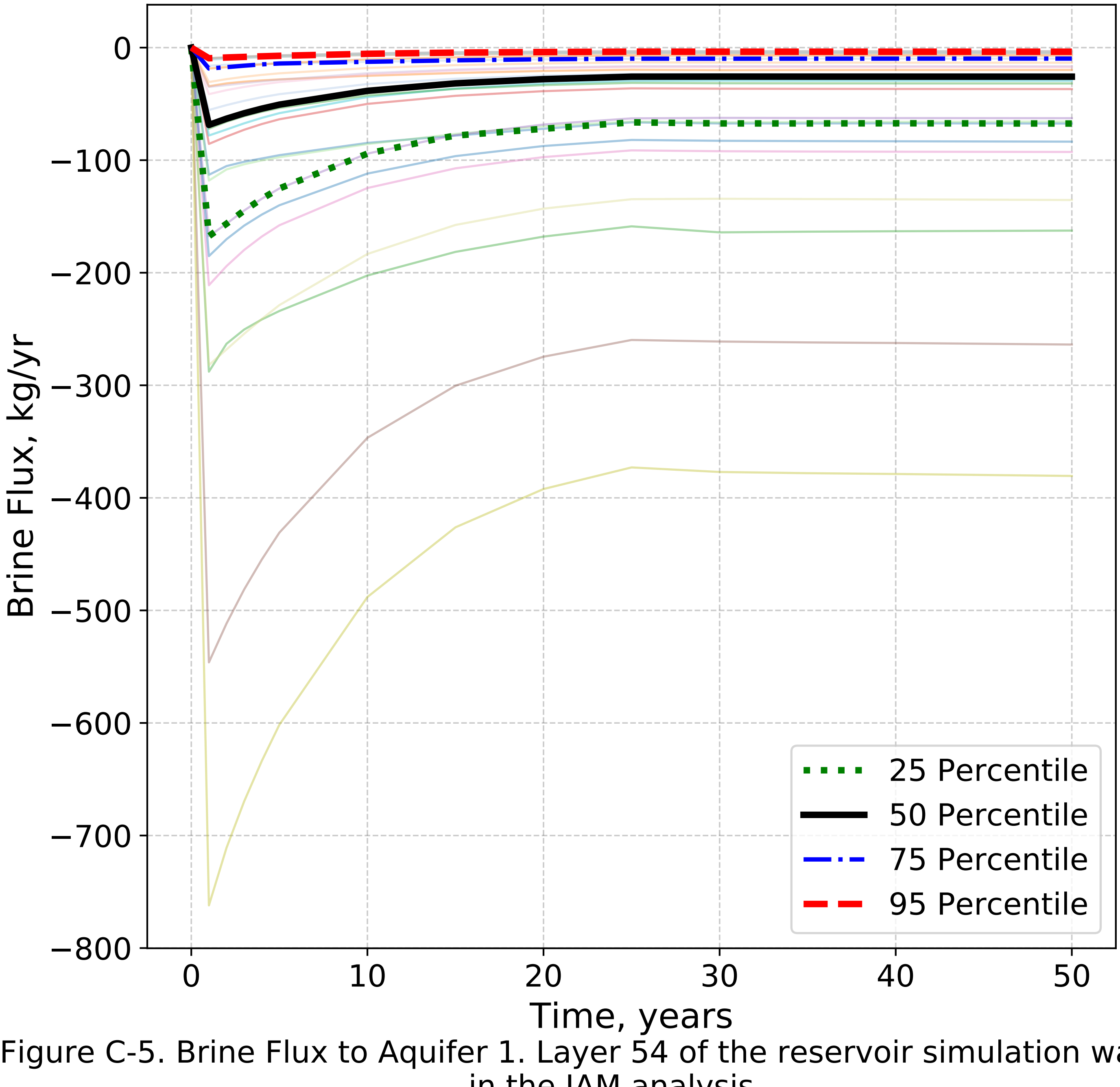

Figure C-5. Brine Flux to Aquifer 1. Layer 54 of the reservoir simulation was used in the IAM analysis.

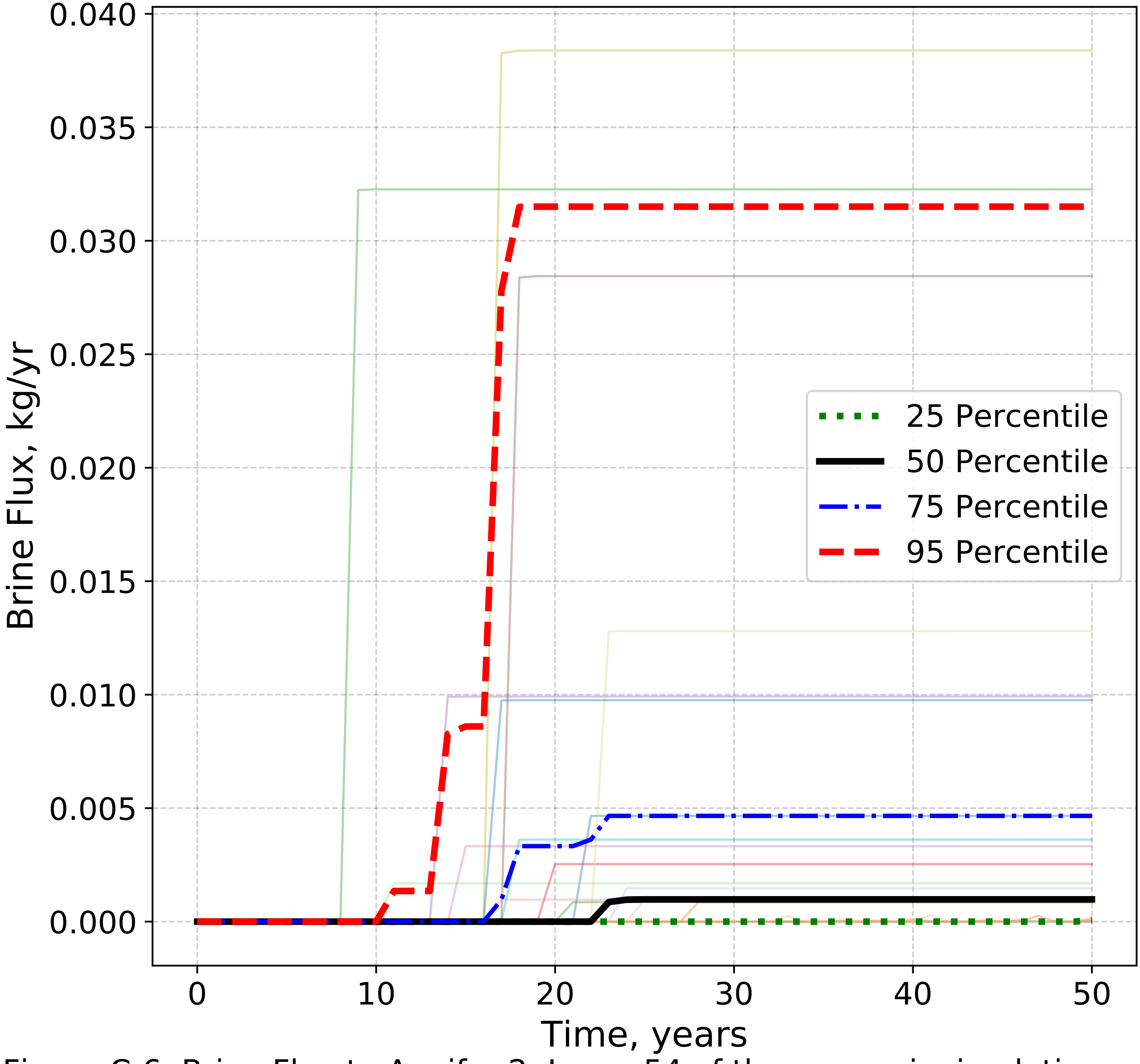

Figure C-6. Brine Flux to Aquifer 2. Layer 54 of the reservoir simulation was used in the IAM analysis.

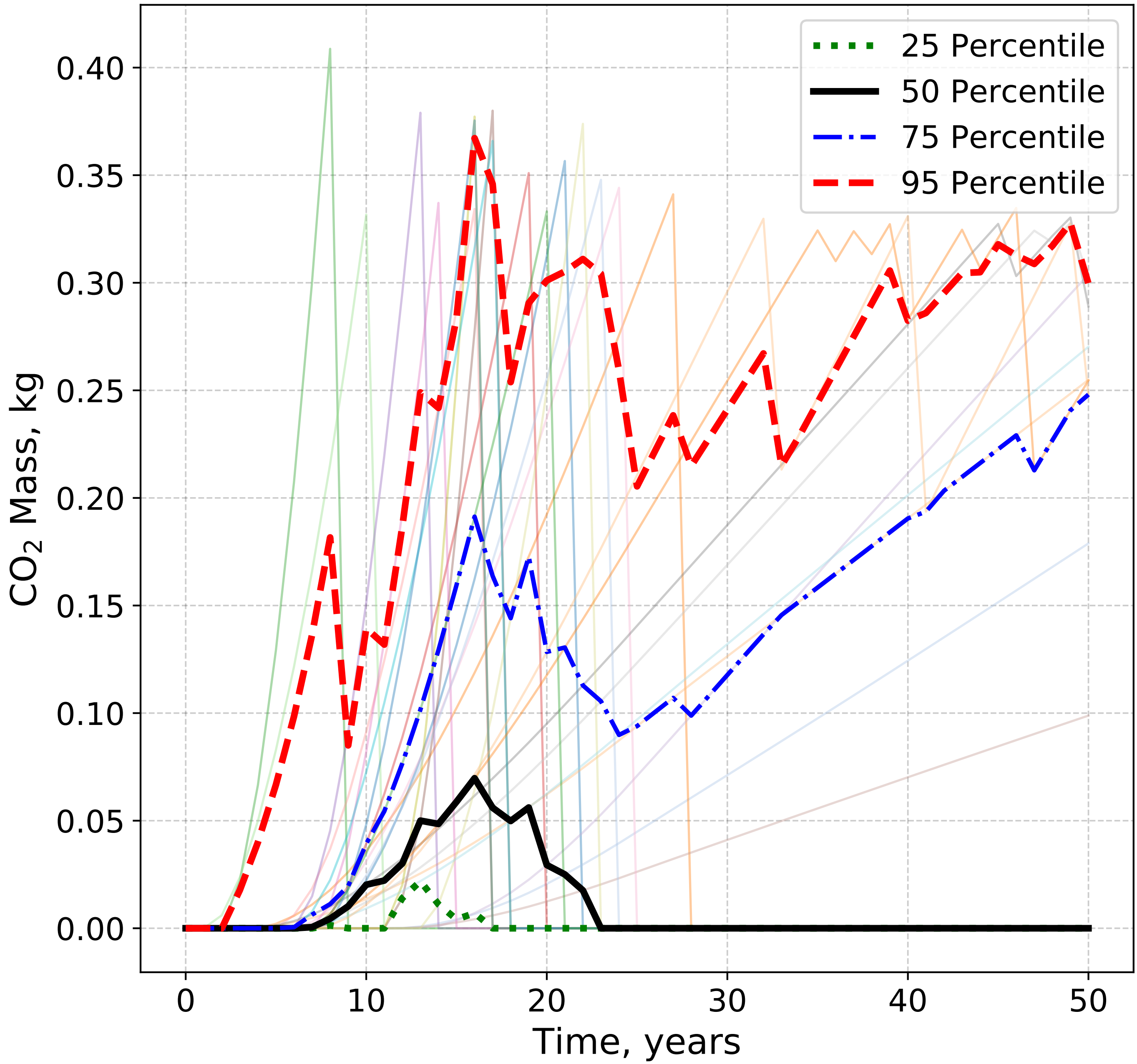

Figure C-7. CO_2 Mass to Aquifer 1. Layer 54 of the reservoir simulation was used in the IAM analysis.

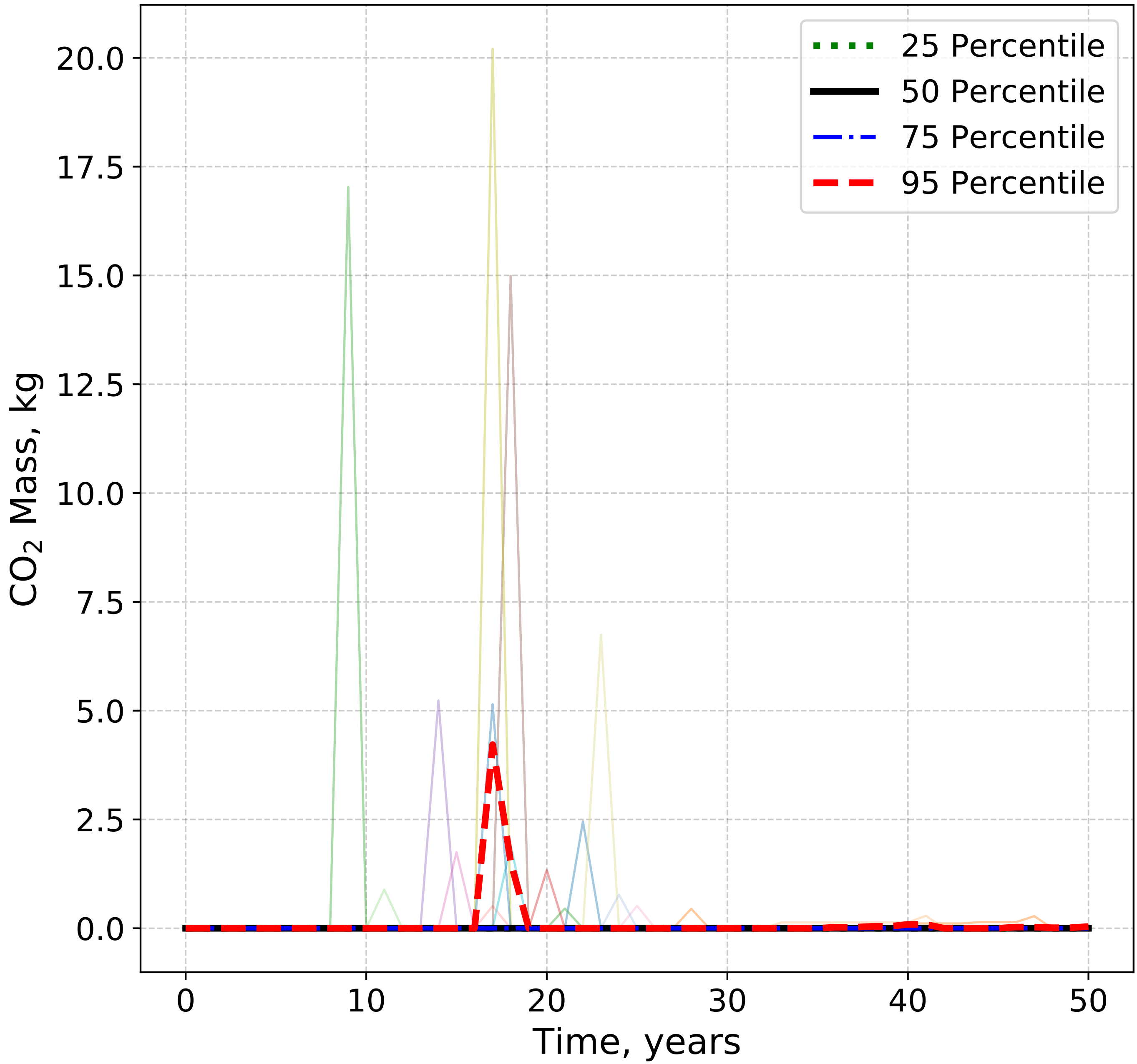

Figure C-8. CO_2 Mass to Aquifer 2. Layer 54 of the reservoir simulation was used in the IAM analysis.

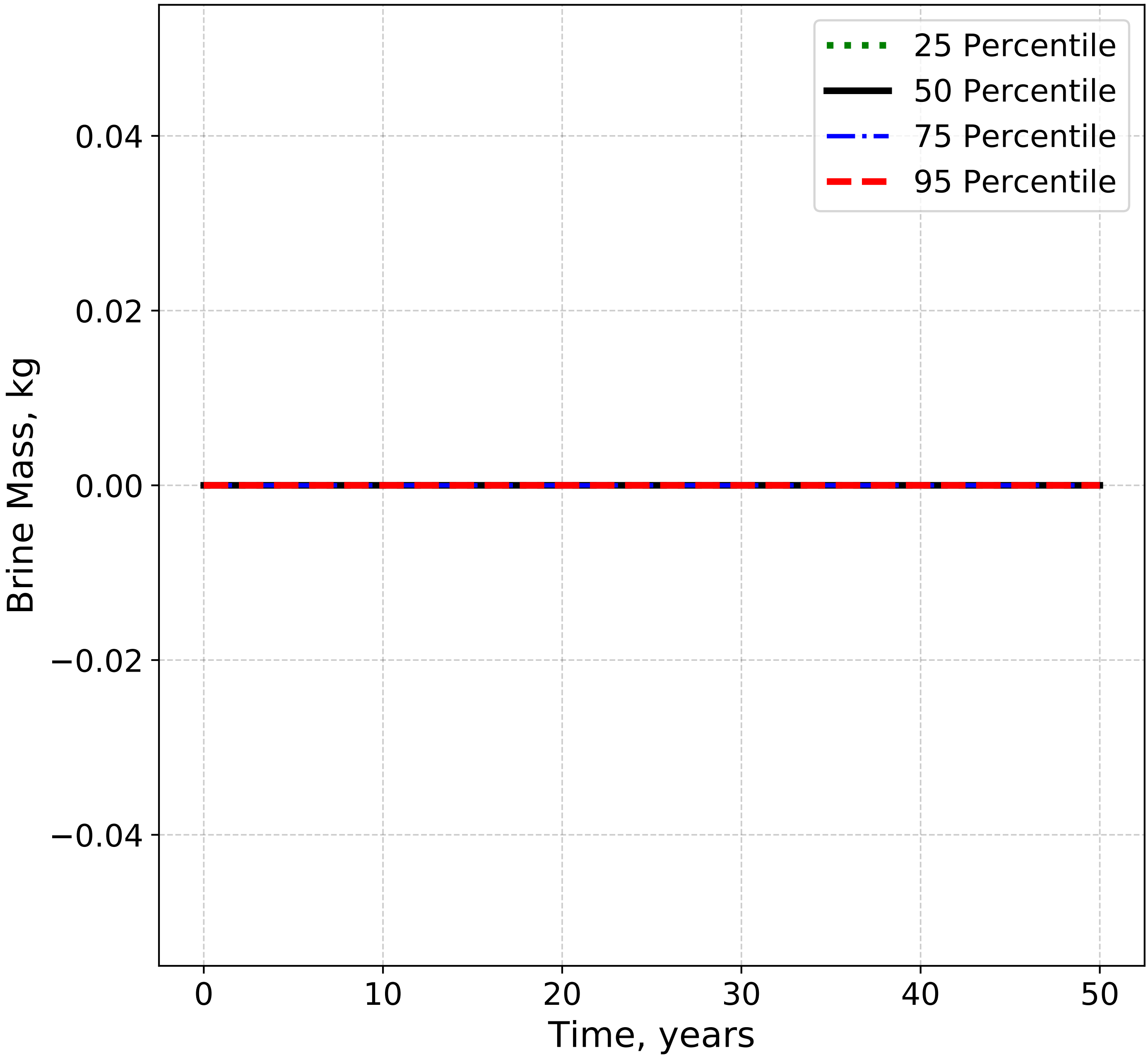

Figure C-9. Brine Mass to Aquifer 1. Layer 54 of the reservoir simulation was used in the IAM analysis.

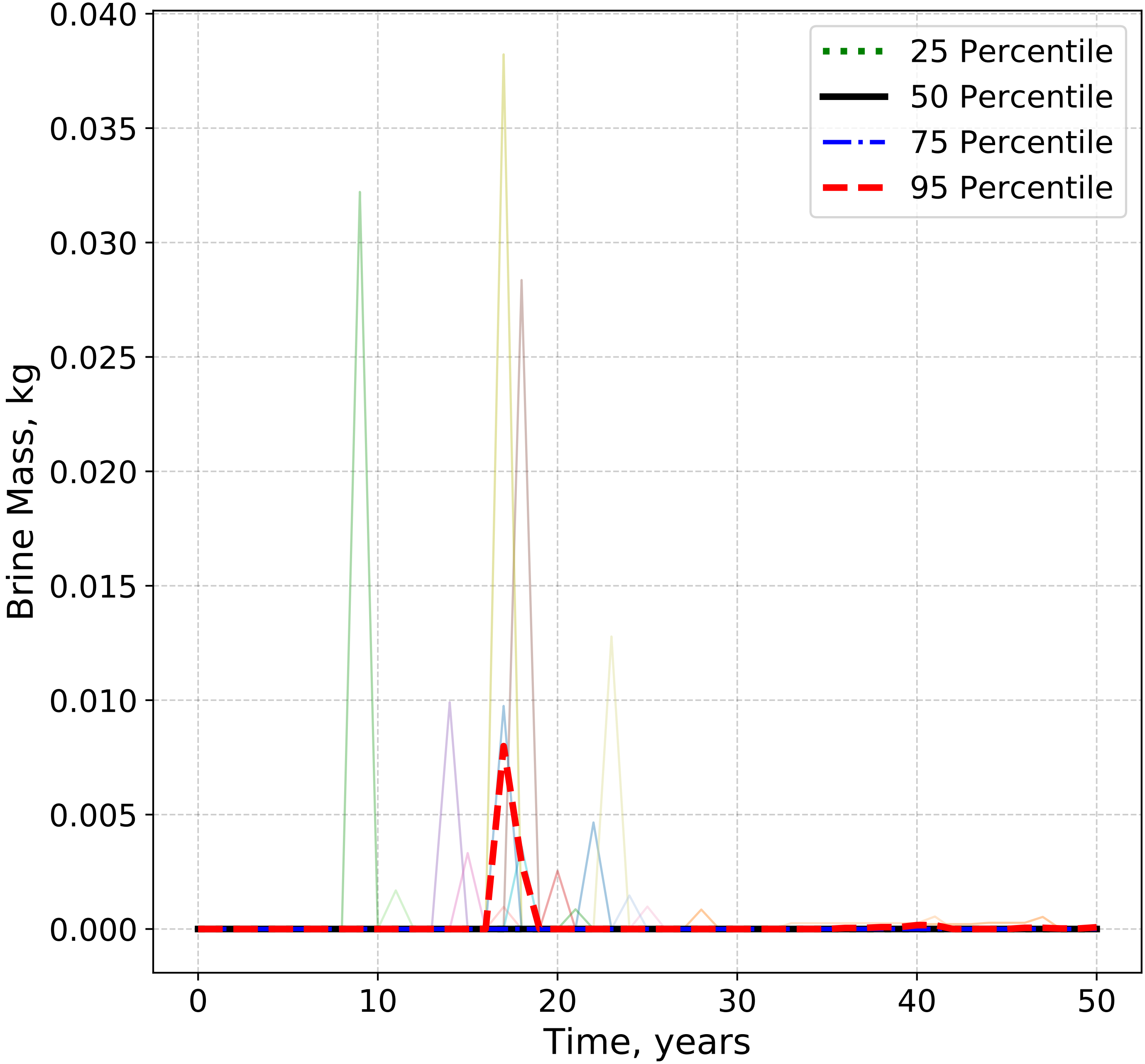

Figure C-10. Brine Mass to Aquifer 2. Layer 54 of the reservoir simulation was used in the IAM analysis.

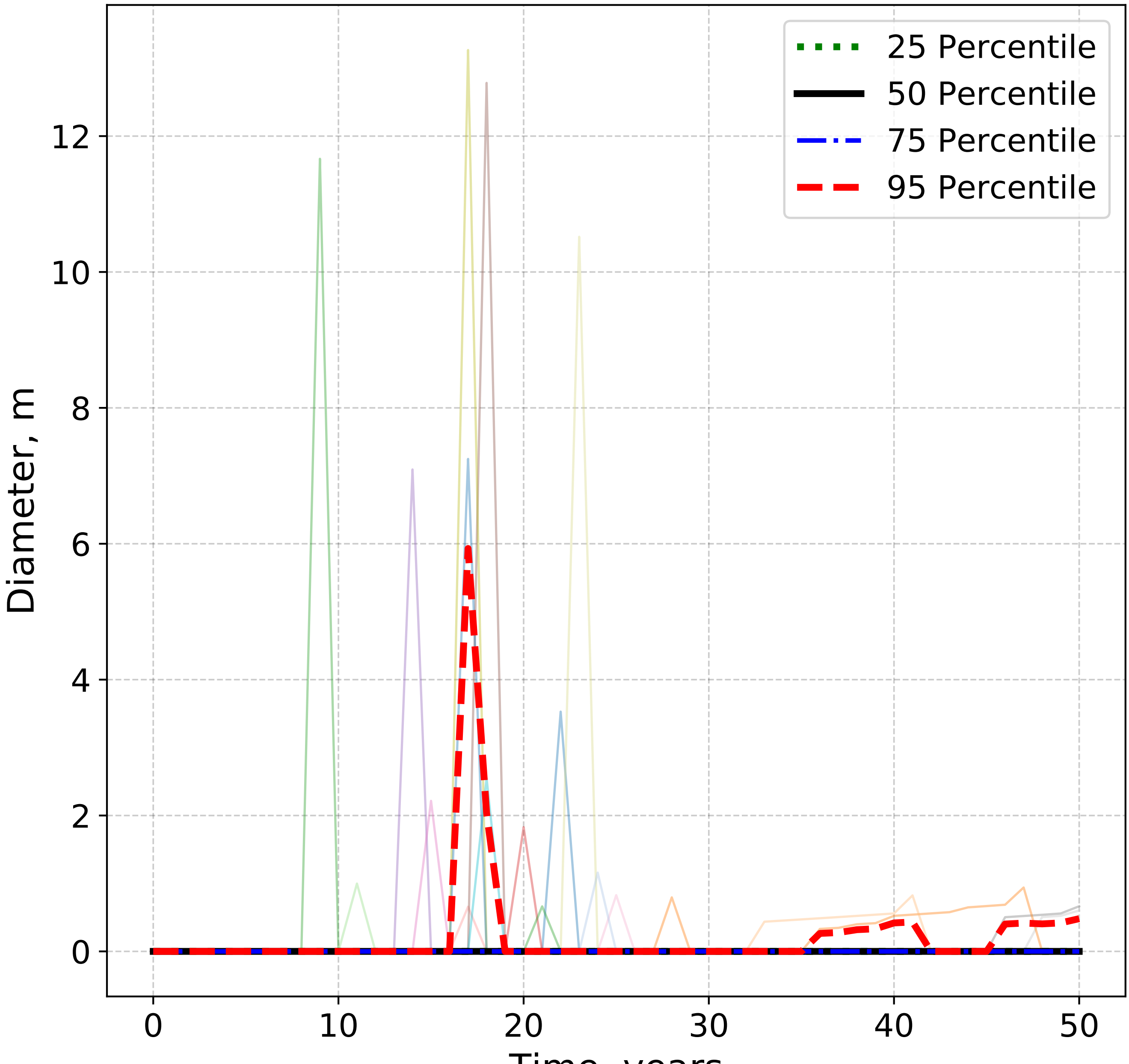

Figure C-11. pH Impact to Aquifer 2 in the Horizontal Direction. Layer 54 of the reservoir simulation was used in the IAM analysis.

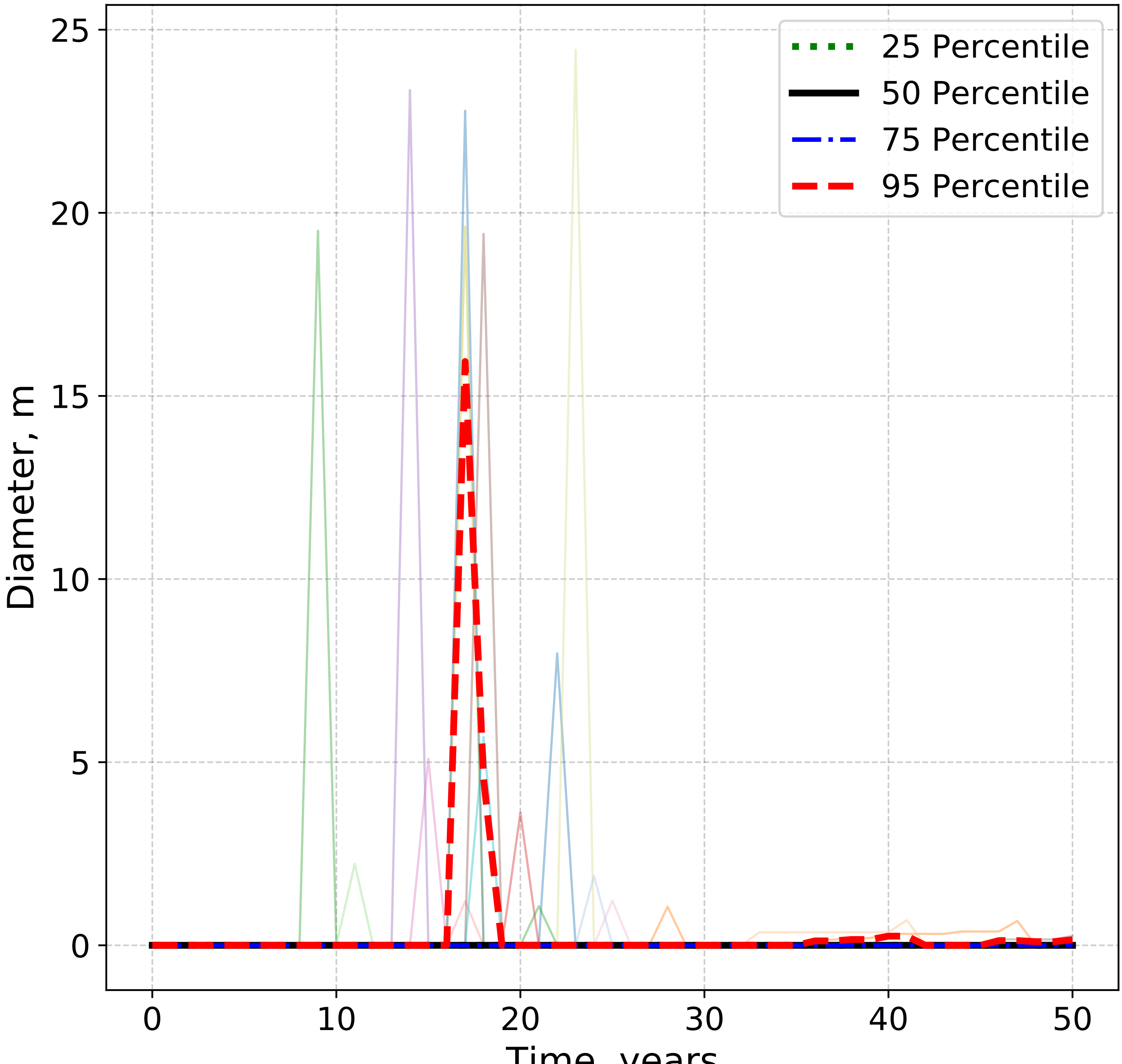

Figure C-12. pH Impact to Aquifer 2 in the Vertical Direction. Layer 54 of the reservoir simulation was used in the IAM analysis.

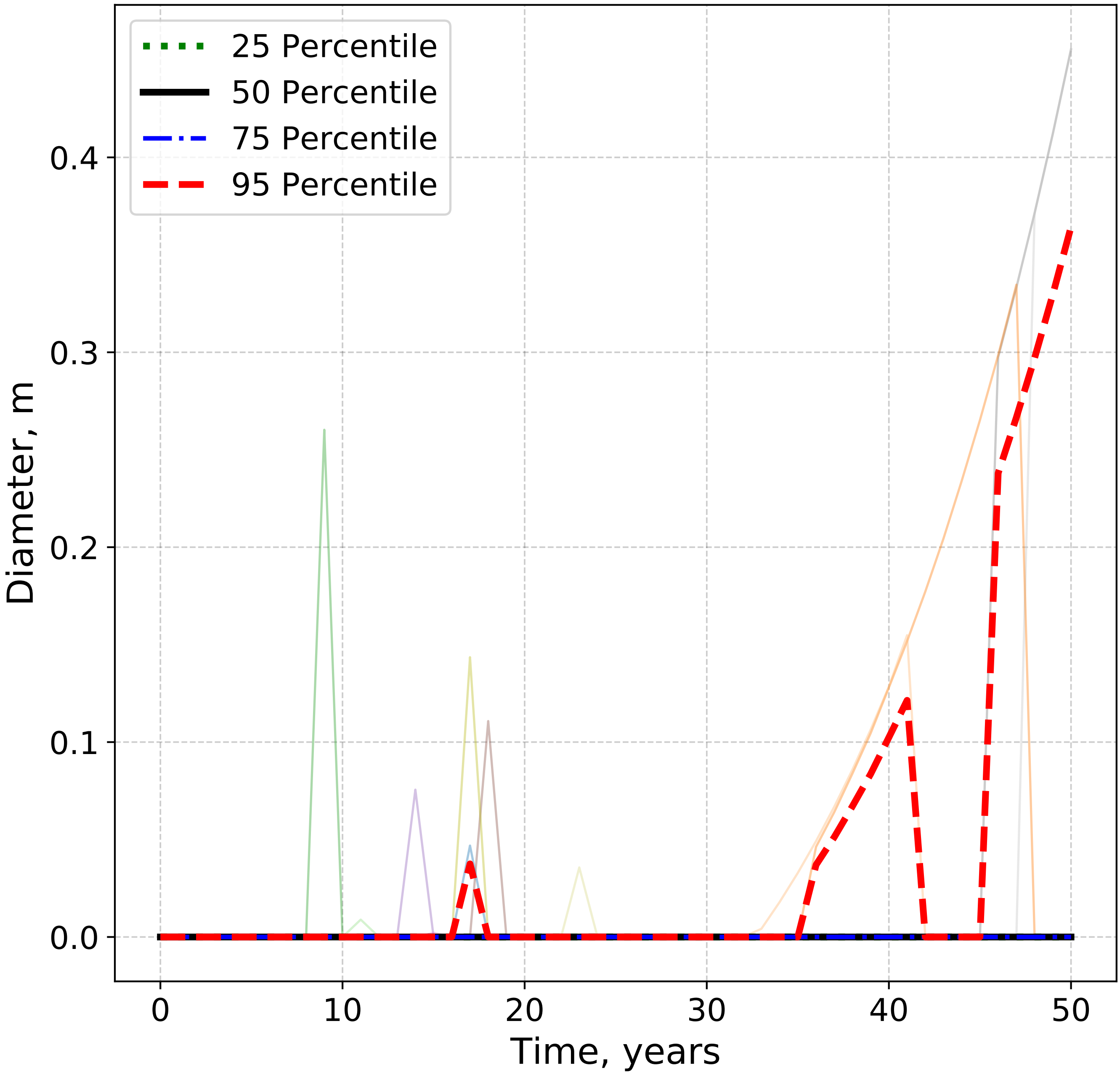

Figure C-13. Pressure Impact to Aquifer 2 in the Horizontal Direction. Layer 54 of the reservoir simulation was used in the IAM analysis.

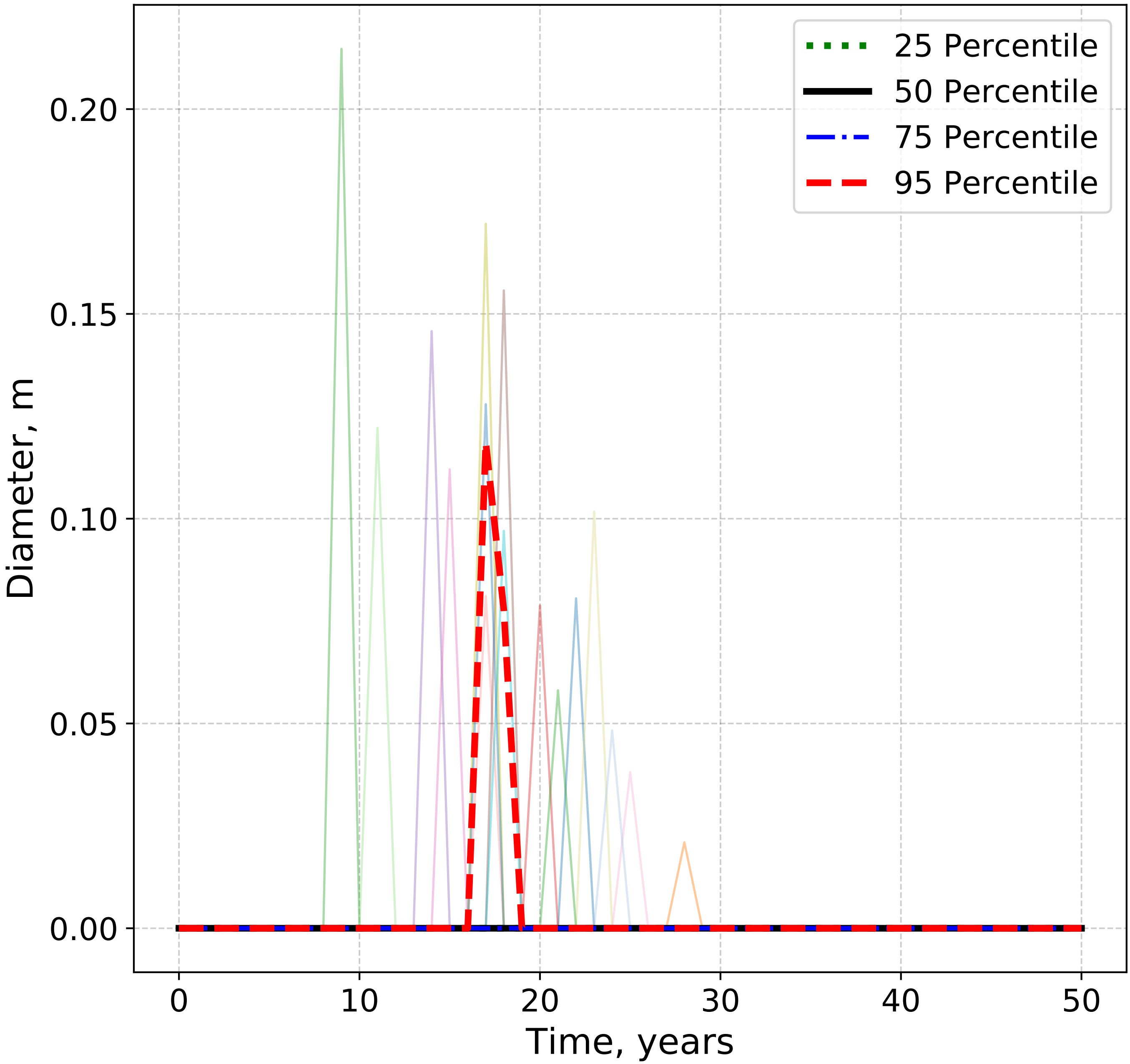

Figure C-14. Pressure Impact to Aquifer 2 in the Vertical Direction. Layer 54 of the reservoir simulation was used in the IAM analysis.

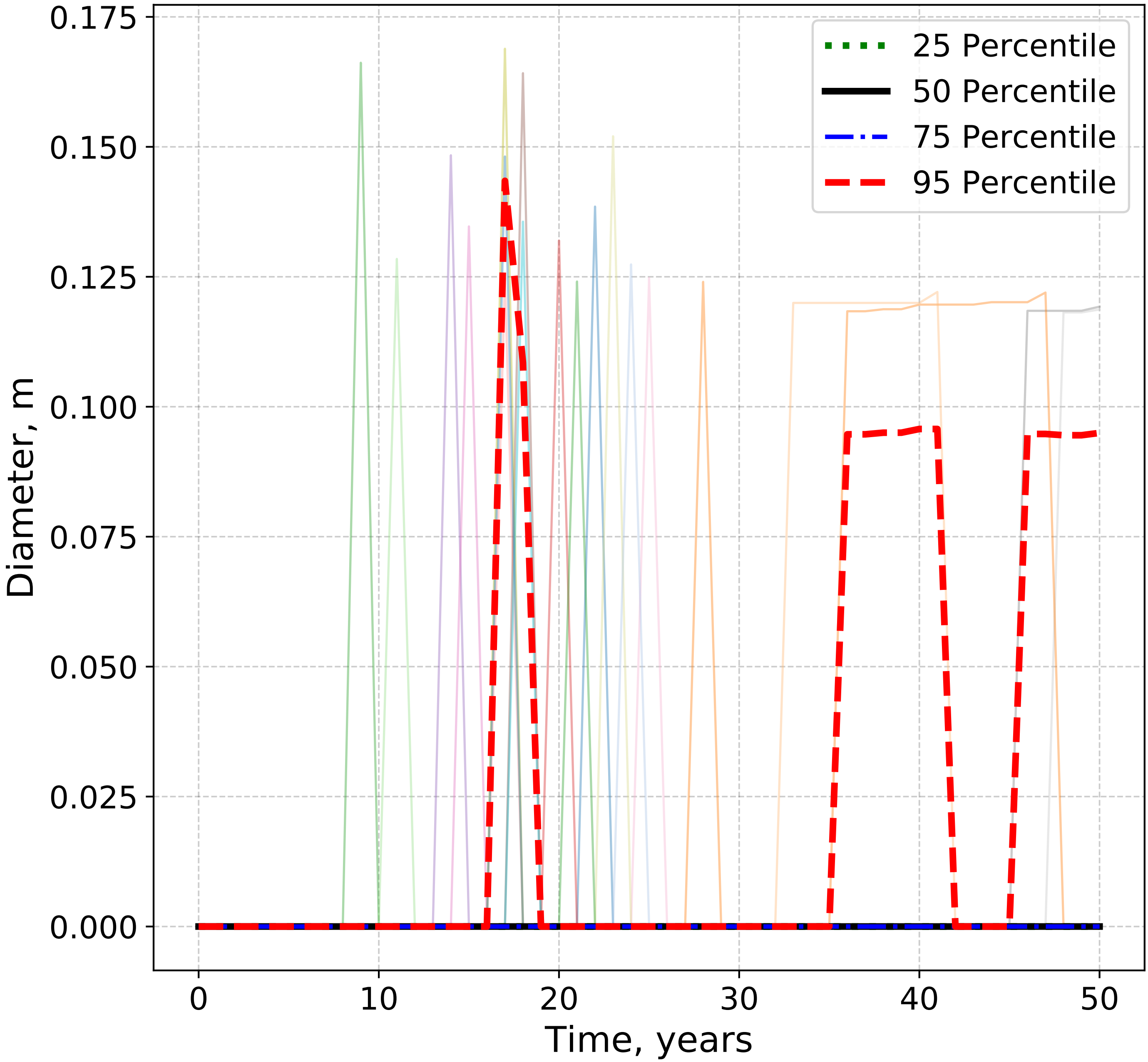

Figure C-15. TDS Impact to Aquifer 2 in the Horizontal Direction. Layer 54 of the reservoir simulation was used in the IAM analysis.

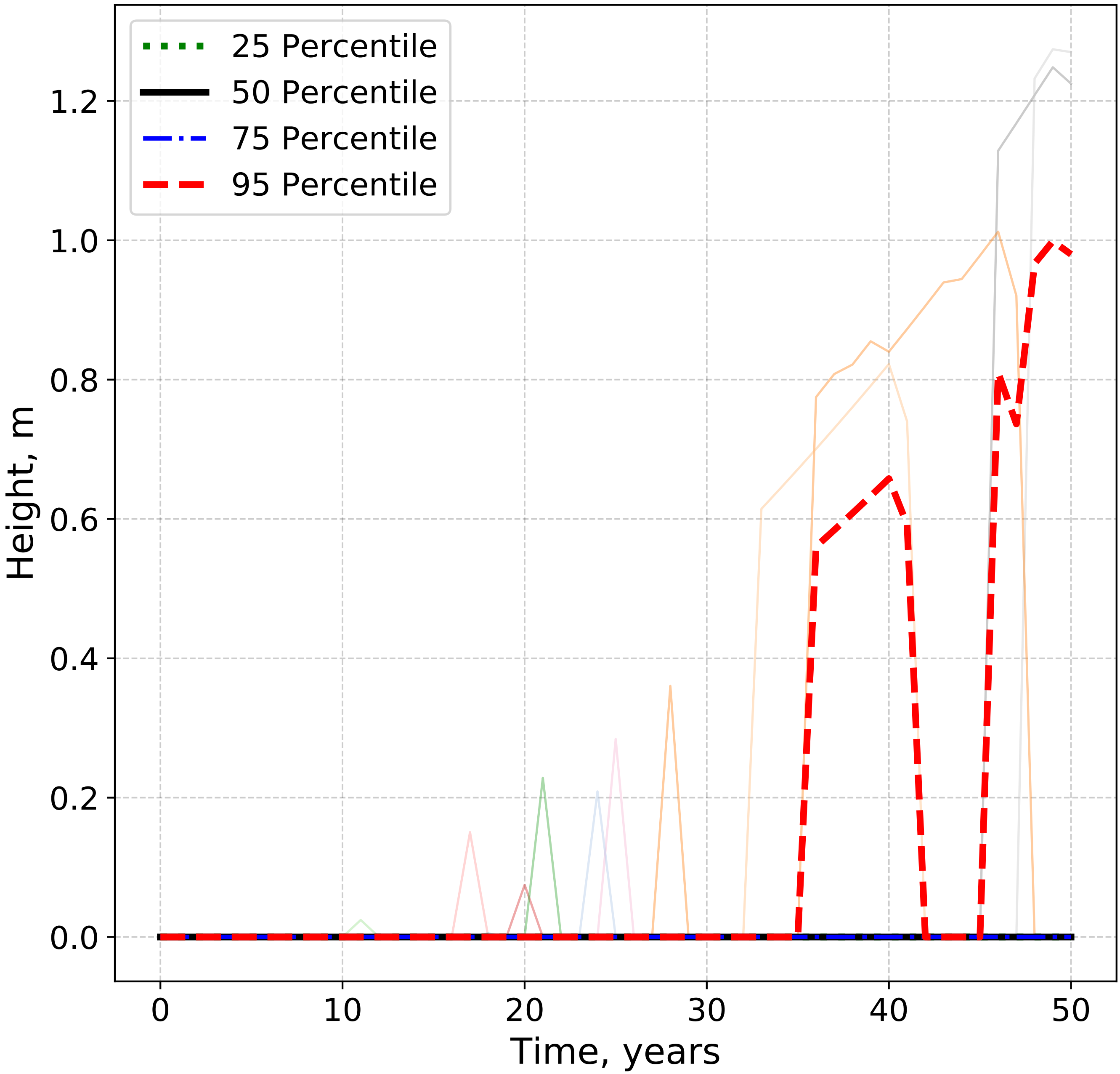

Figure C-16. TDS Impact to Aquifer 2 in the Vertical Direction. Layer 54 of the reservoir simulation was used in the IAM analysis.

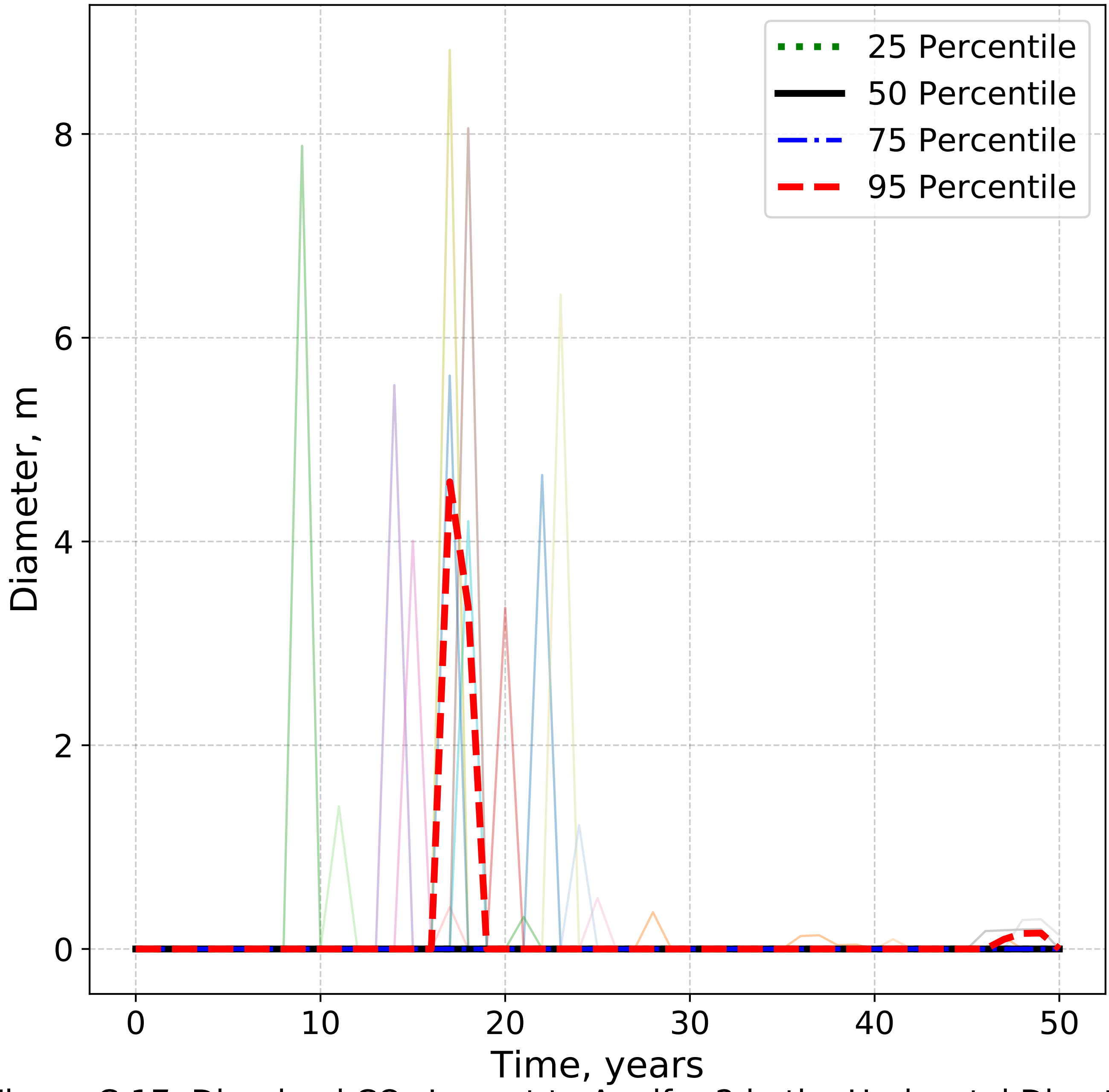

Figure C-17. Dissolved CO_2 Impact to Aquifer 2 in the Horizontal Direction. Layer 54 of the reservoir simulation was used in the IAM analysis.

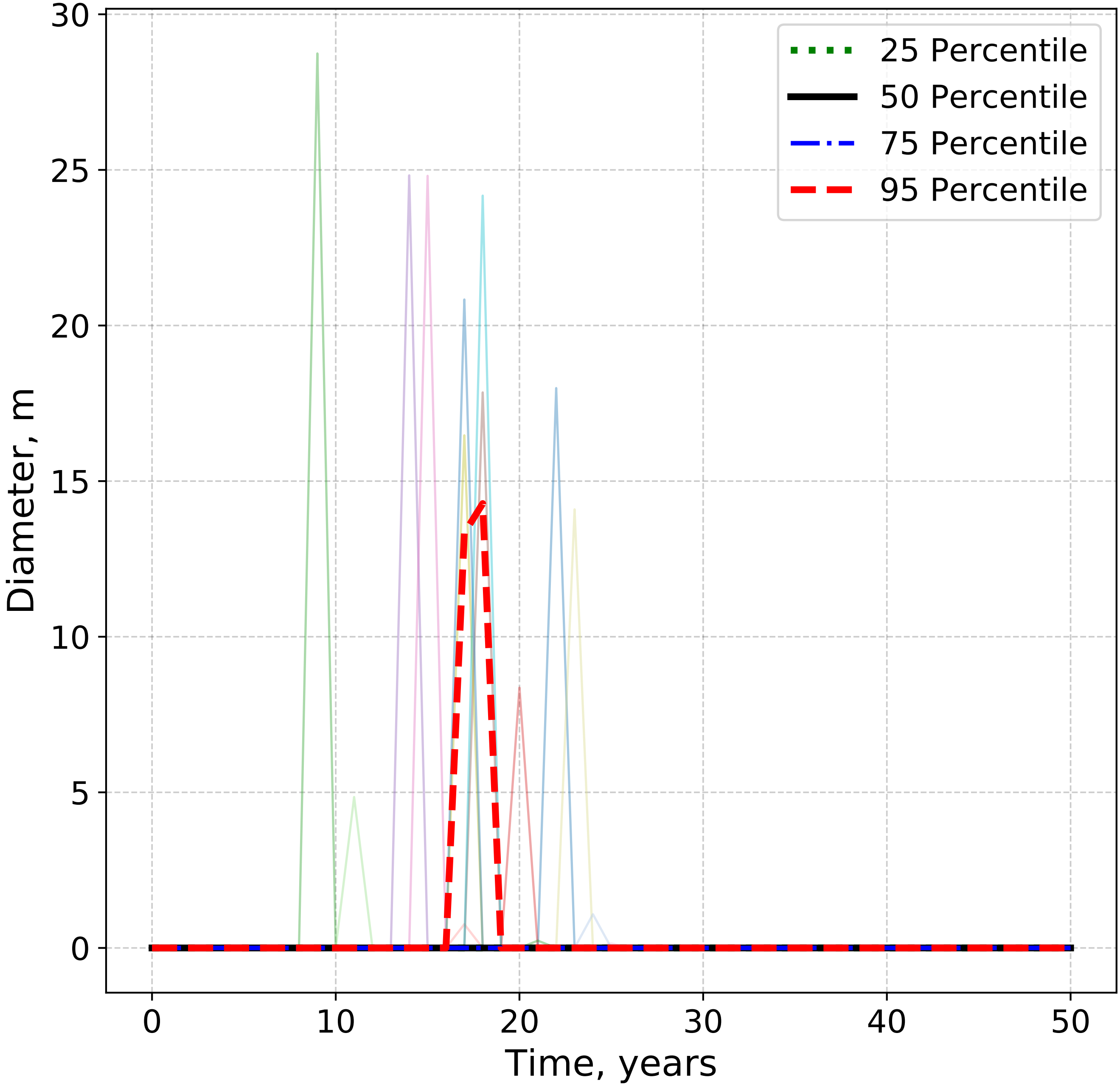

Figure C-18. Dissolved CO_2 Impact to Aquifer 2 in the Vertical Direction. Layer 54 of the reservoir simulation was used in the IAM analysis.

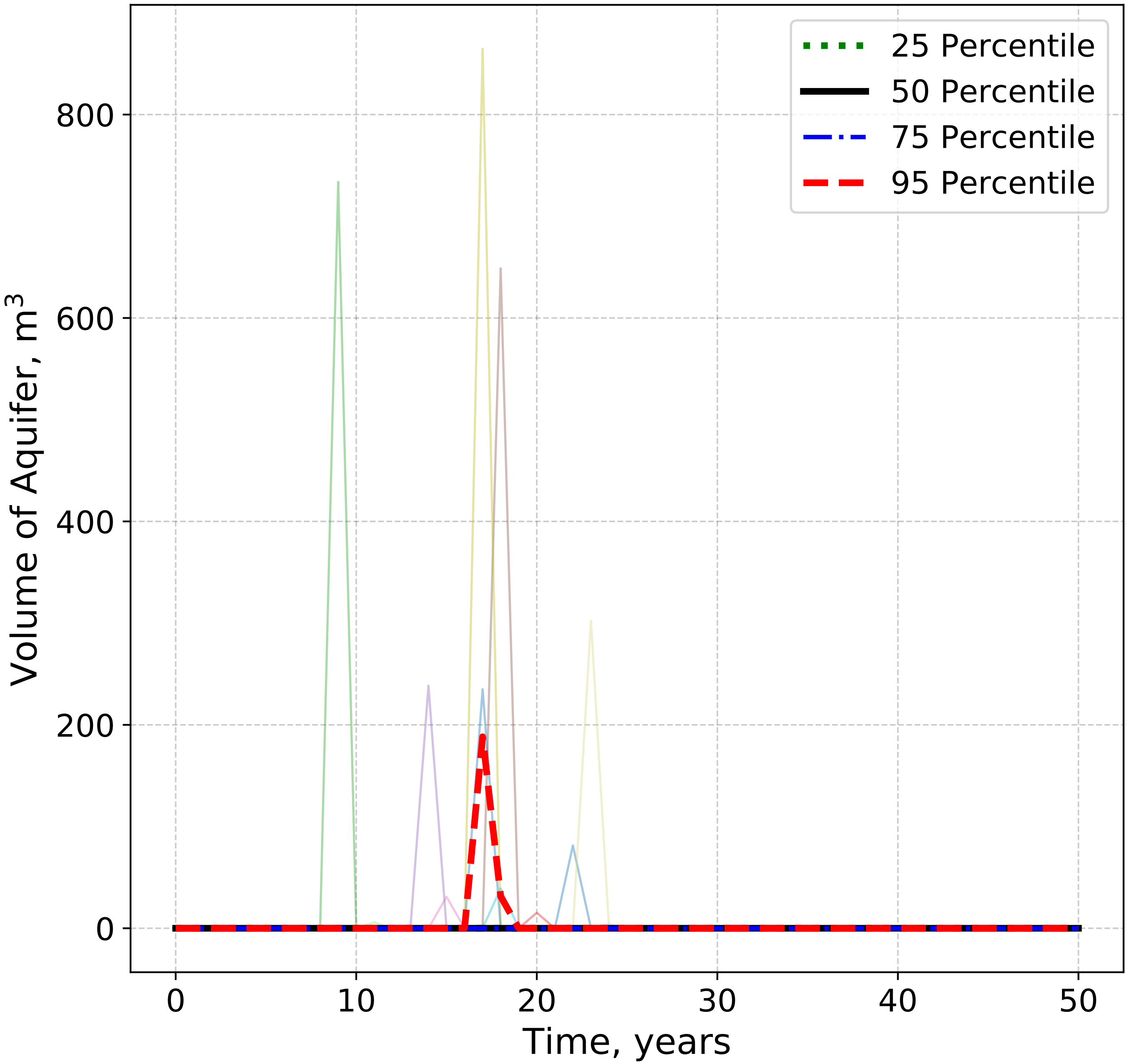

Figure C-19. pH Impact to Aquifer 2. Layer 54 of the reservoir simulation was used in the IAM analysis.

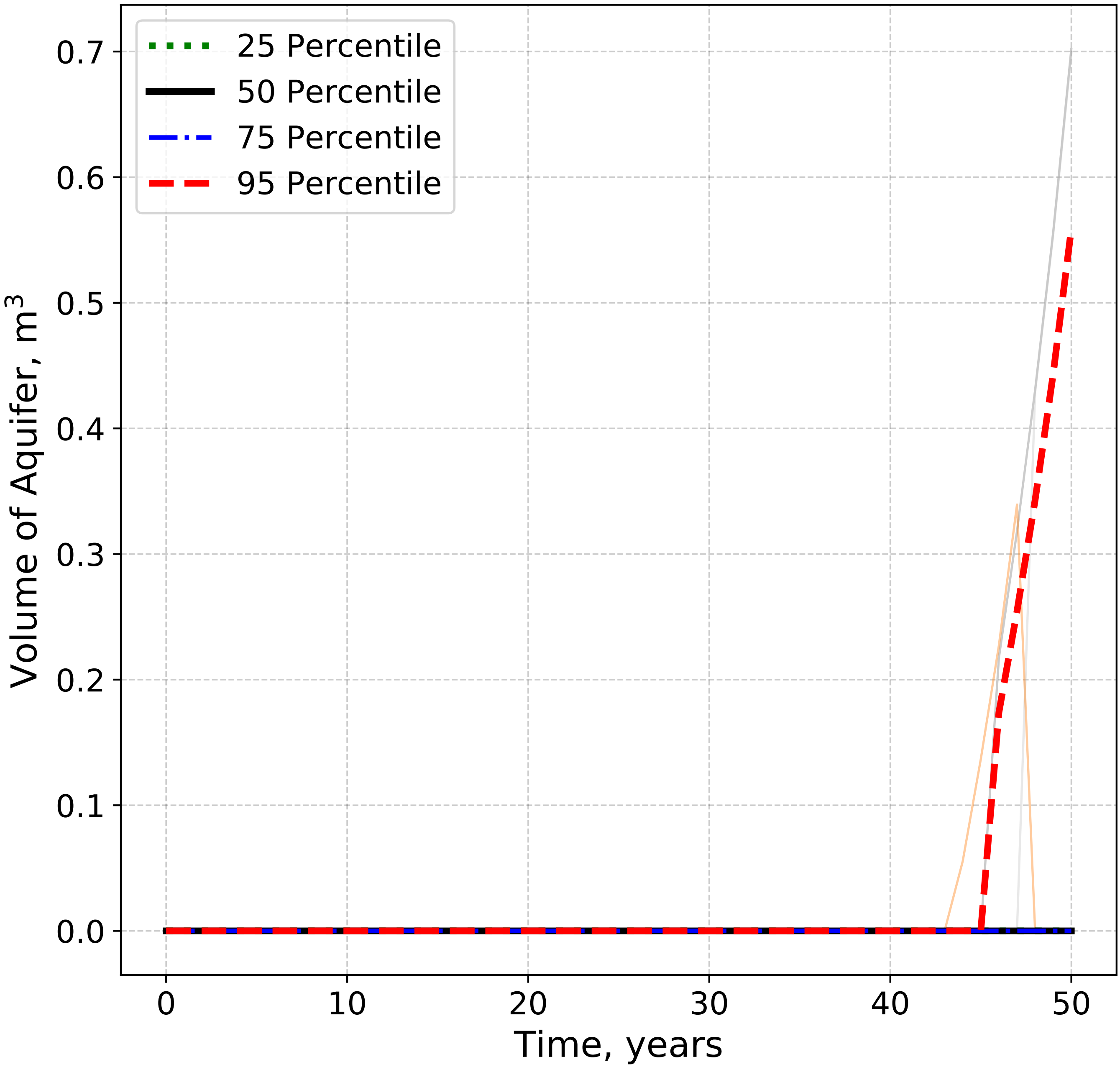

Figure C-20. Pressure Impact to Aquifer 2. Layer 54 of the reservoir simulation was used in the IAM analysis.

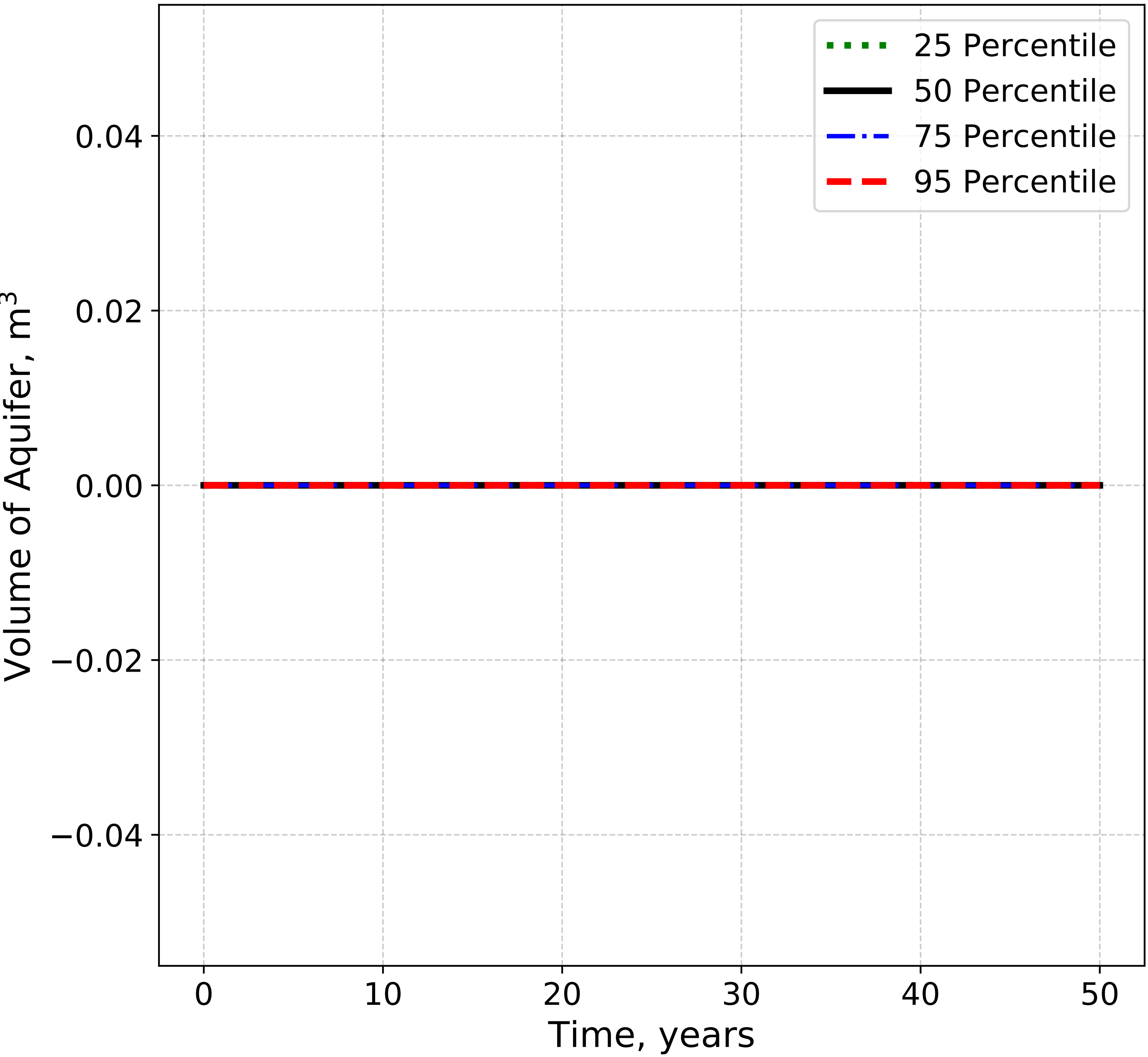

Figure C-21. TDS Impact to Aquifer 2. Layer 54 of the reservoir simulation was used in the IAM analysis.

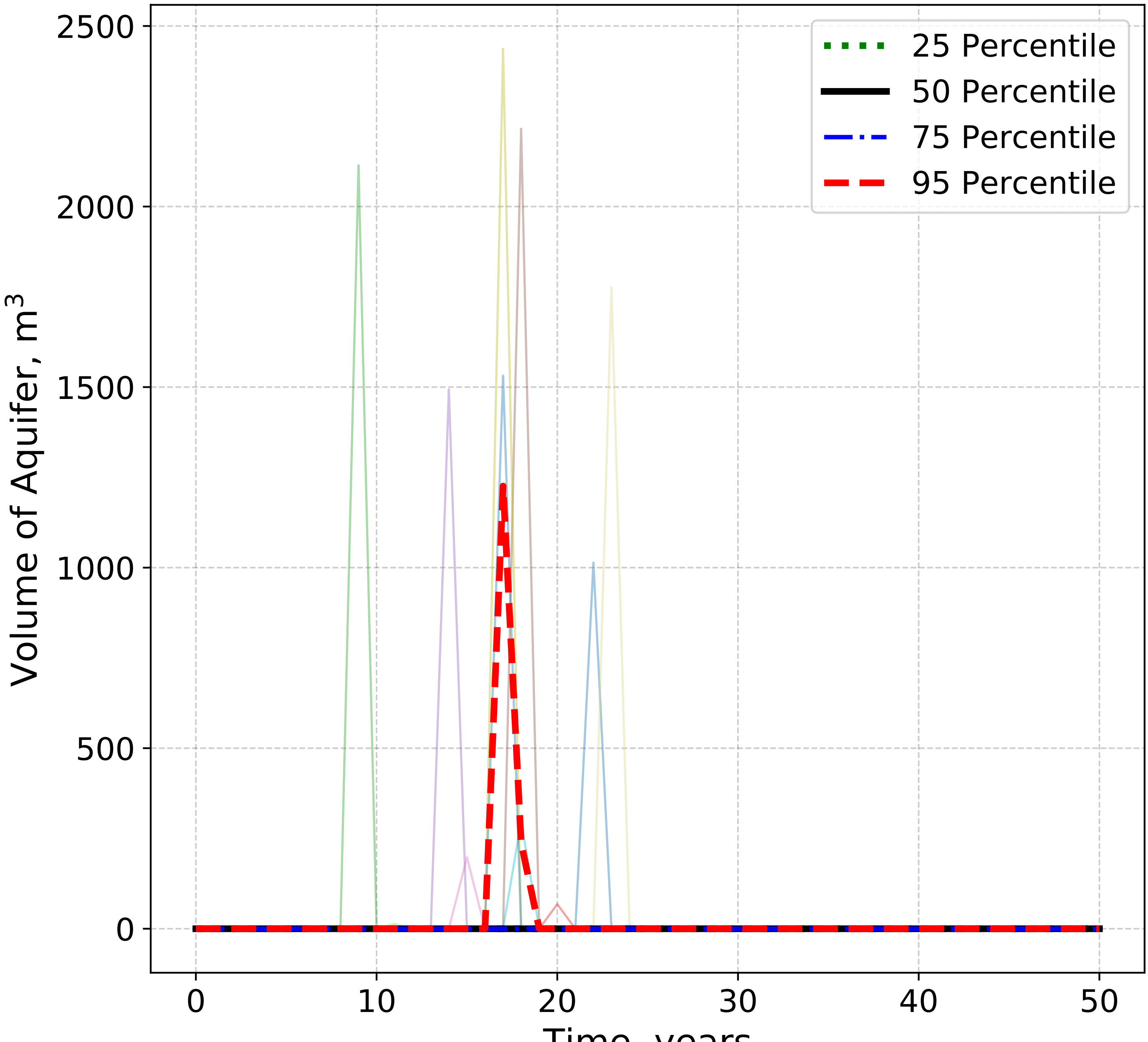

Figure C-22. Dissolved CO_2 Impact to Aquifer 2. Layer 54 of the reservoir simulation was used in the IAM analysis.

Appendix D – NRAP-Open-IAM Results for Conceptual Model with an Intermediate Thickness of Aquifer 1 at the PHH Site Based on the Reservoir Simulation Results of Layer 54

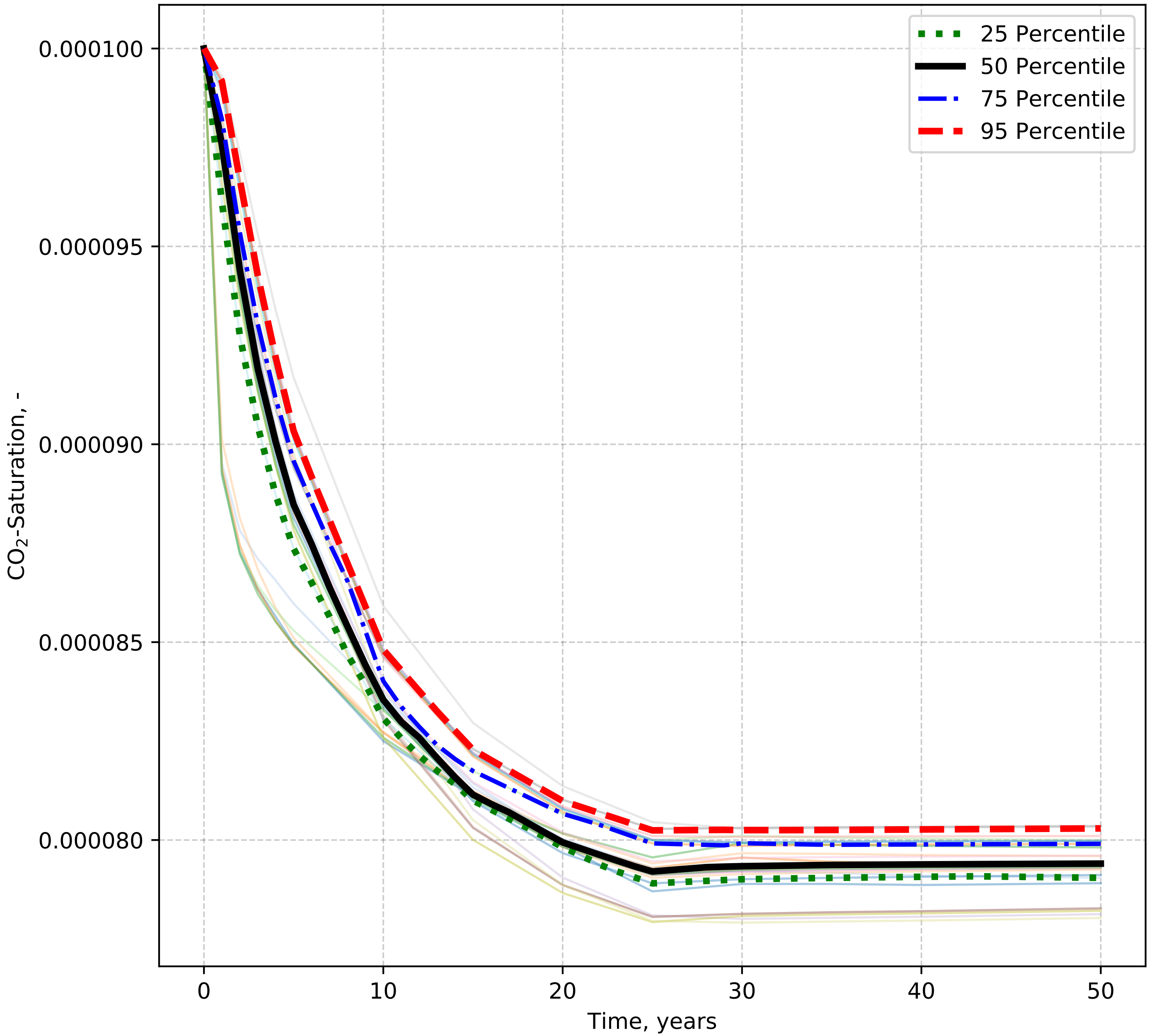

Figure D-1. Saturation History. Layer 54 of the reservoir simulation was used in the IAM analysis.

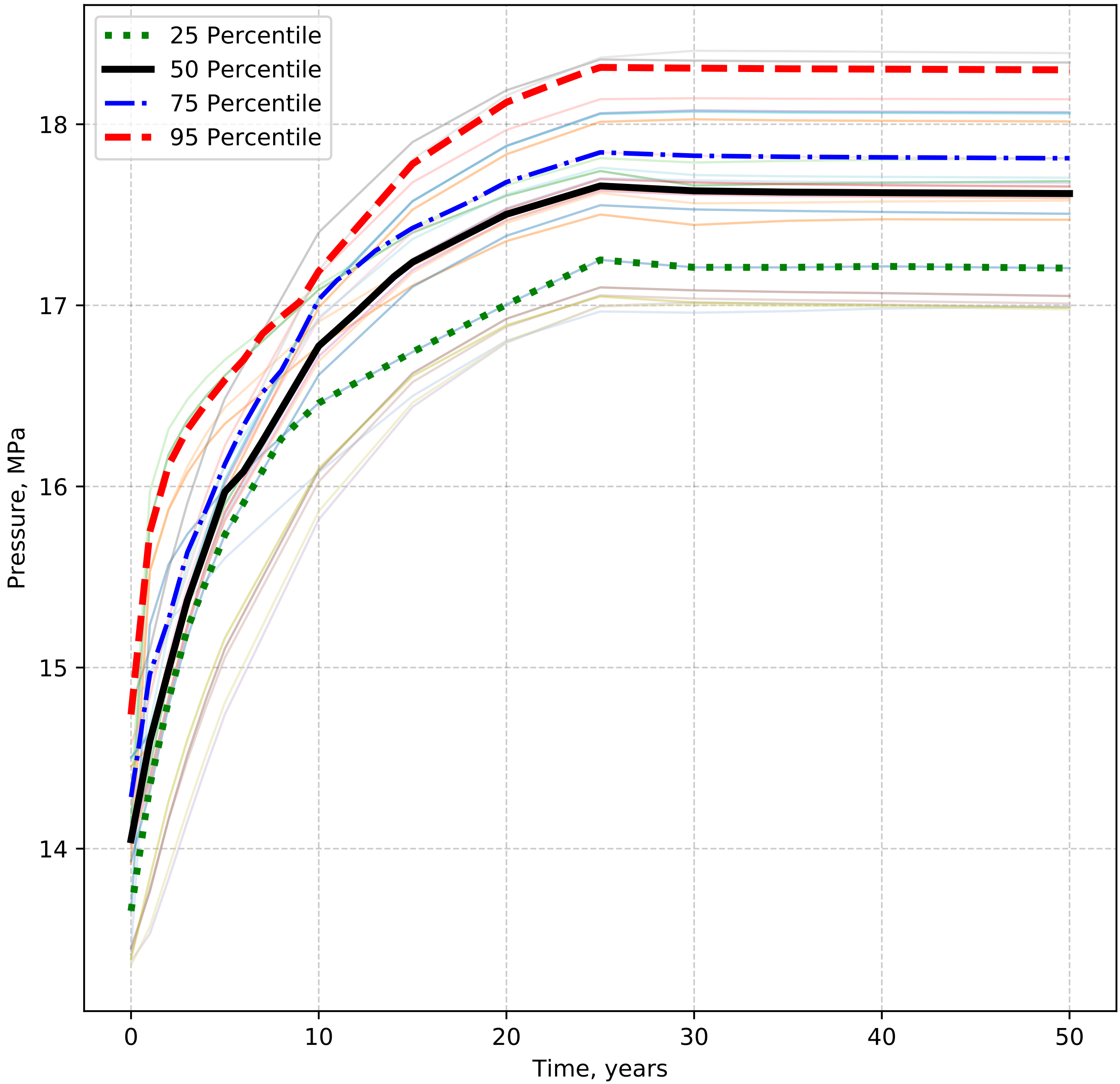

Figure D-2. Pressure History. Layer 54 of the reservoir simulation was used in the IAM analysis.

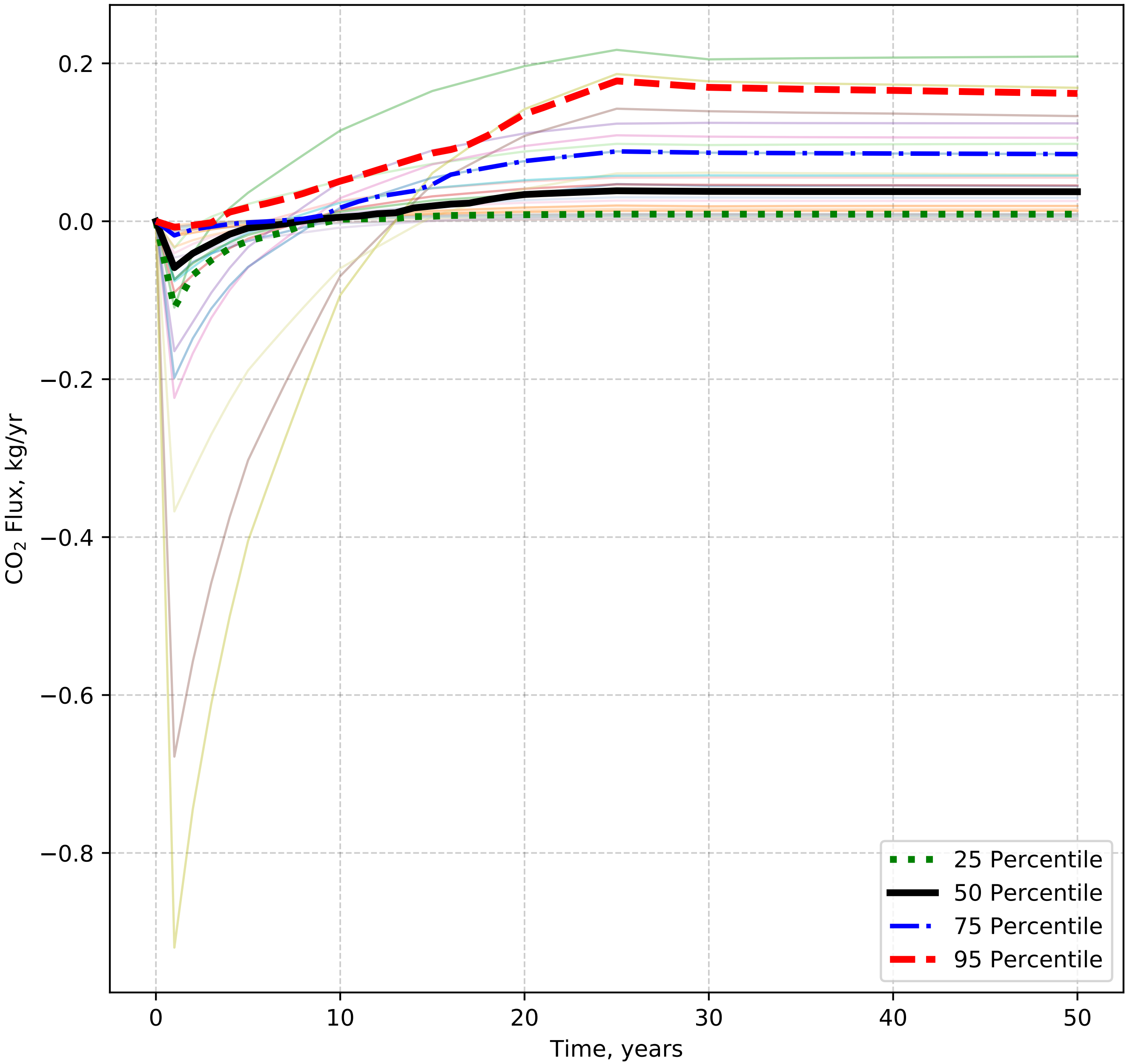

Figure D-3. CO_2 Flux to Aquifer 1. Layer 54 of the reservoir simulation was used in the IAM analysis.

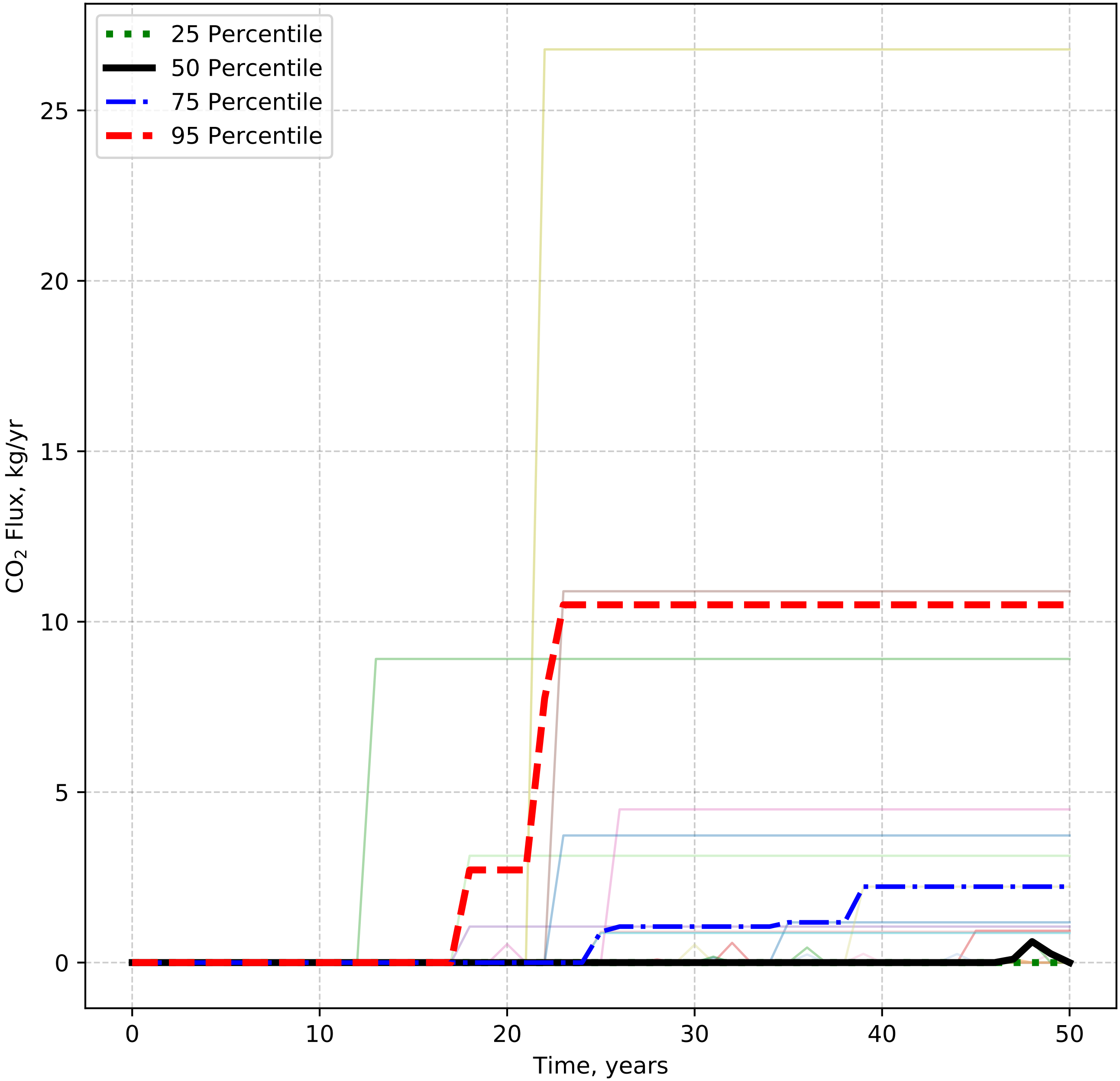

Figure D-4. CO_2 Flux to Aquifer 2. Layer 54 of the reservoir simulation was used in the IAM analysis.

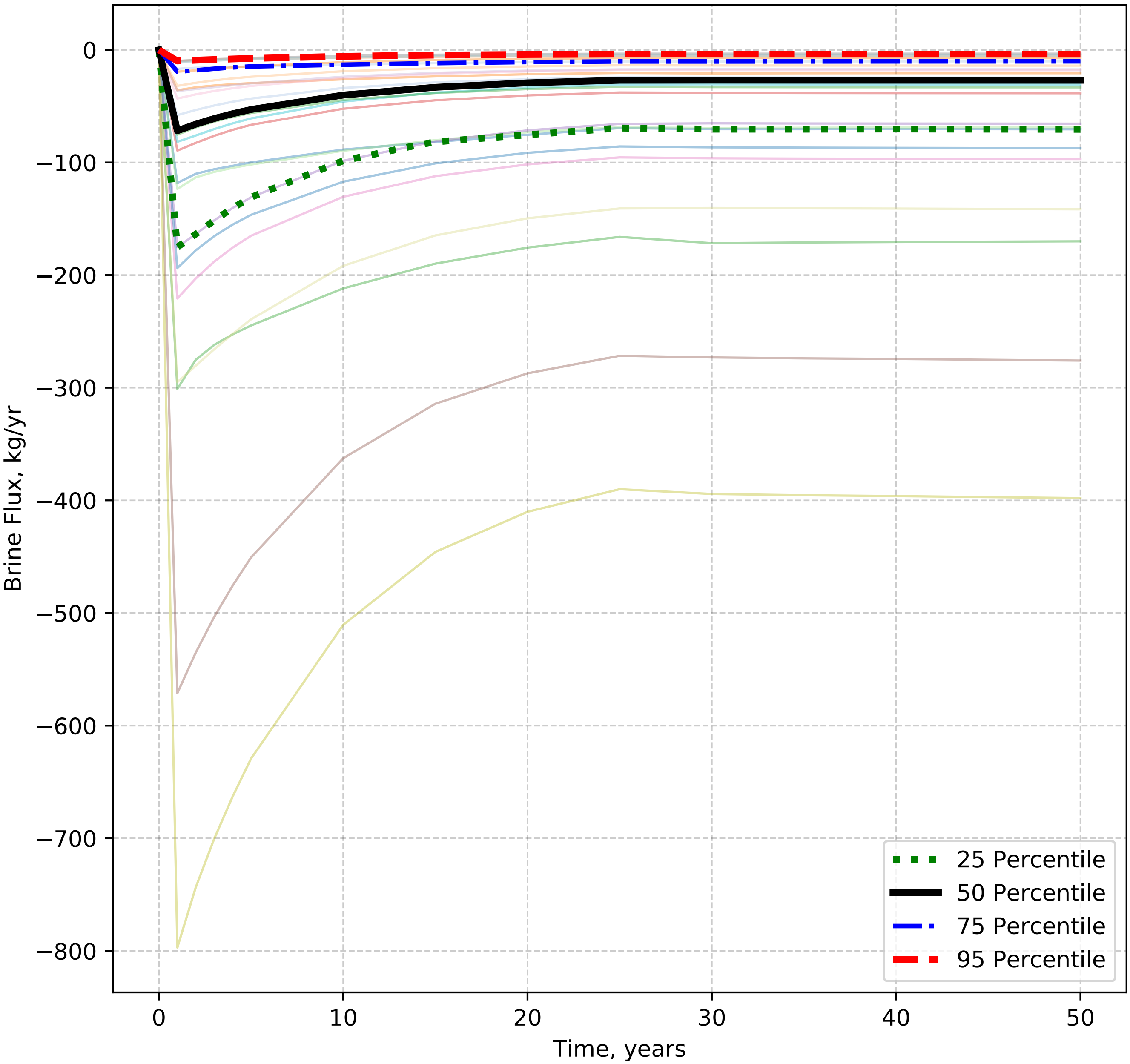

Figure D-5. Brine Flux to Aquifer 1. Layer 54 of the reservoir simulation was used in the IAM analysis.

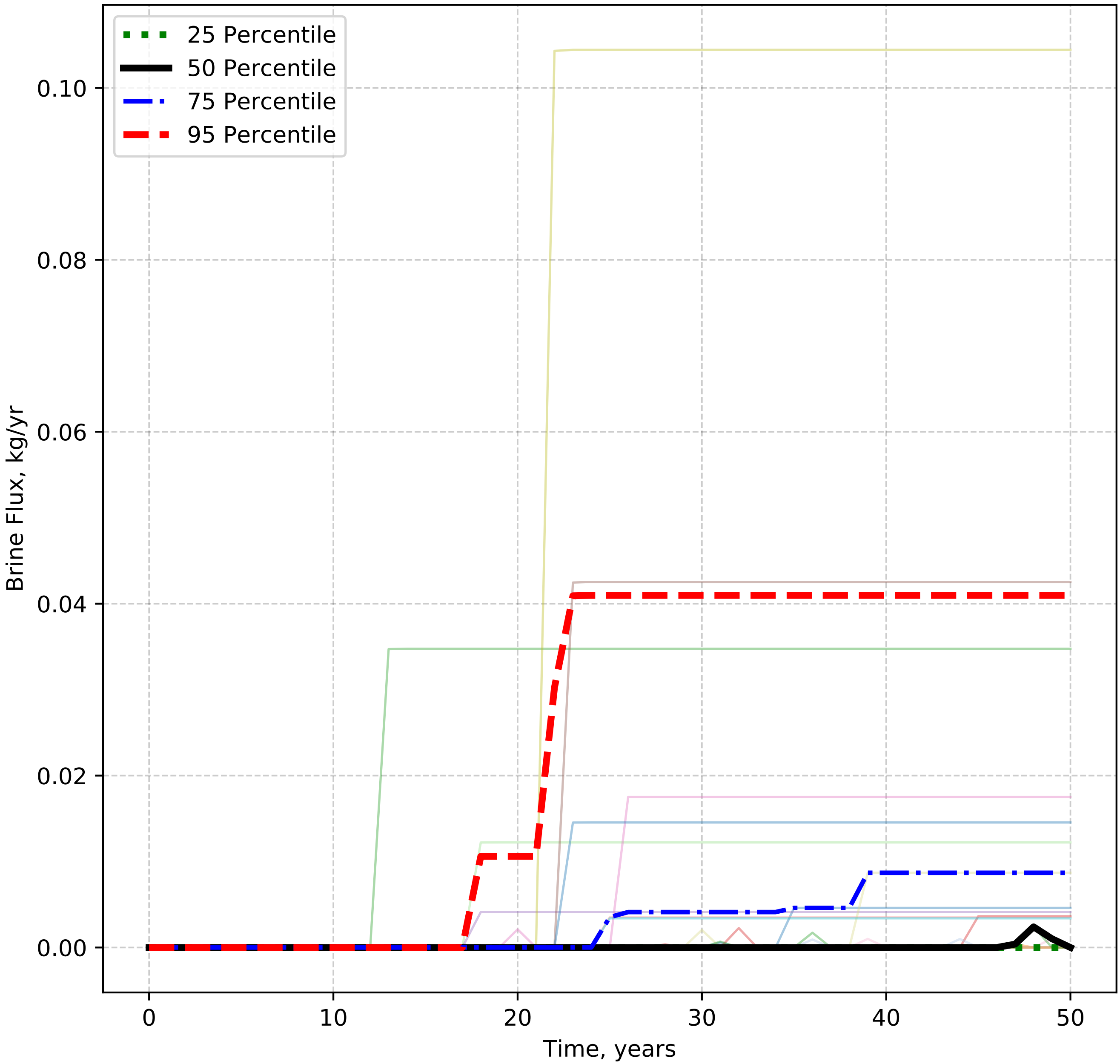

Figure D-6. Brine Flux to Aquifer 2. Layer 54 of the reservoir simulation was used in the IAM analysis.

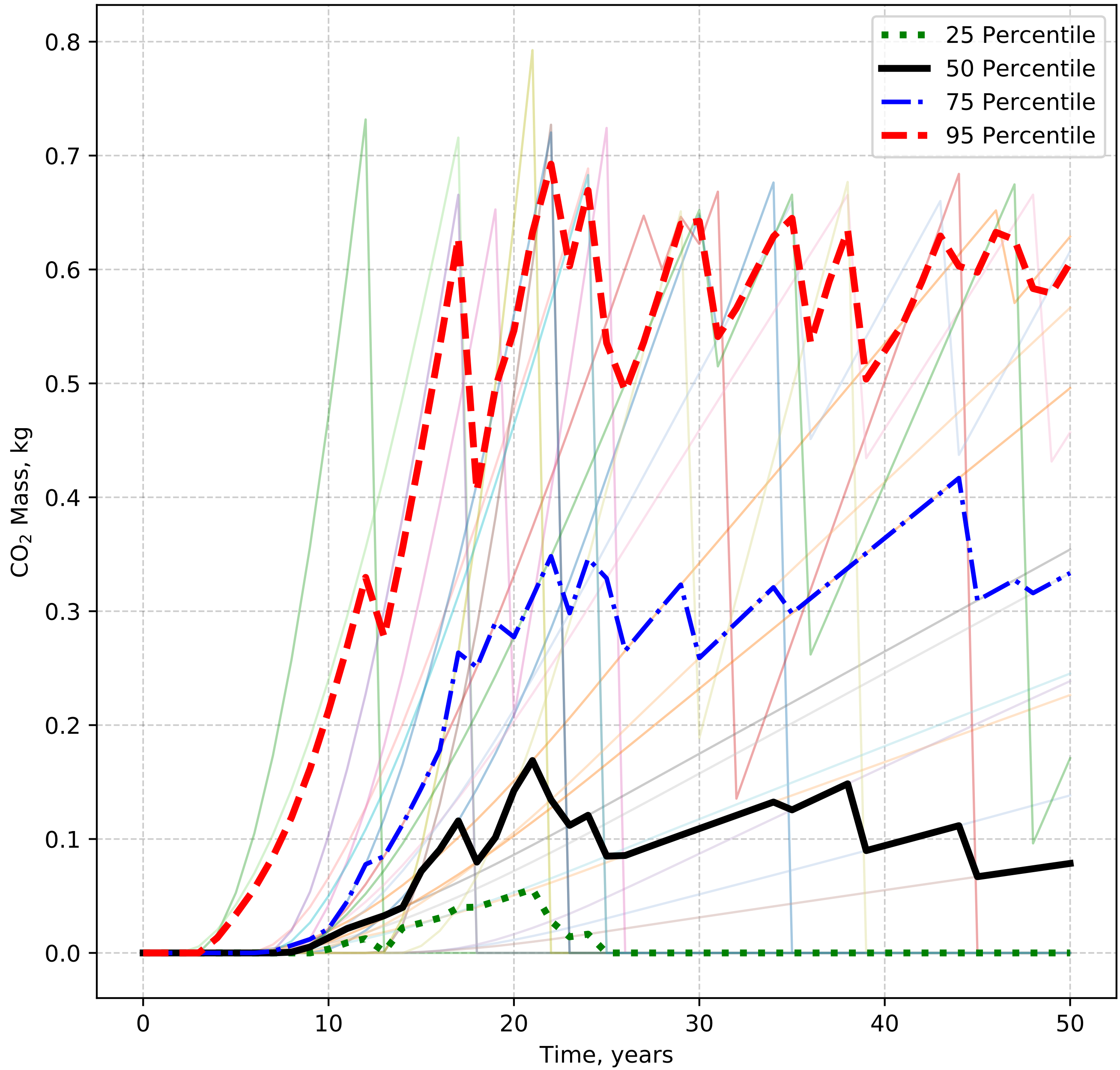

Figure D-7. CO_2 Mass to Aquifer 1. Layer 54 of the reservoir simulation was used in the IAM analysis.

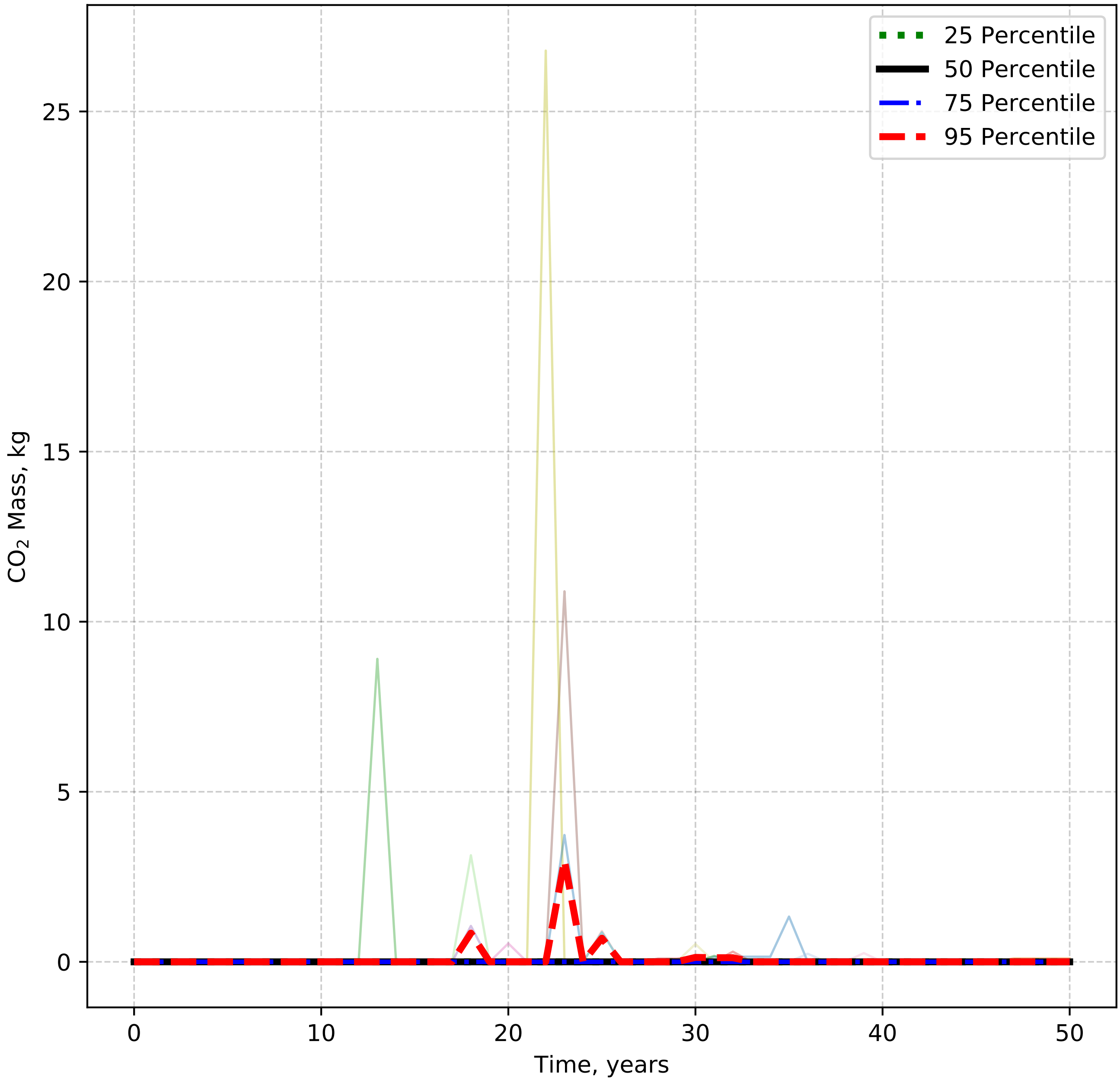

Figure D-8. CO_2 Mass to Aquifer 2. Layer 54 of the reservoir simulation was used in the IAM analysis.

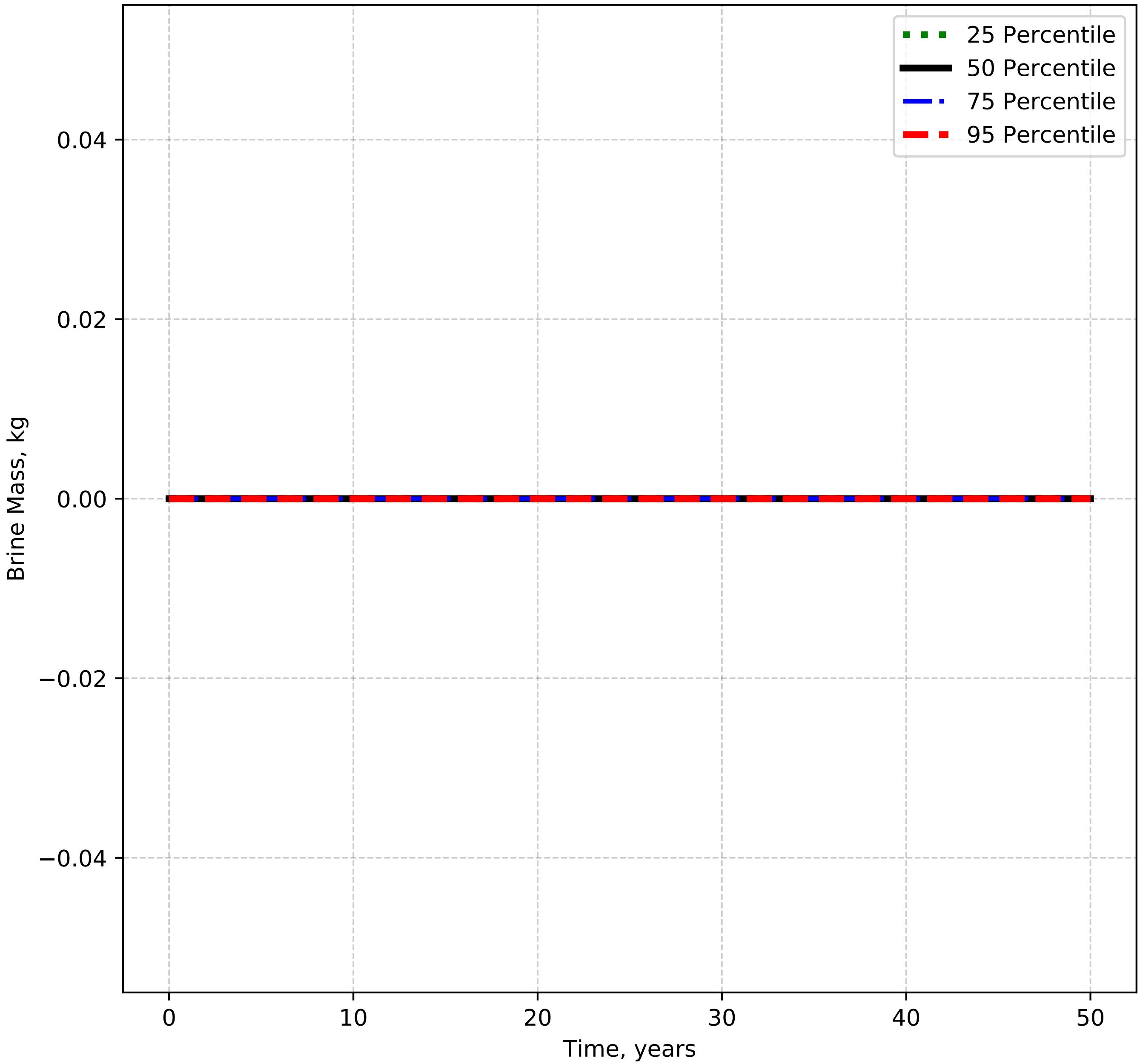

Figure D-9. Brine Mass to Aquifer 1. Layer 54 of the reservoir simulation was used in the IAM analysis.

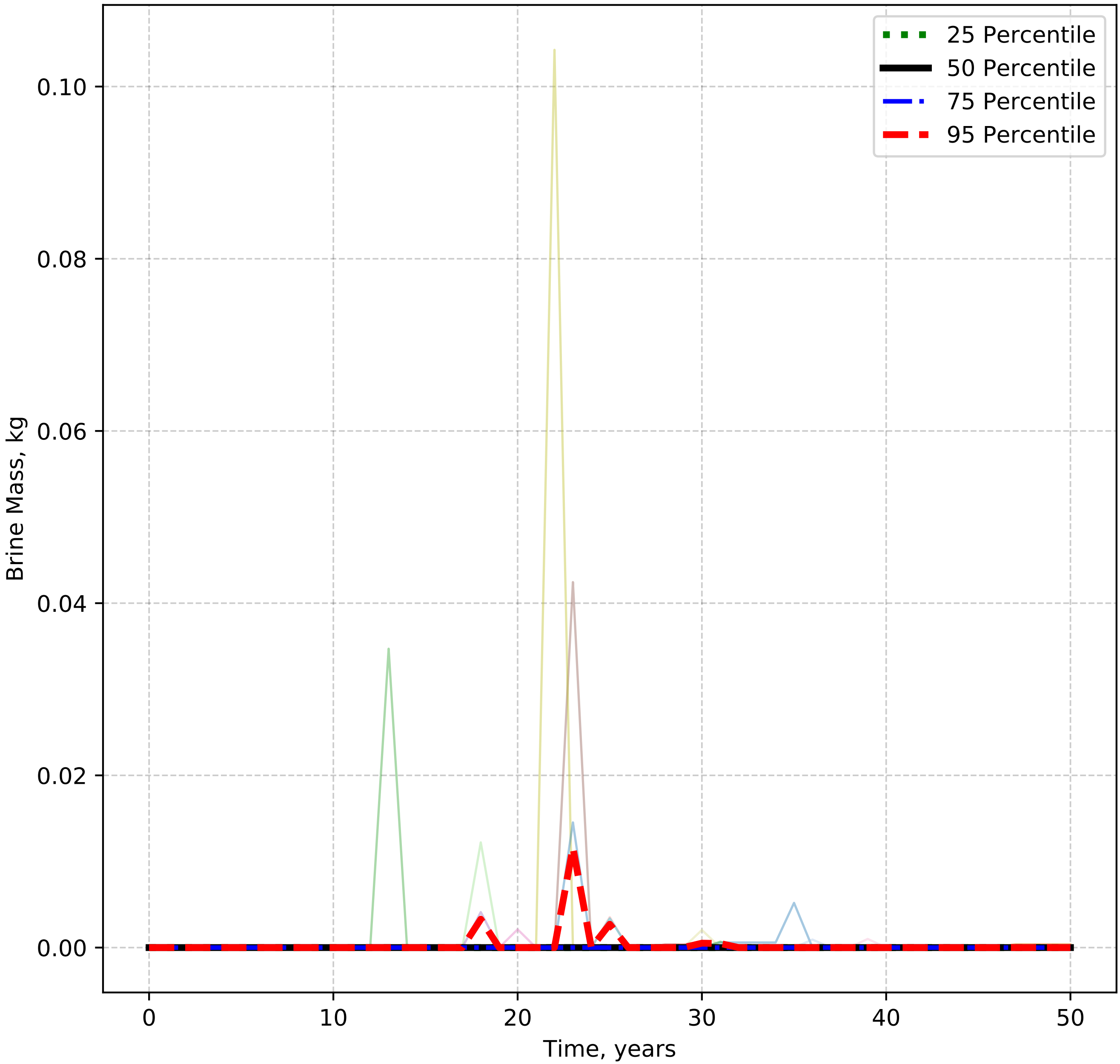

Figure D-10. Brine Mass to Aquifer 2. Layer 54 of the reservoir simulation was used in the IAM analysis.

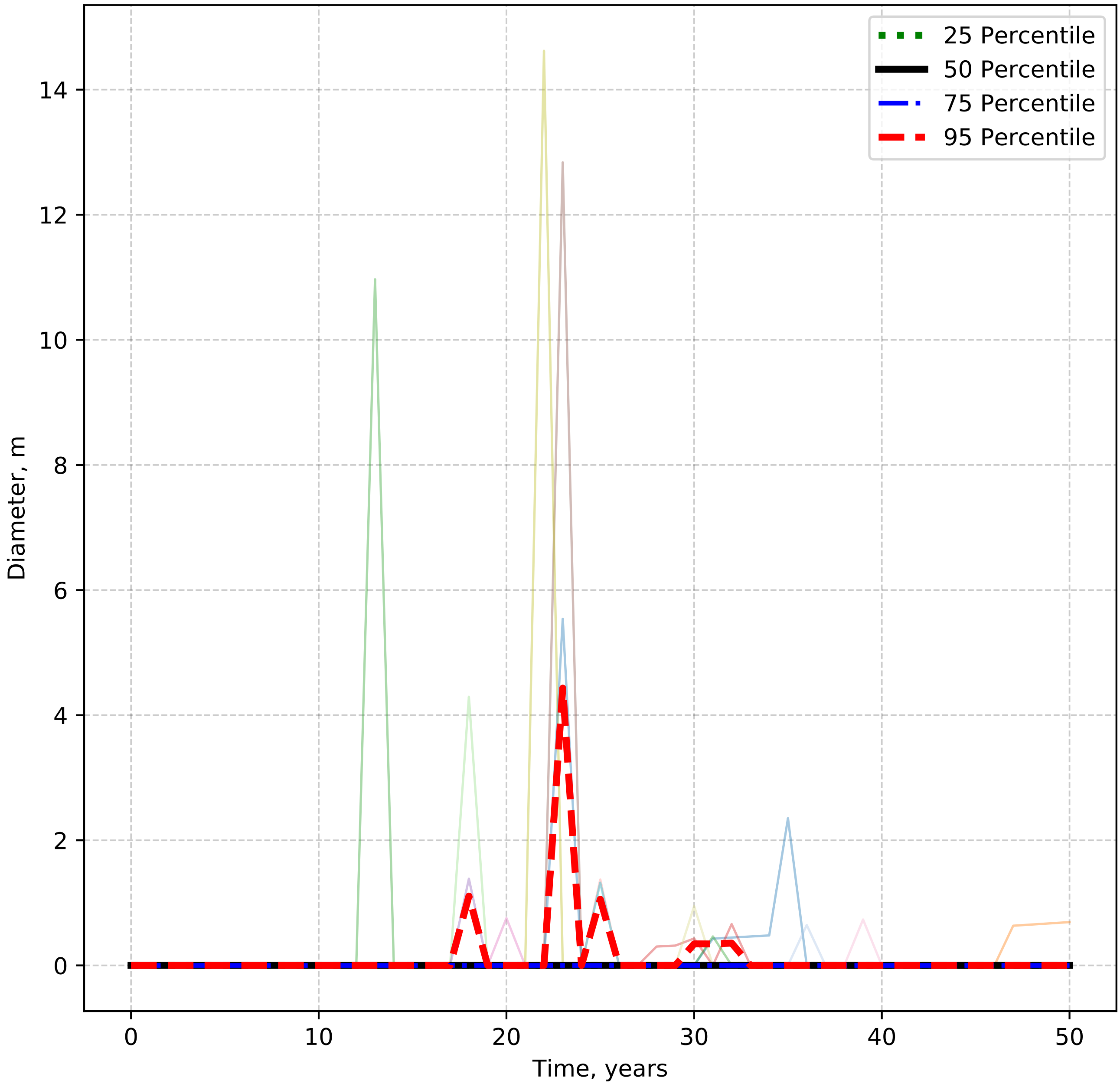

Figure D-11. pH Impact to Aquifer 2 in the Horizontal Direction. Layer 54 of the reservoir simulation was used in the IAM analysis.

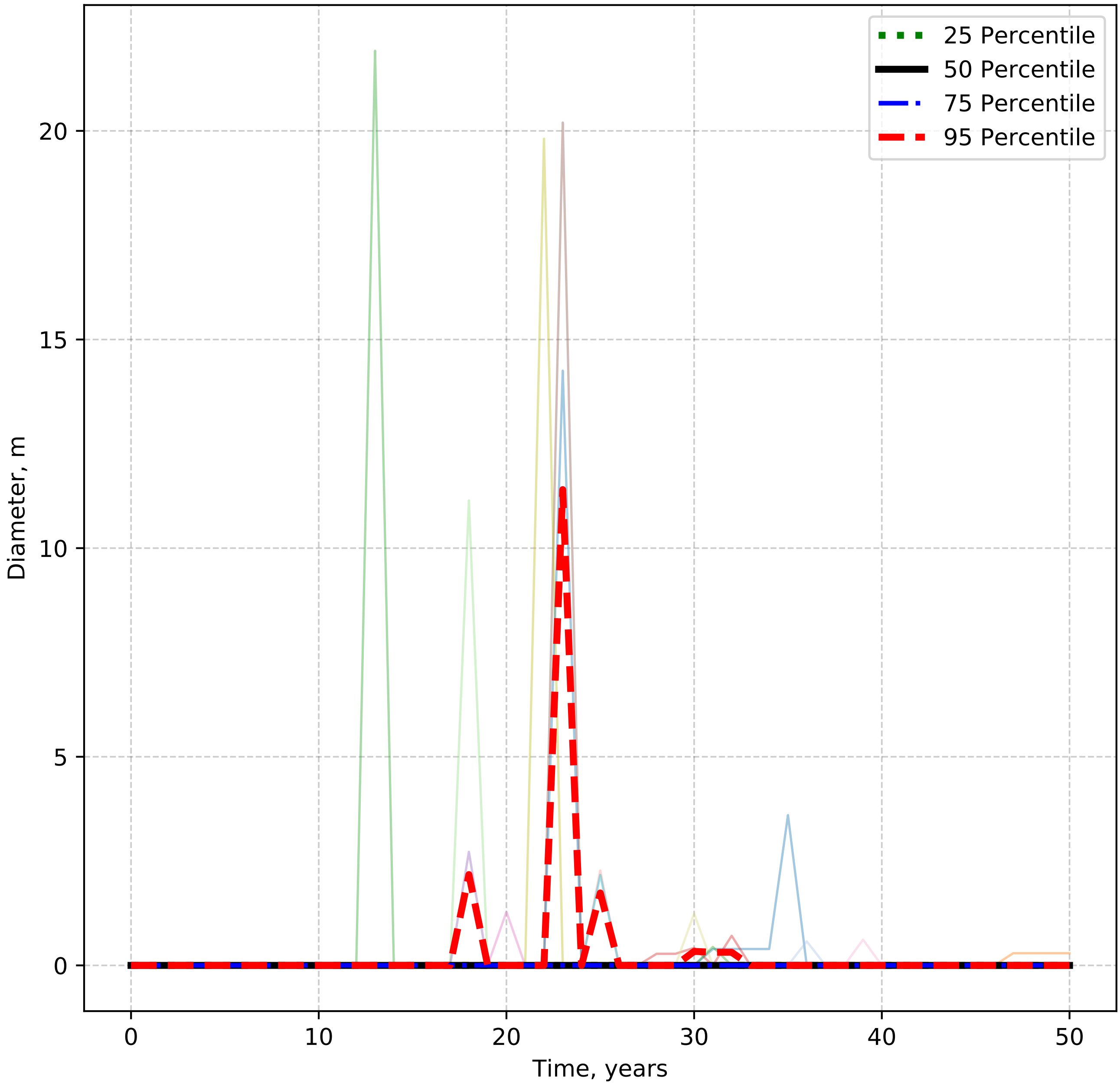

Figure D-12. pH Impact to Aquifer 2 in the Vertical Direction. Layer 54 of the reservoir simulation was used in the IAM analysis.

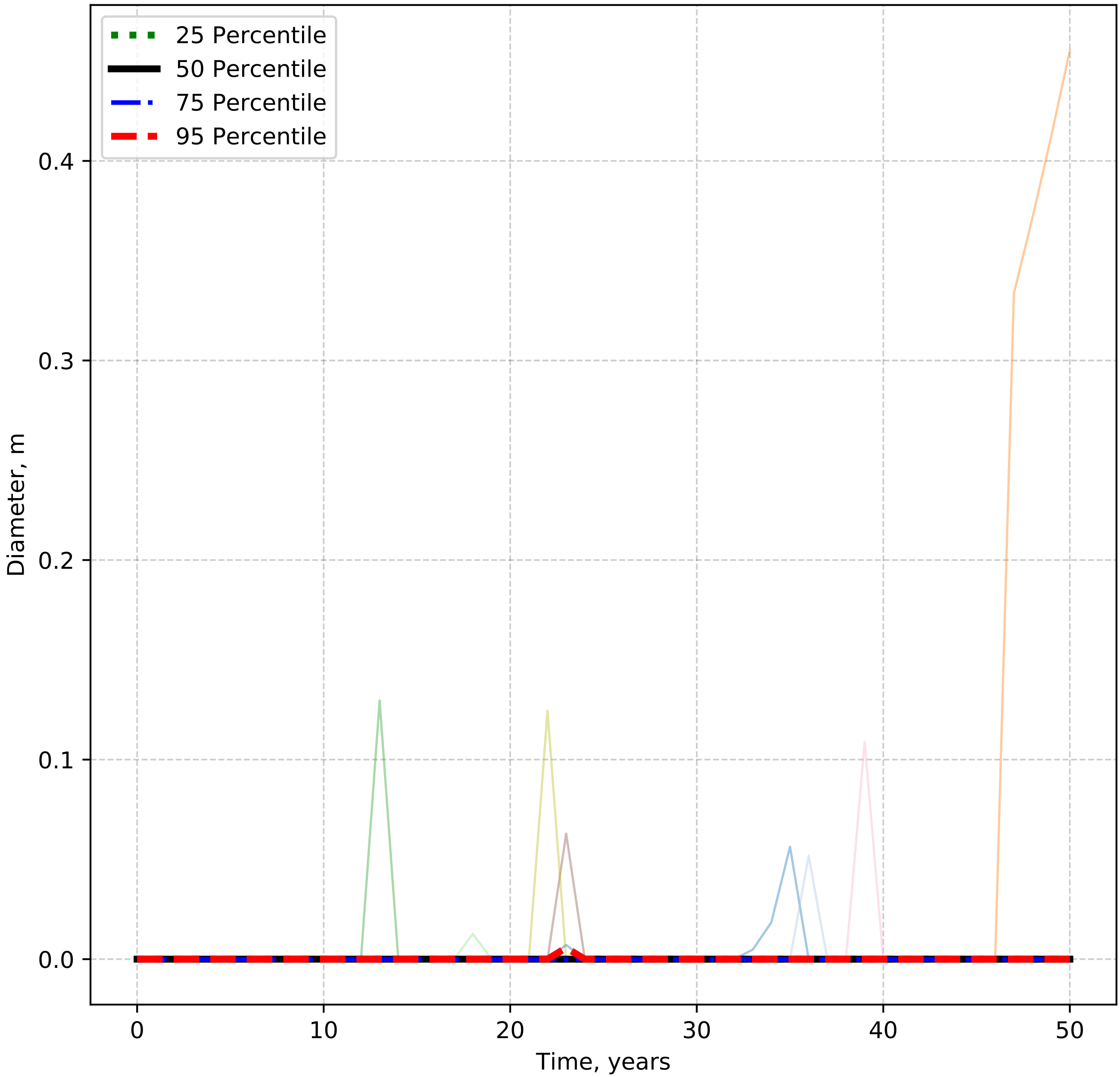

Figure D-13. Pressure Impact to Aquifer 2 in the Horizontal Direction. Layer 54 of the reservoir simulation was used in the IAM analysis.

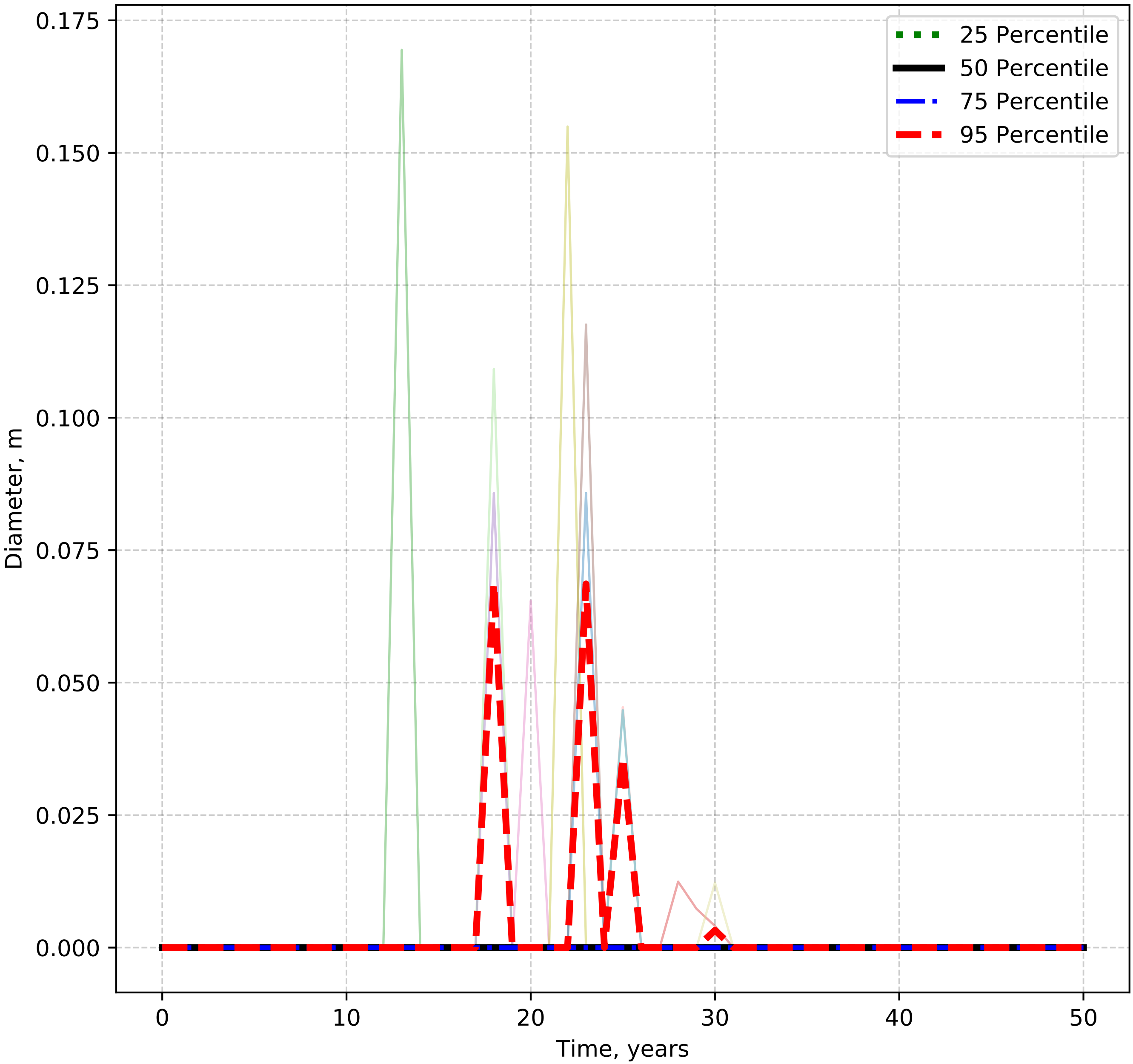

Figure D-14. Pressure Impact to Aquifer 2 in the Vertical Direction. Layer 54 of the reservoir simulation was used in the IAM analysis.

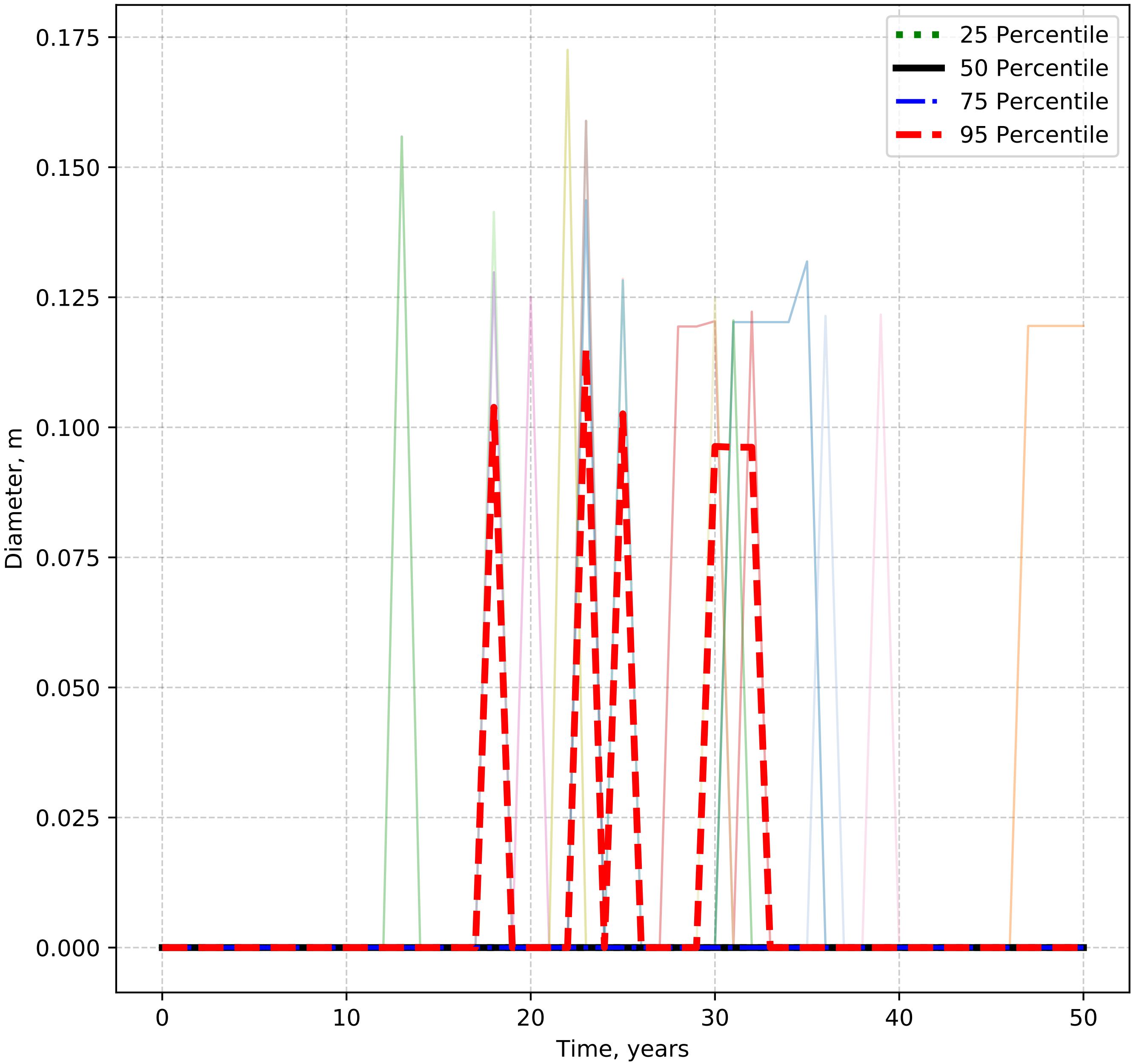

Figure D-15. TDS Impact to Aquifer 2 in the Horizontal Direction. Layer 54 of the reservoir simulation was used in the IAM analysis.

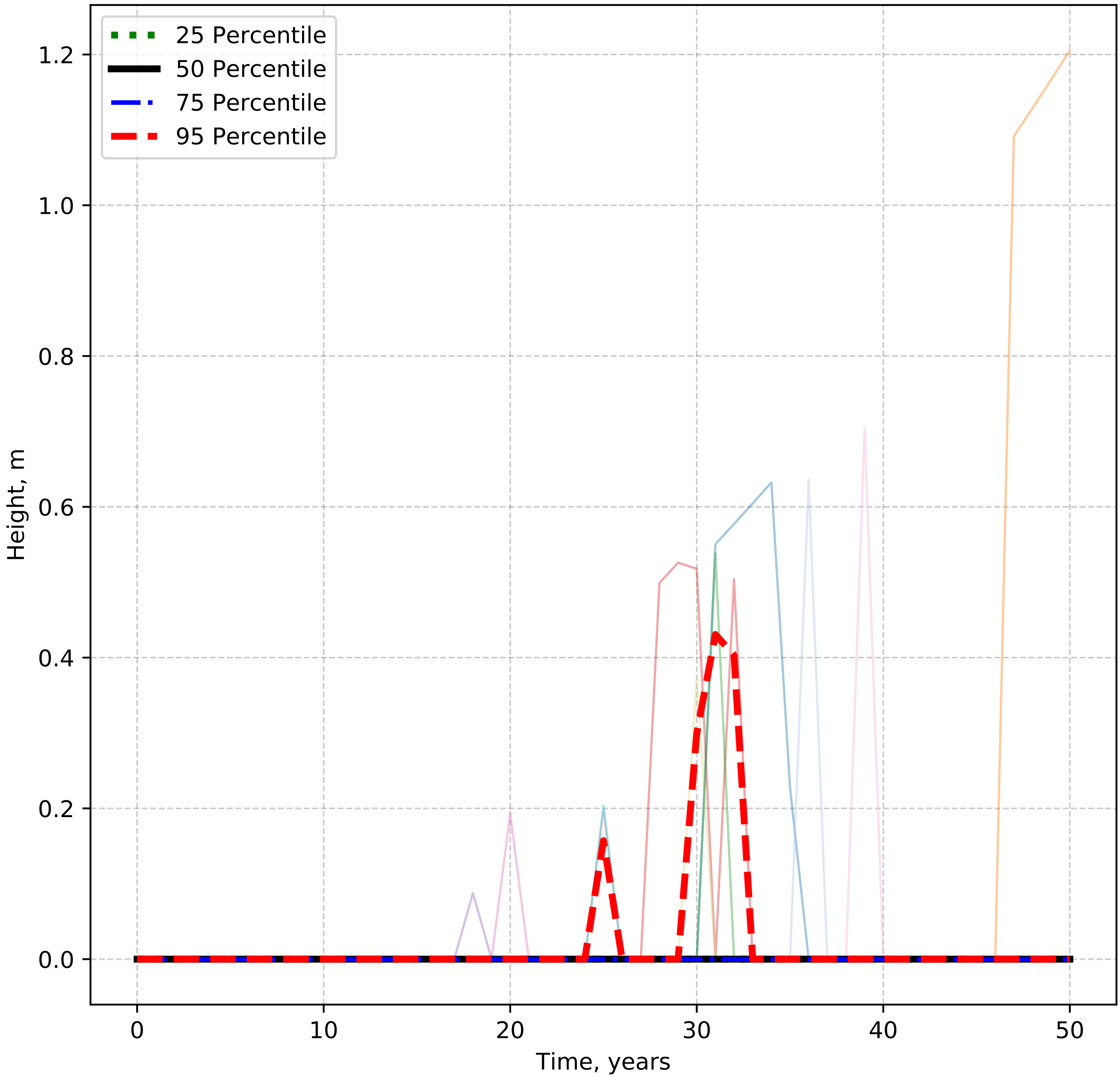

Figure D-16. TDS Impact to Aquifer 2 in the Vertical Direction. Layer 54 of the reservoir simulation was used in the IAM analysis.

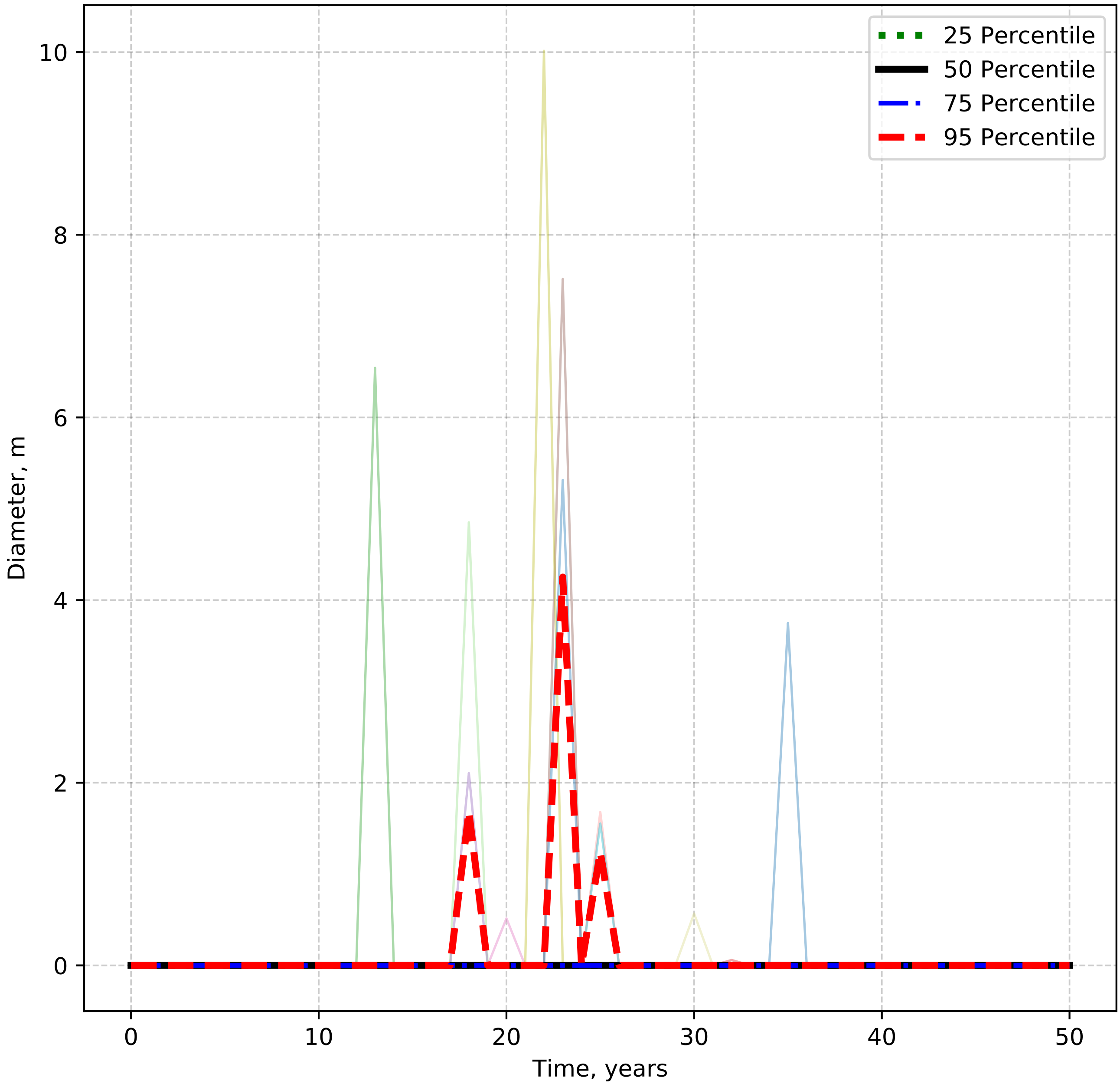

Figure D-17. Dissolved CO_2 Impact to Aquifer 2 in the Horizontal Direction. Layer 54 of the reservoir simulation was used in the IAM analysis.

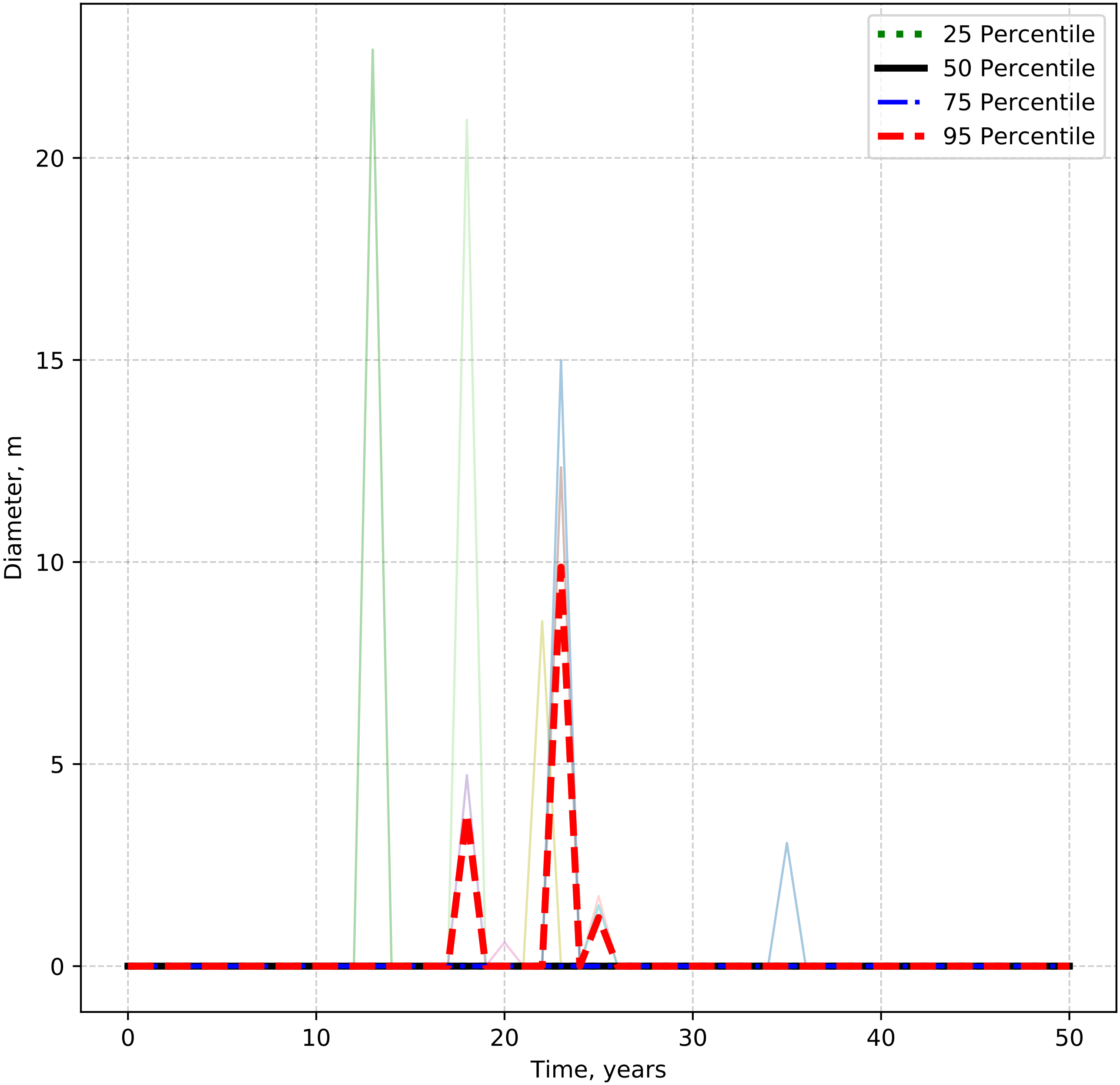

Figure D-18. Dissolved CO_2 Impact to Aquifer 2 in the Vertical Direction. Layer 54 of the reservoir simulation was used in the IAM analysis.

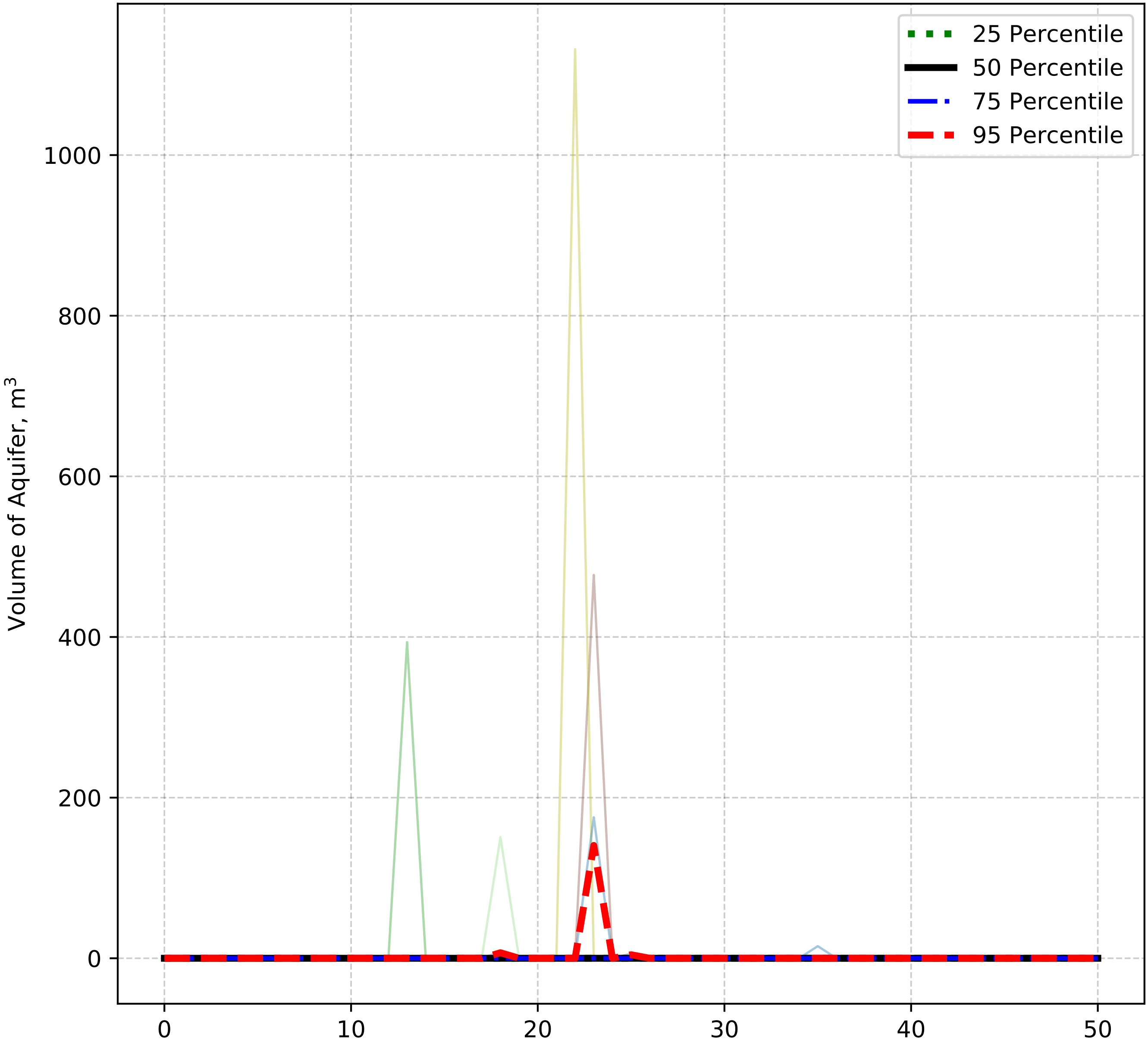

Figure D-19. pH Impact to Aquifer 2. Layer 54 of the reservoir simulation was used in the IAM analysis.

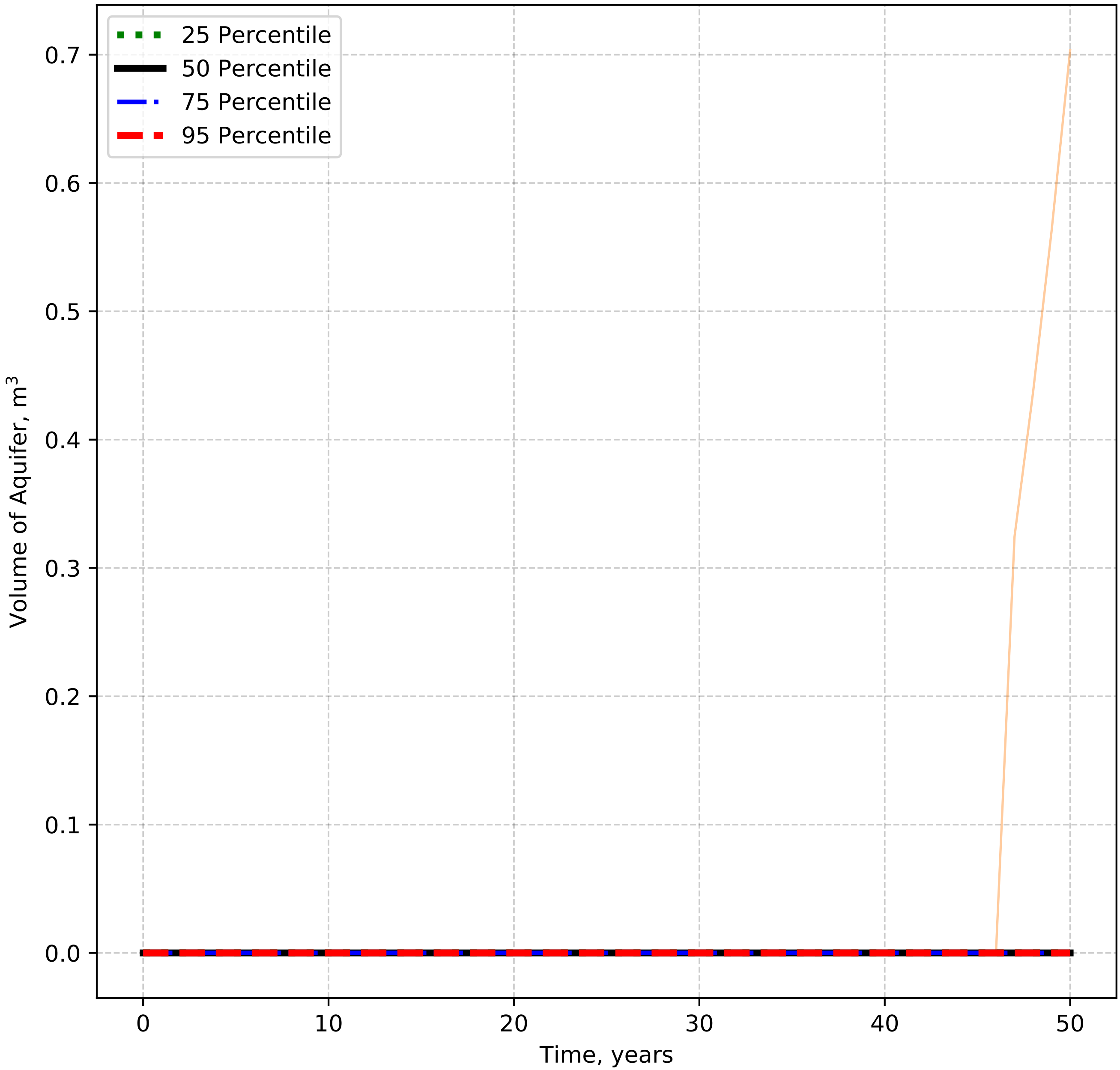

Figure D-20. Pressure Impact to Aquifer 2. Layer 54 of the reservoir simulation was used in the IAM analysis.

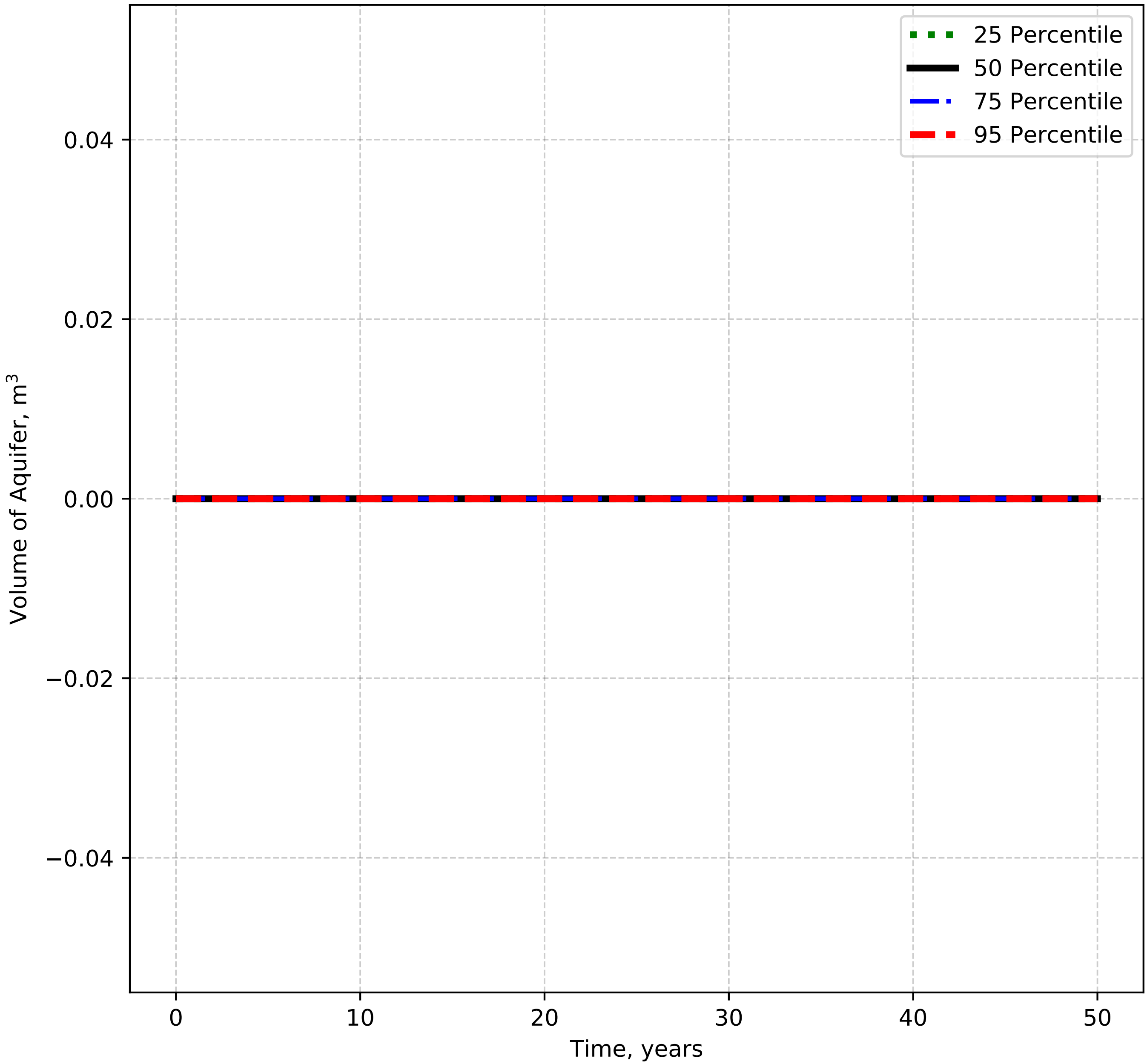

Figure D-21. TDS Impact to Aquifer 2. Layer 54 of the reservoir simulation was used in the IAM analysis.

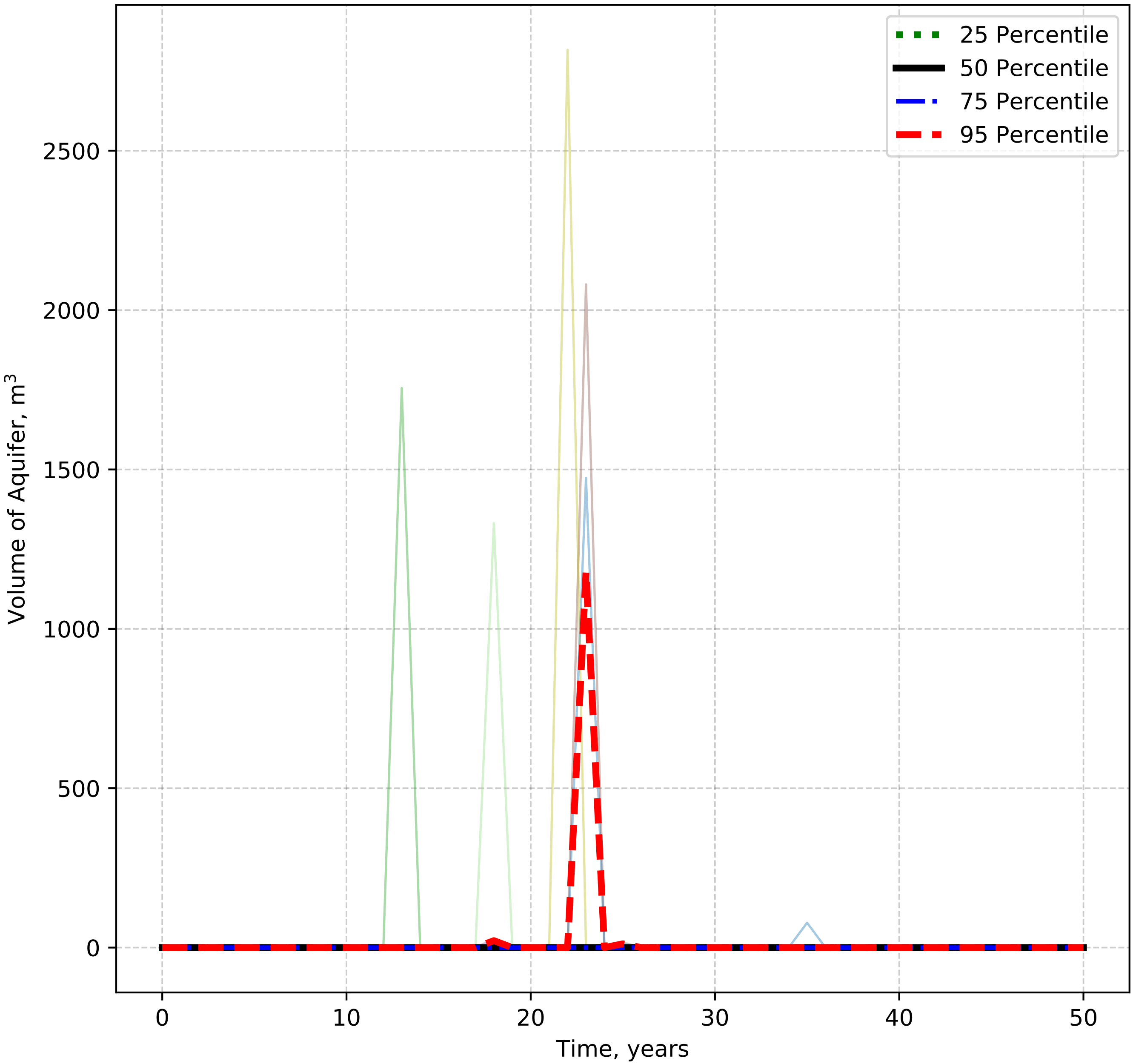

Figure D-22. Dissolved CO_2 Impact to Aquifer 2. Layer 54 of the reservoir simulation was used in the IAM analysis.

Appendix E – NRAP-Open-IAM Results for Conceptual Model with a Small Thickness of Aquifer 1 at the PHH Site Based on the Reservoir Simulation Results of Layer 54

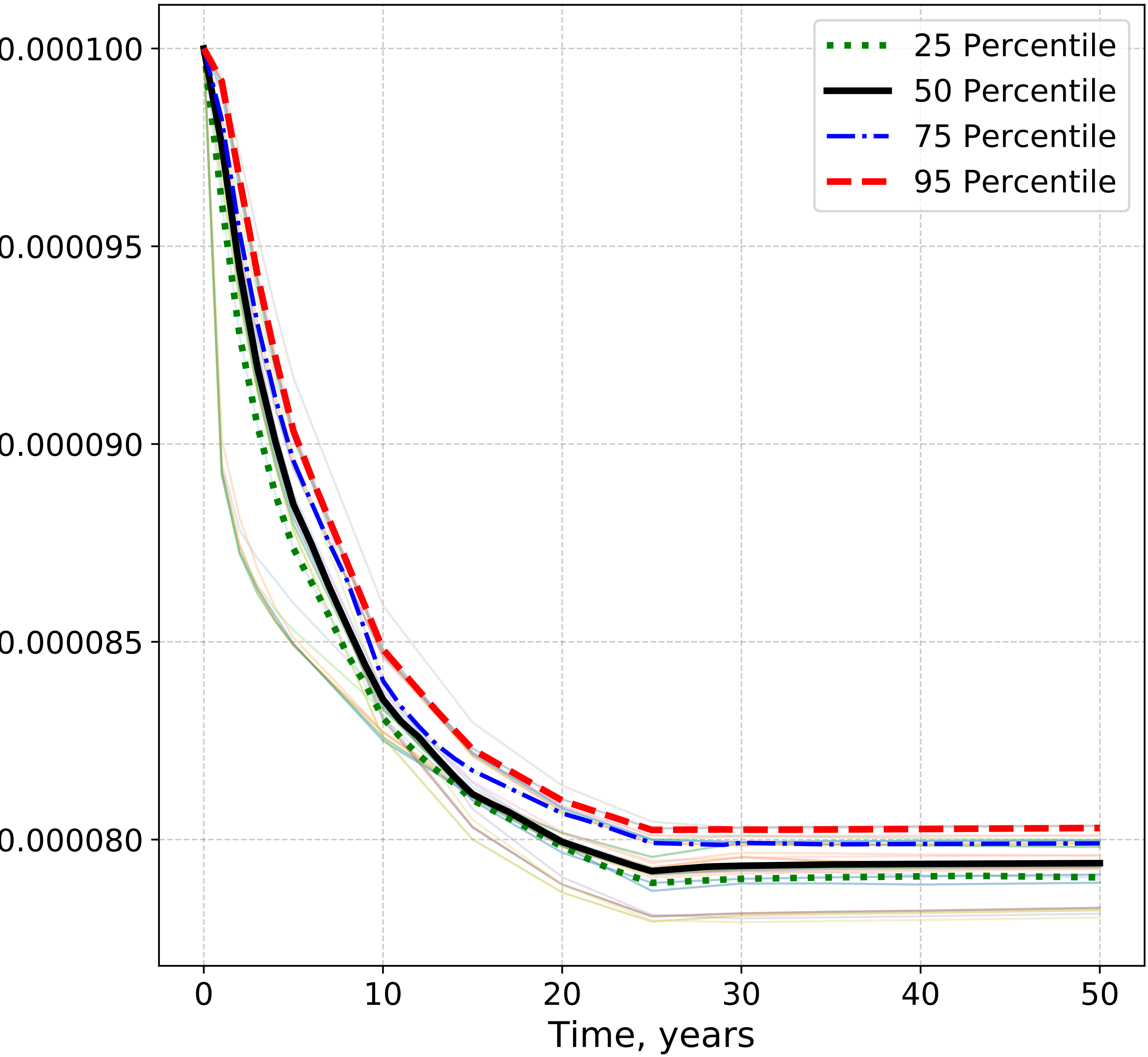

Figure E-1. Saturation History. Layer 54 of the reservoir simulation was used in the IAM analysis.

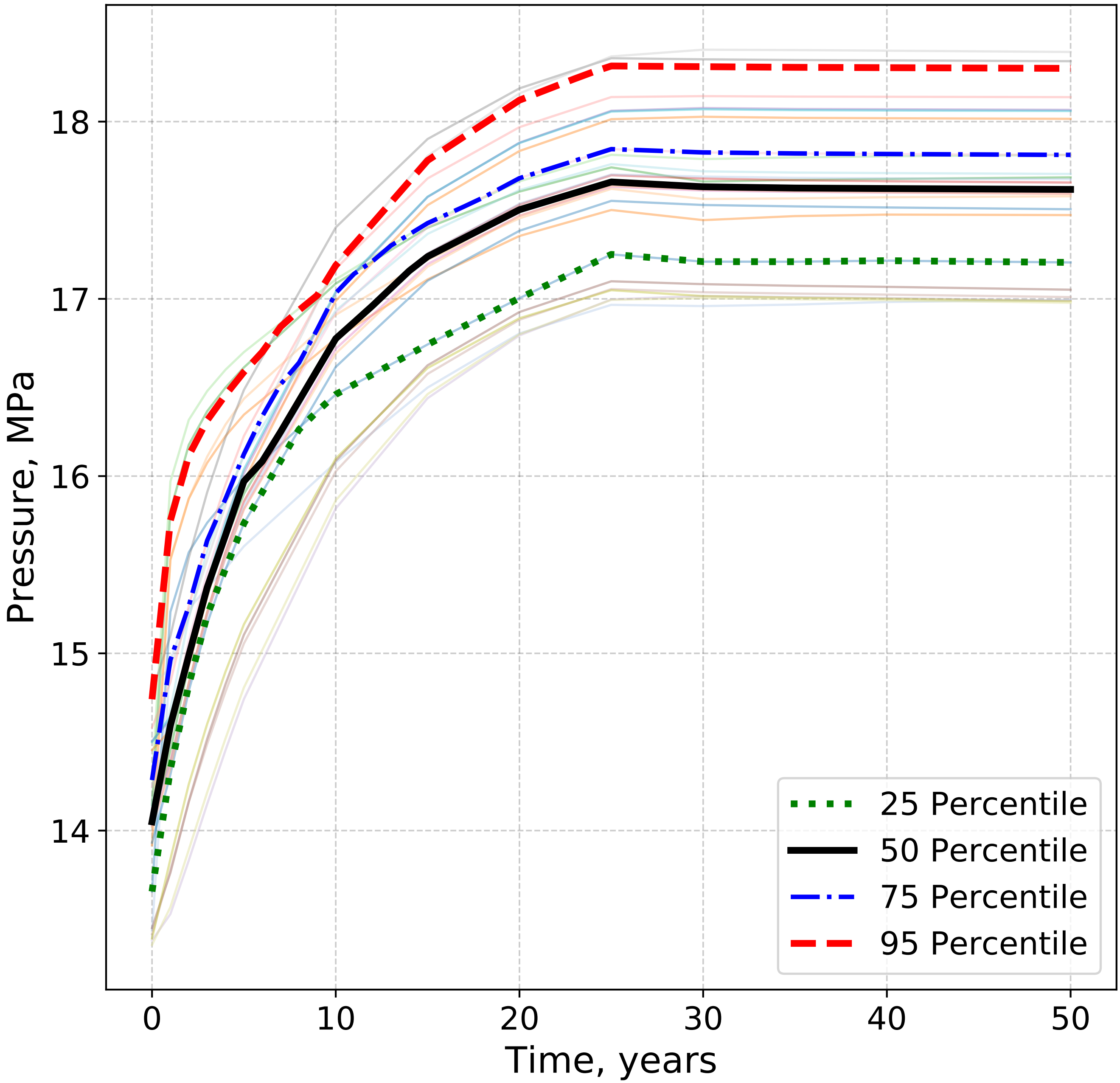

Figure E-2. Pressure History. Layer 54 of the reservoir simulation was used in the IAM analysis.

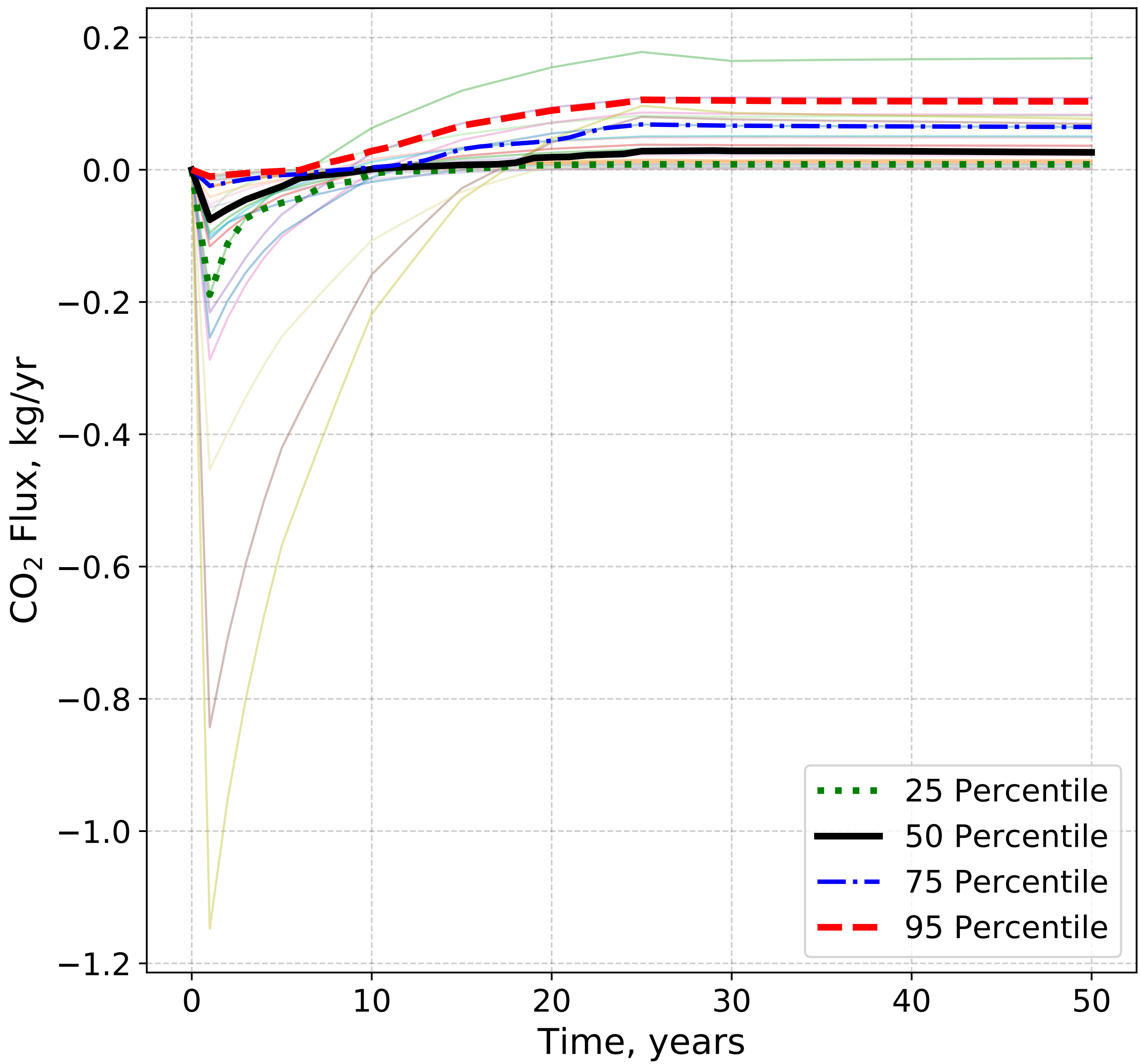

Figure E-3. CO_2 Flux to Aquifer 1. Layer 54 of the reservoir simulation was used in the IAM analysis.

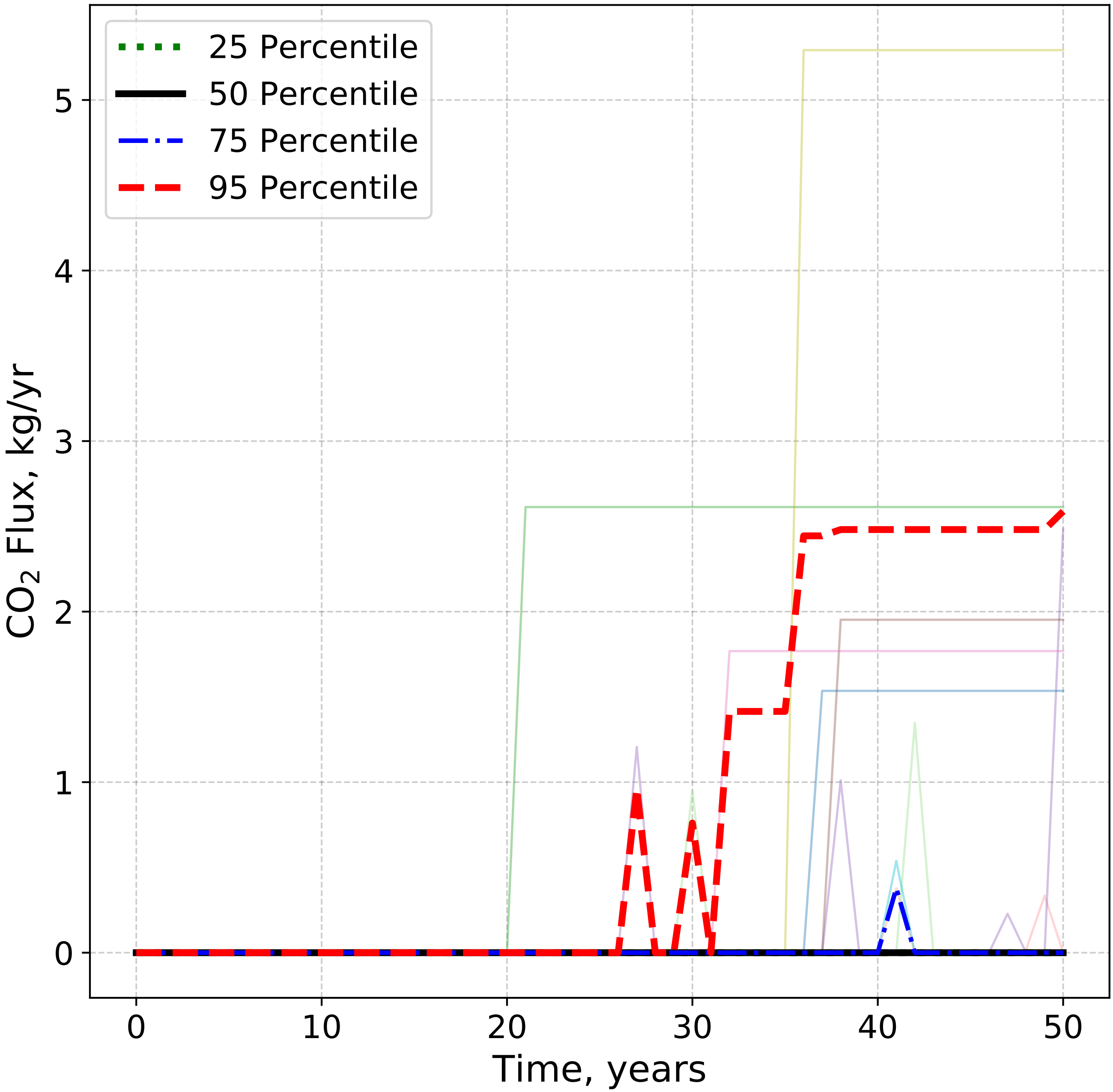

Figure E-4. CO_2 Flux to Aquifer 2. Layer 54 of the reservoir simulation was used in the IAM analysis.

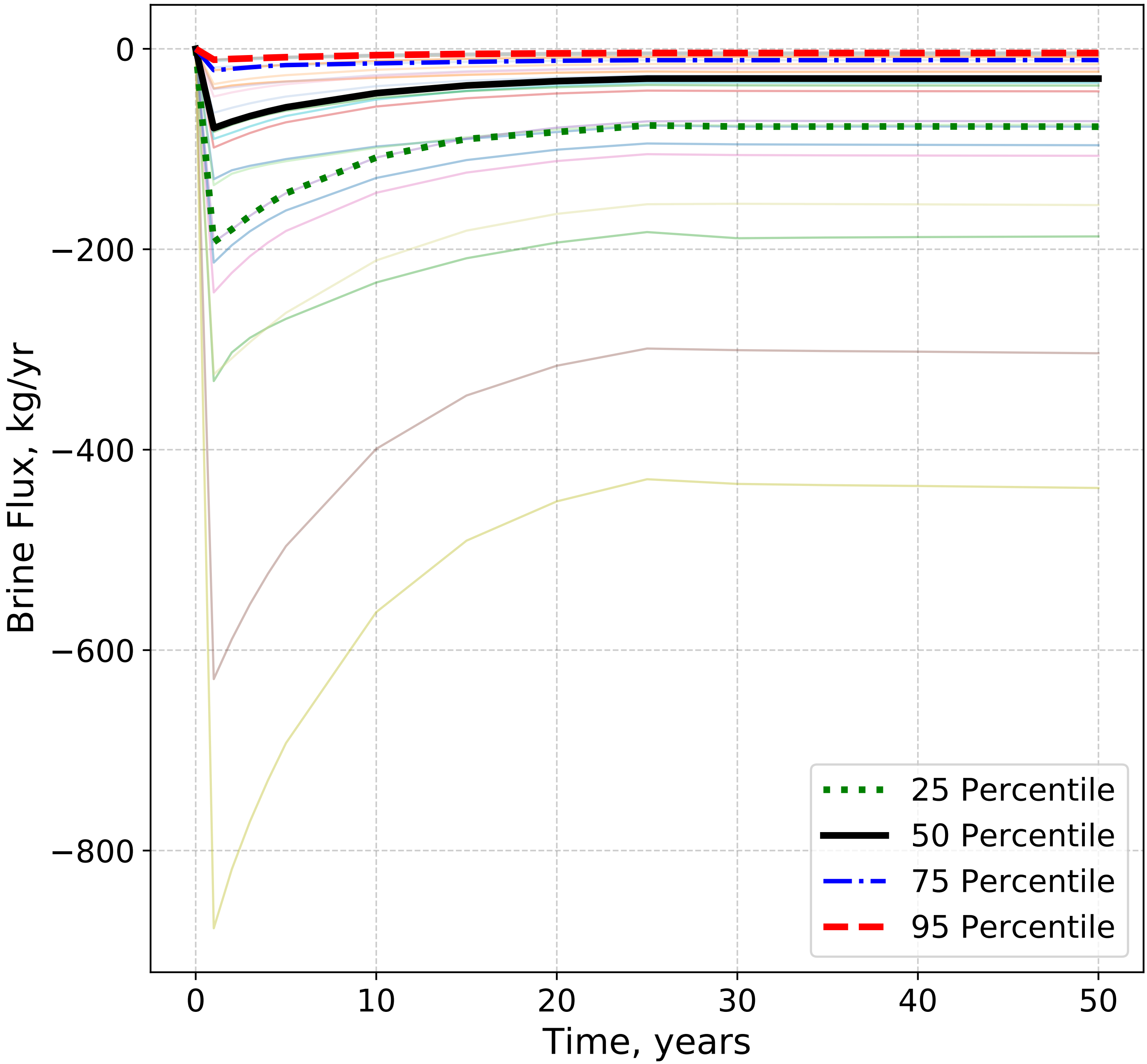

Figure E-5. Brine Flux to Aquifer 1. Layer 54 of the reservoir simulation was used in the IAM analysis.

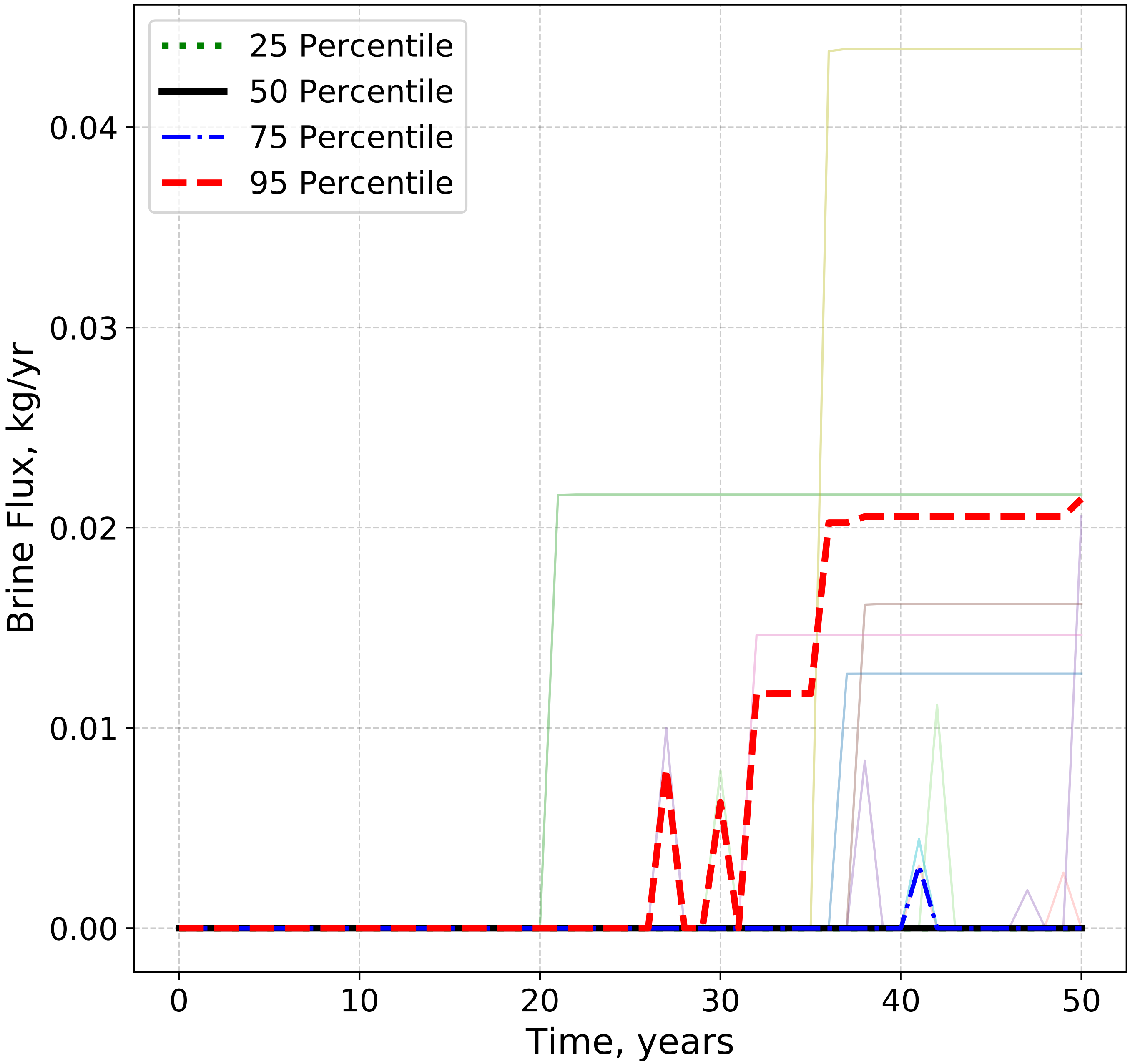

Figure E-6. Brine Flux to Aquifer 2. Layer 54 of the reservoir simulation was used in the IAM analysis.

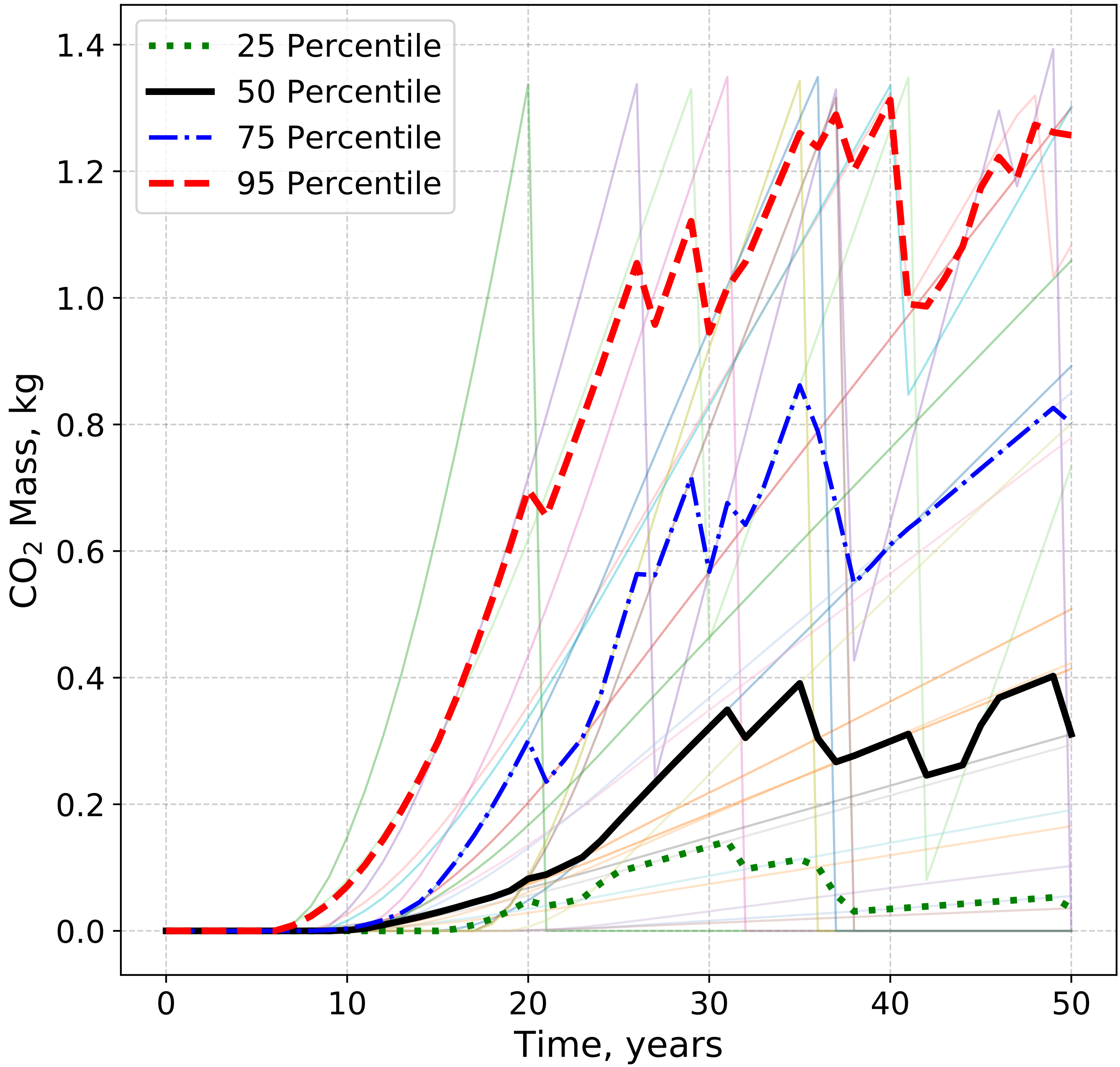

Figure E-7. CO_2 Mass to Aquifer 1. Layer 54 of the reservoir simulation was used in the IAM analysis.

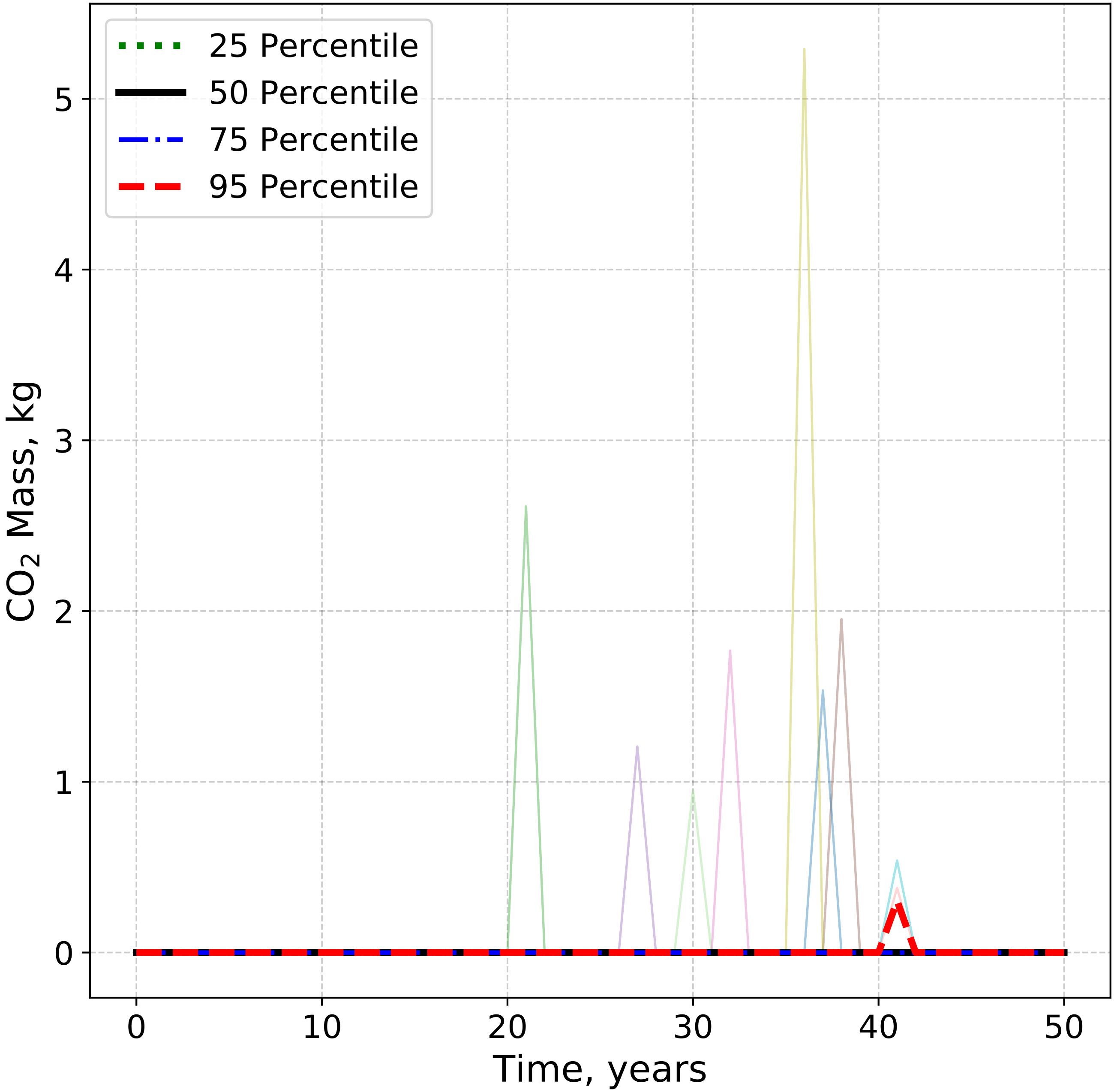

Figure E-8. CO_2 Mass to Aquifer 2. Layer 54 of the reservoir simulation was used in the IAM analysis.

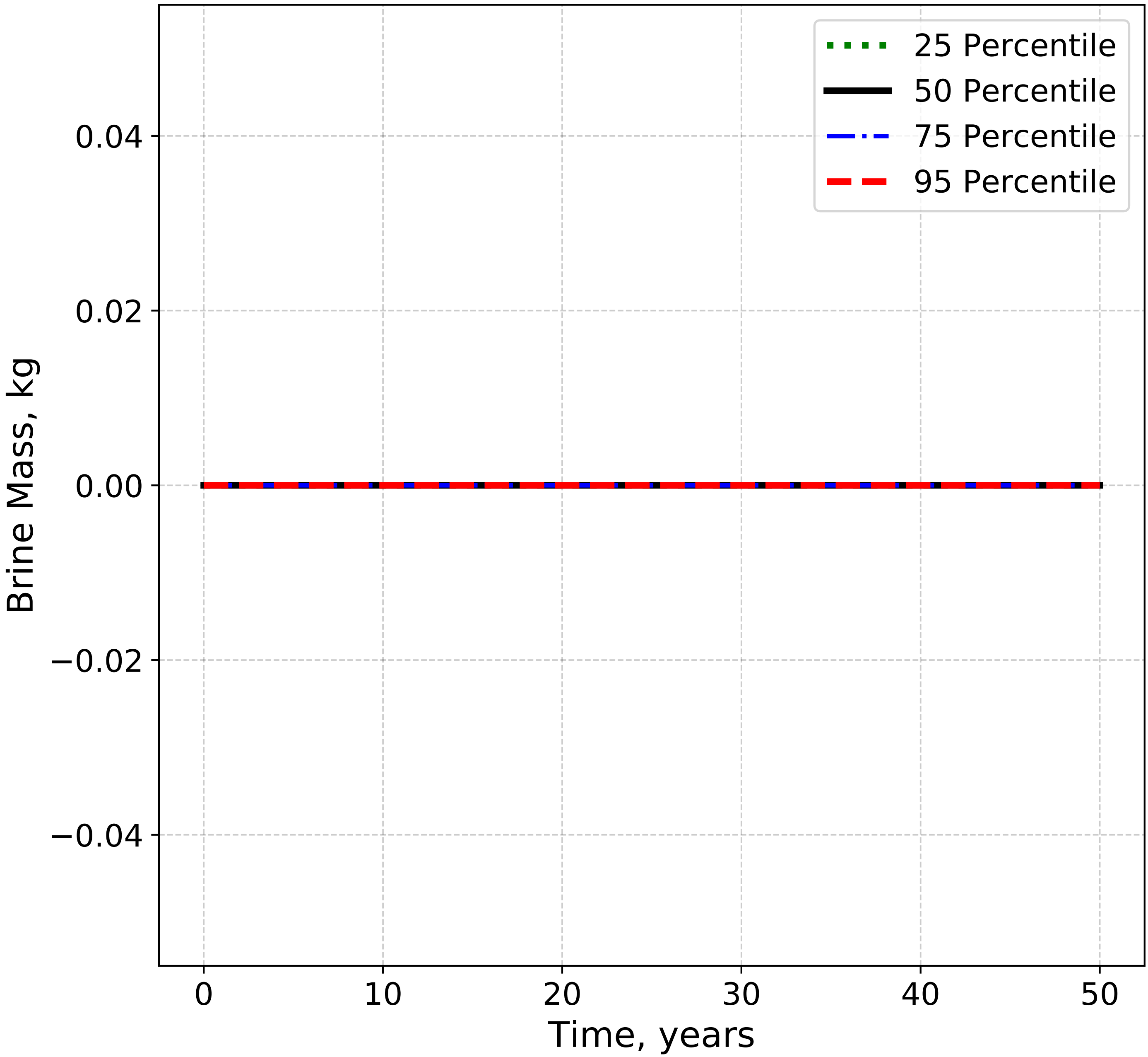

Figure E-9. Brine Mass to Aquifer 1. Layer 54 of the reservoir simulation was used in the IAM analysis.

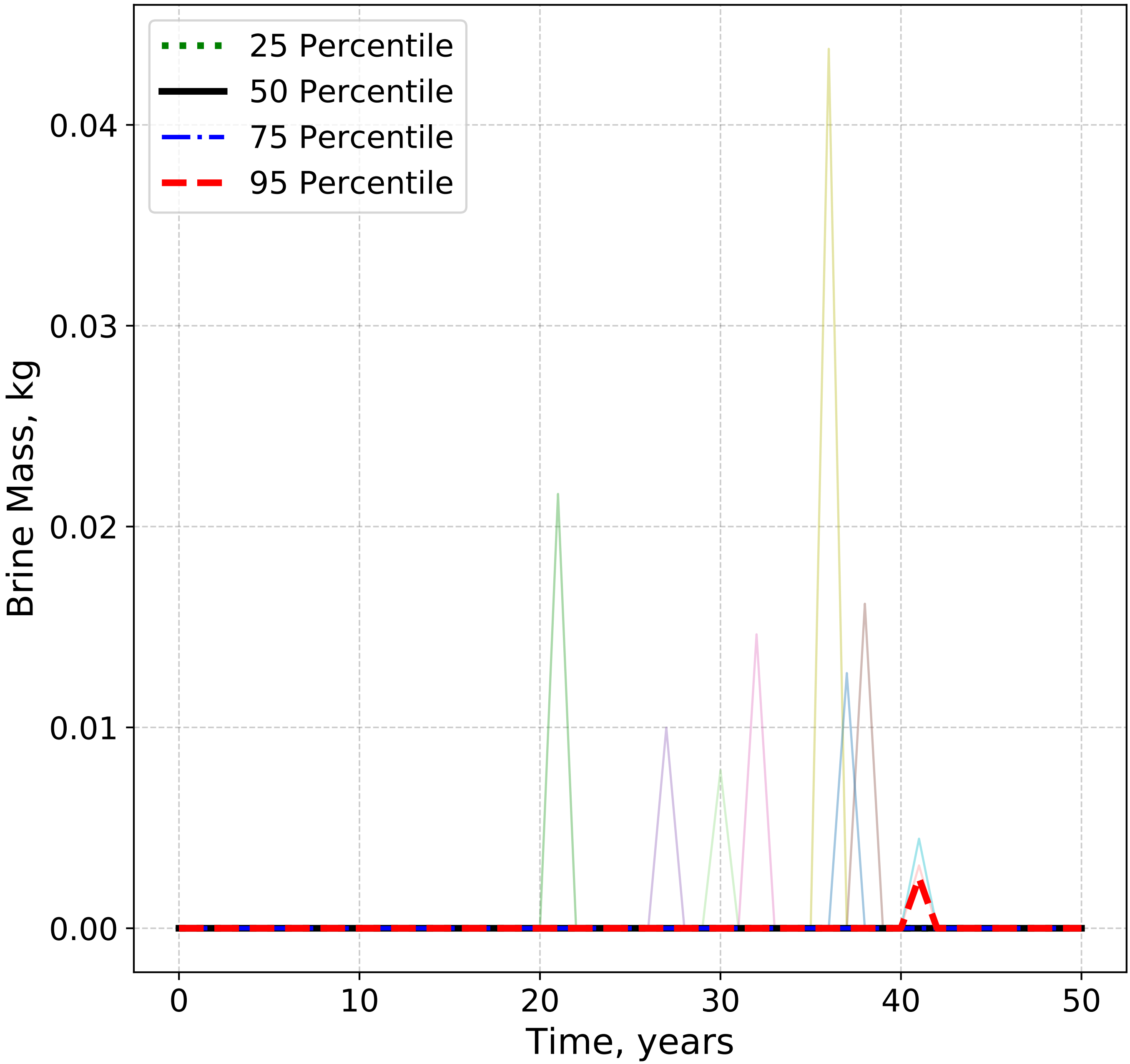

Figure E-10. Brine Mass to Aquifer 2. Layer 54 of the reservoir simulation was used in the IAM analysis.

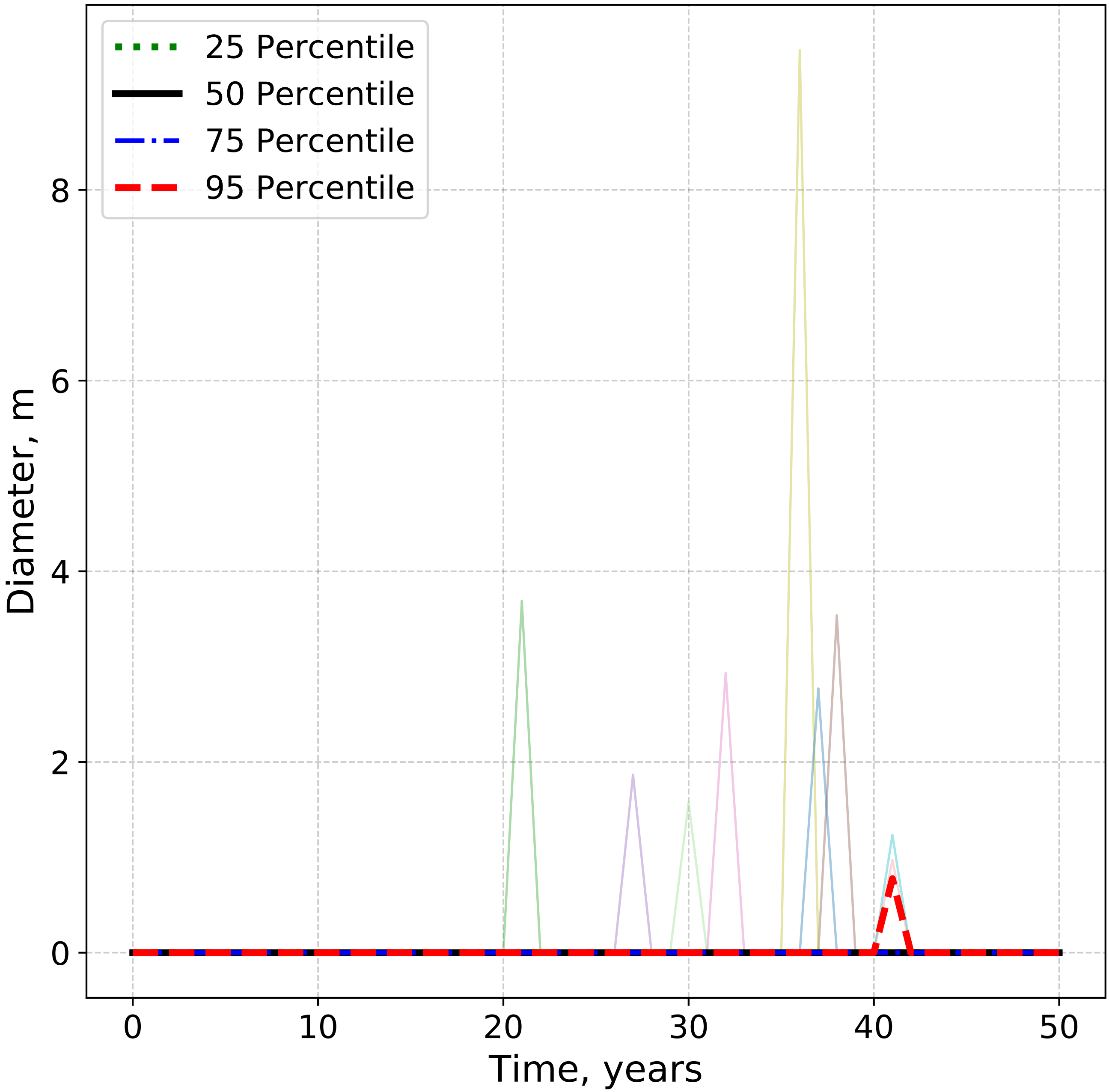

Figure E-11. pH Impact to Aquifer 2 in the Horizontal Direction. Layer 54 of the reservoir simulation was used in the IAM analysis.

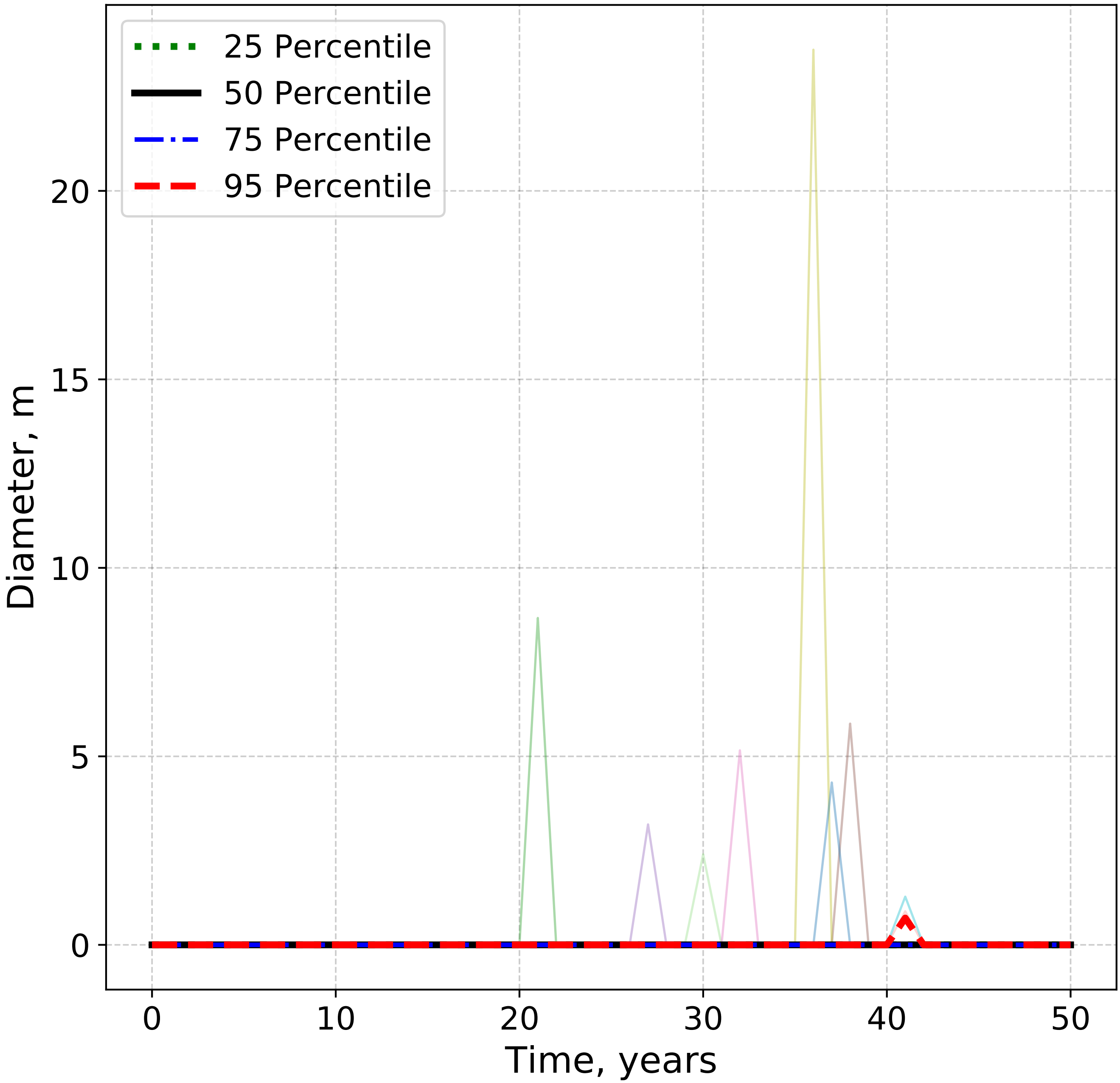

Figure E-12. pH Impact to Aquifer 2 in the Vertical Direction. Layer 54 of the reservoir simulation was used in the IAM analysis.

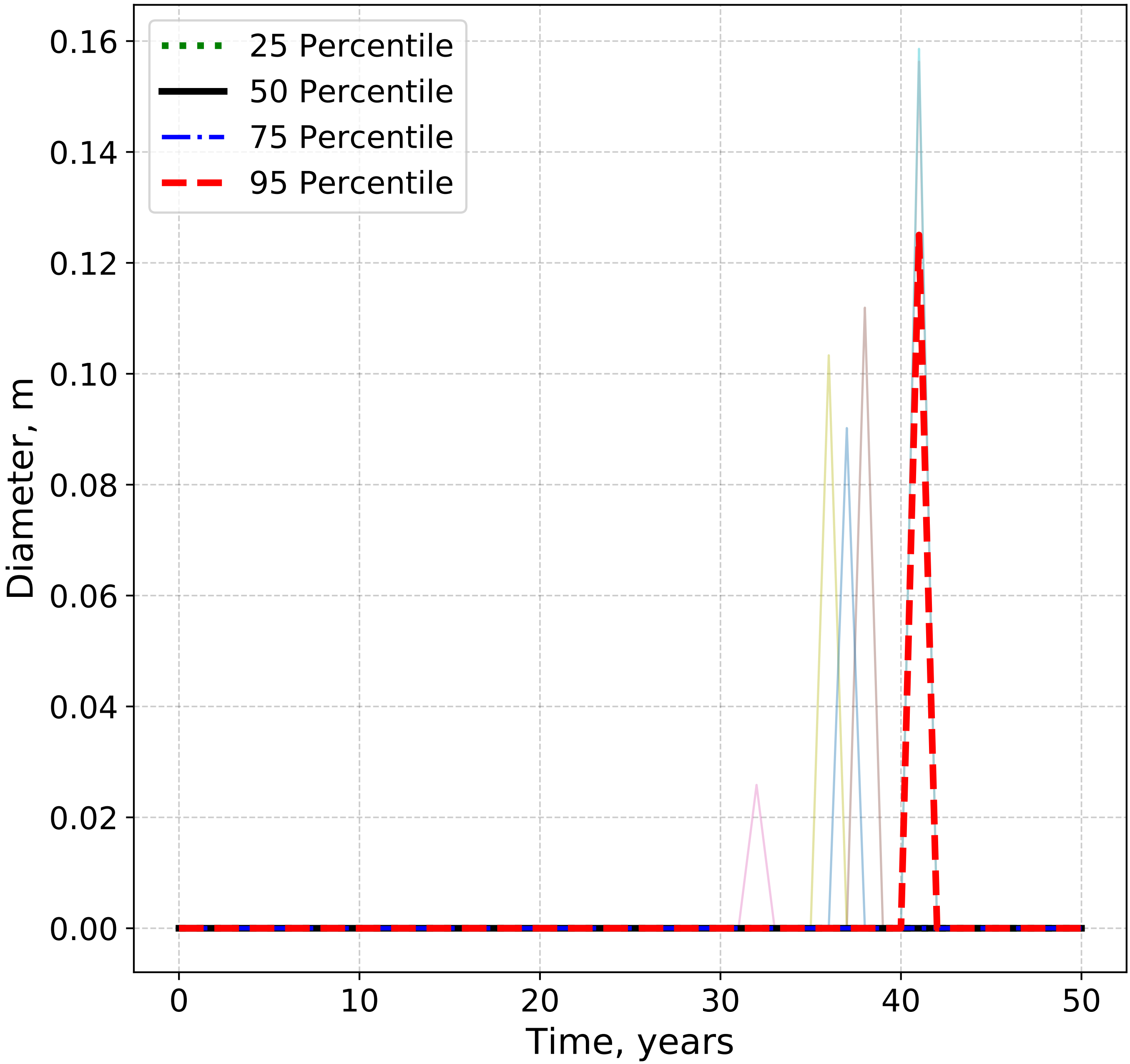

Figure E-13. Pressure Impact to Aquifer 2 in the Horizontal Direction. Layer 54 of the reservoir simulation was used in the IAM analysis.

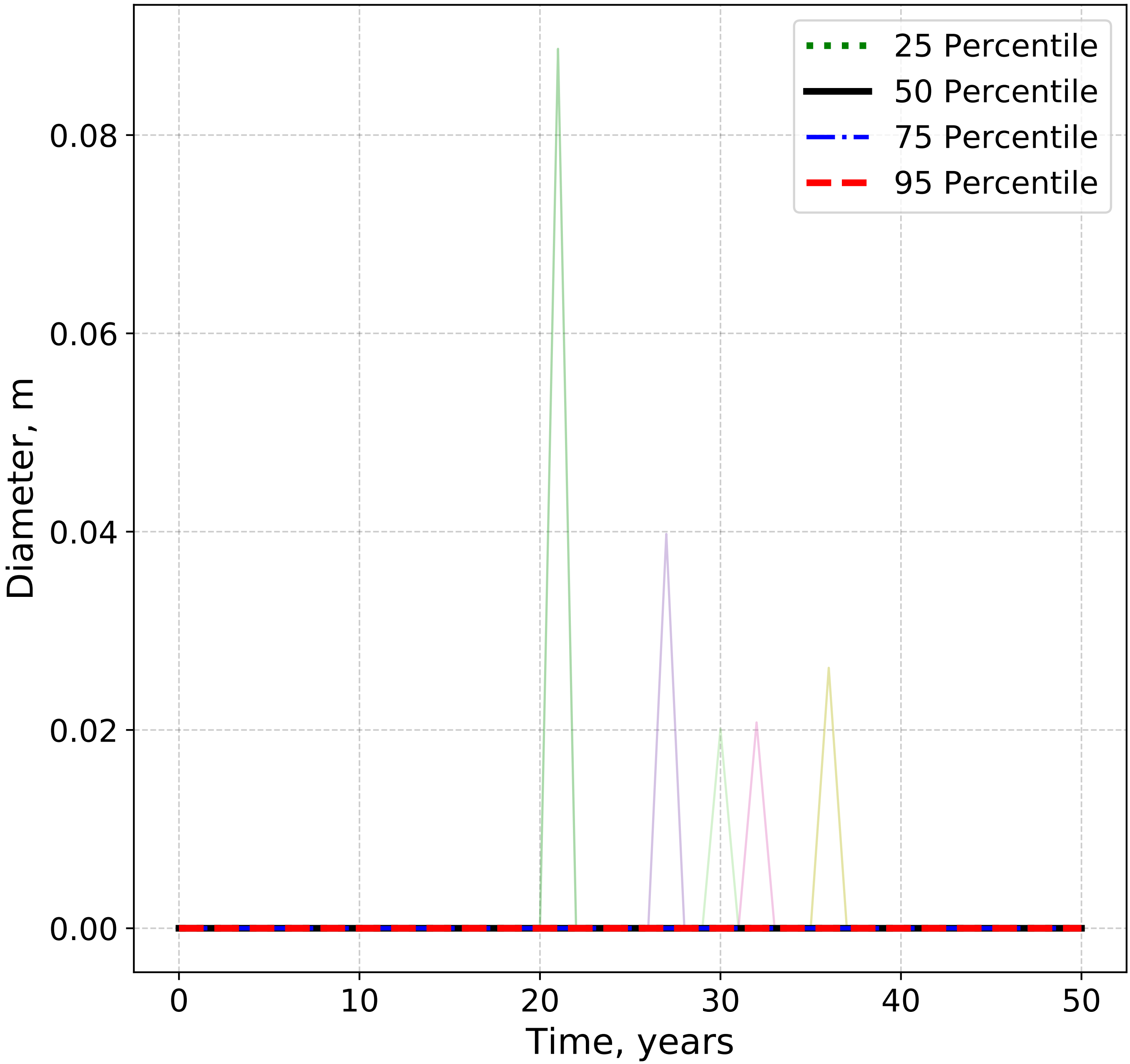

Figure E-14. Pressure Impact to Aquifer 2 in the Vertical Direction. Layer 54 of the reservoir simulation was used in the IAM analysis.

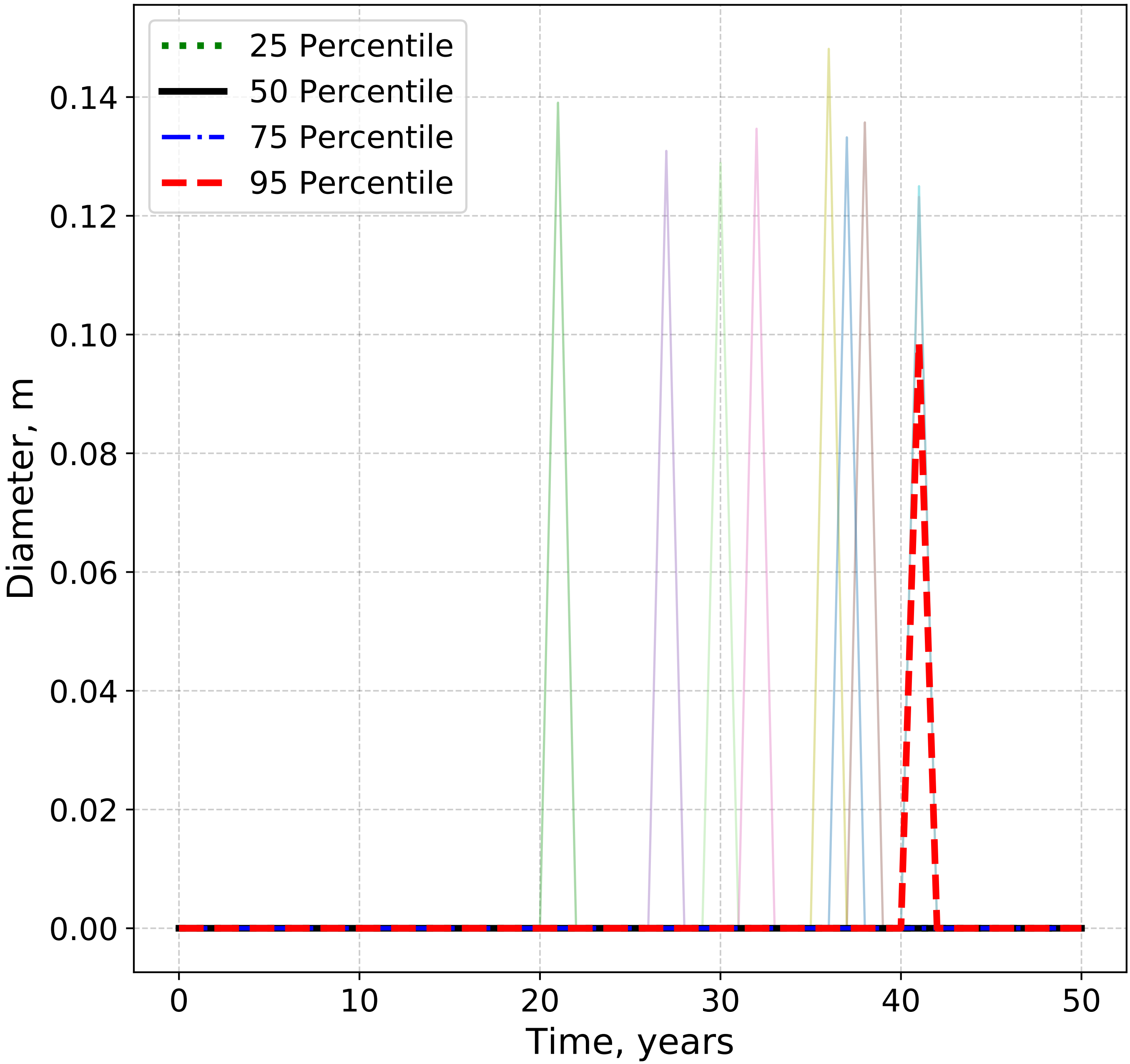

Figure E-15. TDS Impact to Aquifer 2 in the Horizontal Direction. Layer 54 of the reservoir simulation was used in the IAM analysis.

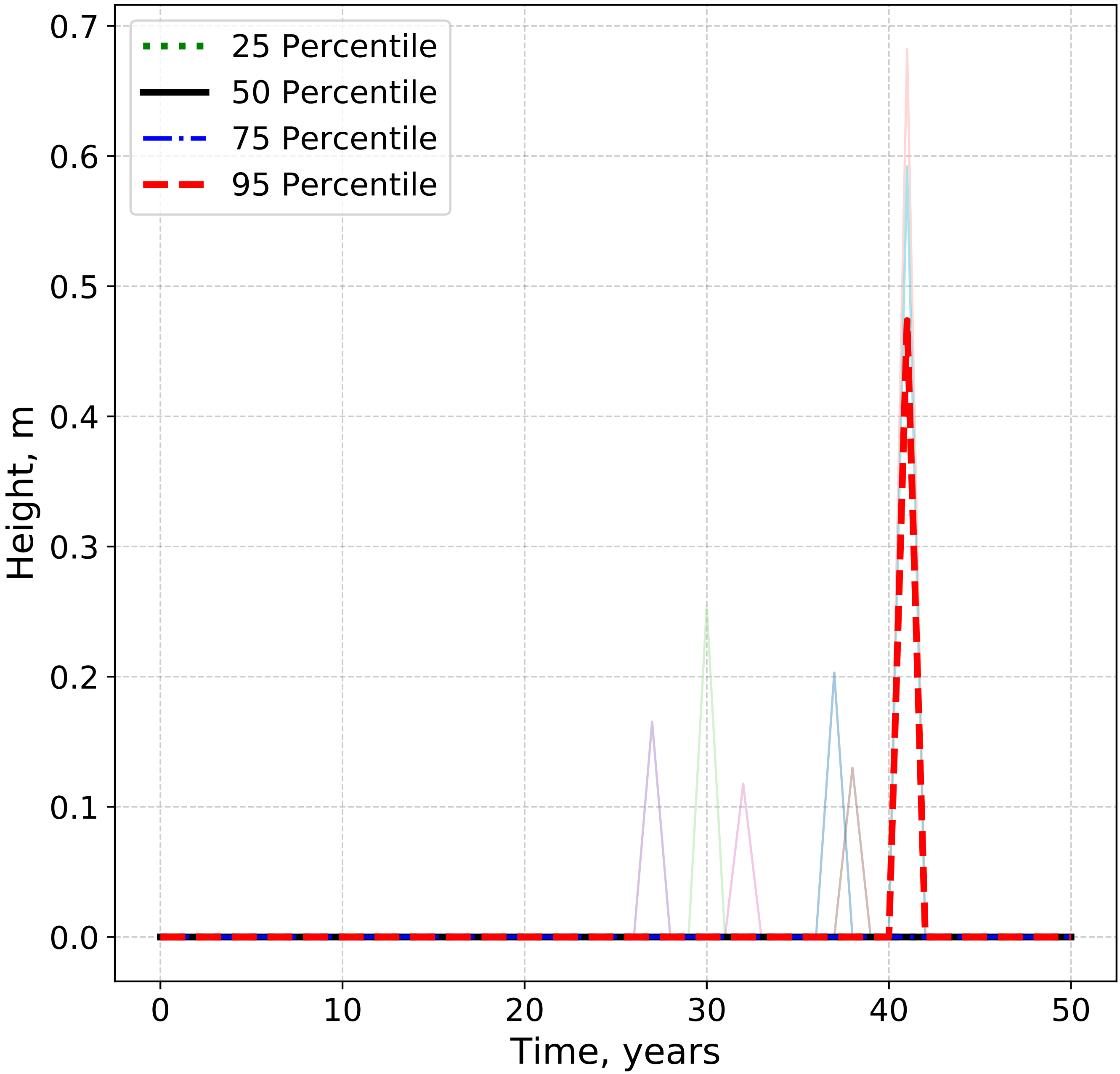

Figure E-16. TDS Impact to Aquifer 2 in the Vertical Direction. Layer 54 of the reservoir simulation was used in the IAM analysis.

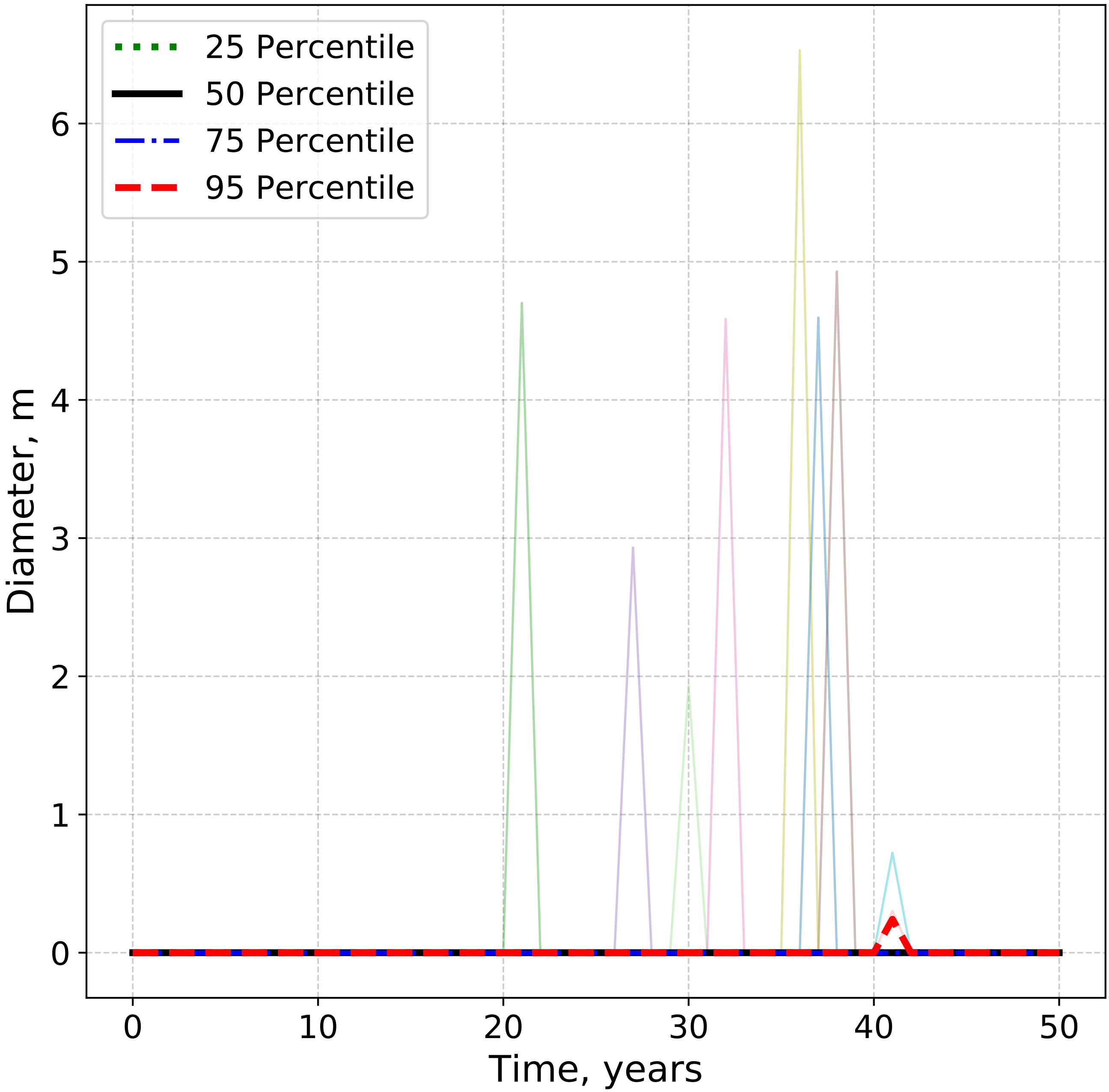

Figure E-17. Dissolved CO_2 Impact to Aquifer 2 in the Horizontal Direction. Layer 54 of the reservoir simulation was used in the IAM analysis.

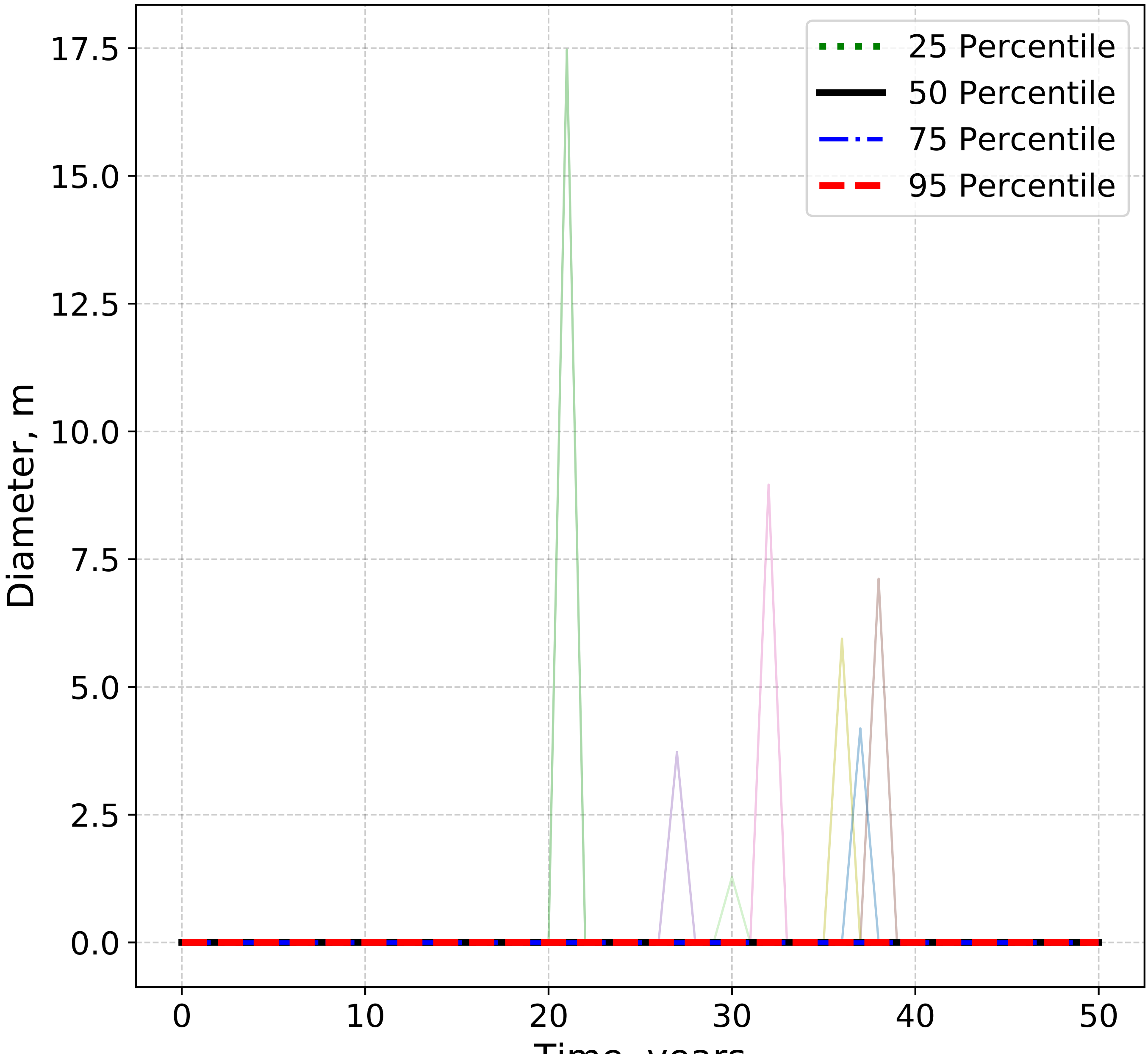

Figure E-18. Dissolved CO_2 Impact to Aquifer 2 in the Vertical Direction. Layer 54 of the reservoir simulation was used in the IAM analysis.

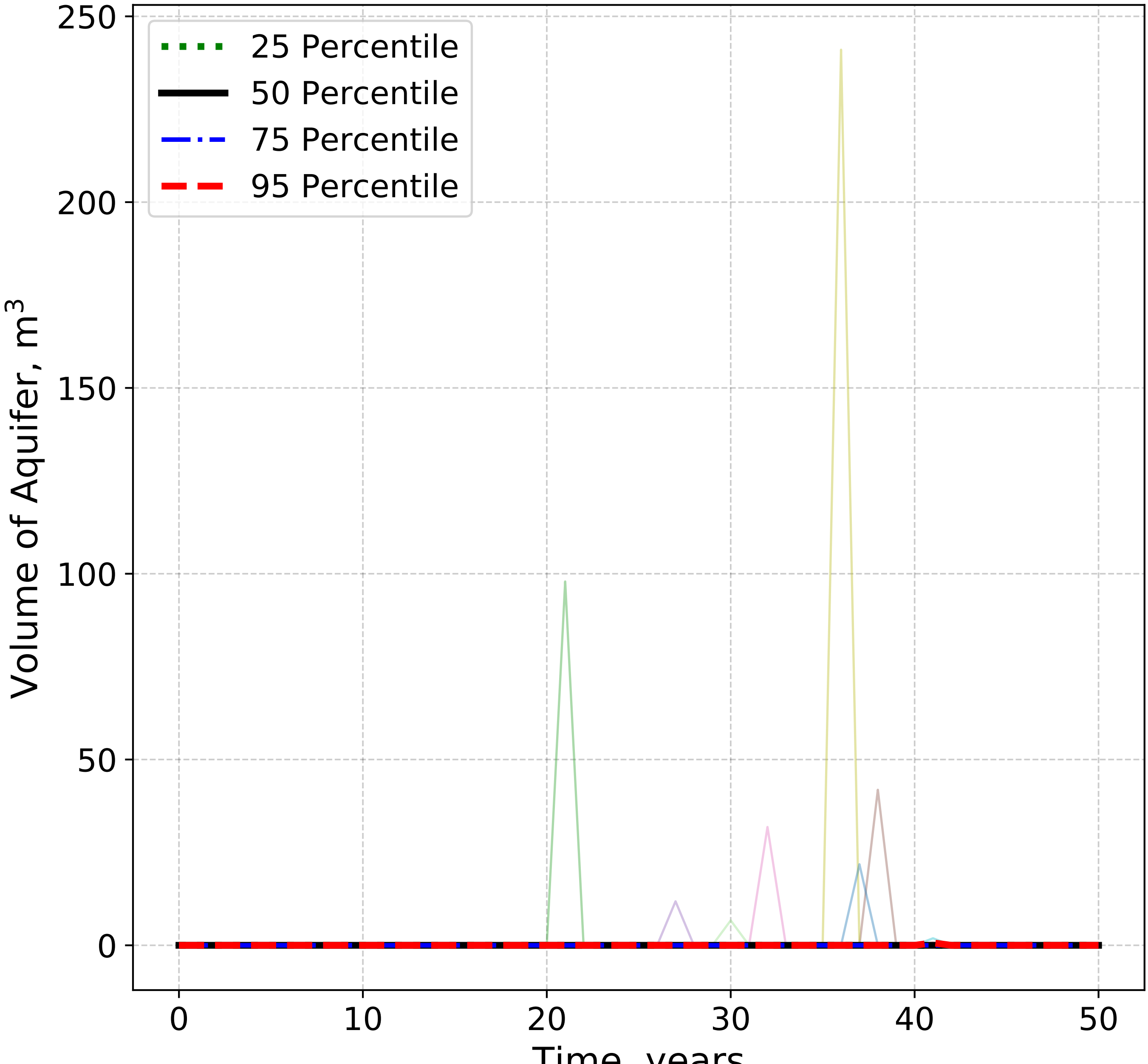

Figure E-19. pH Impact to Aquifer 2. Layer 54 of the reservoir simulation was used in the IAM analysis.

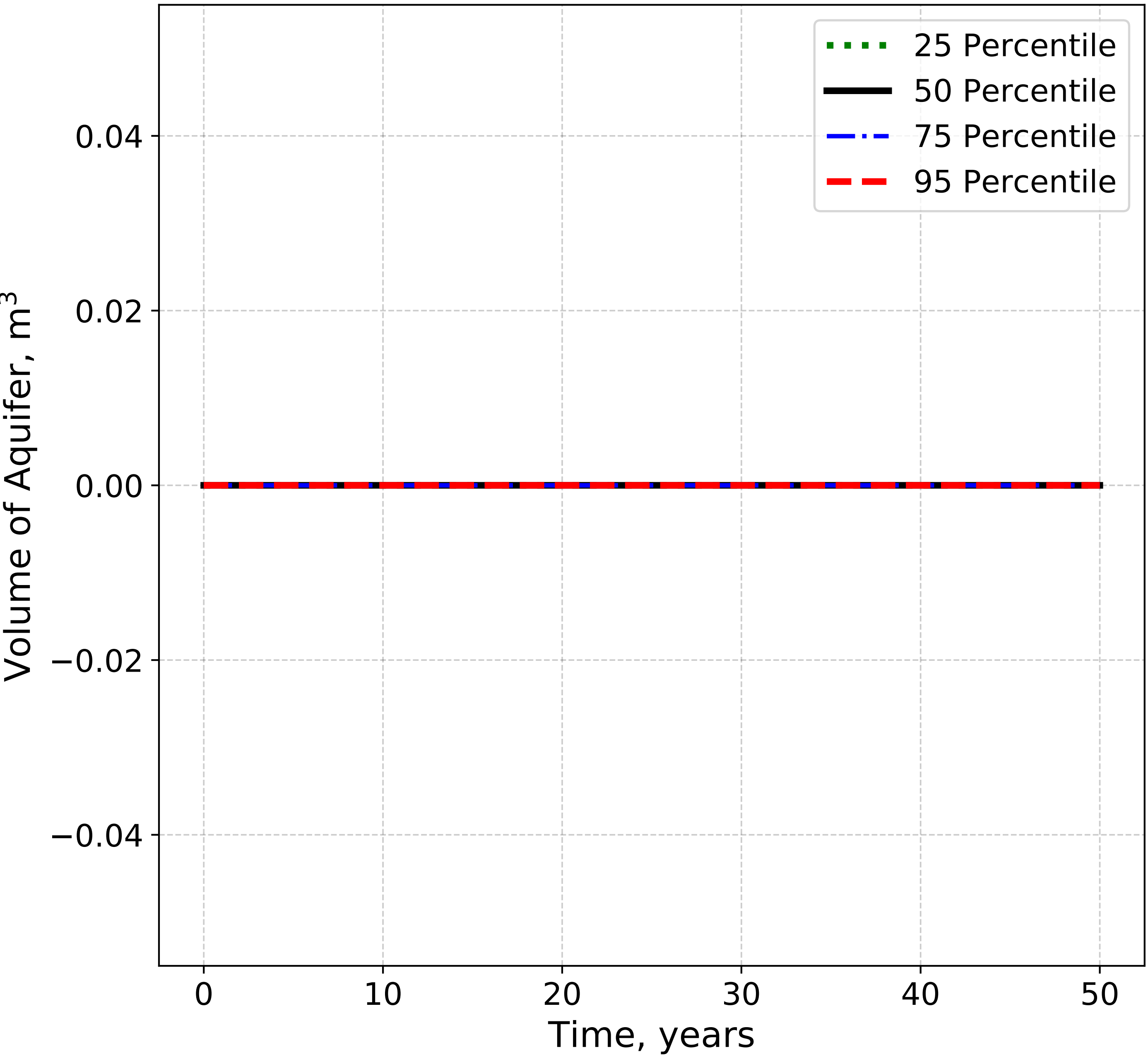

Figure E-20. Pressure Impact to Aquifer 2. Layer 54 of the reservoir simulation was used in the IAM analysis.

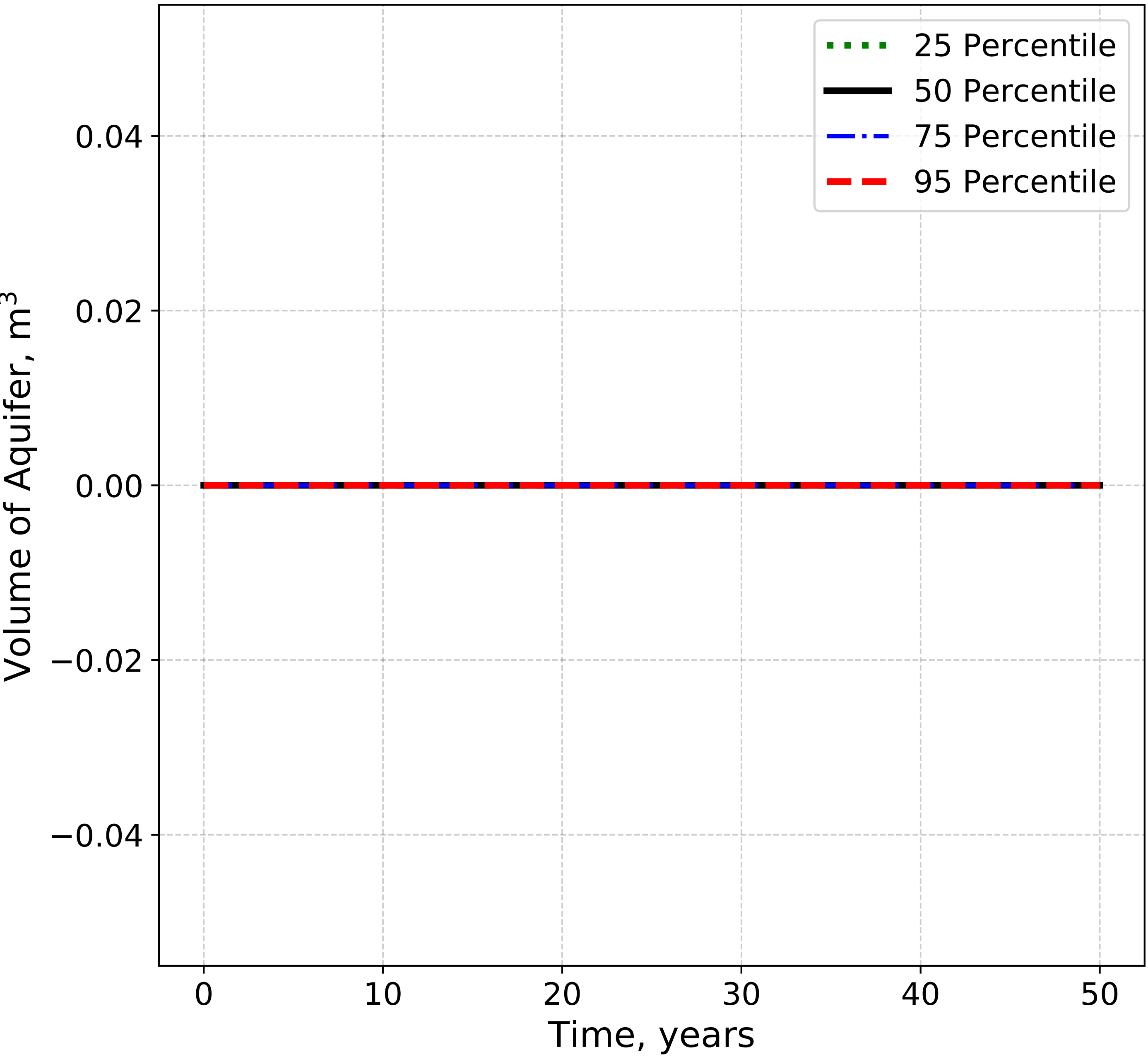

Figure E-21. TDS Impact to Aquifer 2. Layer 54 of the reservoir simulation was used in the IAM analysis.

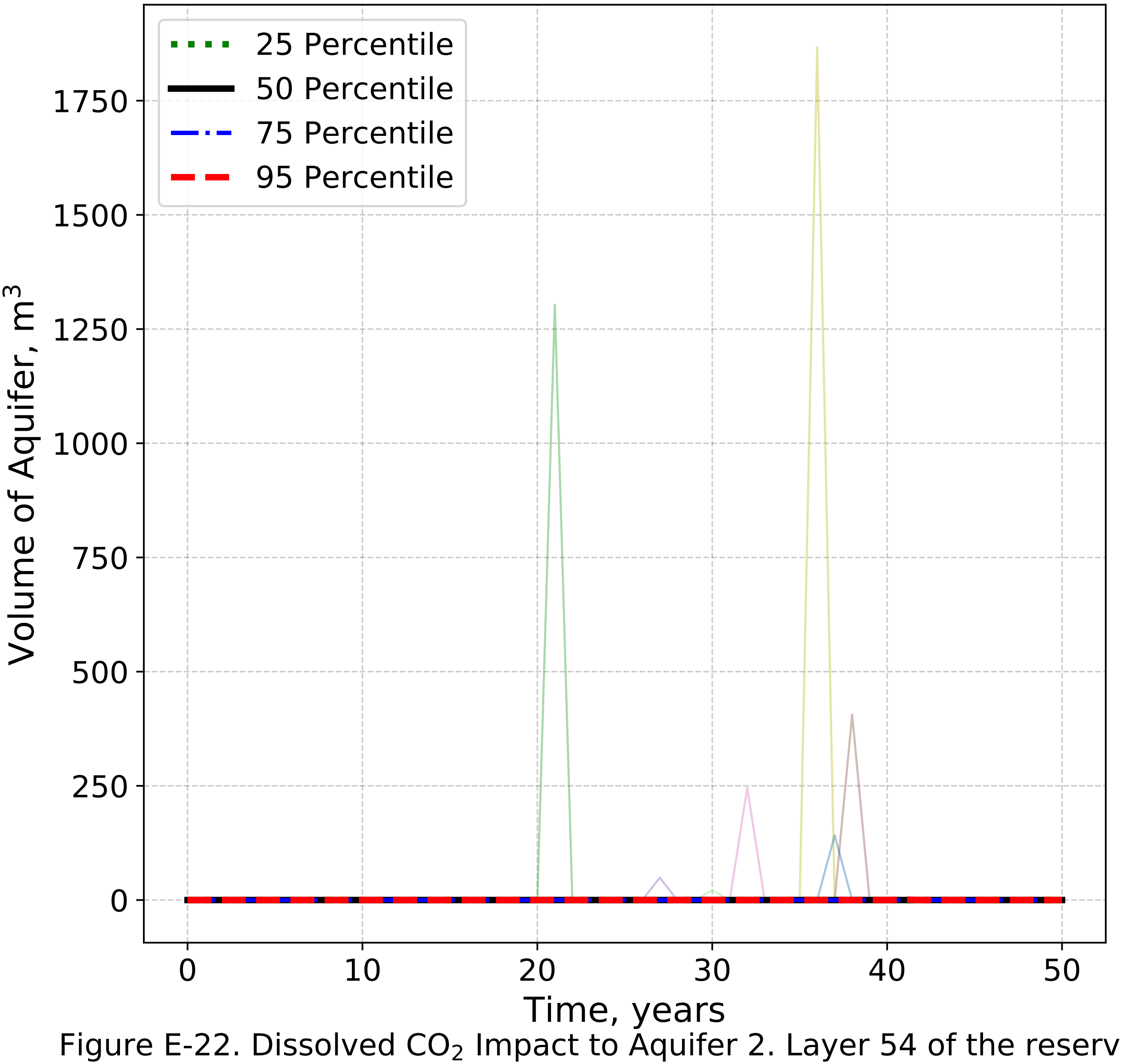

Figure E-22. Dissolved CO_2 Impact to Aquifer 2. Layer 54 of the reservoir simulation was used in the IAM analysis.

Appendix F – SOSAT User Interface

To run SOSAT, all required parameters are set in the four tabs of the SOSAT user interface (see below). The analysis routine is launched and provided two distinct plots and their associated data: the posterior distribution plot and the fault activation probability plot. The screenshots below illustrate how input parameters are provided.

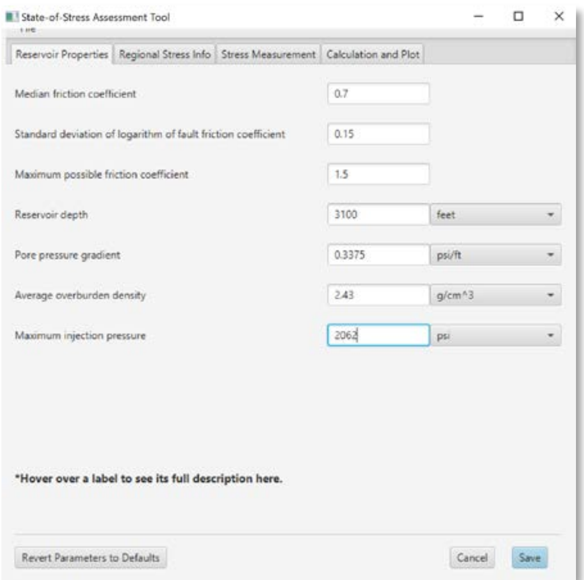

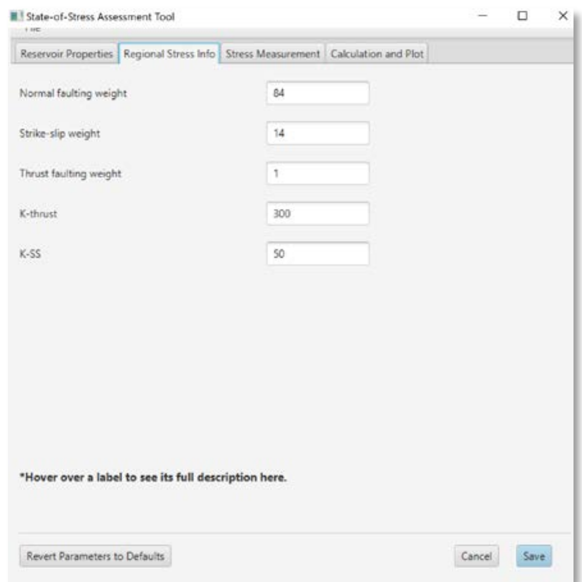

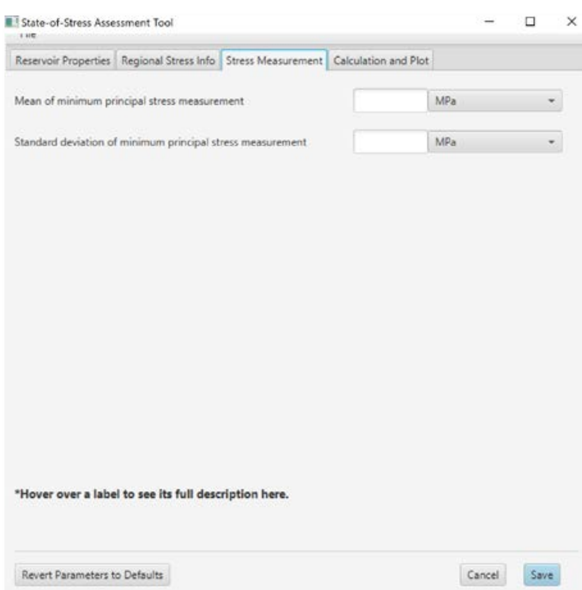

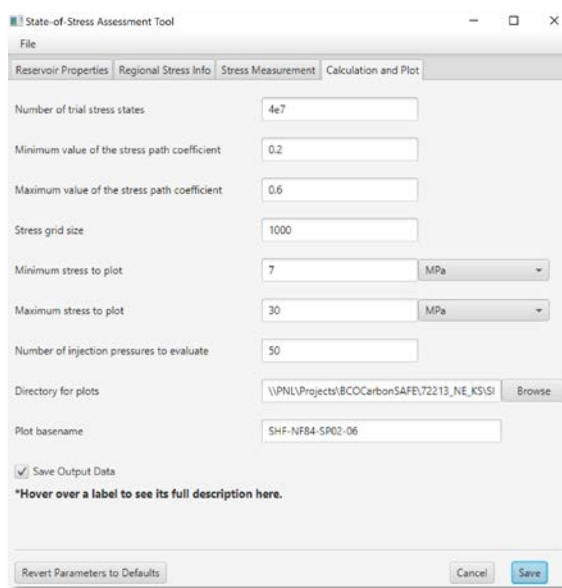

Pacific Northwest National Laboratory

902 Battelle Boulevard
P.O. Box 999
Richland, WA 99354
1-888-375-PNNL (7665)

www.pnnl.gov